Title
Understanding Star Formation and AGN Activity at z~2-3

Author
Hainline, Kevin Nicholas

Publication Date
2012

Peer reviewed|Thesis/dissertation

University of California
Los Angeles

Understanding Star Formation and AGN Activity at $z \sim 2-3$

A dissertation submitted in partial satisfaction
of the requirements for the degree
Doctor of Philosophy in Astronomy

by

Kevin Nicholas Hainline

2012

Abstract of the Dissertation

Understanding Star Formation and AGN Activity at $z \sim 2-3$

by

Kevin Nicholas Hainline

Doctor of Philosophy in Astronomy

University of California, Los Angeles, 2012

Professor Alice E. Shapley, Chair

There is compelling evidence that the growth of supermassive black holes and the stellar populations of their host galaxies are intricately linked. At the same time, the exact relationship between the buildup of stellar mass and the growth of supermassive black holes is still not well understood. At $z \sim 2$, both star-formation and Active Galactic Nuclei (AGN) activity in the universe were at peak levels, and this epoch is ideal for exploring the coevolution of stars and supermassive black holes. This dissertation examines high-redshift galaxies, looking at the particular properties of star-forming galaxies, the stellar populations of AGNs and the relationship between black hole and star-formation activity at $z \sim 2-3$. I have used the magnification afforded by gravitational lensing of $z \sim 2$ star-forming galaxies to measure important physical properties of the stars and gas in these galaxies. Using near-IR spectroscopy, I have calculated the metallicities, ionization parameters, star-formation rates, and dynamical masses for two galaxies which help to explain the differences between local- and high- redshift star-forming galaxies. The third and fourth chapters of this work cover the analysis of a sample of $z \sim 2-3$ AGNs drawn from the UV-selected Lyman Break Galaxy

(LBG) survey. I present a rest-frame UV composite spectrum for this sample of AGNs. This spectrum shows many emission and absorption features, such as HI Lyman-alpha, NVλ1240, NIV]$\lambda\lambda$1483,1486, CIV$\lambda\lambda$1548,1550, HeIIλ1640, and CIII]$\lambda\lambda$1907,1909. Redshifted SiIVλ1394 absorption provides evidence for outflowing high-ionization gas in these objects at speeds of 10^3 km/s. Finally, by using optical, near-IR, and mid-IR photometry, which covers the rest-frame UV to near-IR portions of the galaxies spectral energy distributions, I have modeled the SEDs of the AGNs that comprise this sample. I have developed a unique dual-component modeling approach that allows me to correct for the presence of an AGN. Based on these results, I have explored the relationship in the host galaxy between AGN activity, maturity of the stellar population, and regulation of star formation.

The dissertation of Kevin Nicholas Hainline is approved.

Van M. Savage

Jean L. Turner

Matt A. Malkan

Alice E. Shapley, Committee Chair

University of California, Los Angeles

2012

To my Mom and Dad,

the anti-parents.

Table of Contents

List of Figures

List of Tables

Acknowledgments

The completion of my doctoral dissertation would not have been possible but for the support of many people. Most importantly, I wish to acknowledge Alice Shapley, who could not have been a better advisor, astronomy role model, and friend. I am indebted to her for the many hours she spent preparing for observing runs, reviewing results, revising papers, and helping to guide my research. I am a far different, and a far better, astronomer now than I was when I first walked into her office four years ago, and this is due to her patience, intelligence, and kindness.

I am heavily indebted to the various collaborators who have given their time assisting with observations, data analysis, and discussion. In particular, I would like to thank Jenny Greene, whose insight was invaluable in the completion of this dissertation. Her thoughtful (and quick) comments on each draft greatly strengthened the science presented in this work. Naveen Reddy, Dawn Erb, and Chuck Steidel were also quite helpful, and I cannot thank them enough for the time they gave.

I would also like to thank Matt Malkan, who first introduced me to active galactic nuclei, and served as my advisor for the first two years of my graduate career. Jean Turner, who sits on my dissertation committee, and the rest of the UCLA Astronomy Faculty have been very helpful as I have progressed as a graduate student, and I would like to thank them. The graduate students in the department have also been the best group of friends I could ask for, and I would not have been able to survive this experience without their support. In particular I wish to thank Kathy Kornei for always being just down the hallway

ready to answer even my silliest questions, Ian Crossfield, the astronomical Abbot to my Costello, Jeff Chilcote, without whom the planetarium would probably have crumbled to the ground, Kristin Kulas, the other half of the blind-offset dream team, David Rodriguez, Puerto Rico's best Chewbacca impressionist, and Chris Crockett, the person I most want to see each year at the AAS (and also, due to his height, the easiest to find). The graduate department at UCLA is a wonderful place due to the quality of the students that have attended.

My family and friends have also been very supportive during the creation of this dissertation, and I wish to thank them. To my parents, thank you for never telling me that "astronomer" was not a viable career option. Thank you to my brother Robert, for your kindness, and also for being more into sports when we were younger, which allowed me to be the nerd of the family. Thank you to David Schimon and Julia Fornaca, who will always go out for late night pie. Thank you to Nick Aase, who would drop anything, at any time, to watch *Jurassic Park* with me. Finally, thank you to the beautiful Rachel Mykkanen, who taught me patience, and instilled in me a sense of understanding that I sorely needed. You are so important, Rachel.

Chapter 2 is a version of Hainline et al. (2009) and is reproduced by permission of the AAS. I thank Xin Liu, Anna Quider, Thomas Diehl, and Huan Lin for their assistance. I also acknowledge Lindsay King for kindly providing the VLT/FORS2 $\mathcal{R}$-band image of the Cosmic Horseshoe used in the paper.

Chapter 3 is a version of Hainline et al. (2011) and is reproduced by permission of the AAS. I thank Dawn Erb and Max Pettini for very helpful discussions. I also acknowledge the referee, David Alexander, for a thorough and constructive report, which significantly improved the paper.

Chapter 4 is a version of a paper recently submitted to the Astrophysical

Journal. I wish to thank both James Aird and Alison Coil for helpful discussions regarding the completeness of the AGN sample.

The data contained in this work were obtained at the W.M. Keck Observatories on Mauna Kea, Hawai'i. I wish to extend special thanks to those of Hawaiian ancestry on whose sacred mountain we are privileged to be guests. Without their generous hospitality, most of the observations presented herein would not have been possible. I also wish to thank the many incredibly helpful telescope operators and staff scientists at the Keck Observatory, Gemini Observatory, and Carnegie Observatories.

Vita

2006	B.S. (Physics), Harvey Mudd College, Claremont, CA.
2006 - 2010	Teaching Assistant, Astronomy Department, UCLA, Los Angeles, California.
2008	M.S. (Astronomy), UCLA.
2008–present	Research Assistant, Astronomy Department, UCLA.

Publications and Presentations

Tommasin, S., Spinoglio, L., Hainline, K.N., Malkan, M. A., Smith, H. Seyfert Galaxies in the Local Universe: Analysis of Spitzer Spectra of a Complete Sample. *Memorie della Societa Astronomica Italiana.* v.79, p.1275 (2008).

Hainline, K.N., Shapley, A.E., Kornei, K.A., Pettini, M., Buckley-Geer, E., Allam, S.S.; Tucker, D.L., Rest-Frame Optical Spectra of Three Strongly Lensed Galaxies at $z \sim 2$. *The Astrophysical Journal.* v.701, Issue 1, pp.52-65 (2009).

Hainline, K.N., et al. 2010, Bulletin of the American Astronomical Society, 42, #383.03

Hainline, K.N., Shapley, A.E., Greene, J.E., Steidel, C.C. The Rest Frame Ultraviolet Spectra of UV-Selected Active Galactic Nuclei at $z \sim 2-3$. *The Astrophysical Journal*. v.733, Issue 1, article id. 31 (2011).

Kulas, K.R., Shapley, A.E., Kollmeier, J.A., Zheng, Z., Steidel, C.C., Hainline, K.N. The Kinematics of Multiple-Peaked Ly-alpha Emission in Star-Forming Galaxies $z \sim 2-3$. *The Astrophysical Journal*. v.745, Issue 1, article id. 33 (2012).

Hainline, K.N., et al. 2012, Bulletin of the American Astronomical Society, 44, #202.05

Hainline, K.N., Shapley, A.E., Greene, J.E., Steidel, C.C., Reddy, N.A., Erb, D.K. Stellar Populations of UV-Selected Active Galactic Nuclei Host Galaxies at $z \sim 2-3$. submitted to *The Astrophysical Journal*. (2012).

CHAPTER 1

Introduction

We observe a very diverse population of galaxies in the nearby universe, including star-forming disk galaxies as well as quiescent elliptical galaxies. These galaxies contain stars, gas and dust as well as a central supermassive black hole. In some galaxies, supermassive black holes accrete gas and emit radiation across the electromagnetic spectrum, and are described as active galactic nuclei (AGNs). Understanding the ways in which the components of a galaxy have interacted across cosmic time to produce the population of local galaxies is one of the fundamental questions in modern astronomy. We can use the finite speed of light along with state-of-the-art modern telescopes to gaze backwards to cosmic epochs when galaxies were still forming, interacting, and evolving to the present day.

This thesis explores how both star formation and AGN activity relate to galaxy evolution through an examination of the universe two to three billion years after the Big Bang ($z \sim 2 - 3$). Galaxies in this period of the universe's history have been found to be quite different from those observed locally, and we can compare the detailed properties of both local and high-redshift galaxies to understand these differences. Specifically, this dissertation addresses two groups of galaxies. First, I examine a trio of highly star-forming, gravitationally-lensed galaxies, which were observed in order to understand how star formation affects galactic gas properties at high redshift. The second population I've observed is a group of galaxies that contain both star formation and AGN activity, two

processes that are hypothesized to have a strong effect on galaxy evolution. This dissertation will attempt to address key issues such as: (1) Why do distant star-forming galaxies appear have to different gas properties as compared to the bulk of their local counterparts? (2) What types of outflows are driven by distant AGNs? (3) How do the presence of AGNs affect the properties of their host galaxies? (4) Does a link exist between supermassive black holes and their surrounding stars as early as two billion years after the Big Bang? The answers to these questions are fundamental for a full understanding of the evolution of galaxies in the universe.

1.1 Star Formation in Galaxies

One of the primary processes in the life cycle of a galaxy is the formation of new stars. Our own galaxy, the Milky Way, has a star-formation rate (SFR) of only a few new solar masses each year (Chomiuk & Povich 2011; Kennicutt & Evans 2012). As our Galaxy is composed of roughly one hundred billion solar masses of stars, the SFR must have been far higher in the past, and indeed, SFRs of tens to thousands of solar masses per year have been observed for distant star-forming galaxies (Erb et al. 2006b; Reddy & Steidel 2004; Reddy et al. 2006b; Chapman et al. 2005). The process of star formation requires the accumulation of molecular gas in large clouds, which eventually collapse under the influence of gravity. The resulting population of stars will have a wide range of masses, as described by an "initial mass function" (IMF) that indicates the number of stars within a given volume of space as a function of stellar mass. These stars will range from the numerous, low-mass, brown dwarf stars to the rarer, highest-mass stars. These latter stars are thousands or even millions of times brighter than the sun, and they are largely responsible for the UV to optical emission observed in star-forming galaxies. As they age, the highest-mass stars will emit

fast outflows and eventually die in powerful supernova explosions. These two processes can have a significant impact on a galaxy's interstellar medium (ISM), enriching, heating, and potentially expelling the gas that could form new stars. The evolution of a galaxy, then, is linked strongly to the evolution of the stars being born and interacting with the galaxy's ISM.

In order to discern the effects that a given stellar population has had on a galaxy's ISM, it is necessary to compare star formation in the local universe to what is observed at high redshift. Star formation has been studied in detail both in our own Milky Way, as well as in individual nearby star-forming galaxies at sub-kpc scales (see Blanton & Moustakas 2009, for a review). The Sloan Digital Sky Survey (SDSS), which mapped out $\sim 35\%$ of the sky, assembled a statistical sample of almost a million nearby galaxies (York et al. 2000). This optical survey, which included both imaging and spectroscopic modes, has provided an excellent insight into the bulk properties of local star-forming galaxies. Brinchmann et al. (2004) used spectroscopy and imaging for $\sim 10^5$ galaxies from the SDSS to examine how the SFR varied as a function of galaxy physical parameters such as stellar mass, size, and concentration. A complementary examination was performed by Tremonti et al. (2004), who examined a similarly large sample of SDSS objects at $z \sim 0.1$, and traced out the local relationship between a galaxy's stellar mass and the gas-phase metallicity. For both studies, SDSS spectroscopy was used to calculate the strengths of various strong optical emission lines, which arise in HII regions in galaxies, excited by starlight. The relative strengths of such emission lines are often used as a probe for many other physical conditions in the HII regions in star-forming galaxies, such as electron density, temperature, and ionization state of the gas (Alloin et al. 1979; Pagel et al. 1979; McCall et al. 1985; Dopita & Evans 1986; Kewley & Dopita 2002; Pettini & Pagel 2004).

While the SDSS has been an important source of data for calibrating local star-formation diagnostics, using these same indicators at higher redshifts is much more difficult. At higher redshifts, important emission lines become harder to detect, both by virtue of the low fluxes, and also the fact that key optical diagnostic features are shifted into the near-infrared (near-IR). In the near-IR, the atmosphere absorbs much of the light, and strong sky emission lines and a bright thermal background makes observations of weak galaxy emission difficult. Emission-line diagnostics at intermediate and high redshifts have been observed for smaller samples thus far (Pettini et al. 2001; Shapley et al. 2004; Erb et al. 2003; van Dokkum et al. 2004, 2005; Kriek et al. 2007). One useful optical line emission diagnostic diagram is the "BPT" diagram (Baldwin et al. 1981), which separates star-forming galaxies and AGN according to the optical line ratios [NII]/Hα and [OIII]/Hβ; star-forming galaxies fall in a region of lower [NII]/Hα for a range of values of [OIII]/Hβ. Shapley et al. (2005a) examined 12 star-forming galaxies at $1.0 < z < 1.5$, and found that star-forming galaxies at these redshifts, when compared to those observed locally, have intrinsically different rest-frame optical line ratios and fall in a different position on the BPT diagram. Similar results were found for 20 star-forming galaxies at $z \sim 1.0 - 1.5$ in Liu et al. (2008) and four $z \sim 2$ star-forming galaxies from Erb et al. (2006a). This offset in BPT diagram position was hypothesized to arise from differences between local and high-redshift galaxies in the HII region electron density, ionizing spectrum hardness, ionization parameter, shock excitation, or AGN contribution, the understanding of which requires a careful analysis of the emission lines for high-redshift galaxies.

The high S/N necessary for characterizing HII region physical conditions in high-redshift galaxies can be provided by gravitational lensing from a massive object along the line-of-sight. The process of gravitational lensing conserves

the surface brightness of a lensed galaxy while the galaxy's size increases. This increases the total luminosity of the lensed galaxy and makes these objects ideal targets for spectroscopy. Chapter 2 of this thesis will describe observations of three strongly-lensed star-forming galaxies at $z \sim 2$. The boost in S/N ratio from gravitational lensing provides an unusually detailed view of the physical conditions in these objects. A full complement of high S/N rest-frame optical emission lines is measured, spanning from rest frame 3600 to 6800 Å, which allow me to estimate the dynamical masses, extinction, electron densities, and ionization parameters for two of the three objects (the third is estimated to be an AGN). The data presented for these lensed galaxies help understand (at high S/N) the differences observed between high-redshift star-forming regions and those observed locally.

1.2 Identifying Galaxies at High Redshift

The second half of my dissertation addresses a sample of AGNs at high redshift. While galaxies in the local universe are easier to study due to their proximity, the history of the star-formation rate density in the universe indicates that star-formation activity peaked at $z \sim 2-3$ (Hopkins 2004; Hopkins & Beacom 2006; Reddy et al. 2007). In order to understand the effects that such high star formation has had on galaxy evolution at these redshfits, it is important to examine large samples of galaxies. It is not economical to spend observing time obtaining individual spectroscopic redshifts without a method of pre-selecting galaxies to be in a redshift range of interest.

Many techniques have been developed that use imaging as a first step to identify targets for spectroscopic followup. Imaging can be used to observe a large number of galaxies at once, with enough photometric depth to detect faint

galaxies (Steidel et al. 1996; Franx et al. 2003; van Dokkum et al. 2003; Daddi et al. 2004). Most relevant for the work in this thesis, star-forming galaxies can be selected at $z \sim 2-3$ by virtue of the shape of their rest-frame UV spectra energy distributions (SEDs). The intergalactic medium (IGM) absorbs a majority of the light at wavelengths shorter than 912 Å, often called the "Lyman break" in a galaxy SED. Steidel et al. (1996, 2003) examined the $UG\mathcal{R}$ colors of galaxies to identify large numbers of star-forming galaxies (the Lyman-Break Galaxies, or LBGs) at $z \sim 3$, as the U and G filters span the Lyman break at this redshift. It is also possible to use the same filters to identify star-forming galaxies at lower redshifts ($z \sim 1.5-2.5$) by virtue of their flat spectra longward of HI Lyman-α (the BX and BM objects; Steidel et al. 2004; Adelberger et al. 2004). As this method utilizes a specific range in SED shapes, the galaxies selected by their $UG\mathcal{R}$ colors are highly star-forming, and suffer only minimal to moderate extinction, since the effects of dust would alter the spectral slope.

For this dissertation, in order to understand AGN host galaxy ISM and stellar properties, we rely on the analysis of multi-wavelength imaging and spectroscopy, which have been used to describe the full sample of $z \sim 2-3$ LBGs. One important tool utilized in understanding the population of star-forming galaxies at $z \sim 2-3$ is stellar population synthesis (SPS) modeling, wherein theoretical galaxy SED templates are compared to the observed SED of a target galaxy in order to estimate galaxy properties such as stellar mass, age, extinction, and SFR. The results indicate that $z \sim 2-3$ star-forming galaxies are characterized by SFRs of $10-100 M_{\odot}$ yr^{-1}, stellar masses between $1-5 \times 10^{10} M_{\odot}$, and moderate amounts of dust extinction (Shapley et al. 2001; Reddy & Steidel 2004; Erb et al. 2006b). Another important aspect of UV-selected star-forming galaxies is their UV spectra, which contains important emission and absorption features that probe the galaxy's ISM. The rest-frame UV spectra for the $z \sim 3$ LBGs

were examined in detail in Shapley et al. (2003). To overcome the lower S/N in individual spectra, these authors created stacked composite spectra, and were able to observe important UV features that traced gas properties and kinematics. The spectra were separated by measured properties such as Lyα equivalent width (EW) to determine important spectral trends within the sample. Other studies of the UV spectra of the UV-selected star-forming galaxy sample have shown that these objects are host to galaxy-scale outflows of up to hundreds of km/s (Pettini et al. 2001; Adelberger et al. 2003, 2005a; Shapley et al. 2003; Steidel et al. 2004, 2010). In Chapters 3 and 4, we follow the methodology demonstrated in, Shapley et al. (2003), Shapley et al. (2005b), Shapley et al. (2006), and Reddy et al. (2012), but on a sample of UV-selected AGNs at $z \sim 2 - 3$.

1.3 Active Galactic Nuclei

Alongside star formation, the presence of an AGN in a galaxy has also been hypothesized to alter a galaxy's gas content. AGNs, the luminous centers of many galaxies, are powered by the accretion of gas onto a supermassive black hole. This process produces emission that in some cases can meet or exceed the combined stellar light in the host galaxy. AGNs in the local and high-redshift universe are found with vastly different properties, which is often attributed to to the different orientations at which they are observed (Antonucci 1993). In Type I, or "broad-line" AGNs, we are observing regions closer in towards the black hole, where highly-excited and fast-moving gas is observed to produce broad emission lines. Alternately, in Type II, or "narrow-line" AGNs, the central region is obscured by dust close to the black hole, and their spectra show only narrow emission lines produced from excited regions farther away. A host of evidence exists which supports this scenario (see Bianchi et al. 2012, and references therein), although

it has been challenged by studies of how the ratio between these two AGN Types depends on luminosity (Barger et al. 2005a; Simpson 2005). Type II AGNs allow for detailed studies of AGN host galaxies, as central obscuration blocks much of the emission from near the black hole. Understanding what triggers an AGN, the timescales of AGN activity, and the effects an AGN may have on the properties of the galaxy has been central to AGN studies since their discovery in the middle of the 20th century.

One of the most important discoveries in modern AGN research is the link between the mass of the central black hole in galaxies and the properties such as stellar mass, luminosity, or velocity dispersion of the surrounding galaxy bulge stars (Kormendy & Richstone 1995; Magorrian et al. 1998; Ferrarese & Merritt 2000). This relationship between the central black hole and the surrounding stars has been observed in the local universe to be quite tight across a wide range in black hole masses, but the reasons for its existence are still unclear. Central black holes grow through gas accretion, which causes them to show active galactic nucleus emission (Salpeter 1964; Lynden-Bell 1969; Shakura & Sunyaev 1973; Soltan 1982; Rees 1984), and this gas accretion could also be feeding the creation of the bulge stellar population. The tightness of the relation suggests that galaxies hosting classical bulges are growing together with their black holes. This theory implies that nuclear star-formation should be tied to AGN activity in local galaxies, which is seen, but with considerable scatter (Wild et al. 2007; Baum et al. 2010; Diamond-Stanic & Rieke 2012). It is thought that the energy output from an AGN can heat or remove gas from galaxies, which would tie star formation to AGN activity. The correlations between black hole mass and bulge properties may offer evidence of this so-called AGN feedback (Silk & Rees 1998; Murray et al. 2005; Hopkins et al. 2008). Jahnke & Macciò (2011) and Peng (2007) theorize, however, that the relationship between black hole mass and

bulge stellar properties is a natural consequence of galaxy mergers, which does not require some form of feedback linking the two populations. It is important, then, to examine the relationship between the central black hole and the host stellar population at higher redshifts, when these two populations were forming. Using lensed quasars at $1 < z < 4.5$, Peng et al. (2006) uncovered evidence that black holes hosted by bulges with a given stellar mass are more massive than those observed locally. An analysis of the host galaxies of Type II objects will help to better explore this relation at high redshift.

The distribution of colors and masses of galaxies seen in the local universe has been theorized to arise from the AGN activity in the high-redshift universe, which may remove or heat gas, quenching star-formation (Hopkins et al. 2006; Menci et al. 2006; Croton et al. 2006). As such, AGN host galaxies can be studied at higher redshift to search for evidence for AGN feedback as it is occurring. Studies of outflows from AGNs has been mixed. Krug et al. (2010) demonstrated that outflows observed for local IR-faint AGNs were similar to those observed for similar, non-active, starburst galaxies, indicating that star formation was the primary driver for the outflowing gas. Similar results were found for a sample of AGNs as compared to similar non-AGN ULIRGs in Rupke et al. (2005a). Work on AGN outflows at high redshift focuses on the extended line emission in individual systems or small samples of AGNs alone (Nesvadba et al. 2008; Alexander et al. 2010), and it is difficult to decouple the effects of star formation and the effects of an AGN on gas kinematics. This difficulty can be overcome by comparing samples of AGNs to similar non-active hosts, ideally at high-redshift, when AGN activity was more prominent.

AGN host galaxy demographics, specifically galaxy color and the related star-formation properties, are also often used to understand the effects of an AGN on

its host. Locally, optically identified AGNs are often found to reside in massive ($\log(M_*/M_\odot) > 10$), red, early-type galaxies (Kauffmann et al. 2003), similar to what is seen for radio-loud AGNs (Best et al. 2005). The identification of local AGNs predominantly in red galaxies supposes that AGNs may have played a part in shutting off star formation. Indeed, out to intermediate redshifts, AGNs are observed to lie in a region on a galaxy color-magnitude diagram between the blue and red regions of galaxies (Nandra et al. 2007; Salim et al. 2007; Coil et al. 2009; Hickox et al. 2009; Schawinski et al. 2010), although dust obscuration does push some star-forming AGN hosts towards redder colors (Cardamone et al. 2010; Rovilos et al. 2011). Silverman et al. (2008), however, found that X-ray selected AGNs at $z \sim 1$ often reside in galaxies with higher star-formation rates than similar-mass non-active galaxies, and that the AGN fraction is higher in the blue cloud. Xue et al. (2010), using a mass-matched sample of X-ray selected AGNs, showed that the fraction of AGNs remains constant as a function of color. While AGN hosts selected by many different methods at high redshifts are massive (Erb et al. 2006c; Kriek et al. 2007; Mainieri et al. 2011; Kocevski et al. 2012; Santini et al. 2012), the Silverman et al. and Xue et al. results indicate the importance of controlling for stellar mass when making AGN host galaxy comparisons. Recently, Aird et al. (2012) examined Type II AGNs out to $z \sim 1$ and concluded that the prevalence of AGNs at high masses and red colors is a selection effect related to the underlying Eddington ratio distribution. These authors find that AGNs are more likely to be found in higher mass, redder galaxies because they are easier to detect than the lower mass black holes found in lower mass galaxies. It is necessary to carefully examine a sample of AGNs alongside similar non-active galaxies (matched in stellar mass) to disentangle the effects of star-formation activity from AGN activity.

In Steidel et al. (2002), a population of AGNs were identified at $z \sim 3$ from

the LBG sample by the presence of UV emission lines. This sample of AGNs included both narrow-line and a broad-line objects. These AGNs were found to be hosted by the same dark matter halos as those of the parent population of non-active LBGs (Steidel et al. 2003; Adelberger et al. 2005b), and thus were an ideal sample for examining how the presence of an AGN affects the host galaxy. In Chapters 3 and 4 of this dissertation, I focus on the Type II AGNs in this sample, as dust obscuration towards the central regions of these objects allows for an analysis of the host galaxy. The $z \sim 3$ sample from Steidel et al. (2002) has been increased through the addition of similarly selected Type II AGNs at $z \sim 2$. In Chapter 3, I detail the creation of a UV composite for these AGNs which shows evidence for $\sim 10^3$ km s^{-1} outflows of highly ionized gas. In Chapter 4, I discuss the careful stellar population synthesis modeling for these AGNs, describing the host galaxy properties, and the demographics of the sample. Together, these two chapters represent a significant step in the understanding of why AGNs are found in certain types galaxies, and the effects that an active supermassive black hole can have on its host at $z \sim 2 - 3$, when black holes and stellar bulges were both actively growing.

CHAPTER 2

Rest-Frame Optical Spectra of Three Strongly Lensed Galaxies At z∼2

2.1 Introduction

A wealth of information about star-forming galaxies is contained in their optical spectra. The ratios of the fluxes of optical emission lines can be used to understand the physical conditions of the gas and stars in star-forming regions, including metallicities, temperatures, densities, and ionization parameters. Near-infrared spectroscopy is used to study these properties in high-redshift galaxies, as the strong rest-frame optical lines are redshifted into the near-IR at $z > 1.5$. These lines include [OII]λ3727, Hβ, [OIII]$\lambda\lambda$5007,4959, Hα, [NII]λ6584, and [SII]$\lambda\lambda$6717,6731, and can be used to infer the oxygen abundance, electron density and ionization parameter in HII regions.

Results from a small existing sample indicate that $z \sim 2$ galaxies have intrinsically different rest-frame optical line ratios from those in the bulk of nearby HII regions and Sloan Digital Sky Survey (SDSS) star-forming galaxies (Erb et al. 2006a; Shapley et al. 2005b; Liu et al. 2008). This difference appears in the emission-line diagnostic diagram of [OIII]/Hβ vs. [NII]/Hα, where high-redshift star-forming regions are found offset from an extremely tight sequence formed by local objects (Kauffmann et al. 2003). The offset may be caused by differences

in the SFR, average ionization parameter, shape of the stellar ionizing spectrum, HII electron density, or the increased contribution of an AGN or shocked gas to the integrated spectra. Based on the analysis of SDSS local star-forming galaxies, Brinchmann et al. (2008) suggest that an elevated ionization parameter due to high electron densities and non-zero escape fractions of hydrogen ionizing photons is the primary factor. Specifying the cause of this offset using direct measurements from high-redshift galaxies will provide new insight into the physical conditions and chemical abundances of the gas in which the stars were being formed during the epoch when the star-formation activity of the Universe was at its peak (Madau et al. 1996; Steidel et al. 1999; Bouwens et al. 2007).

The optimal redshift range for this type of analysis using ground-based near-IR spectroscopy is $z = 2.0 - 2.5$. In this range, the largest number of strong and weak nebular emission lines falls within the windows of atmospheric transmission and bluewards of the bright thermal IR background at $\lambda \geq 2.35\mu$m. However, $z \sim 2$ UV-selected galaxies typically have faint magnitudes ($K_{Vega} > 20.0$ mag) and small angular sizes ($\leq 1''$). Thus, it is difficult to obtain the high S/N spectra that are necessary for a truly detailed view of high-redshift star-forming regions using anything but long integration times with the largest telescope apertures. This problem can be addressed by taking advantage of the boost provided by gravitational lensing, which magnifies and offers more sensitive views of distant galaxies.

The best-studied high-redshift lensed galaxy is MS 1512-cB58 ($z = 2.73$, Yee et al. 1996), a typical $\sim L^*$ Lyman break galaxy (LBG). The high magnification (~ 30, Williams & Lewis 1996; Seitz et al. 1998) of cB58 has allowed for unusually sensitive analyses of the galaxy's rest-frame UV (Pettini et al. 2000, 2002), optical (Teplitz et al. 2000), IR (Siana et al. 2008), and far-IR (Sawicki 2001; Baker et al.

2001) spectra and photometry. In particular, rest-frame optical spectra were used to calculate dust extinction, virial mass, chemical abundances, and SFRs. Recently, new search techniques for strongly-lensed high-redshift galaxies have yielded additional candidates which have been spectroscopically confirmed to lie at $z > 2$ (Allam et al. 2007; Smail et al. 2007). Three of these candidates, SDSS J090122.37+181432.3 ($z = 2.26$, hereafter referred to as SDSS J0901+1814, Diehl et al. 2009), the Cosmic Horseshoe ($z = 2.38$; Belokurov et al. 2007), and the Clone ($z = 2.00$; Lin et al. 2009) are at redshifts even better-suited to rest-frame optical spectroscopy than cB58. Analysis of the rest-frame optical spectra of these objects presents a unique opportunity to study both HII region physics and the difference between local star-forming galaxies and those at high-redshift.

In this chapter, we analyze Keck II NIRSPEC spectra for these three lensed objects. In §2.2 we describe the observations, data reduction, and line flux measurements. We discuss several physical quantities derived from these line fluxes in §2.3. We investigate how our objects compare to other objects at $z \sim 2$ in §2.4, and review the physical quantities for these objects in order to explain the differences in the physical conditions between high-redshift and local HII regions. Finally, we conclude in §2.5. Throughout, we assume a cosmology with $\Omega_M = 0.27$, $\Omega_\Lambda = 0.73$, and $H_0 = 71$ km s^{-1} Mpc^{-1}.

2.2 Observations and Data Reduction

2.2.1 NIRSPEC Observations

We obtained near-IR spectra on 2008 February 19 using the NIRSPEC spectrograph (McLean et al. 1998) on the Keck II telescope. Our targets included three strongly lensed high redshift galaxies: SDSS J090122.37, the Cosmic Horseshoe,

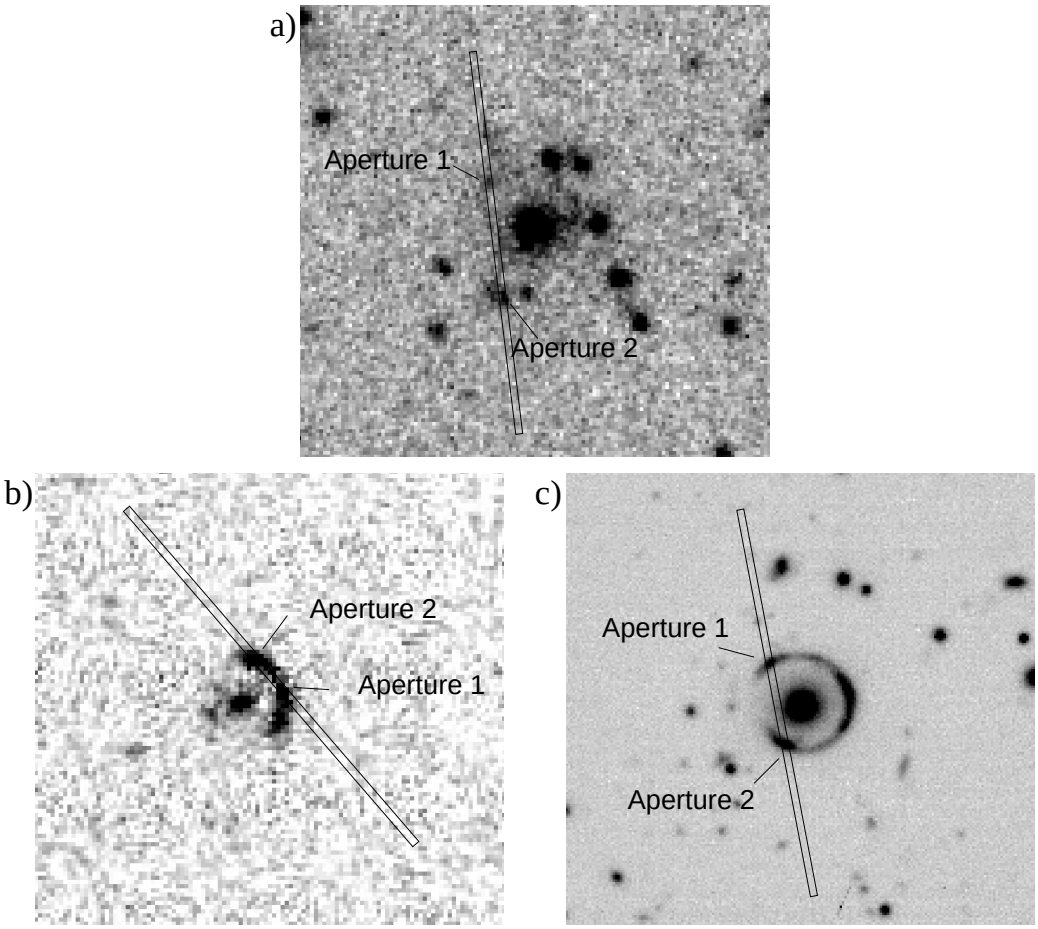

Figure 2.1 Images of the Objects with the NIRSPEC slit overlaid, defining the various apertures used in this chapter. a) SDSS J0901+1814, from a SDSS r-band image, b) The Clone, from a SDSS g-band image, and c) The Cosmic Horseshoe, from a VLT/FORS2 R-band image (Lindsay King, private communication). The NIRSPEC slit shown is $0\farcs76 \times 42''$, and the separation between the different apertures are $12\farcs52$ for SDSS J0901+1814, $3\farcs95$ for the Clone., and $8\farcs82$ for the Cosmic Horseshoe.

and the Clone (Diehl et al. 2009; Belokurov et al. 2007; Lin et al. 2009). At $z \sim 2$, several strong rest-frame optical lines fall within windows of atmospheric transmission in the near-IR. Hα and [NII] fall within the NIRSPEC 6 (similar to K-band) filter for all three objects. Hγ, [OIII]λ4363, Hβ, and [OIII]$\lambda\lambda$4959,5007 fall in the NIRSPEC 5 (similar to H-band) filter for the Cosmic Horseshoe and SDSS J090122.37, and NIRSPEC 4 for the Clone. [OII] and [NeIII] fall in the NIRSPEC 3 (similar to J-band) filter for the Cosmic Horseshoe and SDSS J090122.37, and NIRSPEC 2 for the Clone. Exposure times for the different filters ranged from 3×600 s to 9×600 s, and are listed in Table 2.1. All targets were observed with a $0\farcs76 \times 42''$ long slit. Conditions were photometric during the night and seeing ranged from $0\farcs4$ - $0\farcs9$. The spectral resolution as determined from sky lines was ~ 10 Å for the NIRSPEC-2, -3, -4, and -5 filters, and ~ 15 Å for the NIRSPEC-6 filter. For each object, we placed the slit across two of the lensed images to look for variation in the line ratios between them. The slit position angles (in degrees east of north) were 7.22° for SDSS J090122.37, 10.73° for the Cosmic Horseshoe, and 219.97° for the Clone, and were determined by the locations of high surface brightness knots in the optical lensed images. The separation between the different apertures are $12\farcs52$ for SDSS J090122.37, $8\farcs82$ for the Cosmic Horseshoe, and $3\farcs95$ for the Clone. Images of the objects with slits overlaid are presented in Figure 2.1.

2.2.2 Data Reduction and Optimal Background Subtraction

Data reduction was performed following the procedure described in Liu et al. (2008), where the sky background was subtracted using an optimal method on the two-dimensional spectral images (Kelson 2003, Becker, private communication). One notable exception to this procedure addressed the matter of pattern noise.

Table 2.1. Galaxies Observed with Keck II NIRSPEC

NAME	R.A. (J2000)	Dec. (J2000)	$z_{\mathrm{H}\alpha}$	$r(mag)$	$g-r(mag)^a$	Exposure (s)	Band
SDSS J0901+1814	09 01 22.37	18 14 32.35	2.2586	20.6	0.52, 0.21	3 × 600	J
						6 × 600	H
						6 × 600	K
Cosmic Horseshoe	11 48 33.14	19 30 3.20	2.3813	19.0	0.29, 0.25	3 × 600	J
						9 × 600	H
						8 × 600	K
Clone	12 06 2.09	51 42 29.52	2.0026	19.0	0.39, 0.30,	3 × 600	J
					0.34	3 × 600	H
						3 × 600	K

Note. — Units of right ascension are hours, minutes, and seconds, and units of declination are degrees, arcminutes and arcseconds.

[a]These colors are listed for apertures 1, 2, and in the case of the Clone, the full aperture as shown in Figure 2.1.

A large fraction of the exposures taken in 2008 February were affected by pattern noise, which consisted of a constant positive or negative offset in the mean count level in every 8$^{\mathrm{th}}$ row of the upper-right hand quadrant of the NIRSPEC CCD images. Prior to the standard reduction procedure, we removed this pattern noise in all 75 of the science images.

Sky subtraction for the Cosmic Horseshoe observations required extra care, due to the presence of continuum emission in the slit from the outskirts of the lensing galaxy (a luminous red galaxy at $z = 0.444$; Belokurov et al. 2007). Indeed, the first stage of sky subtraction typically consisted of a simple difference of adjacent, dithered exposures. The dithers adopted for this target were (unfortunately) similar in size to the spacing between the positions of the Horseshoe and lens images, leading to the subtraction of the lens continuum (rather than blank sky) from the Horseshoe in some pairs of exposures. We quantified and corrected for this effect using pairs of exposures in which no oversubtraction occurred.

One-dimensional spectra were extracted from these two-dimensional reduced images along with error spectra. For all three of our objects we extracted aper-

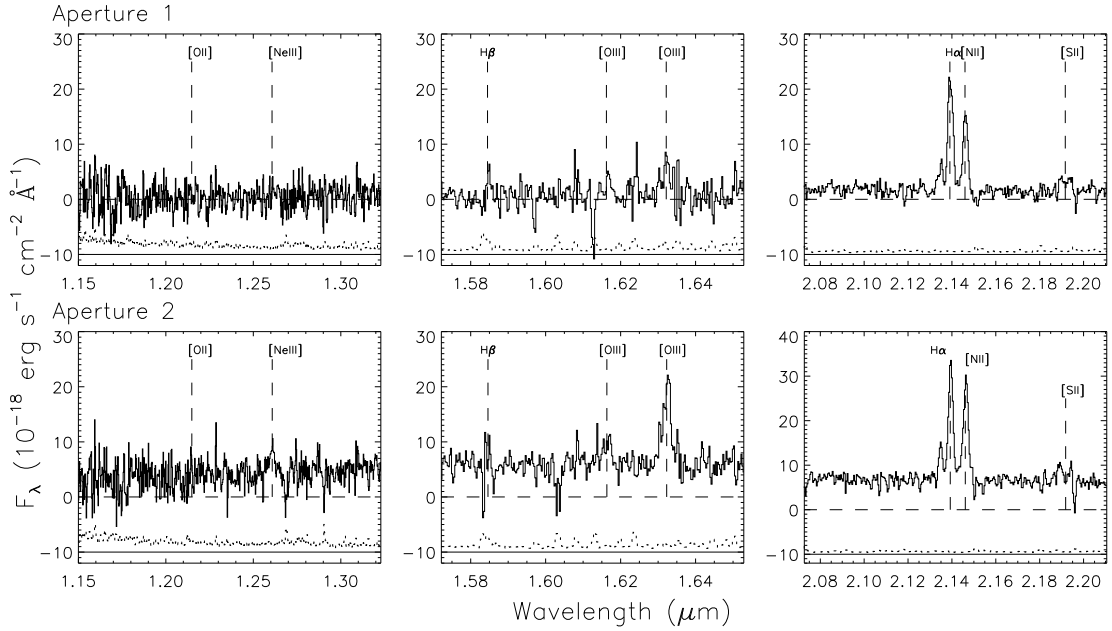

Figure 2.2 NIRSPEC spectrum of SDSS J0901+1814. The top row contains the J, H, and K-band spectra for aperture 1, while the bottom row shows those for aperture 2. Apertures 1 and 2 are as labelled in Figure 2.1. The positions of the prominent emission lines are indicated. The dotted lower spectrum indicates the 1σ errors offset vertically by -10×10^{-18} erg s^{-1} cm^{-2} Å^{-1} for clarity. Larger errors occur at the position of the sky lines and at points of high atmospheric extinction.

tures for each of the two lensed images covered. For the Clone, the lensed objects almost overlapped, so we extracted a third, full aperture that extended along the slit across both lensed images. These spectra were then flux-calibrated using A-type star observations according to the method described in Shapley et al. (2005b) and Erb et al. (2003).

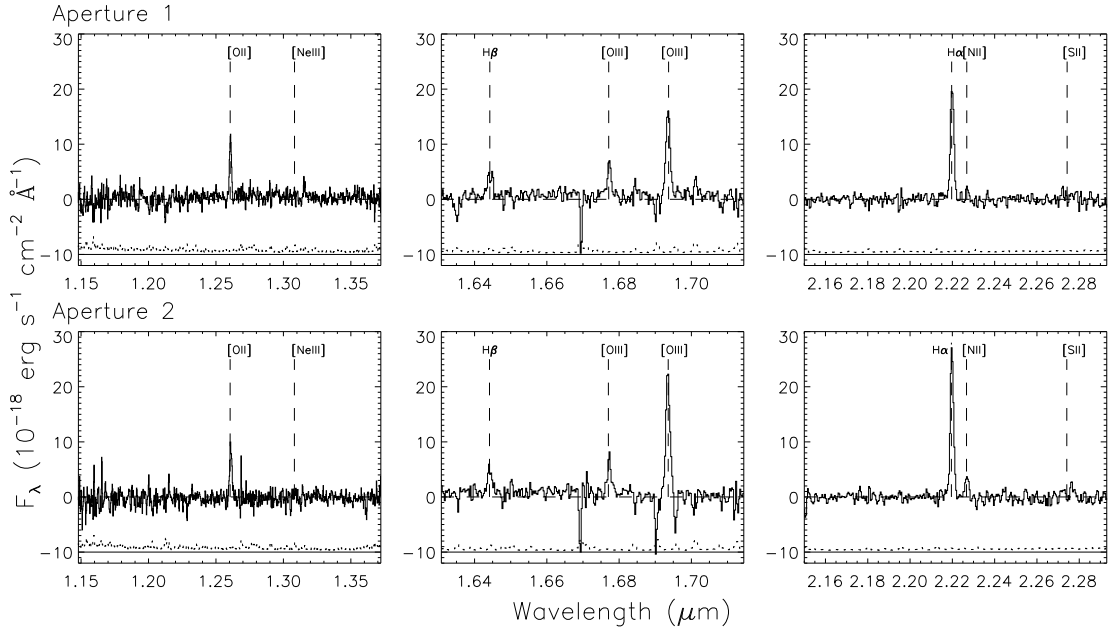

Figure 2.3 NIRSPEC spectrum of the Cosmic Horseshoe. The top row contains the J, H, and K-band spectra for aperture 1, while the bottom row shows those for aperture 2. Apertures 1 and 2 are as labelled in Figure 2.1. The positions of the prominent emission lines are indicated. The dotted lower spectrum indicates the 1σ errors offset vertically by -10×10^{-18} erg s^{-1} cm^{-2} Å^{-1} for clarity. Larger errors occur at the position of the sky lines and at points of high atmospheric extinction.

2.2.3 Line Flux Measurements

One-dimensional, flux-calibrated spectra are shown along with the error spectra in Figures 2.2, 2.3, and 2.4. The error spectrum represents the 1σ uncertainty in the flux at each wavelength. In addition, zoomed-in regions of select portions of the spectra are featured in Figures 2.5 and 2.6. The redshifts of the lensed objects were measured by fitting a Gaussian profile to the Hα emission feature. In all cases, the redshifts from the separate components of the lensed image pairs

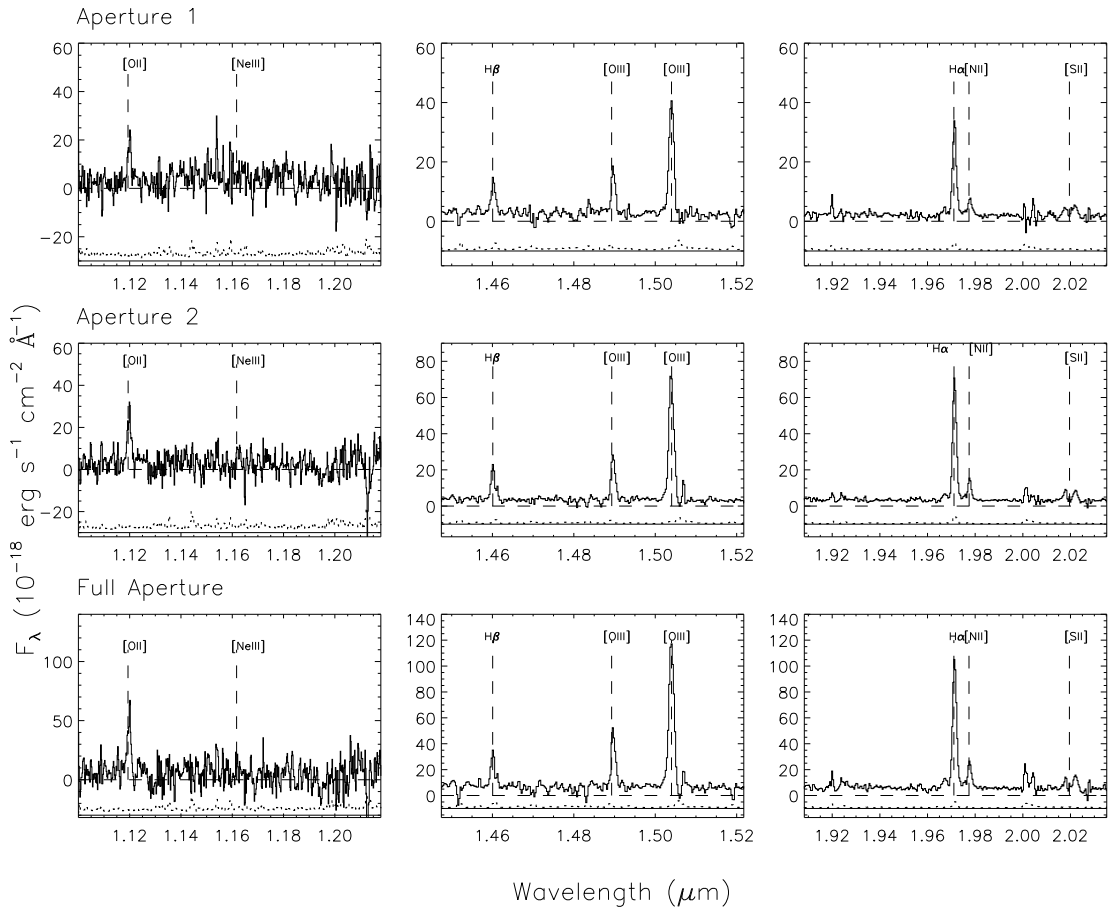

Figure 2.4 NIRSPEC spectrum of the Clone. The top row contains the J, H, and K-band spectra for aperture 1, the second row shows those for aperture 2, and the bottom row shows those from the full aperture. Apertures 1 and 2 are as labelled in Figure 2.1. The positions of the prominent emission lines are indicated. The dotted lower spectrum indicates the 1σ errors offset vertically by -30×10^{-18} erg s^{-1} cm^{-2} Å^{-1} for the J-band spectra, and -10×10^{-18} erg s^{-1} cm^{-2} Å^{-1} for the H- and K-band spectra for clarity. Larger errors occur at the position of the sky lines and at points of high atmospheric extinction.

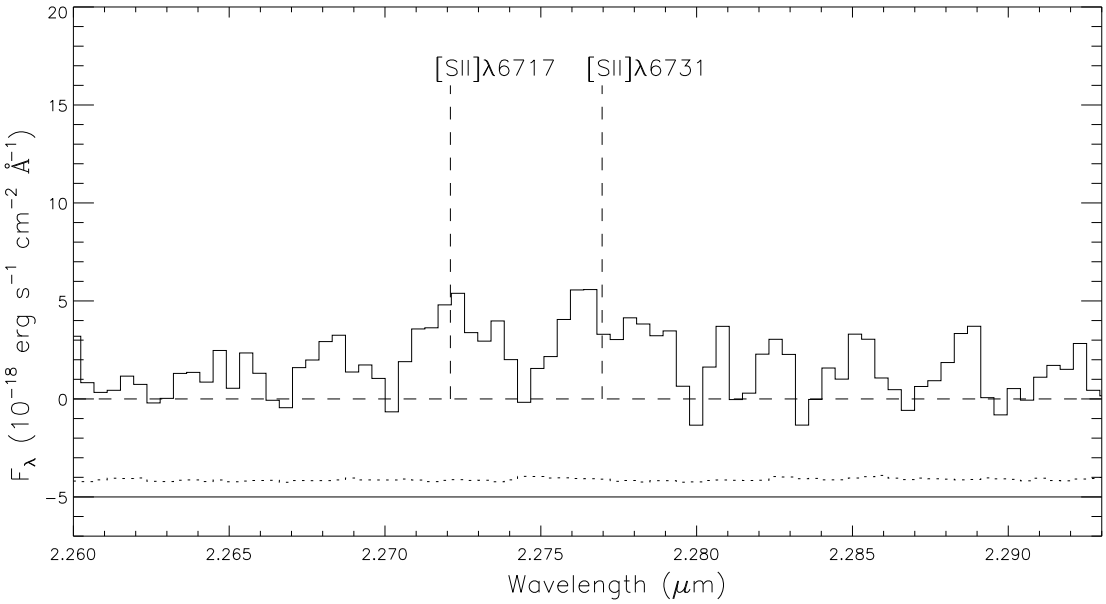

Figure 2.5 NIRSPEC summed spectra from both Cosmic Horseshoe apertures, for the [SII] doublet. The dotted lower spectrum indicates the 1σ errors offset vertically by -5×10^{-18} erg s^{-1} cm^{-2} Å^{-1} for clarity.

agreed to within $\Delta z/(1+z) = 0.0001$ ($\Delta v = 27 - 30$ km s^{-1}).

The lines that we set out to measure were [OII]$\lambda\lambda$3726,3729, [NeIII]λ3869, Hγ, [OIII]λ4363, Hβ, [OIII]$\lambda\lambda$4959,5007, Hα, [NII]λ6584, and [SII]$\lambda\lambda$6717,6732. Line fluxes were determined by fitting Gaussian profiles using the IRAF task, SPLOT. The Hβ, Hγ, and [OII]$\lambda\lambda$3726,3729 lines were measured individually, while the pairs of [OIII]$\lambda\lambda$4959,5007, Hα and [NII]λ6584, and [SII]$\lambda\lambda$6717,6732 were fitted simultaneously. With this method, we fixed the central wavelength and FWHM based on the best-fit parameters for the brighter line and then obtained a combined fit for the relative fluxes of the two lines.

In some cases, we had to measure specific lines through different methods because of the presence of sky lines, or the weak fluxes of the lines. For the

Cosmic Horseshoe and, to a lesser extent, the Clone, sky systematics were an issue. In both objects, the Hβ line was detected, but its wavelength coincided with that of a strong sky line. Accordingly, we treated the measured Hβ line flux as a lower limit. In §2.3, we describe a method for recovering the actual Hβ flux in the face of sky systematics. We measured a lower limit on the line flux for the Hβ and [SII]λ6732 features of aperture 2 of SDSS J0901+1814 as these lines were over-subtracted on one side during the sky subtraction process. We placed upper limits on the [OIII]λ4363 line fluxes in all apertures, and on the [NeIII]λ3869 line fluxes in all but aperture 1 of SDSS J0901+1814 where it was detected. We summed the flux across both of the [SII] lines for aperture 1 of both SDSS J0901+1814 and the Cosmic Horseshoe due to the low flux from the individual lines.

Uncertainties in line fluxes were estimated using a Monte Carlo approach. For each aperture and filter, we generated five hundred artificial spectra. Fake spectra were created by perturbing the flux at each wavelength of the true spectrum by a random amount consistent with the 1σ error spectrum. Line fluxes were measured from these simulated spectra using the same procedure that was applied to the actual data. The standard deviation of the distribution of line fluxes measured from the artificial spectra was adopted as the error on each line flux measurement. Emission-line fluxes and associated uncertainties are given in Table 2.2.

2.3 Physical Quantities

The flux measurement of rest-frame optical emission lines allows us to probe the physical state of the interstellar gas in the target objects. Because of the magnification provided by gravitational lensing, we have detected lines with a higher signal-to-noise ratio (S/N) than what is typically seen in unlensed high-redshift

Table 2.2. Emission Line Fluxes[a]

	SDSS J0901+1814	SDSS J0901+1814	Cosmic Horseshoe	Cosmic Horseshoe	Clone	Clone	Clone
Aperture	1	2	1	2	1	2	Full
$\sigma_{H\alpha}$[b]	131±5	112±4	69±4	58±3	71±8	73±6	80±4
$F_{[OII]}$	<9.0	<10.0	18.8±0.9	20.0±1.0	29.0±3.0	47.0±3.0	85.0±5.0
$F_{[NeIII]\lambda3869}$	<8.0	19.0±3.0	<4.0	<4.0	<17.0	<16.0	<28.0
$F_{[H\gamma]}$	-	-	3.0±1.0	4.6±0.4	6.0±2.0	11.2±0.7	21.0±1.0
$F_{[OIII]\lambda4363}$	-	-	<1.5	<1.6	<2.6	<2.4	<4.3
$F_{H\beta}$	5.0±2.0	>4[c]	8.0±1.0	7.0±1.0	15.0±2.0	25.0±2.0	33.0±4.0
$F_{H\beta,inf}$[d]	-	-	12.6±0.3	16.2±0.3	15.4±0.6	36.0±1.0	53.0±1.2
$F_{[OIII]\lambda4959}$	8.0±2.0	11.0±2.0	7.5±0.8	9.6±0.5	20.0±1.0	35.0±1.0	58.0±2.0
$F_{[OIII]\lambda5007}$	18.0±4.0	39.0±3.0	21.9±0.6	31.2±0.6	56.0±1.0	106.0±1.0	173.0±2.0
$F_{H\alpha}$	63.0±2.0	72.0±1.0	43.4±0.9	53.9±0.9	61.0±2.0	132.0±4.0	202.0±5.0
$F_{[NII]\lambda6584}$	42.0±1.0	64.0±1.0	4.0±0.7	8.7±0.7	10.8±0.9	21.0±1.0	39.0±2.0
$F_{[SII]\lambda6717}$	12.0±1.0[e]	11.0±1.0	6.0±2.0[e,g]	4.0±1.0[g]	5.5±0.9	10.0±1.0	9.0±2.0
$F_{[SII]\lambda6732}$	12.0±1.0[e]	>6.4[f]	6.0±2.0[e,g]	6.0±1.0[g]	7.3±0.9	10.0±1.0	12.0±3.0

[a]Emission line flux and error in units of 10^{-17} ergs s^{-1} cm^{-2}

[b]One-dimensional Hα velocity dispersion and error in units of km s^{-1}.

[c]A sky line coincided with Hβ for aperture 2 of SDSS J0901+1814, and the line flux value was found by summing only the positive flux, instead of fitting the line with a Gaussian.

[d]These inferred Hβ values are calculated from the observed broadband $g-r$ color and the value for Hα, as described in §2.3.3.

[e]This value corresponds to the sum of the flux across both lines, with error.

[f]A sky line coincided with [SII]λ6732 for SDSS J0901+1814, aperture 2, and the line flux value was found by summing only the positive flux, instead of fitting the line with a Gaussian.

[g]The spectra from apertures 1 and 2 were summed for the Cosmic Horseshoe in order to better measure the [SII] line fluxes. The measured values were $F_{[SII]\lambda6717} = 8 \pm 2$, and $F_{[SII]\lambda6732} = 8 \pm 2$.

objects. We can measure dust extinction from the ratios of the Balmer lines of Hα, Hβ, and Hγ, while the Hα line offers the highest S/N measure of the gas velocity dispersion, as well as the SFR of the galaxy. The set of [OIII]$\lambda\lambda$4959,5007, [OII]$\lambda\lambda$3726,3729, [NII]λ6584 and Balmer emission lines provides multiple methods of determining the gas-phase oxygen abundance. The ratio of [OII] and [OIII] lines offers a probe of the ionization parameter of the star-forming regions. Finally, we can use our detection of the [SII]$\lambda\lambda$6717,6732 lines and an upper limit of the [OIII]λ4363 line to estimate the electron density and electron temperature of the gas. Table 2.3 lists several relevant line ratios and the physical quantities derived from them, as described in the sections below.

2.3.1 AGN Contamination

We measured the ratio of [NII]/H$\alpha = 0.65 \pm 0.03$ and 0.88 ± 0.03 for the two apertures of SDSS J0901+1814. Such high ratios, especially in the second aperture, cannot be produced in star-forming regions from photoionization by massive stars (Kewley et al. 2001a; Kauffmann et al. 2003). We therefore infer the presence of an AGN. With insights from the lens model for this system, the AGN can be probed on smaller scales than is typically possible at $z \sim 2$. Such analysis, however, is outside the scope of the current work. For our study of the majority of physical quantities, we focus on the Cosmic Horseshoe and the Clone, where the line fluxes do not appear to be contaminated by the presence of an AGN.

2.3.2 Velocity Dispersion

The velocity dispersion is a measure of the dynamics of the gas bound to the galaxy by gravity. We used Hα line widths to estimate velocity dispersion after correcting for the instrumental resolution. The velocity dispersions were calcu-

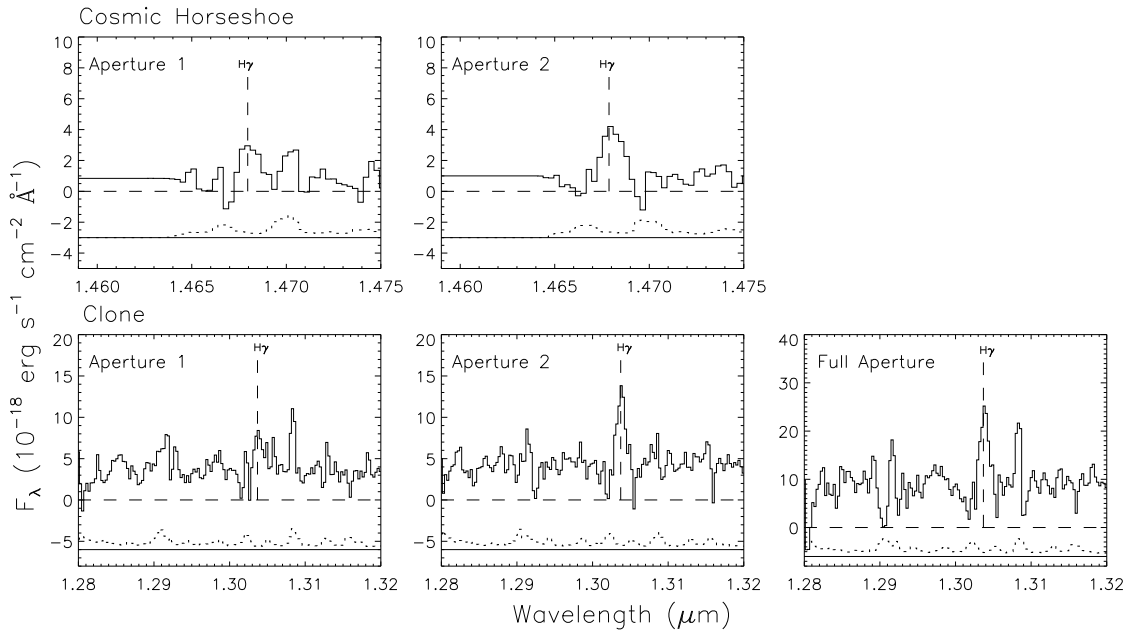

Figure 2.6 NIRSPEC spectra of the Hγ lines for the target objects. The dotted lower spectra indicate the 1σ errors offset vertically by -5×10^{-18} erg s^{-1} cm^{-2} Å^{-1} for clarity.

lated by σ = FWHM/2.355 $\times \frac{c}{\lambda}$, where the FWHM is the full width at half maximum in wavelength after subtraction of the instrumental resolution ($14-15$ Å in the K-band) in quadrature. The velocity dispersions we measured were 131 ± 5 km s^{-1} and 112 ± 4 km s^{-1} for the apertures of SDSS J0901+1814, 69 ± 4 km s^{-1} and 58 ± 3 km s^{-1} for the apertures of the Cosmic Horseshoe, and 71 ± 8 km s^{-1}, 73 ± 6 km s^{-1}, and 80 ± 4 km s^{-1} for the two apertures and the full aperture of the Clone. Uncertainties in velocity dispersion were estimated using the same Monte Carlo approach that was applied to line fluxes.

2.3.3 Dust Extinction

It is important to understand the effects of dust extinction on the various line fluxes, as reddening by dust is highly wavelength dependent and thus can alter the observed flux ratios of widely spaced emission lines from their intrinsic values. Extinction in $z \geq 2$ star-forming galaxies is commonly estimated from rest-frame UV colors and an application of the Calzetti et al. (2000) starburst attenuation law. The Calzetti law appears to provide a fairly accurate description on average of the reddening and attenuation of the UV stellar continuum in both nearby and distant starburst galaxies (Reddy & Steidel 2004; Reddy et al. 2006b). The degree of dust extinction in star-forming regions can also be estimated from the Balmer lines of hydrogren, because these strong optical lines have intrinsic ratios that are well described by atomic theory. Under the assumption of Case B recombination (Osterbrock 1989) and for T = 10,000 K, the Balmer ratios are set. Any deviations in the observed line ratios are then attributed to dust extinction. Calzetti (2001) demonstrates that, in local star-forming galaxies, the stellar continuum suffers less reddening than the ionized gas, expressed as $E(B-V)_{\rm star} = 0.44E(B-V)_{\rm gas}$. Furthermore, Calzetti (2001) suggests that the reddening of the Balmer lines in nearby UV-selected starbursts is better described by a foreground dust distribution and traditional Milky Way extinction curve (Cardelli et al. 1989). On the other hand, Erb et al. (2006b) present evidence that, in $z \sim 2$ star-forming galaxies, $E(B-V)_{\rm star} \simeq E(B-V)_{\rm gas}$ and a Calzetti et al. starburst extinction law applied to both UV-continuum and Hα emission lines gives rise to the best agreement between UV- and Hα-derived SFRs. Our new observations of the Cosmic Horseshoe and the Clone allow for a detailed comparison of different estimates of extinction in high-redshift star-forming galaxies.

First, we used the observed broadband $g - r$ color for our objects and an assumed intrinsic SED to obtain an estimate of $E(B - V)$. The SED model assumed was a Bruzual & Charlot (2003) solar metallicity, constant SFR model with stellar age of 570 Myr, as Erb et al. (2006c) find a median age of 570 Myr for star forming regions of galaxies at $z \sim 2$. We used SDSS g and r magnitudes for the Cosmic Horseshoe, and in the case of the Clone, the Apache Point Observatory SPIcam g and r magnitudes of the individual apertures presented in Lin et al. (2009). The $E(B - V)$ values we calculated were 0.16, 0.13 for the Cosmic Horseshoe, and 0.28, 0.21, and 0.24 for the Clone.

Next, extinction was estimated based on rest-frame optical emission lines. In both the Cosmic Horseshoe and the Clone, we have detected three of the most prominent Balmer lines: Hα, Hβ, and (because of the magnification afforded by gravitational lensing) Hγ. Unfortunately, in both objects, Hβ lines lay over prominent sky lines with systematically negative residuals, yielding in some cases unphysically low values of Hβ/Hγ. Osterbrock (1989) gives the value of Hβ/Hγ under Case B recombination as 2.14. Because reddening will only serve to increase this ratio, our measured values of less than 2.14 in aperture 2 of the Horseshoe and the full aperture of the Clone suggest that, in general, our measured Hβ values were systematically low as a result of the residual error in subtraction of the coincident sky line. Hγ does not appear to suffer from the same systematic sky residuals as Hβ, and therefore we used a comparison of the observed and intrinsic ratios of Hα/Hγ to infer $E(B-V)_{\rm gas}$, assuming an intrinsic Hα/Hγ ratio of 6.12 (Osterbrock 1989). To increase the S/N of the Hγ feature, we combine spectra from individual apertures of each object to obtain an average Hα/Hγ and $E(B - V)_{\rm gas}$. The observed Hα/Hγ ratios imply values of $E(B - V)_{\rm gas}$ of 0.45 ± 0.04 and 0.28 ± 0.04 for the Cosmic Horseshoe and the Clone, respectively.

The value of $E(B-V)_{\rm gas}$ for the Cosmic Horseshoe is almost three times higher than that inferred from the rest-frame UV continuum. While this difference at first appears to support the prescription from Calzetti et al. (2000), regarding the relative extinction of starlight and ionized gas, we argue in section 2.3.4 that the $g-r$-based estimate of $E(B-V)$ provides a more robust estimate of the ionized gas extinction. In contrast, both $g-r$ and Hα/Hγ provide consistent estimates of dust extinction in the Clone, i.e., $E(B-V)_{\rm star} \simeq E(B-V)_{\rm gas}$. It is also worth noting that, over the wavelength range probed by our NIRSPEC spectra, the Calzetti et al. (2000) and Cardelli et al. (1989) extinction curves yield very similar values for $E(B-V)_{\rm gas}$, as well as extinction-corrected line ratios. In all subsequent discussion, we adopt the Calzetti et al. (2000) extinction law and $E(B-V)$ values based on rest-frame UV colors.

One important application of our derived $E(B-V)$ values is for inferring Hβ fluxes, independent of sky residuals. We follow a similar methodology to that of Lemoine-Busserolle et al. (2003), and calculate the Hβ flux based on the observed Hα flux, the intrinsic ratio of 2.86 between Hα and Hβ, and our estimated $E(B-V)$ based on $g-r$ colors. Accordingly, $F_{H\beta} = F_{H\alpha}/2.86 \times 10^{-0.4E(B-V)(\kappa_\beta - \kappa_\alpha)}$. In this expression, κ_β and κ_α refer to the extinction coefficients in the Calzetti et al. curve at the wavelengths of Hβ and Hα, respectively. Inferred Hβ fluxes are listed in Table 2.2 and used in the calculation of physical quantities in subsequent sections.

2.3.4 Star-Formation Rate

SFRs were calculated from Hα luminosities based on the calibrations of Kennicutt (1998), but including a normalization factor of 1.8 to convert from a Salpeter (1955) initial mass function (used by Kennicutt) to a Chabrier (2003) initial

Table 2.3. Calculated Physical Values

	Cosmic Horseshoe	Cosmic Horseshoe	Clone	Clone	Clone
Aperture	1	2	1	2	Full
R_{23}	3.82±0.13	3.78±0.11	6.88±0.35	5.25±0.18	5.97±0.18
${R_{23}}^a$	4.08±0.15	3.95±0.12	7.45±0.40	5.52±0.20	6.36±0.20
$N2$	-1.04±0.07	-0.79±0.04	-0.75±0.04	-0.79±0.02	-0.72±0.02
$O3N2$	1.28±0.08	1.08±0.04	1.31±0.05	1.26±0.03	1.23±0.02
$12+\log(\mathrm{O/H})_{R_{23}}$	8.85±0.05	8.85±0.05	8.55±0.05	8.70±0.05	8.63±0.05
$12+\log(\mathrm{O/H})_{{R_{23}}^a}$	8.82±0.05	8.84±0.05	8.50±0.05	8.68±0.05	8.60±0.05
$12+\log(\mathrm{O/H})_{N2}$	8.31±0.18	8.45±0.18	8.47±0.18	8.45±0.18	8.50±0.18
$12+\log(\mathrm{O/H})_{O3N2}$	8.32±0.14	8.38±0.14	8.31±0.14	8.33±0.14	8.34±0.14
O_{32}	1.56±0.09	2.00±0.12	2.61±0.26	2.98±0.20	2.73±0.17
${O_{32}}^a$	1.28±0.07	1.70±0.10	1.84±0.18	2.28±0.15	2.01±0.12
$\mathrm{F_{[SII]\lambda6717}/F_{[SII]\lambda6734}}$	-	0.7±0.2	0.8±0.1	1.0±0.1	0.7±0.1
${\mathrm{L_{H\alpha}}}^c$	17	17	7	7	7
${\mathrm{L_{H\alpha}}}^{a,c}$	26	26	15	15	15
${\mathrm{L_{H\alpha}}}^{b,c}$	66	66	17	17	17
${\mathrm{SFR_{H\alpha}}}^d$	73	73	32	32	32
${\mathrm{SFR_{H\alpha}}}^{a,d}$	113	113	64	64	64
${\mathrm{SFR_{H\alpha}}}^{b,d}$	289	289	75	75	75
$E(B-V)_{g-r}$	0.16	0.13	0.28^e	0.21^e	$0.24^{e,f}$
$E(B-V)_{\mathrm{H\alpha/H\gamma}}$	0.45	0.45	0.28	0.28	0.28

[a]These values are corrected for reddening by the broadband $g-r$ derived $E(B-V)$ values

[b]These values are corrected for reddening by $E(B-V)$ values derived from Hα/Hγ values and assuming Case B recombination

[c]Hα luminosity in units of 10^{42} ergs s^{-1}, corrected for gravitational lensing, and summed across both apertures

[d]SFR in units of $\mathrm{M_\odot\ yr^{-1}}$, corrected for gravitational lensing and summed across both apertures

[e]g and r magnitudes taken from Lin et al. (2009)

[f]g and r magnitudes for the full aperture of the Clone are taken from the flux of the individual apertures

mass function. Lensing serves to increase the measured Hα luminosity, and thus the SFR, by the magnification factor of the lensed image. In order to correct for lensing, we used the published lensing solutions for the Cosmic Horseshoe (Dye et al. 2008; Belokurov et al. 2007) and the Clone (Lin et al. 2009). The published magnification factors apply to the entirety of the Einstein ring and not to the individual knots that we targeted on our NIRSPEC apertures. We therefore used the VLT R and SDSS r-band images to find the fraction of the flux in the total Einstein ring that fell onto the slit (0.11 for the Cosmic Horseshoe and 0.30 for the Clone). Under the assumption that the rest-frame UV flux in these bands is proportional to the flux in Hα, we divided the measured Hα luminosity (for both apertures) by the fraction of flux that fell into the slit versus the total flux in the ring. This calculation yielded the Hα luminosity for the entirety of the ring, which we could then convert to a lensed SFR and divide by the magnification to find the unlensed SFR. For the Cosmic Horseshoe, the magnification factor for the lens is 24 ± 2 (Dye et al. 2008), and adopting this lensing model, we calculated an unlensed SFR of 73 $M_\odot$ yr^{-1} without correcting for reddening, 113 $M_\odot$ yr^{-1} with the broadband $g-r$ color reddening correction and 289 $M_\odot$ yr^{-1} for the Hα/Hγ reddening correction. For the Clone, the magnification factor given for the lens is 27 ± 1 (Lin et al. 2009), and under this assumption, the unlensed SFR was 32 $M_\odot$ yr^{-1} without correcting for reddening, 64 $M_\odot$ yr^{-1} with the broadband $g-r$ color reddening correction and 75 $M_\odot$ yr^{-1} with the Hα/Hγ reddening correction. Based on the quoted uncertainties in the magnification factors and $E(B-V)$ values, the formal errors on the lensing- and dust-corrected SFRs are $\sim 15\%$, yet these errors do not fully reflect hard-to-quantify uncertainties in the fraction of the Hα flux that fell into our slit and the underlying stellar absorption affecting the Balmer lines, and systematics in the lensing models.

SFRs can also be estimated from rest-frame UV luminosities, according to

the relation presented in Kennicutt (1998). We use the optical photometry from Belokurov et al. (2007) and Lin et al. (2009) to obtain such estimates for the Cosmic Horseshoe and the Clone, respectively, again converting from a Salpeter to Chabrier IMF. We calculate an extinction-corrected $SFR_{UV} = 65 - 80\ M_{\odot}$ yr^{-1} for the Cosmic Horseshoe, where the range reflects the uncertainty in inferred $E(B-V)$ values ($\sim 0.13 - 0.16$, see Table 2.3) and magnification factor. The UV-derived SFR is significantly lower than the SFR based on Hα if the Hα extinction correction is calculated from Hα/Hγ. Much better agreement is found when the $E(B-V)$ value used to correct Hα is based on the $g-r$ color. We therefore conclude that, in the case of the Cosmic Horseshoe, the $g-r$ color is a more reliable tracer of the extinction of both stars and gas than the Hα/Hγ ratio. For the Clone, we find an extinction-corrected $SFR_{UV} = 60 - 110\ M_{\odot}$ yr^{-1}, corresponding to $E(B-V)$ values of $\sim 0.21 - 0.28$. This UV-derived SFR agrees very well with the extinction-corrected Hα SFR (regardless of whether $g-r$ or Hα/Hγ is used to extinction-correct Hα). In conclusion, we present the extinction properties of the Cosmic Horseshoe and the Clone, along with a comparison of their Hα and UV SFRs. These results support the findings of Erb et al. (2006b), that $E(B-V)_{\rm star} \simeq E(B-V)_{\rm gas}$ in $z \sim 2$ star-forming galaxies.

2.3.5 Metallicity

Our NIRSPEC measurements include a large number of rest-frame optical emission line fluxes, enabling the calculation of gas-phase metallicities for our objects. The gas-phase metallicity reflects the integrated products of previous star formation, modulated by gas inflow and outflow. Typically, oxygen is used to probe gas metallicity in star-forming galaxies as it is the most abundant heavy element, and is promptly released into the interstellar medium following a burst of star

formation. Furthermore, the emission lines from the various ionization states of oxygen are strong and easily measurable in the rest-frame optical. In this chapter, solar abundance is defined as 12 + log(O/H) = 8.66 (Allende Prieto et al. 2002; Asplund et al. 2004).

For local galaxies, the oxygen abundance can be inferred from the electron temperature by comparing auroral lines (such as [OIII]λ4363) to nebular emission lines (e.g. [OIII]$\lambda\lambda$4959,5007). Weak auroral lines are difficult to measure in high-redshift galaxies, where the ratios of various strong emission lines are used as a proxy for metallicity. These ratios have been calibrated as oxygen abundance indicators in local HII regions. The magnification from the strong-lensing has made it possible to obtain a large set of high quality measurements of emission lines in relatively short exposure times. We therefore can compare three strong-line ratios as oxygen abundance indicators: $R_{23} \equiv$ ([OII]λ3727 + [OIII]$\lambda\lambda$4959,5007/Hβ), $N2 \equiv$ log([NII]/Hα), and $O3N2 \equiv$ log{([OIII]λ5007/Hβ) / ([NII]λ6584/Hα)}. $N2$ and $O3N2$ have been calibrated using direct O/H measurements for local HII regions by Pettini & Pagel (2004), and we used the R_{23} calibration from Tremonti et al. (2004), which has been calibrated with photoionization models. The observed strong-line ratios and inferred metallicities are listed in Table 2.3.

The R_{23} indicator was introduced by Pagel et al. (1979), and is widely used for measuring local metal abundances if the fluxes of [OIII] and [OII] are known. Tremonti et al. (2004) provided an analytical fit to the R_{23} - metallicity relation for a set of local SDSS galaxies:

$$12 + \log(\mathrm{O/H}) = 9.185 - 0.313x - 0.264x^2 - 0.321x^3 \qquad (2.1)$$

where $x = \log R_{23}$. Since R_{23} is double valued for the larger values of the ratio, this formula is only valid for the high metallicity branch of the R_{23}-abundance re-

lation. This relationship has a 1σ scatter of 0.05 dex for the sample of star-forming galaxies presented in Tremonti et al. (2004), though this error may underestimate the true systematic uncertainty (Kennicutt et al. 2003). For R_{23}, we used the values for the Hβ flux that we inferred from the broadband color-derived value of $E(B-V)$. R_{23} is sensitive to reddening because of the large wavelength difference between [OIII]λ5007 and [OII]λ3727. The observed [and extinction corrected] R_{23} values that we calculated for our objects were 3.82[4.07], 3.79[3.96] for the two apertures of the Cosmic Horseshoe, and 6.86[7.41], 5.25[5.52], and 5.93[6.32] for the two apertures and the full aperture of the Clone. The R_{23} values for apertures 1 and 2 of the Cosmic Horseshoe correspond to metallicities of 12+log(O/H) = 8.85[8.82] and 8.85[8.84], respectively. These are high relative to solar metallicity. For the Clone, the inferred metallicities for apertures 1, 2 and the full aperture are 12+log(O/H) = 8.55[8.50], 8.70[8.68], and 8.64[8.60], respectively. These values range from slightly subsolar to solar.

The $N2$ indicator is related to the oxygen abundance by:

$$12 + \log(\mathrm{O/H}) = 8.90 + 0.57 \times \mathrm{N2} \tag{2.2}$$

which is valid for $7.50 < 12 + \log(\mathrm{O/H}) < 8.75$. The relationship has a 1σ scatter of ± 0.18 dex on the y-intercept (Pettini & Pagel 2004). We found values of $N2 = -1.04$ and -0.79 (12+log(O/H) = 8.31 and 8.45) for the Cosmic Horseshoe, and -0.75, -0.79, and -0.72 (12+log(O/H) = 8.47, 8.45, and 8.50) for the Clone. These values all indicate a subsolar gas metallicity.

We also measured values of the $O3N2$ indicator for our objects. This indicator is related to oxygen abundance by:

$$12 + \log(\mathrm{O/H}) = 8.73 - 0.32 \times \mathrm{O3N2} \tag{2.3}$$

which is valid for $8.12 < 12+\log(\mathrm{O/H}) < 9.05$, with a 1σ scatter of ± 0.14 dex (Pettini & Pagel 2004). The errors shown for our oxygen abundances are dominated by the systematic uncertainties from the calibration, as opposed to measurement errors. For $O3N2$, we used the values of Hβ that were calculated from the $g-r$ color, as described in §2.3.3. The values that we calculated are 1.28, 1.08 ($12+\log(\mathrm{O/H}) = 8.32$ and 8.38) for the Cosmic Horseshoe, and 1.31, 1.26, and 1.23 ($12+\log(\mathrm{O/H}) = 8.31$, 8.33, and 8.34) for the Clone. These values indicate subsolar metallicities in the gas. The $N2$ and $O3N2$ indicators do not need to be dereddened due to the close spacing of the [NII], Hα lines and [OIII], Hβ lines.

The $N2$ and $O3N2$ indicators yield consistent metallicities of ~ 0.5 solar for both the Cosmic Horseshoe and the Clone. However, the R_{23} indicator points to a significantly higher, and supersolar, metallicity in the Cosmic Horseshoe. Such systematic discrepancies between R_{23} and other indicators are well known among local star-forming galaxies, and reflect the current limitations of strong-line abundance indicators (Kewley & Ellison 2008; Kennicutt et al. 2003). For the Clone, R_{23} indicates a metallicity that is only slightly higher than, and statistically consistent with, the values implied by $N2$ and $O3N2$. As we will discuss in §2.4.2, the differences in metallicity for the Cosmic Horseshoe and the Clone based on R_{23} may reflect the relative positions of these objects with respect to the emission-line excitation sequence of local objects.

2.3.6 Ionization Parameter

The local ionization state in an HII region is often characterized by the ionization parameter, U, which is the ratio between the density of ionizing photons and the density of hydrogen atoms. Commonly, ionization parameters are estimated using O_{32} = ([OIII]$\lambda\lambda$4959,5007 / [OII]$\lambda\lambda$3726,3729), and corrected for reddening. We

estimate extinction based on the observed $g - r$ colors. Our values of O_{32}, both uncorrected [and corrected] for extinction, are 1.56[1.28], 2.00[1.70] for the two apertures of the Cosmic Horseshoe, and 2.61[1.84], 2.98[2.28], and 2.73[2.01] for the two apertures and the full aperture of the Clone. Lilly et al. (2003) showed that a vast majority of local objects (from a Nearby Field Galaxy Survey B-selected local galaxy sample from Jansen et al. (2000)) have a value of $O_{32} < 1$, while the available data for objects at $z > 2$ (Pettini et al. 2001) indicate $O_{32} > 1$ (Pettini et al. 2001).

The value of O_{32}, however, is dependent not only on ionization parameter, but also, to a lesser extent, on metallicity (Kewley & Dopita 2002; Brinchmann et al. 2008). Kewley & Dopita (2002) provide formulae for relating observed values of O_{32} to ionization parameter, $\log(U)$, using photoionization models spanning a range of metallicities. We apply the relations for both 0.5 and $1.0Z_{\odot}$ models to translate our extinction-corrected O_{32} measurements into $\log(U)$ values. The adopted models reflect the range of metallicities inferred for the Cosmic Horseshoe and the Clone. At higher metallicities, a given value of O_{32} corresponds to a higher ionization parameter, so the $0.5Z_{\odot}$ models yield a lower bound to the inferred ionization parameters. Assuming $Z = 1.0Z_{\odot}$, we find $\log(U)$ ranging from -2.4 to -2.5 and -2.3 to -2.4 for the apertures of the Cosmic Horseshoe and the Clone, respectively. At $Z = 0.5Z_{\odot}$, the corresponding ionization parameters range from $\log(U) = -2.7$ to -2.8 and -2.5 to -2.6, i.e., $0.2 - 0.3$ dex lower. The $\log(U)$ values inferred for 0.5 and $1.0Z_{\odot}$ models are very similar to the high ionization parameters (relative to local SDSS galaxies) inferred by Brinchmann et al. (2008) for the $z > 2$ objects in Pettini et al. (2001).

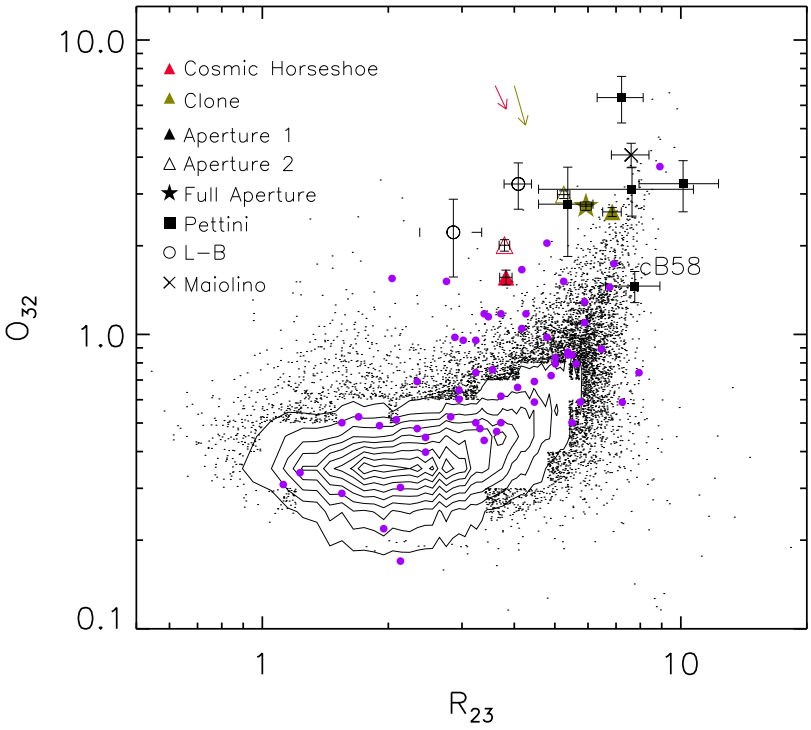

Figure 2.7 O_{32} versus R_{23} diagram. The apertures of the Cosmic Horseshoe and the Clone are plotted along with star-forming galaxies at local, intermediate, and high redshifts. The black points and contours represent SDSS local AGNs and star forming galaxies that satisfy the criteria described in §2.4.2. A selection of $0.47 < z < 0.92$ objects from Lilly et al. (2003) are shown in purple. High-redshift points include five $z \sim 3$ LBGs from Pettini et al. (2001), two lensed $z \sim 1.9$ objects from Lemoine-Busserolle et al. (2003), and a composite spectrum of nine $z \sim 3.5$ LBGs from Maiolino et al. (2008). Symbols are described in the legend. The values on this plot are not corrected for dust extinction, however the red and green arrows indicate, respectively, the small impact of extinction corrections on the Cosmic Horseshoe and Clone data points. Such dust corrections will shift points downwards and to the right. The objects at $z \geq 2$ are systematically displaced on average with respect to the lower-redshift sample towards larger values of O_{32}, at fixed values of R_{23}. This empirical trend is evidence for higher ionization parameters at fixed metallicity (Kewley & Dopita 2002).

2.3.7 Electron Temperature and Density

The [SII]$\lambda\lambda$6717,6732 line ratio is sensitive to the electron density of an ionized gas. We used this line ratio in our objects to calculate the electron density for the ionized nebular gas. Similarly, the ratio ([OIII]$\lambda\lambda$4959, 5007 / [OIII]λ4363) is used to measure the electron temperature, as [OIII] has an energy-level structure that results in upper level emission lines with different excitation energies, whose relative strengths thus depend strongly on temperature. We used the IRAF procedure TEMDEN to calculate a range of densities and temperatures based on these line ratios.

Upper limits on the electron temperatures were measured from the [OIII] line ratios, since we were only able to measure upper limits for the [OIII]λ4363 line flux. For the lowest densities ($\sim$100 cm^{-3}), the upper limits on the temperatures were 12,900 K and 12,200 K for the two apertures of the Cosmic Horseshoe and 13,200 K, 9,700 K and 10,000 K for the two apertures and the full aperture of the Clone, respectively. Changes in the density over the range 100 to 5000 cm^{-3} altered the calculated temperatures only very slightly.

We calculated densities from the measured [SII] line ratios in all apertures except for aperture 1 of the Cosmic Horseshoe, which had insufficient S/N. We also summed both apertures of the Cosmic Horseshoe to obtain an average, higher S/N, [SII] line ratio estimate for the galaxy. In the calculation of densities we assumed a standard temperature of 10,000 K, consistent with our limits on electron temperatures. For each object the $\pm 1\sigma$ range in electron density was then derived from errors on the observed line ratios. For the Cosmic Horseshoe, Aperture 2, the $\pm 1\sigma$ range in electron density is $840 - 6900$ cm^{-3}; for the summed Cosmic Horseshoe apertures, the corresponding range is $320 - 1600$ cm^{-3}. For the Clone, apertures 1, 2, and full, we find ranges of $1110 - 2960$ cm^{-3}, $530 - 1020$ cm^{-3}, and

$1270 - 2540$ cm^{-3}. Despite the large uncertainties in the precise value of inferred electron density, the empirical fact remains that the high-redshift lensed targets exhibit systematically lower doublet ratios from what is typically observed in emission-line galaxies in the local universe (Liu et al. 2008).

2.4 Analysis

2.4.1 Comparison to the $z \sim 2$ Population

Recent studies have been undertaken to understand the physical conditions of $z \sim 2$ objects (Erb et al. 2006a; Liu et al. 2008) and the observations presented here enable comparisons of the Cosmic Horseshoe and the Clone with the larger population of star-forming galaxies at similar redshifts. The Cosmic Horseshoe and the Clone, based on their *ugr* colors, satisfy the criteria for UV-selected objects at $z \sim 2$ (Steidel et al. 2004). In the following analysis, we compare the physical quantities calculated from the rest frame optical line fluxes to those calculated in other high-redshift objects.

SFRs in high redshift objects have been measured in a variety of ways. We calculated lensing-corrected values for the SFR of $\sim 113\ M_{\odot}$ yr^{-1} based on our method of dereddening the Hα fluxes for the Cosmic Horseshoe (i.e., from the $g - r$ color) and $64 - 75\ M_{\odot}$ yr^{-1} based on our method of dereddening for the Clone (i.e., from both the $g - r$ color and Hα/Hγ ratio). The average SFRs for a population of $z \sim 2$ galaxies from Erb et al. (2006b) is $\langle SFR_{H\alpha} \rangle = 31 \pm 18\ M_{\odot}$ yr^{-1}. Our lensed targets are therefore more actively star-forming than average, but within the range spanned by the sample in Erb et al. (2006b). However, we caution that our calculated values depend on the magnification given by the particular lensing models that we used. For comparison, based on the Hα flux

and magnification factor of ~ 30 (Teplitz et al. 2000; Seitz et al. 1998) and with the assumption of a Chabrier initial mass function and Calzetti et al. (2000) dust extinction law with an estimated $E(B-V)_{\rm gas} = 0.06$ (Siana et al. 2008), the SFR for MS1512-cB58 is $SFR(H\alpha) = 14\ M_{\odot}\ {\rm yr}^{-1}$.

Erb et al. (2006c) measure an average velocity dispersion for a sample of $z \sim 2$ objects (with AGN removed) of $\langle\sigma\rangle = 108 \pm 5$ km s^{-1}, and a standard deviation of 86 km s^{-1}. Our objects show a smaller velocity dispersion than the average, but are within the sample's large standard deviation. While SDSS J0901+1814, in particular aperture 2, displays AGN-like line ratios, the velocity dispersions are very close to the average values for other $z \sim 2$ objects, indicating that SDSS J0901+1814 could be a narrow-line AGN. The dust extinction values that we infer from the $g-r$ color for the Cosmic Horseshoe are similar to the mean $E(B-V)$ value of 0.16 ± 0.01 from Erb et al. (2006c), while the Clone appears to be dustier than average, based on its $g-r$ color and Hα/Hγ ratio. Both objects are well within the range of extinction values spanned by $z \sim 2$ star-forming galaxies.

Our values for $N2$ ranged from -0.72 to -1.04, within the interval spanned by the sample of $z \geq 2$ galaxies from Erb et al. (2006a). Values of R_{23} span from 4.0 to 7.4, resulting in a range of metallicities that are slightly subsolar to slightly greater than solar, between 12+log(O/H) = 8.5 to 8.8. Values for R_{23} from Pettini et al. (2001) for LBGs at $z \sim 3$ are within this range, between 4.0 and 12.3, including a value of $R_{23} = 8.3$ for MS 1512-cB58. Lilly et al. (2003) plot star-forming galaxies at intermediate redshift ($0.47 < z < 0.92$) by their values for O_{32} versus R_{23}, and we reproduce their diagram in Figure 2.7, adding the Cosmic Horseshoe and Clone, along with SDSS local AGNs and star forming galaxies that satisfy the criteria described in §2.4.2. To place our new observations in the context of other, similar measurements at high redshift, we also plot five LBGs

at $z \sim 3$ from Pettini et al. (2001), two lensed objects at $z \sim 1.9$ from Lemoine-Busserolle et al. (2003), and the composite $z \sim 3.5$ spectrum from Maiolino et al. (2008), based on nine individual LBGs. In this plot, note that all of the values are as measured, and none have been dereddened. The effect of correcting the points for the Cosmic Horseshoe and Clone for dust extinction is indicated with reddening vectors. This diagram shows how objects at $z \geq 2$ have larger values of O_{32} (indicative of high values of the ionization parameter) for a given value of R_{23} (and thus, metallicity), relative to the sample from Lilly et al. (2003).

A common property of $z \geq 2$ star-forming galaxies is the kinematic evidence for star-formation feedback in the form of large-scale gas outflows (Pettini et al. 2001; Shapley et al. 2003). With measurements of the nebular, systemic redshifts for both the Cosmic Horseshoe and Clone, as well as rest-frame UV absorption-line spectra, it is possible to search for the signature of outflows. Using Keck II Echelle Spectrograph and Imager (ESI; Sheinis et al. 2002) rest-frame ultraviolet spectra of the Cosmic Horseshoe and the Clone, Quider et al. (2009) and Quider et al. (2010) analyze several of the strongest interstellar absorption features for kinematic evidence of large-scale gas outflow. In this analysis, redshifts measured for interstellar absorption lines were compared with those of Hα and UV stellar photospheric features. For both targets, the slits were placed in the same position that was used for the NIRSPEC observations, and the spectra from the two apertures were summed to increase the signal-to-noise ratio. In the Cosmic Horseshoe, the average outflow velocity for the low-ionization interstellar absorption lines (e.g., SiII λ1260, the OI + SiII λ1303 doublet, SiII λ1527, AlII λ1671) is $\langle v_{out,low} \rangle = 146$ km s^{-1}, and $\langle v_{out,high} \rangle = 167$ km s^{-1} for the high-ionization features (e.g., SiIV $\lambda\lambda$1394,1403, AlIII λ1855, AlIII λ1863). In the Clone, three low-ionization iron lines (FeII λ2344, 2383, and 2600) were used to measure interstellar kinematics. These three lines indicate similar offsets, and the average

outflow velocity is $\langle v_{out,low} \rangle = 154$ km s^{-1}. The outflow velocities observed in the Cosmic Horseshoe and Clone are consistent with those calculated for star-forming galaxies at $z \sim 2$ (Steidel et al. 2004). Also, for comparison, the outflow velocity observed in MS 1512-cB58 is ~ 255 km s^{-1} (Pettini et al. 2002).

The Hα velocity dispersion, σ, allows us to calculate the virial masses of our objects when combined with estimates of their sizes, using the half-light radius, $r_{1/2}$. We use the equation given by Pettini et al. (2001) for virial mass, assuming an idealized case of a sphere of uniform density:

$$M_{\rm vir} = 1.2 \times 10^{10} M_{\odot} \frac{\sigma^2}{(100\,{\rm km\,s^{-1}})^2} \frac{r_{1/2}}{\rm kpc} \tag{2.4}$$

The lensing models for both the Cosmic Horseshoe and the Clone yield estimates of the intrinsic half-light radii, allowing us to calculate the virial masses of the objects.

The lensing model for the Cosmic Horseshoe (Dye et al. 2008) produces a source plane image with two objects, a "northern" and a "southern" source. These objects are lensed into ring-like distributions in the image plane, with slightly different morphologies. Accordingly, the relative contribution of the two sources varies as a function of position in the combined Einstein ring. The fainter, northern source, according to the Dye et al. (2008) model, contributes mostly to the portion of the Einstein ring that is not probed by our slit position, although the light from this source does contribute a small fraction of the emission in what we call aperture 1. The southern source, the more prominent of the two, is the only contributor to the emission in aperture 2 and constitutes the majority of the light in aperture 1. From the composite of the reconstructed source plane image, we estimated a half-light radius of the southern source of $\sim 0\farcs3$, which, at this redshift, and, for our adopted cosmology, corresponds to a size of $r_{1/2,CH} =$

2.5 kpc. Thus, using the velocity dispersion for the second aperture, since it corresponds only to the southern source in the reconstructed image, we calculate a virial mass of the Cosmic Horseshoe of $M_{vir,CH} = 1.0 \times 10^{10} M_{\odot}$.

For the Clone, the lensing models described in Lin et al. (2009) and Allam et al. (2009, in preparation) yield estimates of the half-light radius in the reconstructed source plane of $\sim 0\farcs3$. At this redshift, the corresponding physical radius is $r_{1/2,Clone} = 2.9$ kpc. The virial mass we calculated for the Clone, using the velocity dispersion from the full aperture, was $M_{vir,Clone} = 2.2 \times 10^{10} M_{\odot}$. Both the dynamical masses calculated for the Cosmic Horseshoe and the Clone are similar to the dynamical masses for objects at $z \sim 2$ from Erb et al. (2006c).

While the line flux ratios for the Clone are very similar between the apertures, the Dye et al. (2008) lensing model might help to explain the difference in the line flux ratios observed between the two apertures of the Cosmic Horseshoe. For instance, as seen in Table 2.2 and Figure 2.3, the [NII] and Hα lines vary in strength with relation to each other. One possible hypothesis concerns the level of contribution from the "northern" source to the first aperture of the lensed ring. If the gas in the fainter, northern source was at a lower metallicity, it would slightly lower the [NII]/Hα line ratio of aperture 1 compared to aperture 2, which is what is observed in our data. Future analysis will be undertaken with the lensing model in order to disentangle the contribution from each object in the source plane.

In summary, we have shown that the SFRs, extinction values, metallicities, outflow velocities, and dynamical masses for our objects are relatively typical of those found among UV-selected star-forming galaxies at $z \sim 2$ (Steidel et al. 2004). We conclude that the Cosmic Horseshoe and the Clone are a representative sample of the luminous segment of the population of $z \sim 2$ objects. Future

multi-wavelength observations of the broadband spectral energy distributions of the lensed targets will allow us to characterize their stellar masses and ages and therefore evolutionary states.

2.4.2 The Offset in the [NII]/Hα vs. [OIII]/Hβ diagram for High-Redshift Galaxies

Recently, Shapley et al. (2005b), Erb et al. (2006a), and Liu et al. (2008) have presented evidence indicating a difference between HII regions in high-redshift galaxies and those in local galaxies. The physical conditions in these regions are often probed by using the well known empirical diagnostic diagram of Baldwin, Phillips, & Terlevich (1981) (hereafter BPT). This diagram separates star-forming galaxies and AGNs according to the optical line ratios [NII]/Hα and [OIII]/Hβ; star-forming galaxies fall in a region of lower [NII]/Hα for a range of values of [OIII]/Hβ. It has been demonstrated that a fraction of high redshift star-forming galaxies at $z \sim 1-2$ lie offset from the local population of HII regions and star-forming galaxies, displaced towards higher [NII]/Hα and [OIII]/Hβ values. The strongly lensed, $z \sim 2$ objects are plotted on the BPT diagram in Figure 2.8 along with local emission-line objects from the fourth data release (DR4) of the SDSS (York et al. 2000; Adelman-McCarthy et al. 2006). The SDSS objects were selected to have [NII], Hα, [OIII], and Hβ line detections with S/N > 5. Also plotted on the diagram are curves designed to separate star forming galaxies and AGNs; one line is from Kauffmann et al. (2003) that demarcates star-forming galaxies and AGNs on an empirical basis, and the other from Kewley et al. (2001a) that represents a limit to the line-flux ratios that can be produced for star forming regions from photoionization plus stellar population synthesis models.

For both the Cosmic Horseshoe and the Clone, we plot two points for each

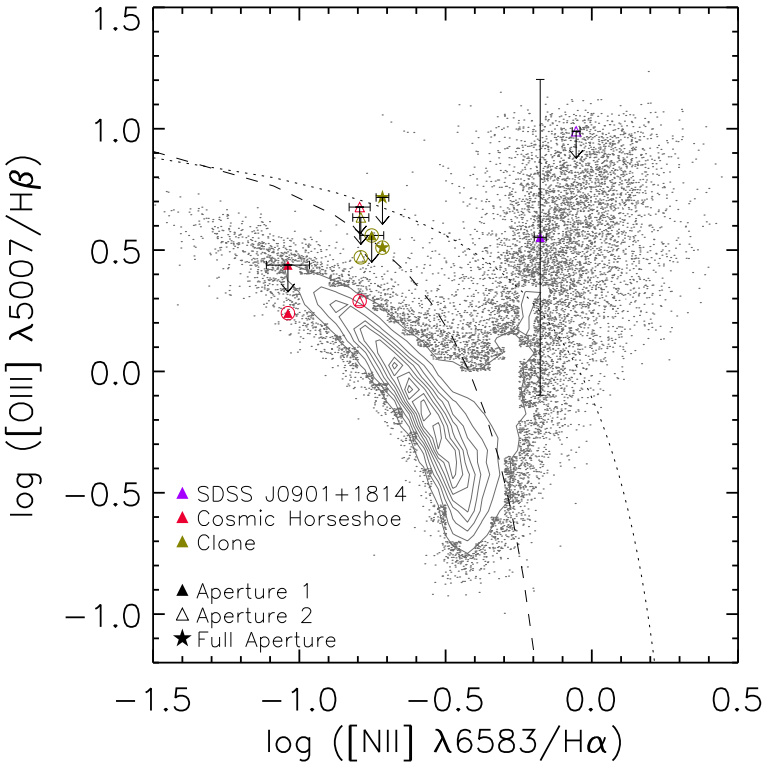

Figure 2.8 HII region diagnostic plot of log[NII]/Hα and log[OIII]/Hβ emission line ratios. The grey points and contours represent SDSS local AGNs and star forming galaxies that satisfy the criteria described in §2.4.2, while the lensed objects are as labelled in the legend. The circled objects are those where the Hβ flux values were inferred from the $g-r$ color and Hα fluxes. SDSS J0901+1814 points show large error bars due to the presence of a sky line on the Hβ line in both apertures. The dashed line is an emprical demarcation between star-forming regions and AGNs from Kauffmann et al. (2003) based on the SDSS galaxies, whereas the dotted line is the theoretical limit for star-forming galaxies from Kewley et al. (2001a). Local star-forming galaxies and HII regions exist in a well-defined excitation sequence due to photoionization by massive stars, and these are found to the left and below the curves. The apertures of the Clone, even with the inferred values of Hβ, are on average offset from this excitation sequence.

aperture, one for each of method of calculating Hβ fluxes. First, we plot upper limits on [OIII]/Hβ to reflect the fact that the measured Hβ is a lower limit due to sky-subtraction residuals. Next, we plot circled symbols using the values of Hβ flux inferred from Hα and the $g-r$ color as described in §2.3.3. While SDSS J0901+1814 lies in the region occupied by local AGNs, the two apertures of the Clone both appear in the area above the local star-forming regions. For the inferred Hβ values, the line ratios for the Clone are shifted towards higher [OIII]/Hβ by $0.2-0.3$ dex, relative to star-forming SDSS galaxies with similar [NII]/Hα ratios. Alternatively, the Clone is shifted towards higher [NII]/Hα by 0.6 - 0.7 dex compared to SDSS galaxies with similar [OIII] / Hβ ratios. The interpretation is less straightforward for the Cosmic Horseshoe. Indeed, the [OIII]/Hβ upper limit for its second aperture is also offset from the local emission-line sequence, yet adopting the Hβ value based on the Hα flux and $g-r$ color places this aperture on the top edge of the locus of low-redshift galaxies. On the other hand, using the Hα/Hγ ratio to estimate the Hβ flux results in an [OIII]/Hβ ratio that is midway between the two plotted symbols for this aperture, and, again, offset with respect to the local emission-line sequence. Our best estimate for aperture 2 of the Cosmic Horseshoe is that its point on the BPT diagram lies somewhere between top of the local emission-line sequence and the symbol indicating the upper limit for the aperture. In contrast, the point for aperture 1 of the Cosmic Horseshoe is consistent, or even below, the local emission-line sequence, depending on which value of Hβ is adopted. Identifying the origin of the emission-line ratio variations within the Cosmic Horseshoe clearly requires a more detailed investigation, in concert with the lensing model for this system. Such analysis is outside the scope of the current work.

We have not corrected our Hβ fluxes for possible stellar absorption at this wavelength. Stellar absorption would lead to an underestimate of the flux, and

push the points upward on the BPT diagram. However, as noted in Shapley et al. (2005b) and Erb et al. (2006a), the stellar Hβ absorption line should have an equivalent width of only $W_{abs} \leq 5$ Å (Charlot et al. 2002). Given that the Clone has $W_{H\beta} \geq 20 - 30$ Å, and the Cosmic Horseshoe does not have significant continuum detected in the spectral region near Hβ, stellar absorption is not significant. Furthermore, we defer application of this correction until the underlying stellar populations for the Cosmic Horseshoe and the Clone have been better constrained by deeper spectroscopy and multi-wavelength photometry.

While the Cosmic Horseshoe does not display the same clear offset as the Clone on the BPT diagram, when considered as a *population*, the sample of $z \sim 2$ objects with line ratio measurements (i.e., those presented in this chapter as well as those in Erb et al. 2006a) appears to be offset on average from local galaxies. We have demonstrated that the Cosmic Horseshoe and Clone are typical of $z \sim 2$ star-forming galaxies in many respects, and also display several striking differences with respect to local galaxies in terms of their physical properties. As such, we will use the special insights afforded by gravitational lensing into the physical conditions in the Cosmic Horseshoe and Clone to explain the properties of the $z \sim 2$ population as a whole. We recognize the simplification associated with drawing conclusions based on only two objects, and the fact that a significantly larger sample of galaxies with the complete set of rest-frame optical emission lines is required to characterize the full $z \sim 2$ population. The discussion of the Cosmic Horseshoe and the Clone that follows represents the initial step in the direction of such a statistical study.

An important point of contrast between local star-forming galaxies in the SDSS and our high-redshift targets is the rate of star-formation activity. Shapley et al. (2005b) report an aperture-corrected mean SFR for a local sample of SDSS

galaxies of 2.0 $M_{\odot}$ yr^{-1}. These authors also noted that offset objects in the BPT diagram (both at high redshift and in the local SDSS sample) seem to exhibit elevated SFRs relative to the local average, and this is further demonstrated in a small sample of extreme SDSS galaxies in Liu et al. (2008). We estimate lensing-corrected SFRs in the Clone and Cosmic Horseshoe that are even higher than those presented in Shapley et al. (2005b), more than an order of magnitude larger than the average SDSS SFR.

The higher rate of star formation might lead to a larger reservoir of ionizing photons, which is reflected in the ionization parameter. Brinchmann et al. (2008) demonstrated that the diagnostic line ratios in the BPT diagram are strongly dependent on the ionization parameter. However, while previous discussion of the offset has only provided possible explanations that could lead to this effect, our measurement of a host of lines, such as [OII]$\lambda\lambda$3726,3729 in the magnified objects, allows us to test this discussion more quantitatively. To date, only a small sample of ionization parameter measurements have been obtained for objects at $z \geq 2$ (Pettini et al. 2001; Lemoine-Busserolle et al. 2003; Maiolino et al. 2008). In both the Cosmic Horseshoe and the Clone, our measurements of O_{32} indicate higher values of the ionization parameter than seen in even the most extreme low-z UV selected galaxies from Contini et al. (2002), or a sample of star-forming galaxies at intermediate redshift ($0.47 < z < 0.92$) from Lilly et al. (2003). Figure 2.7 illustrates this point very clearly, in that, at fixed metallicity (i.e., R_{23}) high-redshift galaxies are offset on average towards significantly higher O_{32} (i.e., ionization parameter). If O_{32} values were considered in isolation, the differences in O_{32} between low- and high-redshift samples could simply be attributed to metallicity differences. However, the addition of R_{23} measurements indicates that there is a real effect towards systematically higher ionization parameters at high redshift.

Another idea discussed in Brinchmann et al. (2008) and Liu et al. (2008) is that the higher ionization parameter that might lead to this offset on the BPT diagram is due to a higher density in the HII regions. The [SII]$\lambda\lambda$6717,6732 line ratio allowed us to measure the density of the star forming regions in the Cosmic Horseshoe and the Clone, and the low resulting ratios indicated high densities of about $\sim 10^3$ cm^{-3}, which is an order of magnitude higher than the values encountered in local starbursts (Kewley et al. 2001b). The ESI spectra analyzed by Quider et al. (2009) and Quider et al. (2010) also show another independent measure of the density in the form of the [CIII]λ1907/CIII]λ1909 line ratio. With this line ratio, values of about 1.5 and above are in the low density regime, while values from 0.2 and lower are in the high density regime. For the Cosmic Horseshoe, deblending the two lines in a smoothed spectrum yields a line ratio of 1.1 ± 0.2, and for the Clone, the line ratio is 1.2 ± 0.2. The values for the Cosmic Horseshoe and the Clone indicate densities ranging from $5000 - 22000$ cm^{-3} and $3000 - 17000$ cm^{-3}, respectively. These are at least as high as those derived from the [SII] doublet (Osterbrock 1989). Brinchmann et al. (2008) calculate that densities of this order would account for an increase in the ionization parameter, which might lead to the observed offset on the BPT diagram.

2.5 Conclusions

We present NIRSPEC rest-frame optical spectra of three strongly-lensed $z \sim 2$ galaxies. These include SDSS J0901+1814 ($z = 2.26$), which, due to its observed line ratios, is possibly contaminated by an AGN; and two star-forming galaxies, the Cosmic Horseshoe ($z = 2.38$) and the Clone ($z = 2.00$). The general physical properties of the Cosmic Horseshoe and the Clone are representative

of the properties found for star-forming galaxies at the same redshift. Specifically, we have measured the SFR from the Hα luminosity, corrected for reddening and magnification from the lensing, and found it to be high yet typical of other measurements of high-redshift star formation (SFR = $\sim$ 110 $M_{\odot}$ yr^{-1} for the Cosmic Horseshoe and $\sim$ 70 $M_{\odot}$ yr^{-1} for the Clone). We have also used the R_{23}, $N2$, and $O3N2$ methods to calculate the metallicity of the HII regions, and found that, while there are differences among the metallicities calculated from these indicators, we can still constrain the metalliticies to range from slightly sub-solar to solar. The dynamical masses calculated from Hα velocity dispersions and the half-light radii of the reconstructed sources are on the order of 10^{10} $M_{\odot}$, which is typical of the dynamical masses of UV-selected star-forming galaxies at $z \sim 2$. Finally, ESI rest-frame UV spectra provide evidence for the existence of outflowing gas with a velocity on the order of $\sim 150 - 200$ km s^{-1} for the Cosmic Horseshoe and the Clone, which are also similar to outflows seen in other high-redshift galaxies (Pettini et al. 2001; Steidel et al. 2004; Adelberger et al. 2003). In the future, it will be valuable to model the stellar populations of our lensed targets using multi-wavelength broadband photometry, and therefore obtain constraints on their stellar masses and ages.

The combination of strong lensing and NIRSPEC observations has allowed us to probe physical conditions that to date have been largely unexplored at $z \geq 2$. The measurements of the [SII]$\lambda\lambda$6717,6732 line ratio indicated high densities ($\sim 10^3$ cm^{-3}) in these regions, in agreement with the densities derived from [CIII]λ1907/CIII]λ1909 line ratios for both objects. Large ionization parameters were measured by using O_{32}, which further indicates the high ionization state of the gas in high-redshift objects. The high values for the ionization parameter, density, and SFR in both the Cosmic Horseshoe and the Clone help in understanding why, on average, the population of high-redshift objects are offset on

the BPT diagram, a standard diagnostic for star-forming regions (Shapley et al. 2005b; Erb et al. 2006a; Liu et al. 2008). The exceptional data quality enables the measurement of quantities that previously were only speculation for $z \sim 2$ galaxies. These results offer more concrete evidence of the different conditions under which star formation occurs in galaxies at high redshift, yet a statistical sample is still required to place the results on firmer ground. Future observations with the Multi-Object Spectrometer for Infra-Red Exploration (MOSFIRE) instrument recently deployed on the Keck I telescope will allow for the assembly of a much larger sample of rest-frame optical emission lines for this type of analysis.

CHAPTER 3

The Rest Frame Ultraviolet Spectra of UV-Selected Active Galactic Nuclei at $z \sim 2-3$

3.1 Introduction

In order to explain observations of massive galaxy evolution in the universe, current models of galaxy formation require a form of energetic feedback that is thought to result from the effects of a central active galactic nucleus (AGN) (Croton et al. 2006; Somerville et al. 2008; Di Matteo et al. 2008). Energy and momentum input from the AGN into the galaxy's interstellar medium (ISM) can serve to heat or remove gas so that it is no longer available for star formation. "AGN feedback" has been presented as one of the major factors giving rise to the red sequence in massive galaxies (Silk & Rees 1998; Kauffmann et al. 2003). Furthermore, every galaxy bulge appears to contain a supermassive black hole (Kormendy & Richstone 1995), whose mass is correlated with bulge properties such as stellar velocity dispersion (Merritt & Ferrarese 2001; Gültekin et al. 2009). These correlations offer evidence of coupling between the formation of the black hole and bulge, which may result from the effects of AGN feedback (Silk & Rees 1998; Murray et al. 2005; Hopkins et al. 2008). Outflows have been observed in strongly star-forming galaxies over a range of redshifts (Franx et al. 1997; Shapley et al. 2003; Martin 2005; Steidel et al. 2010; Rupke et al. 2005a), and

post-starburst galaxies at $z \sim 0.6$ (Tremonti et al. 2007). For AGNs, outflows have been observed in local Seyfert galaxies (Crenshaw et al. 2003; Krug et al. 2010), and at higher redshifts in broad absorption line quasars (Korista et al. 2008; Ganguly & Brotherton 2008), radio galaxies (Nesvadba et al. 2006, 2008), and ULIRGs (Alexander et al. 2010). However, at early times, outflows have thus far not been fully examined in a sample of active galaxies that can be quantitatively compared to a non-active sample with similar host galaxy properties. This chapter examines the outflow properties of such a sample at $2 \leq z \leq 3$, when both star-formation density and black hole (BH) accretion were at their peak (Madau et al. 1996; Ueda et al. 2003; Richards et al. 2006; Reddy et al. 2008; Silverman et al. 2008).

The rest-frame UV portion of a galaxy spectrum is ideally suited for the study of the ISM. In star-forming galaxies, this spectral region contains emission or absorption from HI Lyman α, as well as low- and high-ionization metal absorption lines that have been used to infer the presence of outflows (Pettini et al. 2000, 2001, 2002; Shapley et al. 2003). At $z \sim 2-3$, the rest-frame UV part of the spectrum is shifted into the observed optical, and is accessible using ground-based facilities. At these redshifts, individual galaxy spectra have low continuum signal-to-noise (S/N), which makes robust absorption line measurements challenging. With a large enough sample, however, a higher S/N composite spectrum can be created, allowing measurements of the global properties and spectral trends within the sample. Shapley et al. (2003) and Steidel et al. (2010) have used such composite spectra to explore the outflow properties of UV-selected star-forming galaxies at $z \sim 2-3$.

Because the black hole accretion disk and broad-line region are obscured from view, the light from a narrow-lined AGN is not dominated by emission from

the central source, but rather that of the host galaxy. The ability to study the host galaxy allows for a comparison between the galaxy-scale properties of a sample of narrow-lined AGNs and those of a similar non-AGN sample. In order to undertake such a study, we augment the sample of narrow-lined UV-selected AGNs at $z \sim 3$ presented in Steidel et al. (2002), extending it to include objects at $z \sim 2$. The original sample enabled, for the first time, an estimation of the fraction of star forming galaxies within the Lyman Break Galaxy (LBG) survey that showed evidence for AGN activity on the basis of their rest frame UV spectroscopic properties. With the expanded sample of AGNs, we construct composite spectra that reveal the properties of outflowing gas in these objects. The galaxies that harbor these narrow-lined AGN were selected on the basis of their broadband rest-frame UV colors, and should have host galaxies similar to those of the non-AGN LBGs. As this AGN sample appears to be hosted by galaxies drawn from the same parent population as the non-AGN LBG sample (Steidel et al. 2002; Adelberger & Steidel 2005b), we can conduct a controlled experiment to understand how the AGN impacts the gas properties of the host galaxy.

The sample of UV-selected AGNs is presented in §3.2, while in §3.3 we describe the creation of the AGN composite spectrum. This spectrum and its basic properties are shown in §3.4, including the detection of blueshifted high-ionization absorption features. In §3.5, we examine spectral trends within the AGN sample that are highlighted by separating objects according to Lyα equivalent width (EW), UV magnitude, and redshift. We conclude in §3.6 with a discussion placing the results from the composite spectrum analysis into the context of our understanding of AGNs. Throughout our analysis, we assume $\Omega_{\rm M} = 0.27$, $\Omega_{\Lambda} = 0.73$, and $H_0 = 71$ km s^{-1} Mpc^{-1}.

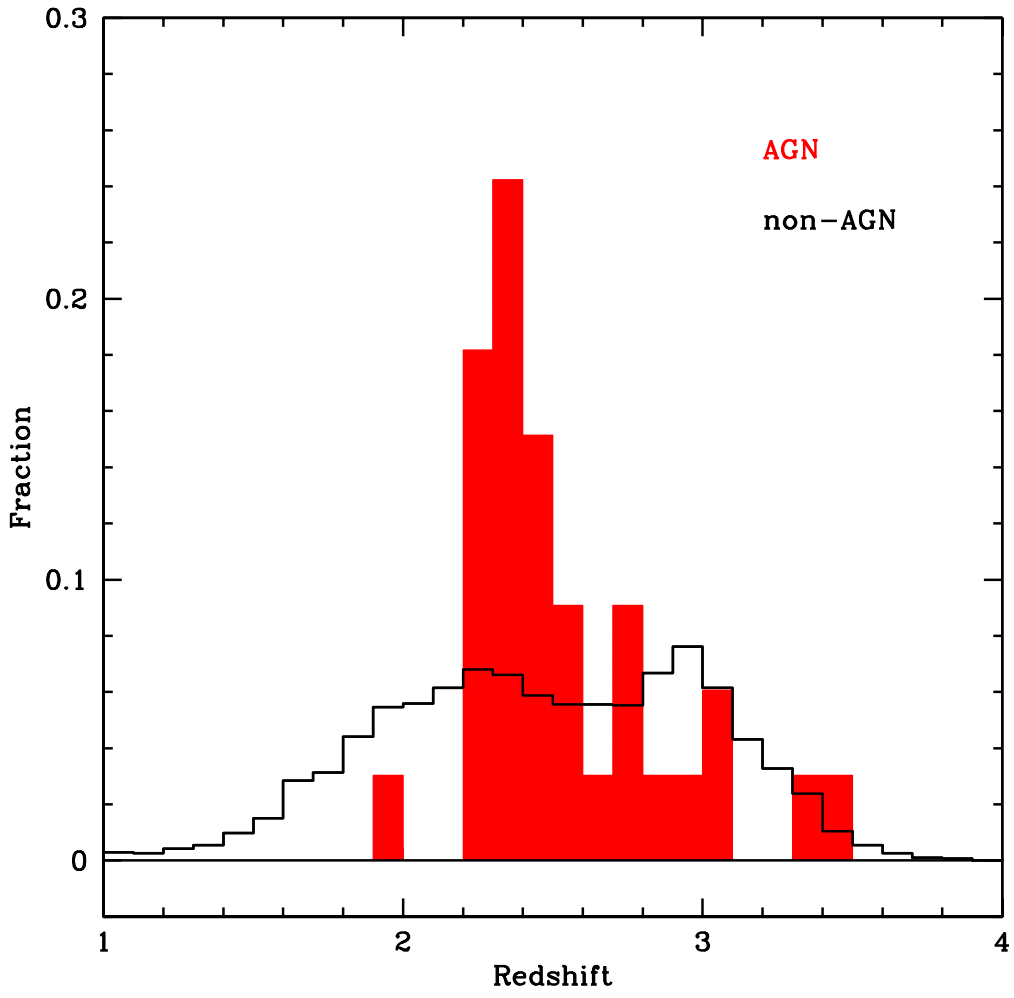

Figure 3.1 The normalized redshift distribution for our sample of UV-selected narrow-lined AGNs, compared to the redshifts of the $z \sim 2-3$ UV-selected non-AGN sample.

3.2 The UV-Selected AGN Sample and Observations

Table 3.1. UV-Selected Narrow-Lined AGN Sample

FIELD	OBJECT	RA (J2000)	DEC (J2000)	$\mathcal{R}$ (mag)	$z_{Ly\alpha}$[a]	Emission Line Detections			
Q0000	C7	00:03:28.85	-26:03:53.3	24.21	3.431	NV	CIV	HeII	CIII]
Q0000	C14	00:03:30.39	-26:01:20.7	24.47	3.057	NV	CIV	HeII	n.c.[b]
CDFb	D3	00:53:43.02	12:22:02.5	24.75	2.777	NV	CIV	HeII	CIII]
Q0100	BX172	01:03:08.46	13:16:41.7	23.50	2.312	NV	CIV	HeII	n.c.
Q0142	BX186	01:45:17.47	-09:45:08.0	25.18	2.361	...[c]	CIV	...	n.c.
Q0142	BX195	01:45:17.68	-09:44:54.2	23.56	2.382	NV	CIV	HeII	n.c.
Q0142	BX256	01:45:15.74	-09:42:12.5	23.91	2.321	NV	n.c.	n.c.	n.c.
Q0201	oC12	02:03:56.16	11:36:30.1	24.83	2.357	NV	CIV	HeII	...
Q0256	md37	02:59:02.21	00:12:03.4	24.06	2.803	NV	CIV	...	CIII]
Q0933	MD38	09:33:48.60	28:44:32.3	22.61	2.763	...	CIV	HeII	n.c.
Q1217	BX46	12:19:19.94	49:40:22.7	23.85	1.980	NV	...	...	n.c.
HDF	MMD12	12:37:19.80	62:09:56.0	24.36	2.648	NV	CIV	...	CIII]
HDF	BMZ1156	12:37:04.34	62:14:46.3	24.62	2.211	NV	CIV	HeII	CIII]
HDF	BMZ1384	12:37:23.15	62:15:38.0	23.98	2.243	NV	CIV	HeII	CIII]
HDF	BX160	12:37:20.07	62:12:22.7	24.02	2.461	NV	CIV	...	...
Westphal	MM47	14:17:57.39	52:31:04.5	24.30	3.027	...	CIV	HeII	n.c.
Westphal	MMD58	14:17:18.29	52:28:53.9	25.36	2.596	...	n.c.[d]	HeII	...
Q1422	d14	14:24:47.44	22:48:04.3	24.30	2.245	NV	CIV	...	CIII]
Q1422	c73	14:24:46.41	22:55:45.5	24.88	3.382	NV	n.c.	n.c.	n.c.
Q1422	md109	14:24:42.58	22:54:46.6	23.69	2.229	NV	CIV	HeII	CIII]
Q1623	BX151	16:25:29.61	26:53:45.0	24.60	2.441	NV	CIV	HeII	n.c.
Q1623	BX454	16:25:51.42	26:43:46.3	23.89	2.422	NV	CIV	...	...
Q1623	BX663	16:26:04.58	26:48:00.2	24.14	2.435	NV	CIV	HeII	...
Q1623	BX747	16:26:13.46	26:45:53.2	22.55	2.441	NV	CIV	HeII	n.c.
Q1623	BX827	16:26:19.31	26:45:15.3	25.15	2.506	...	CIV	...	n.c.
Q1700	MD157	17:00:52.19	64:15:29.3	24.35	2.295	NV	CIV	HeII	CIII]
Q1700	MD174	17:00:54.54	64:16:24.8	24.56	2.347	NV	...	...	n.c.
Q2233	D3	22:36:16.12	13:55:19.2	23.93	2.795	NV	CIV	HeII	CIII]
Q2233	MD21	22:36:35.83	13:55:42.0	24.80	2.549	NV	CIV	HeII	n.c.
DSF2237a	D11	22:40:02.99	11:52:13.9	25.19	2.959	...	CIV	HeII	CIII]
DSF2237b	MD53	22:39:28.67	11:52:09.5	24.07	2.292	...	CIV	HeII	CIII]
Q2343	BX333	23:46:21.51	12:47:03.2	24.12	2.397	NV	CIV	HeII	CIII]

Table 3.1—Continued

FIELD	OBJECT	RA (J2000)	DEC (J2000)	$\mathcal{R}$ (mag)	$z_{Ly\alpha}$[a]	Emission Line Detections			
Q2346	BX445	23:48:13.20	00:25:15.8	23.66	2.330	NV	CIV	HeII	CIII]

[a]Emission-line redshift, as measured from the Lyα feature.

[b]The feature of interest was not covered by the LRIS spectral range, indicated as "n.c."

[c]The feature of interest was covered by the LRIS spectral range but not significantly detected.

[d]A sky line coincides with the wavelength of CIV.

The narrow-lined AGNs used to construct the composite spectra were discovered in the course of a survey of $z \sim 2-3$ UV-selected galaxies. This survey spans 0.89 degrees^2 across 29 fields and is described in detail in Steidel et al. (2003, 2004) and Reddy et al. (2008). The method for selecting $z \sim 3$ LBGs is based on the fact that the intervening intergalactic medium absorbs most of the photons with wavelengths shortward of the Lyman break at 912 Å. At $z \sim 3$, the Lyman break is shifted to optical wavelengths, and galaxies at this redshift are selected by their position in a $U-G$ vs. $G-\mathcal{R}$ color-color diagram. As described in Steidel et al. (2004) and Adelberger et al. (2004), color criteria have also been developed to identify galaxies with similar intrinsic rest-frame UV colors to the $z \sim 3$ LBGs, but at $z \sim 2$. At this redshift, the observed $UG\mathcal{R}$ colors reflect a flat part of the spectrum redward of the Lyman break for star-forming galaxies. The survey of $z \sim 2-3$ UV-selected galaxies is split into various subsamples based on redshift, including the "BM" ($1.5 \leq z \leq 2.0$), "BX" ($2.0 \leq z \leq 2.5$), and the "C", "D", and "MD" galaxies ($2.7 \leq z \leq 3.3$). From the photometric sample, objects were selected for spectroscopy without regard for their x-ray or morphological properties. Therefore, the fraction of candidates targeted for

spectroscopy should be similar for both AGNs and star-forming galaxies in the UV-selected photometric sample.

The parent UV-selected spectroscopic sample consists of 3059 galaxies, 48 broad-lined AGN, and 33 narrow-lined AGN (which comprise 1% of the sample). Objects were identified as narrow-lined AGN if they showed strong Lyα emission accompanied by significant emission in either NV λ1240 or CIV λ1549, where the FWHM for any of the emission features was less than 2000 km s^{-1}. In some objects, SiIV $\lambda\lambda$1393,1402 or HeII λ1640 was additionally used to indicate the presence of an AGN. In practice, the requirement of strong Lyα emission does not select against finding AGNs with strong nebular emission lines but weak Lyα emission. In the sample of AGNs presented here, Lyα is is on average $\sim 4-5$ times stronger than CIV, which is typically the next strongest feature. Furthermore, no objects were found in the parent sample of UV-selected galaxies with high-ionization emission lines while lacking Lyα emission. The AGN sample presented here serves as a follow-up to the one described in Steidel et al. (2002), now including BM/BX and additional MD objects, doubling the number of discovered AGN. The normalized redshift distributions for the AGN and non-AGN samples are shown in Figure 3.1. The average redshift of the 33 AGNs is $\langle z \rangle = 2.55 \pm 0.31$, with an average $\mathcal{R}$ magnitude of $\langle \mathcal{R} \rangle = 24.2 \pm 0.7$ (a range in $\mathcal{R}$ of $22.55 - 25.72$). For the sample of non-AGNs, reflecting the combined C, D, M, MD, BX, and BM selection windows, the average redshift is $\langle z \rangle = 2.49 \pm 0.59$, with an average $\mathcal{R}$ magnitude of $\langle \mathcal{R} \rangle = 24.4 \pm 0.6$ (a range in $\mathcal{R}$ of $21.66 - 25.97$[1]). Within the AGN sample, there are 2 BM objects, 13 BX, 9 MD, 4 C, 4 D, and 1 M. These represent $\sim 1 - 2\%$ of each photometric class within the parent spectroscopic sample. The full sample is listed in Table 3.1.

[1]The standard $\mathcal{R} = 25.5$ limit was relaxed in the Q1422 field.

When considering the demographics and space density of our sample of AGNs, it is important to consider how their spectroscopic and photometric properties affect their selection, as done for the full sample of non-AGN LBGs in Reddy et al. (2008). To estimate completeness for our sample, we follow the methodology of Steidel et al. (2002), updated for the addition of the $z \sim 2$ sample. Redshifts were measured for the sample of LBGs by virtue of emission and absorption features detected in the spectra. The AGN were selected based on the presence of emission lines in addition to Lyα. In order to estimate an upper limit on the number of AGN that would be unrecognized because of low S/N spectra, we examine the strength of the strongest emission line used to infer the existence of an AGN, CIV λ1549. As discussed above, CIV is, on average, $\sim 20\%$ the strength of Lyα for the set of 33 AGN spectra. As reported in Steidel et al. (2002), the ratio of CIV to Lyα emission in the $z \sim 3$ non-AGN LBG sample is $\leq$1% for the quartile of LBGs having the largest Lyα EW. For the quartile of $z \sim 2$ non-AGN with the strongest Lyα emission, we measure the ratio of CIV to Lyα flux to be 1% (Dawn Erb, private communication). Given the observed range of Lyα EWs in our sample, we conclude that narrow-lined AGNs would only be found in this strong-Lyα quartile. If we assume that all of the CIV emission in the strong-Lyα composite spectrum is originating from a small sample of undetected AGNs with CIV/Lyα ratios of 20%, then the observed CIV/Lyα ratio of 1% in the strong Lyα composite implies that such objects can only make up 5% of the sample. If we then assume that there are no additional unrecognized AGNs in the other three quartiles with weaker Lyα emission, the fractional contribution of unrecognized AGNs to the full $z \sim 2$ non-AGN sample is $\sim 1\%$. Therefore, our observed frequency of $\sim 1\%$ of AGN is likely representative of both the spectroscopic and photometric samples of UV-selected $z \sim 2 - 3$ galaxies.

The AGNs presented here are first identified as high-redshift galaxies based on

their location in $U-G$ vs. $G-\mathcal{R}$ color-color space. Given that the average rest-frame Lyα emission EW for the AGN sample is $\langle W_{Ly\alpha} \rangle = 80$Å, we must consider the effect of Lyα emission on the selection of these objects as a function of redshift. Within certain redshift ranges, Lyα can contribute flux to either the U or G bands and alter the position of an AGN in color-color space such that it scatters into or out of the UV-selected sample. For 19 out of 33 AGNs in our sample at $2.17 \leq z \leq 2.48$ the Lyα feature does not fall within either the U or G band, and therefore Lyα emission contributions are irrelevant. One of these objects, HDF-BMZ1156, has anomalously strong CIV emission, which has a significant impact on the observed broadband rest-frame UV colors. For the remaining AGNs (1 object at $z \leq 2.17$, and 11 at $2.48 \leq z \leq 3.40$), we investigate how Lyα emission affects their inclusion in the UV-selected sample. Using the measured Lyα EW for each object, we correct the U or G band magnitude for Lyα flux as needed in order to characterize the broadband colors in the absence of line emission. This analysis reveals that only 4 out of 12 objects were actually scattered into the selection windows due to the presence of Lyα emission. HDF-BMZ1156 was scattered into the selection window due to its CIV emission. In summary, only 5 out of our 33 AGNs have broadband colors that fail to satisfy the $UG\mathcal{R}$ selection criteria if not for the presence of strong line emission in the U or G filter. On the other hand, the presence of strong Lyα emission may also cause objects to scatter out of the high-redshift galaxy color selection windows. For example, the average Lyα EW of the AGN sample represents a shift of $\Delta G = 0.26$ magnitudes for an object at $z = 2.7$ (and a comparable shift in the U band magnitude for an object at $z = 2.0$). Therefore, objects at $z > 2.48$ with Lyα emission EWs of this strength will not be identified as high-redshift star-forming galaxies if their line-free $G-\mathcal{R}$ color is within ΔG of the blue $G-\mathcal{R}$ edge of the color selection box. For a robust comparison of the rest-frame UV continuum and emission-line

properties of UV-selected AGNs and non-AGNs, the issues of completeness in color-color space as a result of strong line emission are critical. Because emission lines do not significantly affect the U and G magnitudes of UV-selected AGNs at $2.17 \leq z \leq 2.48$, these objects serve as a powerful control sample when we compare the rest-frame UV properties of AGNs and non-AGNs in the following sections.

The AGN spectra were obtained with the LRIS spectrograph at the W.M. Keck Observatory (Oke et al. 1995), using multi-object slitmasks with either $1\farcs4$ or $1\farcs2$ slits. The majority of the spectra in our sample were obtained with either a 300 line mm^{-1} grating blazed at 5000 Å or, following the installation of the blue channel of the LRIS instrument, a 400 groove mm^{-1} grism blazed at 3400 Å. Additionally, a small number of spectra were obtained with the 600 groove mm^{-1} grism blazed at 4000 Å. We refer readers to Steidel et al. (2003, 2004) for a full discussion of the reduction procedures for these data.

3.3 Generating the Composite Spectrum

The current sample of narrow-lined UV-selected AGNs is more than twice as large as the one presented in Steidel et al. (2002). Therefore, the resulting composite spectrum of these objects enables the identification of weak emission and absorption lines not visible in the average of the previous smaller sample. To create the composite spectrum, we took the individual extracted, one-dimensional, flux-calibrated AGN spectra from our sample, and shifted them to the rest frame as described below. The spectra were scaled to a common median in the wavelength range of $1250 - 1380$ Å and then averaged. To exclude positive and negative sky subtraction residuals, we rejected the four highest and lowest outliers at each wavelength of the composite spectrum, which corresponded to $\sim$20% of the data.

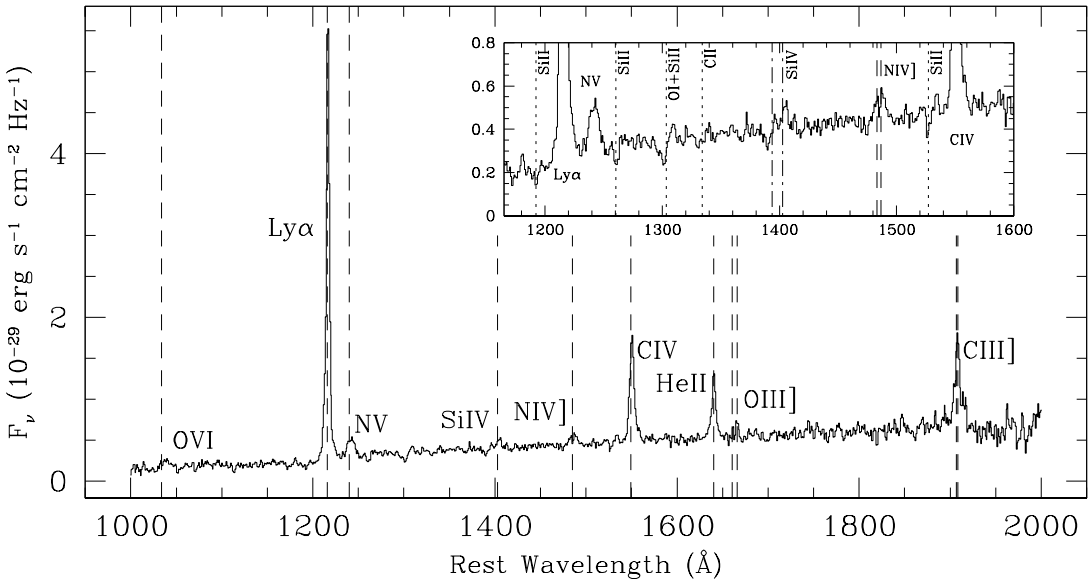

Figure 3.2 The composite rest-frame UV spectrum for 33 narrow-lined AGN at $z \sim 2-3$. These objects were selected by virtue of their emission lines, such as NVλ1240, CIV λ1549, and HeIIλ1640. The dashed lines indicate the locations of emission lines, while the inset highlights some of the more prominent absorption features. Dotted lines are used to mark low-ionization absorption features, and dot-dashed lines indicate high-ionization absorption features.

Composite spectra constructed from the median of the flux values at each wavelength yielded results indistinguishable from those based on composite spectra constructed from the average of the flux values.

In order to construct the composite spectrum, each individual spectrum was shifted to the rest frame, which requires an accurate measurement of the galaxy's systemic redshift. The establishment of an accurate systemic redshift is also necessary for estimating the absolute values of kinematic offsets for different interstellar components in the composite spectrum. The low S/N of the AGN spectra only allows for a measurement of the strongest rest-frame UV features,

such as the emission lines HI Lyα, NV λ1240, CIV λ1549, HeII λ1640, and CIII] $\lambda\lambda$1907, 1909. Absorption features were not detected in enough spectra to be used to calculate redshifts. The spectra for all of our 33 objects contain a Lyα emission feature. However, it is well known that Lyα is not a reliable indicator of the stellar redshift of a galaxy due to resonant scattering of the line (Pettini et al. 2001; Shapley et al. 2003; Adelberger et al. 2003; Steidel et al. 2010), therefore we consider the emission lines associated with AGN activity. As indicated in Table 3.1, NV λ1240, CIV λ1549, HeII λ1640, and CIII] $\lambda\lambda$1907, 1909 were detected in many individual spectra. However, many of these detections do not have the signal-to-noise necessary to calculate an accurate redshift. Furthermore, CIII] $\lambda\lambda$1907, 1909 is a density-sensitive doublet whose blended centroid varies as a function of density, so this feature is also unsuitable for measuring redshifts. In general, CIV and HeII were the two emission features that yielded the highest signal-to-noise detections in the individual spectra. We measure accurate centroids for CIV in 19 of our 33 objects, and HeII in 17 of our 33 objects. We calculated how the redshifts derived from CIV λ1549 and HeII λ1640 compared to the Lyα redshifts. The average (median) difference in velocity between Lyα and CIV λ1549, is $\Delta v = -7$ km s^{-1} (24 km s^{-1}), where a negative [positive] velocity difference indicates blueshift [redshift]. It has previously been shown that the velocities traced by the Lyα and CIV emission lines agree in active galaxies (Buson & Ulrich 1990). However, the average (median) difference in velocity between Lyα and HeII λ1640 is $\Delta v = 173$ km s^{-1} (169 km s^{-1}). As HeII λ1640 is not a resonance line, it serves as a better tracer for the redshift of the stars in the galaxy than either Lyα or CIV λ1549, which are subject to radiative transfer effects (Villar-Martín et al. 2000, 2003).

In the absence of stellar absorption lines, Hα is used in the rest-frame optical to derive redshifts. We compared the redshifts derived from optical spectra for

five AGN from our sample taken with the NIRSPEC instrument on the Keck II telescope (McLean et al. 1998). For these objects, the average (median) velocity difference between Lyα and Hα is $\Delta v = 132$ km s^{-1} (208 km s^{-1}), while the average (median) difference between HeII λ1640 and Hα is $\Delta v = -37$ km s^{-1} (59 km s^{-1}). With this in mind, the average velocity difference between Lyα and HeII λ1640, for composite spectra created with only those objects where both lines were detected in the spectrum, is -196 ± 50 km s^{-1}. We adopted this Lyα-HeII offset for all of the objects in the sample, and added it to each Lyα redshift to estimate the systemic redshift for each object. We note that the composite spectrum is virtually identical if individual HeII redshifts are used to estimate the rest frame for the objects with robust HeII centroid measurements, as opposed to the average Lyα-HeII offset. Furthermore, a stack of the 16 spectra without individual HeII centroid measurements, using the average Lyα-HeII offset to estimate the rest frame, results in a HeII profile centered at zero velocity. These consistency checks indicate the validity of adopting the average Lyα-HeII offset for all spectra in order to estimate the rest frame.

3.4 Features In The Composite Spectrum

The final composite spectrum is shown in Figure 3.2, an average of the spectra for our 33 AGNs. We identify several nebular emission lines, including NV λ1240, CIV λ1549, HeII λ1640, and CIII] $\lambda\lambda$1907, 1909. We also detect NIV] λ1486, which has previously been detected locally in compact planetary nebulae (Davidson et al. 1986), at $z = 3.4$ in the Lynx arc (Fosbury et al. 2003), in high-redshift QSOs (Bentz et al. 2004; Glikman et al. 2007), in a $z = 5.563$ Lyα emitter (Vanzella et al. 2009; Raiter et al. 2010), and in radio galaxies (Vernet et al. 2001; Humphrey et al. 2008). We also detect absorption features shown in

the inset of Figure 3.2. Many of these are observed in the LBG non-AGN composite spectrum from Shapley et al. (2003), including the low-ionization lines, SiII λ1260, OI λ1302+SiII λ1304, SiII λ1527, and high-ionization feature, SiIV $\lambda\lambda$1393,1402.

We measured the rest-frame centroids (and corresponding relative velocities), EWs, and FWHM values for each of the emission lines and absorption lines, which are found in Tables 3.2 and 3.3. Gaussian profiles were fit to the measured spectroscopic features to estimate line centroids. These centroids were then used to estimate velocities relative to the systemic frame. In cases where the lines are a blend of two closely spaced emission or absorption features, a rest-frame blend value was calculated based on the oscillator strengths for the pair and used to estimate the velocity. The EW was calculated by first measuring the values of the continuum on either side of the line of interest, integrating the flux in the line between these points, and then dividing the flux by the average of the continuum values.

3.4.1 Uncertainties

The measurements from the composite spectrum are only meaningful if accompanied by an analysis of the associated errors. The uncertainty on the EW values for the composite spectrum is dependent on both the range of EW of the individual sample galaxies as well as the finite S/N of the composite spectrum. Almost all but the strongest features cannot be measured in individual spectra.

To reflect sample variance and also statistical noise, we used a bootstrap technique outlined in Shapley et al. (2003) to calculate the uncertainties. In this method, we generated 500 fake composite spectra constructed from the sample of spectra used in creating the real composite spectra. Each fake spectrum was

Table 3.2. Absorption Features

Ion	$\lambda^a_{\rm lab}$ (Å)	$\lambda^a_{\rm blend}$ (Å)	$\lambda^b_{\rm obs}$ (Å)	W^c_0 (Å)	Δv^d (km s^{-1})
SiII[e]	1190.42, 1193.28	1192.33	1191.84±1.32	−1.70±0.68	−123±333
SiII[e]	1260.42	-	1260.45±0.94	−2.51±0.55	7±223
OI + SiII[e]	1302.17, 1304.37	1303.27	1300.37±0.94	−2.11±0.34	−667±216
SiIV[f]	1393.76	-	1389.83±0.83	−1.18±0.44	−845±178
SiII[e]	1526.7	-	1526.49±1.00	−0.73±0.27	−41±197

[a]Vacuum wavelength.

[b]Observed wavelength.

[c]Rest-frame EW and 1σ error. The error takes into account both sample variance and the S/N of the composite spectrum (see §2.2).

[d]Relative velocity measured in the systemic rest frame of the composite spectrum, equivalent to the rest frame of the stars.

[e]Low-ionization absorption feature.

[f]High-ionization absorption feature.

constructed in the same way, with the same number of spectra as the actual composite, but with the list of input spectra formulated by selecting spectra at random, with replacement, from the full list of AGN spectra ($\sim$ 36% of sample is replaced by duplicates). With these 500 fake spectra, we measured the line centroids (and velocities) and EWs for all of the emission and absorption features detected in the original composite spectrum. The standard deviation of the 500 individual measurements represents the errors on these values.

3.4.2 Emission Features

The emission features for the full composite spectrum are shown in Table 3.3. The most prominent feature is Lyα, which, for the individual AGN spectra, is always

Table 3.3. Emission Features

Ion	$\lambda^a_{\rm lab}$ (Å)	$\lambda^a_{\rm blend}$ (Å)	$\lambda^b_{\rm obs}$ (Å)	W_0^c (Å)	Δv^d (km s^{-1})
OVI	1031.912, 1037.613	1033.82	1037.94±2.20	6.01±2.20	1196±639
Lyα	1215.67	-	1216.47±0.04	66.39±11.65	197±10
NV	1238.821, 1242.804	1240.15	1242.09±0.64	5.60±1.00	470±154
SiII*[e]	1309.276	-	1309.22±0.54	0.63±0.24	−13±124
SiIV	1402.77	-	1405.02±0.93	1.44±0.58	481±176
NIV]	1483.321, 1486.496	-[d]	1486.59±1.17	2.00±0.78	
CIV	1548.202, 1550.774	1549.06	1550.47±0.38	16.34±2.86	273±74
HeII	1640.405	-	1640.45±0.27	8.07±1.32	8±50
OIII]	1660.809	-	1661.63±1.28	0.32±1.32	148±231
OIII]	1666.150	-	1666.09±0.65	1.10±0.39	−10±118
CIII]	1906.683, 1908.734	-[d]	1908.28±0.80	13.96±4.20	

[a]Vacuum wavelength.

[b]Observed wavelength.

[c]Rest-frame EW and 1σ error. The error takes into account both sample variance and the S/N of the composite spectrum (see §2.2).

[d]Relative velocity measured in the systemic rest frame of the composite spectrum, equivalent to the rest frame of the stars. Relative velocities were not calculated for the density-sensitive N IV] and C III] doublets, for which the blend wavelength depends on the uncertain electron density.

[e]The asterisk indicates that this feature is a fine-structure emission line.

observed in emission. In Shapley et al. (2003), the Lyα feature was detected both in emission and absorption for a sample of 820 non-AGN LBGs. We measure a $\Delta v = +197$ km s^{-1} emission redshift from our composite spectrum, which is slightly lower, but similar to what is observed in the non-AGN LBG sample ($\Delta v = +360$ km s^{-1}). This redshift is due to the scattering of Lyα photons off of redshifted material in the galaxy, which allows the (now off-resonance) photons to escape. The measured EW is $W_{\rm Ly\alpha} = 66$ Å, which is similar to the EW measured from the quartile of non-AGN objects from Shapley et al. (2003) with

the strongest Lyα EW.

The other strong emission lines we see in the composite spectrum are NV λ1240 ($W_{\rm N\ V}$ = 5.6 Å), CIV λ1549 ($W_{\rm C\ IV}$ = 16.3 Å), HeII λ1640 ($W_{\rm He\ II}$ = 8.1 Å), and CIII] $\lambda\lambda$1907, 1909 ($W_{\rm C\ III]}$ = 14.0 Å). The majority of non-AGN LBGs do not show evidence for these features with such large EW values, even in those LBGs with strong Lyα emission (Shapley et al. 2003). Both NV and CIV have redshifts that are similar to the one measured for Lyα. Because we are using a composite spectrum, which has a higher S/N ratio than the individual spectra, we can detect weaker emission lines as well. We detect NIV] λ1486, as well as OVI $\lambda\lambda$1032, 1038, and OIII] $\lambda\lambda$1661, 1666. As mentioned in §3.2, while the EW values of Lyα are similar between the non-AGN and the AGN composite spectra, the strongest emission line indicative of an AGN in the non-AGN spectra is CIV λ1549, which is only seen at 1% the strength of Lyα.

The ratios of strong UV emission lines have been used to understand the underlying shock and photoionization conditions in the gas. Lyα is generally not used for diagnostic purposes because of the resonance scattering and the effects of strong dust attenuation on this line. The ratios of CIV λ1549/CIII] λ1909, CIV λ1549/HeII λ1640, and CIII] λ1909/HeII λ1640 can be used to discriminate between shock and photoionization predictions for narrow emission-line regions in AGNs (Villar-Martin et al. 1997; Allen et al. 1998; Groves et al. 2004). For the full composite spectrum we measure values of the ratios of these lines that are very similar to the range of observed ratios in high-redshift radio galaxies (Villar-Martin et al. 1997; Nagao et al. 2006a; Matsuoka et al. 2009).

3.4.3 Absorption Features

In addition to the strong emission lines seen in the composite spectrum, we detect several weak interstellar absorption features as well, such as the low-ionization lines SiII λ1260, OI λ1302+SiII λ1304, and SiII λ1527. We do not detect CII λ1334 in our composite spectrum, which is a low-ionization absorption feature detected in the non-AGN composite spectrum from Shapley et al. (2003)[2]. The origin of this difference requires further study. The unblended low-ionization lines detected do not show significant blueshifts, in contrast to the blueshifts of $\sim 150-200$ km s^{-1} observed in the non-AGN sample (Shapley et al. 2003; Steidel et al. 2004, 2010). This conclusion is dependent on our definition of the rest frame for the individual spectra. As discussed in §3.3, our method uses the centroid of HeII λ1640 emission as a proxy for the rest frame. On the other hand, the rest frame for the spectra included in the non-AGN LBG composite from Shapley et al. (2003) was established using average relationships between the centroids of rest-frame optical nebular emission lines and those of rest-frame UV features, such as interstellar absorption lines and Lyα emission (Adelberger et al. 2003). Below we discuss how a change in the rest-frame determination would affect our conclusions about interstellar absorption line kinematics. However, we note that, regardless of the rest-frame determination, the observed offset between Lyα emission and low-ionization interstellar absorption lines in the AGN composite spectrum ($\sim$ 200 km s^{-1}) is significantly smaller than the corresponding offset observed in the non-AGN composite ($\sim$ 510 km s^{-1}) – indicating an intrinsic difference in kinematics traced by low-ionization gas. While the observed centroid of OI λ1302+SiII λ1304 may indicate a blueshift, it is most likely contaminated by additional absorption at 1296 Å. This absorption may be due to the stellar

[2]While not detected in the full composite spectrum, CII λ1334 is marginally detected in four of the individual spectra, HDF-BX160, Q0000-C14, Q0100-BX172, and Q1700-MD157.

feature SiIII λ1296 (Chandar et al. 2005), but higher signal-to-noise spectra will be required to confirm this possibility.

We also detect the high-ionization feature SiIV $\lambda\lambda$1393, 1402, both in emission and absorption. We use the stronger SiIV λ1393 feature as a probe of absorption line kinematics. This feature is resolved, with a FWHM greater than 500 km s^{-1}. The SiIV centroid indicates a significant blueshift, -845 ± 178 km s^{-1}, which is several times larger than the one measured in the non-AGN composite spectrum ($\Delta v = -180$ km s^{-1}). This difference is demonstrated in Figure 3.3, which shows both the AGN composite spectrum described here and the non-AGN composite from Shapley et al. (2003), zoomed in on the region around SiIV. One potential cause for concern is the contamination of SiIV absorption profiles by the corresponding SiIV emission lines, given their close proximity in wavelength. The SiIV λ1393 emission line is in fact measured to be narrower than the λ1402 feature, suggesting that its blue edge is attenuated by SiIV λ1393 absorption, which is stronger than absorption from SiIV λ1402. Furthermore, the SiIV λ1393 emission feature is observed to be weaker than that of SiIV λ1402, while the relative oscillator strengths of the doublet members suggest that SiIV λ1393 should be twice as strong as λ1402. Both of these observations indicate the possible blending of SiIV emission and absorption.

In order to quantify the contamination from emission in the observed SiIV λ1393 absorption profile, we require a robust model of the intrinsic SiIV λ1393 emission. Such a model is not straightforward to construct, given that both SiIV λ1393 and λ1402 emission features are affected by absorption, and, furthermore, the SiIV λ1402 emission feature is blended with emission from OIV] λ1401. The ratio between OIV] λ1401 and SiIV λ1402 is not well constrained, but can exceed unity (Hamann et al. 2002; Nagao et al. 2006b), in which case the inferred SiIV

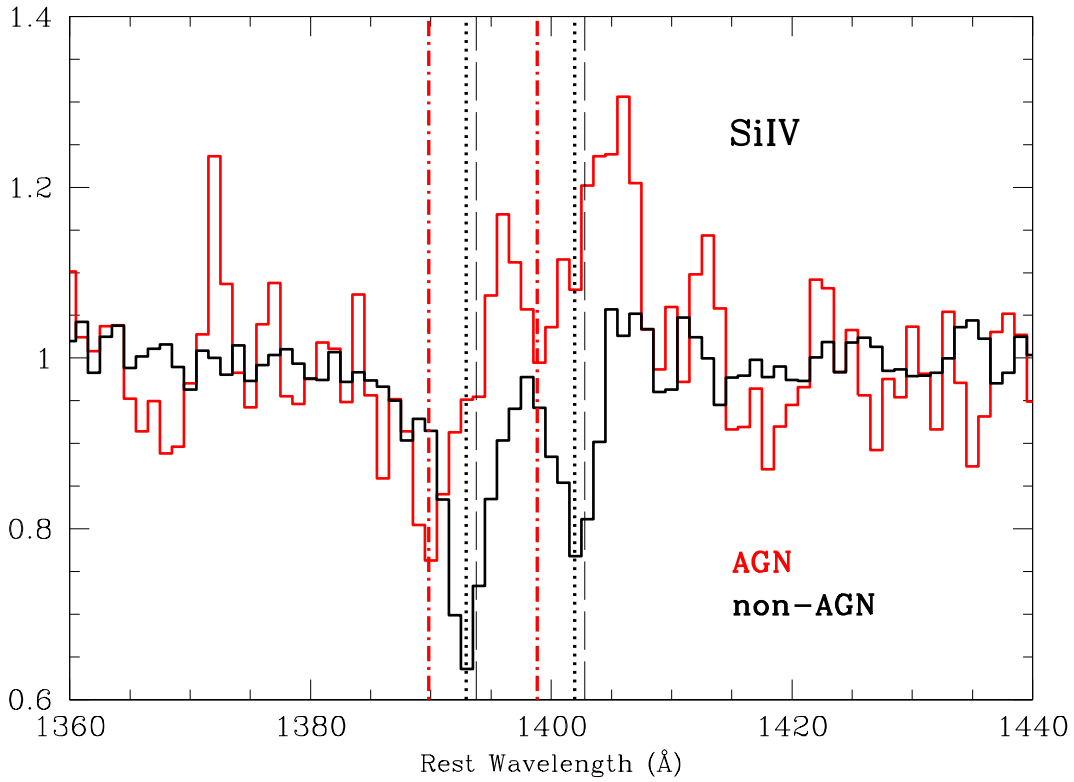

Figure 3.3 Comparison of the blueshift of the SiIV λ1393 and λ1402 line between the continuum normalized AGN composite spectrum (in red) and the non-AGN composite spectrum (in black) presented in Shapley et al. (2003). The long dashed lines mark the rest-frame wavelengths of both SiIV λ1393 and λ1402, while the dotted and dot-dashed lines show the measured blueshifted centroids for the non-AGN and AGN composite spectra, respectively. The measured centroid of the SiIV λ1393 feature indicates a velocity offset of -845 ± 171 km s^{-1} in the AGN composite spectrum, while in the non-AGN spectrum, it is -180 km s^{-1}. Although it is difficult to determine robustly the full SiIV absorption profile in the AGN composite spectrum due to contamination by SiIV emission, we emphasize differences in the blue wing of the λ1393 absorption feature. There is excess absorption at the most blueshifted velocities in the AGN composite relative to that of the non-AGNs.

λ1393 would be much weaker than if all the emission at $\sim$ 1402 Å was due to SiIV. While the potential contamination from SiIV emission prevents us from tracing out the full SiIV absorption profile, we can still assert that absorbing gas exists at a blueshift with a magnitude of 845 km s^{-1}. Furthermore, as shown in Figure 3.3, this highly blueshifted gas in the AGN composite spectrum at ~ -1000 km s^{-1} does not have a corresponding component in the non-AGN composite spectrum, representing a quantitative difference between the velocity profiles of outflowing absorbing gas in the two samples. Here we return to the issue of the discrepancy between the low-ionization SiII absorption-line blueshift measured in the AGN and non-AGN LBG composite spectra. The non-AGN LBG composite spectrum has low-ionization SiII absorption lines blueshifted by $\sim 150 - 200$ km s^{-1}, while the SiII absorption in the AGN composite spectrum does not show the same blueshift. If this difference were due to systematics of the rest-frame determinations, and we instead forced the SiII absorption lines in the AGN composite to have the same blueshifts as those in the non-AGN composite, the blueshift of SiIV would *increase* to $\geq$ 1000 km s^{-1}.

3.4.4 Continuum Shape

Besides the emission and absorption features seen in the composite spectrum, the shape of the underlying continuum can be used to discern the presence of dust in these objects. The continuum shape is is often described by β, the slope of a power law of the form $F_\lambda \propto \lambda^\beta$ fit to the continuum. We used a modified version of the method outlined in Calzetti et al. (1994), using windows of the continuum with little to no activity as anchor points for fitting the power law. For the full composite spectrum, we measured $\beta = -0.314$, while for the full non-AGN LBG composite from Shapley et al. (2003), we measured $\beta = -1.49$, which is

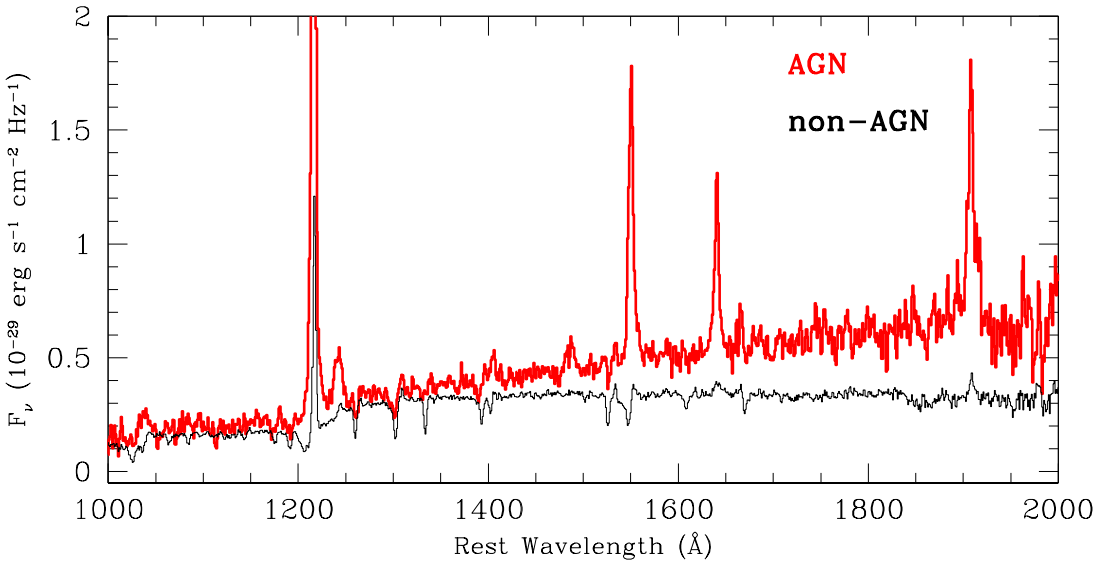

Figure 3.4 Comparison of the continuum slope between the AGN composite spectrum and the non-AGN composite spectrum from Shapley et al. (2003). The AGN composite is significantly redder than the non-AGN composite. The power law slope β, as measured directly from the AGN spectrum, is $\beta = -0.314$, while for the non-AGN spectrum, $\beta = -1.49$.

significantly bluer. A comparison between AGN and non-AGN composite spectra is shown in Figure 3.4. We note here that in a composite spectrum of the control sample of objects at $2.17 \leq z \leq 2.48$, for which Lyα emission does not affect the $UG\mathcal{R}$ photometry, the UV slope is at least as red as in the composite spectrum for our full AGN sample. This result demonstrates that the red UV continuum slope measured for our AGN sample does not simply arise from red objects, which wouldn't satisfy the rest-frame UV selection criteria otherwise, scattering into the UV selection box due to the presence of strong Lyα emission. A full interpretation of the red AGN continuum will be described in Ch. 4, yet preliminary analysis suggests the AGN continuum does not contribute significantly at rest-frame UV wavelengths (Assef et al. 2010).

Aird et al. (2010) argue that the redder rest-frame UV continuum slopes of UV-selected narrow lined AGNs relative to star-forming galaxies can result in a reduced overall selection efficiency in color-color space. However, these authors do not take into account the simultaneous effects of continuum shape and strong emission lines in calculating the AGN selection efficiency, which can have a significant impact on the colors of narrow-lined AGNs in certain redshift ranges (as discussed in §3.2). Our main conclusions about rest-frame UV spectroscopic trends within the UV-selected narrow-lined AGN sample are not significantly affected by these considerations. If anything, the difference we report between AGN and non-AGN continuum slope would be increased by including the spectra of red AGNs that do not fall in the color selection box due to their $G - \mathcal{R}$ colors.

3.5 AGN Spectroscopic Trends

In order to discern spectroscopic trends in the AGN sample, we split the objects into various subsamples based on the properties of the individual spectra. Given the relatively small sample size (33 objects) and our desire to maximize the S/N of the resulting subsample composite spectra, we simply divide the sample in half for these analyses. The properties used to divide our sample include: Lyα emission line EW, rest-frame UV absolute magnitude, and redshift. We do not split our sample by the EW for any of the other emission or absorption lines because most of our spectra do not have high enough S/N to allow for robust measurements of these features. The results for measuring various properties from the composite spectra described in this section are found in Table 3.4.

3.5.1 Lyα Dependencies

Lyα is detected in emission in all of our AGN, with EW values that range from $W_{\mathrm{Ly}\alpha} = 10$Å to $W_{\mathrm{Ly}\alpha} = 300$Å. In contrast, the non-AGNs show Lyα both in emission and absorption. The median value for the Lyα EW in our sample was $W_{\mathrm{Ly}\alpha} = 63$Å, which is where we split the sample, creating a composite spectrum for those spectra with $W_{\mathrm{Ly}\alpha} < 63$Å and those with $W_{\mathrm{Ly}\alpha} > 63$Å. The results of measuring the various properties of the composite spectra are found in Table 3.4. The measured Lyα EW in the strong Lyα composite spectrum is $W_{\mathrm{Ly}\alpha,\mathrm{strong}} = 123 \pm 14$Å, which is almost five times larger than what is measured in the weak Lyα composite spectrum, $W_{\mathrm{Ly}\alpha,\mathrm{weak}} = 28 \pm 5$Å. The Ly$\alpha$ EWs measured from the composite spectra are consistent with the sample mean values of $\langle W_{\mathrm{Ly}\alpha,\mathrm{strong}} \rangle = 141 \pm 15$Å and $\langle W_{\mathrm{Ly}\alpha,\mathrm{weak}} \rangle = 33 \pm 4$Å.

The strong Lyα composite spectrum has significantly larger CIV, HeII, and CIII] EW values than the spectrum with weaker Lyα emission, but only by a factor of two. The same trend is observed when we consider line fluxes as opposed to equivalent widths. For both equivalent widths and fluxes, the change in Lyα is not accompanied by an equivalent change in the strength of emission lines that are primarily sensitive to the level of nuclear activity.

In the strong Lyα EW composite spectrum, most low-ionization (SiII λ1260, CII λ1334, and SiII λ1527) and high-ionization (SiIV $\lambda\lambda$1393, 1402) absorption lines are statistically weaker than the features measured in the weak Lyα EW composite spectrum. This difference is shown in Figure 3.5, which overplots the strong and weak Lyα EW composite spectra. This trend of absorption line strength being anticorrelated with Lyα EW is also seen in the non-AGN LBGs (Shapley et al. 2003). The OI λ1302+SiII λ1304 absorption line, however, is of a similar strength in both spectra. The potential contamination by SiIII λ1296

discussed in Section 3.4.3 is more prominent in the strong Lyα EW composite, while it is not seen in the weak Lyα EW composite. In the weak Lyα EW composite, the OI+SiII feature has a much smaller offset than what is seen in the full composite spectrum. Finally, CII is detected in the weak Lyα spectrum while not present in either the strong Lyα or full composite spectra (see §3.4.3). Beyond the trends in emission and absorption line strength, the two binned spectra do not differ in many other respects. They are not statistically different in UV luminosity or continuum color.

3.5.2 UV Magnitude Dependencies

We calculated the UV magnitude for each of our galaxies using the value for a galaxy's redshift to interpolate the flux at 1500 Å from the $G - R$ color. With this flux, we calculated a UV luminosity and AB magnitude for each object. The normalized UV magnitude distributions for the AGN and non-AGN samples are shown in Figure 3.6. The median magnitude is $M_{UV,AB} = -20.7$, so we split the sample into $M_{UV,bright}$ and $M_{UV,faint}$ subsamples for making composite spectra.

The resulting spectra have Lyα EWs that are statistically similar, while the $M_{UV,faint}$ sample has overall weaker interstellar absorption lines. This difference in interstellar absorption line strength is not as significant as the one observed between the two Lyα composite spectra described in §3.5.1, indicating a stronger connection between Lyα emission strength and interstellar absorption strength, as observed in non-AGN LBGs (Shapley et al. 2003). Additionally, the two spectra separated by M_{UV} are quite different in continuum color. The $\mathrm{M}_{UV,bright}$ composite spectrum is significantly bluer ($\beta_{spec} = -0.67$) than the $\mathrm{M}_{UV,faint}$ composite ($\beta_{spec} = -0.06$), yet both are redder than non-AGN LBG composite ($\beta_{spec} = -1.49$). The average line flux for AGN-sensitive features such as CIV,

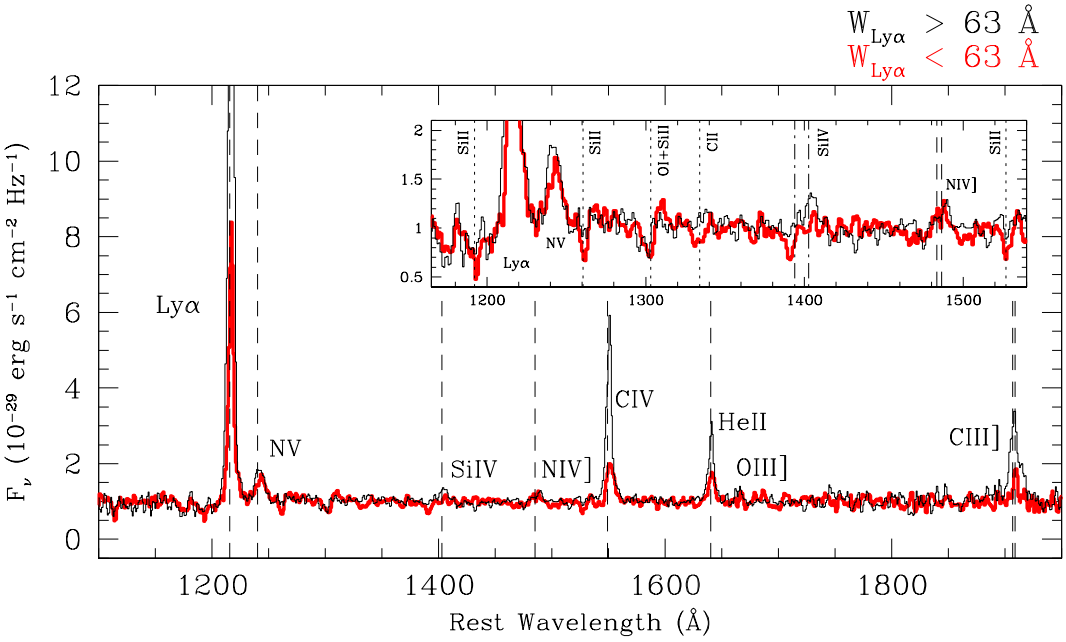

Figure 3.5 Composite spectra of objects separated by Lyα EW. Plotted in black is the continuum normalized composite spectrum from the half of galaxies in our AGN sample with the strongest Lyα emission, while plotted in red is the continuum normalized composite spectrum from the half of galaxies with the weakest Lyα emission. The inset shows a section of the spectra between 1250 and 1540 Å. The absorption lines are significantly weaker in the strong Lyα composite spectrum, which is consistent with the results from Shapley et al. (2003) for non-AGN LBGs. Dashed lines indicate emission lines, dotted lines indicate low-ionization absorption features, and dot-dashed lines indicate high-ionization absorption lines.

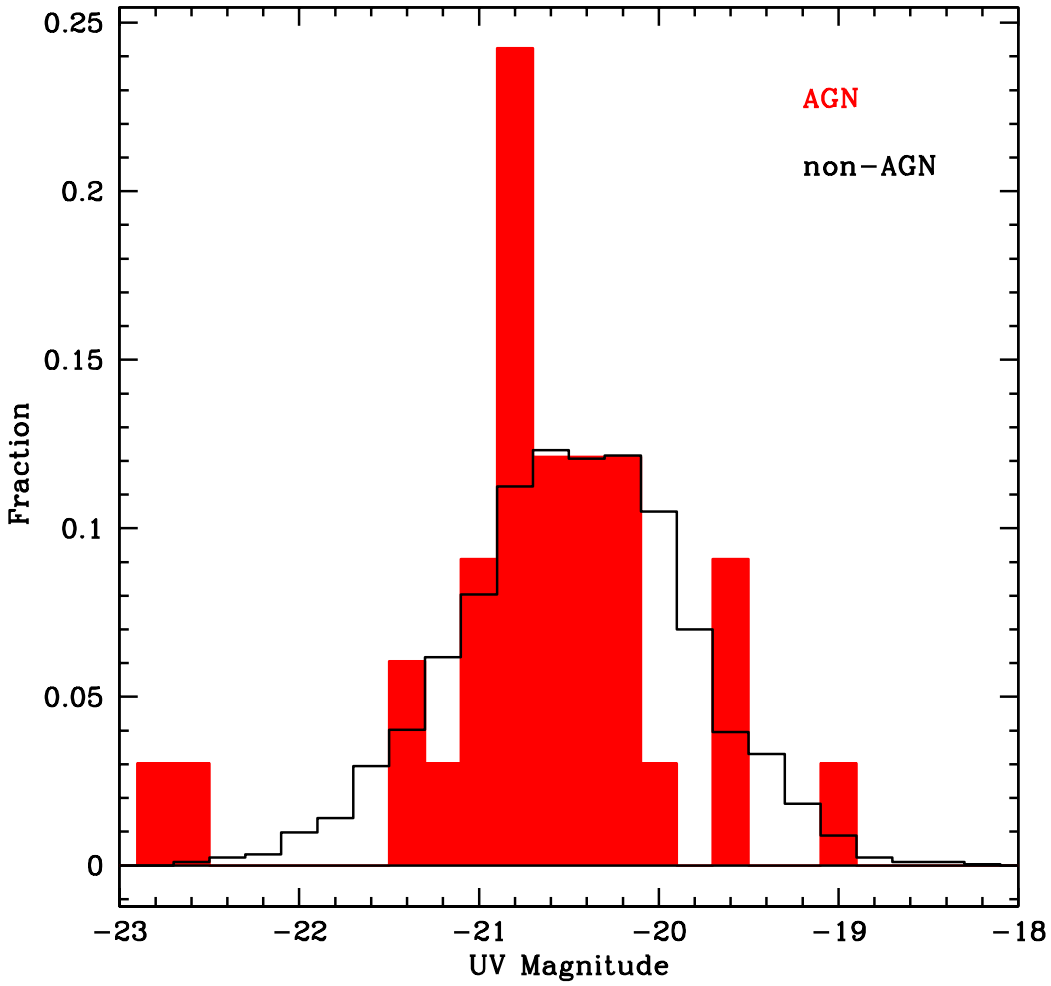

Figure 3.6 The normalized UV absolute magnitude distribution for our sample of UV-selected narrow-lined AGNs, compared to the distribution for the $z \sim 2-3$ UV-selected non-AGN sample.These UV magnitudes were calculated from the $G-\mathcal{R}$ colors and Lyα-derived redshifts for the objects.

HeII, and CIII] is larger in the $M_{UV,bright}$ composite than in the $M_{UV,faint}$ one. If the line fluxes and UV continuum flux density scaled by the same factor, which would indicate a direct connection between nuclear activity and UV continuum emission, the average EWs in the bright and faint composites would also be identical. In fact, the average EWs of the AGN-sensitive features in the $M_{UV,faint}$ sample are larger than those in the $M_{UV,bright}$ sample, suggesting that the relationship between AGN-sensitive emission lines and UV continuum is not direct. While this trend is consistent with the trend observed in broad-lined QSOs (Baldwin 1977), as these are narrow-lined AGNs, with only an obscured view of the central engine, we do not expect that the AGN emission contributes to the overall UV continuum (Assef et al. 2010) in either the bright or faint subsample. The difference in emission-line strength may simply indicate the correlation of AGN activity with additional properties of the host galaxy stellar population. Further population synthesis modeling is required to fully characterize these trends.

3.5.3 Redshift Dependencies

We separated the spectra by redshift at $z = 2.7$, effectively splitting between the $z \sim 3$ LBG sample and the newly added $z \sim 2$ BX/BM and MD objects. There are 9 objects used to generate the $z > 2.7$ composite, and 24 to generate the $z < 2.7$ composite. The results for separating the spectra by redshift are very similar to those seen when separating by $W_{Ly\alpha}$, with the higher redshift sample showing stronger Lyα emission on average. The Lyα EW distribution for the high redshift sample spans the range of 15 to 300 Å ($\langle W_{Ly\alpha,z>2.7} \rangle = 124 \pm 28$), while the Ly$\alpha$ EW distribution for the low redshift sample spans the range of 10 to 145 Å ($\langle W_{Ly\alpha,z<2.7} \rangle = 62 \pm 8$). Given that strong line emission can affect the selection of these objects as a function of redshift, we removed from the analysis

Table 3.4. Spectroscopic Properties of Composite Spectrum Subsamples

	$W_{Ly\alpha} > 63$	$W_{Ly\alpha} < 63$	$M_{UV,bright}$	$M_{UV,faint}$	$z > 2.7$	$z < 2.7$
N_{gal}	16	17	16	17	9	24
$\langle z_{Ly\alpha} \rangle^a$	2.60±0.08	2.49±0.06	2.65±0.08	2.43±0.05	2.94±0.07	2.37±0.02
$\langle M_{UV} \rangle^a$	−20.6±0.2	−20.7±0.2	−21.2±0.1	−20.2±0.1	−21.1±0.2	−20.5±0.1
$\langle W_{Ly\alpha} \rangle^a$	141±15	33±4	78±14	82±17	124±28	62±8
$\langle \beta_{G-\mathcal{R}} \rangle^a$	−0.8±0.2	−1.2±0.1	−1.1±0.2	−0.9±0.2	−1.1±0.4	−1.0±0.1
$\langle \beta_{spec} \rangle^a$	−0.5±0.3	−0.6±0.3	−0.9±0.3	−0.3±0.3	−0.9±0.4	−0.4±0.2
β_{spec}^b	−0.1±0.4	−0.5±0.3	−0.7±0.3	−0.1±0.4	−0.7±0.5	−0.2±0.3
$W_{Ly\alpha}^c$	123±14	28±5	62±18	56±16	103±37	52±8
$W_{NV,1240}^c$	6.23±1.54	4.42±1.01	3.22±0.84	8.21±1.80	4.15±1.66	5.83±1.12
$W_{NIV],1484}^c$	2.13±0.86	1.68±0.53	1.05±0.52	2.51±1.17	3.07±1.36	1.57±0.58
$W_{CIV,1549}^c$	25.21±4.15	7.99±2.56	10.17±3.84	16.40±4.15	40.43±8.06	12.01±2.89
$W_{HeII,1640}^c$	9.16±1.88	5.48±1.71	6.01±1.23	8.13±3.09	14.03±5.29	6.27±1.41
$W_{CIII],1909}^c$	20.85±8.00	6.06±2.66	14.08±5.90	15.62±6.74	36.75±15.58	8.75±2.90
$W_{SiII,1260}^c$	-	−1.81±0.49	−0.87±0.34	-	-	−1.80±0.39
$W_{OI+SiII,1303}^c$	−2.00±0.82	−1.96±0.54	−2.36±0.47	-	-	−2.27±0.54
$W_{SiIV,1393}^c$	-	−1.72±0.74	−1.66±0.55	-	-	−1.34±0.67
$W_{SiII,1527}^c$	-	−1.03±0.53	−0.85±0.35	-	-	−0.79±0.35

[a]Sample average values for the composite spectra.

[b]UV-continuum slope, measured from the composite spectra.

[c]Rest-frame EW in Å, measured from the composite spectra. Positive values indicate emission, while negative values indicate absorption. Uncertainties are calculated as described in §2.2. This table includes absorption and emission measurements with greater than 2σ significance.

the 5 AGNs whose broadband colors only satisfied the $UG\mathcal{R}$ selection criteria because of the presence of Lyα or CIV. Even with these objects removed we still find a larger average Lyα EW for the higher redshift sample. While these differences are suggestive of redshift evolution in the Lyα EW distributions in a similar sense to what is observed in star-forming galaxies over the same redshift range (Reddy et al. 2008; Nilsson et al. 2009), the small sample size precludes us from drawing any firm conclusions.

3.6 Discussion

Analysis of the composite spectrum of the UV-selected AGNs at $z \sim 2-3$ reveals a number of results regarding the nature of AGN activity. We report the detection of weak absorption lines from both low- and high-ionization species. Most strikingly, the high-ionization SiIV absorption feature exhibits a significant blueshift of $\Delta v = -845 \pm 178$ km s^{-1}. The precise value of this blueshift is referenced to our estimate of the rest frame based on HeII λ1640. As discussed in §3.4.3, if we adopt a rest frame in which the low-ionization lines have the same blueshift as those in the non-AGN LBG composite spectrum of Shapley et al. (2003), then the magnitude of the inferred blueshift for SiIV would be even greater. While contamination from SiIV emission prevents us from tracing out the full SiIV velocity profile in absorption, the most strongly blueshifted material appears to be outflowing more rapidly than the associated gas in star-forming galaxies at $z \sim 2-3$ (Shapley et al. 2003; Steidel et al. 2010). Thacker et al. (2006) presents results of a simulation that indicate that pure star formation, even when the full kinetic energy from each supernovae is applied to the outflowing material, can only produce maximum outflow velocities of roughly $v = 600$ km s^{-1}. Their modeling shows that only AGNs and quasars can produce high speed outflows with velocities greater than 10^3 km s^{-1}. Outflows of this magnitude have also been seen in poststarburst galaxies at $z = 0.6$, using OIV $\lambda\lambda$2796, 2803, which are claimed to result from the effects of an AGN (Tremonti et al. 2007).

Previous studies of outflows observed in galaxies with AGNs can be used to place these UV-selected AGN results in context. Krug et al. (2010) presented a study of outflows from a sample of local IR-faint AGN. For the narrow-lined objects, the outflow velocities (as calculated from the NaI D interstellar absorption

line doublet) are on the order of those from starburst galaxies, offering a conclusion that star formation was the process driving the outflows in Seyfert 2 systems. Based on a sample of local infrared-luminous starburst galaxies exhibiting AGN activity, Rupke et al. (2005a) show evidence for high velocity superwinds, which they compare to those from a non-AGN ULIRG sample presented in Rupke et al. (2005b,c). Both have comparable outflow velocities, leading to the conclusion that the momentum and energy required for the outflow could have come equally from a starburst or the AGN. The current work represents the same type of differential comparison between AGNs and their non-active counterparts, but at high redshift, when the black hole and bulge are both actively forming. This analysis highlights the specific effects of the AGN on the outflowing ISM. Relative to work on AGN outflows at high redshift, which has focused on the extended line emission in individual systems or small samples of AGNs alone (Alexander et al. 2010; Nesvadba et al. 2008), the benefit of our analysis lies in our comparison to a control sample of non-AGN star-forming galaxies.

In order to understand how the outflows observed in our sample of AGNs will ultimately affect the galactic gas content, a calculation of the mass outflow rate of the gas is needed. Such a calculation requires knowledge of the outflowing gas metallicity, column density, covering fraction and physical location with respect to the illuminating source. Specifically, it is necessary to determine whether the outflowing gas extends over the scale of the entire galaxy or is confined to the scale of the central engine. Based on current data, we cannot obtain a precise estimate of the location of the gas, metallicity, column density, or covering fraction. Without determinations of these properties, a full comparison to AGN feedback models (e.g. Thacker et al. 2006) cannot be made.

The NIV] λ1486 emission line is detected in our AGN composite. This fea-

ture is not detected in the non-AGN LBG composite (Shapley et al. 2003), and is observed only rarely in broad-lined quasars in the Sloan Digital Sky Survey (Bentz et al. 2004; Jiang et al. 2008). At the same time, NIV] has been detected in the spectra of high redshift radio galaxies (Vernet et al. 2001; Humphrey et al. 2008). In order to determine the origin of the NIV] emission, Humphrey et al. (2008) consider both photoionization and shock models. A comparison of model predictions for line ratios such as NIV] / CIV and NIV] / HeII with those measured in our composite spectrum suggests that the observed NIV] originates in photoionized gas. Our observed line ratios indicate that the gas is of solar or supersolar metallicity and subjected to a hard ionizing spectrum ($f_\nu \propto \nu^\alpha$, where $\alpha \geq -1.0$) with ionization parameter $U \geq 0.05$, where U is defined here as the ratio of ionizing photons to H atoms at the surface of the model photoionized gas slab. On the other hand, shock excitation models cannot explain our high observed values of NIV] / CIV.

The EW of Lyα in the UV spectra of our AGNs is indicative of both the strength of the AGN as well as the properties of star-forming regions. The observed Lyα EW is further modulated by various radiative transfer effects, due to its high scattering cross section. In non-AGN LBGs, the strength of Lyα emission has been shown to correlate with the EW of low-ionization interstellar absorption lines, such that strong Lyα emission is accompanied by weaker interstellar absorption (Shapley et al. 2003). This result can be understood if the escape of Lyα photons is at least partially modified by the covering fraction of neutral gas in the ISM. Additionally, Kornei et al. (2010) show that stronger Lyα emission is coupled with smaller dust obscuration as traced by the slope of the UV continuum, indicating that interaction with dust preferentially destroys Lyα photons, a result consistent with previous work by Shapley et al. (2003), Pentericci et al. (2007), and Verhamme et al. (2008).

When separating our objects according to Lyα EW to create composite spectra, we find that the composite spectrum created from objects with large Lyα EW shows stronger CIII], CIV and HeII emission than the composite spectrum created from objects with smaller Lyα EWs. As shown in Table 3.4, the CIII], CIV, and HeII lines are two to three times weaker in the $W_{Ly\alpha} < 63$ composite spectrum than in the $W_{Ly\alpha} > 63$ composite spectrum. This result suggests that the strength of Lyα emission is modulated at least partially by the level of AGN activity, which is traced by the strength of these other emission lines. However, the fact that the Lyα EW is almost 5 times weaker in the weak Lyα EW composite spectrum indicates additional suppresion of Lyα photons beyond the reduced level of AGN activity. At the same time, the low-ionization interstellar absorption lines that indicate the covering fraction of cool gas are significantly stronger in the weak Lyα composite. Therefore, it is not only the strength of the underlying AGN that separates the objects by Lyα EW, but also the covering fraction of gas that might absorb and reradiate the Lyα emission. This trend agrees with the results of Shapley et al. (2003) for non-AGN LBGs.

In our AGN sample, the UV continuum of the strong Lyα composite is redder than that of the weak Lyα composite, though the difference is not significant. This discrepancy with the trends among non-AGN LBGs from Shapley et al. (2003) and Kornei et al. (2010) may be a result of our small sample size, or potentially because the Lyα flux we observe originates from both the general star-forming ISM as well as the nuclear region. These two sources of Lyα photons may have disjoint properties with respect to the geometry of dust extinction, suppressing the trend observed among the non-AGN LBGs.

In the next chapter, we perform modeling of the spectral energy distributions of the AGN host galaxies, which allows for analysis of the UV spectra separated

by stellar mass and E(B-V). This modeling also helps us uncover spectral trends as a function of galaxy evolutionary state. Finally, we will probe the origin of the strikingly red UV continuum slopes found in the narrow-line UV-selected AGN spectra.

CHAPTER 4

Stellar Populations of UV-Selected Active Galactic Nuclei Host Galaxies at $z \sim 2 - 3$

4.1 Introduction

Active galactic nuclei (AGNs) may play an important role in the evolution of their host galaxies, as evidenced by the the tight correlation between black hole mass and bulge mass in local galaxies (Ferrarese & Merritt 2000; Gebhardt et al. 2000; Gültekin et al. 2009). AGNs and star formation are both fueled by gas accretion processes, and the gas content and temperature in galaxies can be influenced by the energy output from an AGN. This latter process is often used as an explanation for the distribution of luminosities and colors among massive galaxies in the local universe. Feedback from an AGN prevents further star formation, causing galaxy colors to redden as well as contributing to the exponential fall-off at the bright end of the galaxy luminosity function (Hopkins et al. 2006; Croton et al. 2006; Khalatyan et al. 2008; Somerville et al. 2008). However, strong evidence linking the presence of an AGN to the cessation of star formation is still missing (but see Tremonti et al. 2007). One popular method that has been used to examine this possible connection is the comparison of AGN host galaxy stellar populations to those of similar, non-active galaxies. With a controlled examination of the stellar populations of galaxies hosting AGNs, we can understand both

the influence of an AGN on galaxy properties as well as the timescales involved in AGN activity.

AGN host galaxy properties have been studied across a wide range of redshifts. In the local universe, results from AGNs identified based on their optical properties indicate that these objects are hosted by massive ($\log(M_*/M_\odot) > 10$), early-type galaxies (Kauffmann et al. 2003). Similar trends are observed for local radio-loud AGNs; the radio-loud AGN fraction is observed to be $> 30\%$ for galaxies with $\log(M_*/M_\odot) > 11.7$ (Best et al. 2005). Studies of optically- and X-ray-selected AGNs at intermediate redshifts ($z \sim 0.5 - 1.5$) indicate that these AGN host galaxies are massive, with characteristic stellar masses of $\log(M_*/M_\odot)$ ~ 11 (Bundy et al. 2008; Alonso-Herrero et al. 2008; Brusa et al. 2009). If AGNs are responsible for quenching star formation, this effect should be reflected in the optical colors of the host galaxies. Optically-selected AGN hosts in the local universe are found to lie on the red sequence (Schawinski et al. 2007), while, at higher redshifts, both optically-selected and X-ray selected AGNs reside in galaxies in the transition region between the blue and red sequences (Nandra et al. 2007; Salim et al. 2007; Coil et al. 2009; Hickox et al. 2009; Schawinski et al. 2010). However, Silverman et al. (2009) found that X-ray selected AGNs at $z \sim 1$ often reside in galaxies with higher star-formation rates than similar-mass non-active galaxies, and that the AGN fraction is higher in the blue cloud. These results highlight the importance of comparing AGN hosts with control non-AGN samples matched in stellar mass in order to mitigate the selection effects associated with missing low-mass black holes in small galaxies.

To uncover evidence of ongoing processes linking AGNs to their hosts, it is important to examine AGNs at even higher redshifts, during the epoch when the bulge stellar population was forming. At $z \sim 2 - 3$, both the star-formation-

rate density and the black hole accretion rate peak in the universe, and this era is ideal for examining the relationship between AGN host galaxies and similar non-active hosts (Reddy et al. 2008; Hopkins et al. 2007). At these redshifts, it is preferable to limit the study of host-galaxy properties to obscured AGNs, in which the emission from the central engine does not completely outshine the light from the stellar population. Results at $z \sim 2-3$ for UV-selected AGNs (Erb et al. 2006c) and near-IR selected AGNs (Kriek et al. 2007) indicate that narrow-emission-line selected AGNs at these redshifts are mainly found in high mass galaxies ($\log(M_*/M_\odot) \sim 11$). These results are similar to those for X-ray selected AGNs from both the Cosmic Assembly Near-infrared Deep Extragalactic Legacy Survey (CANDELS; Grogin et al. 2011; Koekemoer et al. 2011), and the GOODS and COSMOS fields, which also provide evidence that AGNs are hosted by massive ($\log(M_*/M_\odot) > 10$) galaxies (Mainieri et al. 2011; Kocevski et al. 2012; Santini et al. 2012). These authors also estimate host galaxy colors for AGNs that put them both in the blue cloud and the transition region. Xue et al. (2010) carefully examined X-ray selected AGNs out to $z \sim 2-3$ and found that, when compared to a mass-matched sample of non-active galaxies, AGNs and non-AGNs occupied similar regions of color space, becoming bluer as redshift increases. These results demonstrate that host galaxy properties for large samples of AGNs need to be carefully compared to the properties of a controlled sample of non-active, star-forming galaxies to understand the effects of an AGN on galaxy evolution.

In this chapter, we focus on a sample of UV-selected AGNs at $z \sim 2-3$ drawn from the Lyman break galaxy (LBG) ($z \sim 3$) and the BX/BM samples ($z \sim 2$) (Steidel et al. 2003, 2004). The objects in our AGN sample were identified as Type II AGNs based on narrow emission lines in the rest-frame ultraviolet. In such objects, emission from the central source is obscured from view as the

observer's sightline passes through a central dusty medium. This obscuration provides a better view of the host galaxy surrounding the central AGN. An analysis of the clustering of the UV-selected AGNs indicates that they appear to be hosted by the same dark matter halos as those of the parent population of non-AGN LBGs (Steidel et al. 2002; Adelberger et al. 2005b). The non-AGN LBGs, therefore, provide an ideal control sample with which to compare the AGN LBG host galaxies. Here, we use stellar population synthesis (SPS) modeling to examine the UV through IR SEDs for both UV-selected AGNs and non-AGNs. SPS modeling uses stellar population templates to match the broad spectral energy distribution (SED) of a galaxy and therefore to estimate the properties of the stellar population such as stellar mass, age, extinction, and star-formation rate. There has been much effort to use SPS modeling to characterize the properties of star-forming galaxies across a wide range in cosmic time (Shapley 2011, and references therein), and recently the method has been extended to model AGN host galaxies. However, using this process to examine AGN host properties is made difficult by non-stellar emission from the central source, which has to be carefully modeled alongside the stellar population. Host-galaxy SEDs have been decomposed into stellar and AGN contributions for both X-ray selected Type II AGNs at $z \sim 0.5 - 2.5$ (Mainieri et al. 2011; Santini et al. 2012) and IR-selected AGNs at $z \sim 0.7 - 3.0$ (Hickox et al. 2007). We follow a similar methodology here to characterize the UV-selected AGN host galaxy demographics at $z \sim 2-3$. Accordingly, we build on earlier work from Erb et al. (2006c) and Kriek et al. (2007) using a larger sample of AGNs and a more systematic treatment of AGN host galaxy stellar population modeling and selection effects.

One unique aspect of the UV-selected AGN sample is the set of existing rest-frame UV spectra for both the AGNs and the parent sample of non-AGNs from which they were selected. We can use these spectra to analyze the relationship

between the host galaxy stellar population and observed UV spectroscopic properties. In Chapter 3 (Hainline et al. 2011), we created a composite rest-frame UV spectrum for the UV-selected AGN sample, and studied how the composite varied as a function of UV spectroscopic properties such as emission line equivalent width (EW), UV spectral slope, and galaxy UV luminosity. Here, we use the results from SPS modeling and extend this analysis to examine how the host galaxy properties for this sample of AGNs are reflected in the UV spectra. The UV spectra can also be used to estimate potential selection effects as a function of host galaxy parameters, in order to understand the completeness of our AGN sample, and the relationship between black hole and host galaxy properties.

We describe the AGN sample selection and the data used in the SPS modeling in §4.2. In §4.3, we detail our dual-component ("SPS+AGN") modeling technique to disentangle the emission from the stellar population and the AGN. Specifically, we use this technique on a subset of AGNs with IRAC data to infer how the presence of AGN emission affects the host galaxy parameters derived from SPS fitting. This analysis leads to the calculation of "correction factors," which are then used to model our full set of AGNs and robustly estimate their host galaxy parameters, as detailed in §4.4. In §4.5, we compare the stellar properties for the AGNs to those of non-active star-forming galaxies, including a subsample of galaxies matched in stellar mass. In detail, we compare the AGNs to non-active galaxies using the SFR vs. stellar mass relation, the rest-frame $U - V$ color vs. stellar mass relation, and UV spectroscopic properties. Finally, in §4.6, we consider the origin and implications for the UV spectroscopic trends among AGNs, in terms of sample completeness and the connection between black hole and galaxy mass at $z > 2$. We list our conclusions in §4.7. Throughout this chapter, we adopt the following cosmological parameters: $H_0 = 70\ \mathrm{km\ s^{-1}\ Mpc^{-1}}$; Ω_{tot}, Ω_m, $\Omega_\Lambda = 1, 0.3, 0.7$.

4.2 The UV-Selected AGN Sample and Observations

The narrow-lined AGNs we model in this chapter were selected from a parent sample of 3,059 UV-selected star-forming galaxies at $z \sim 2-3$. LBGs at $z \sim 3$ are chosen due to the absorption of light shortward of the Lyman break at 912 Å by the intervening intergalactic medium (IGM). As this break is redshifted to optical wavelengths for $z \sim 3$ galaxies, such objects can be selected based on their position in a $U-G$ vs. $G-\mathcal{R}$ color-color diagram (Steidel et al. 2003). Similar color criteria have been used to identify galaxies at $z \sim 2$, as the $UG\mathcal{R}$ colors of star-forming galaxies at this redshift correspond to a flat part of the rest-frame UV spectrum redward of the Lyman break (Steidel et al. 2004; Adelberger et al. 2004). The full sample of $z \sim 2-3$ UV-selected star-forming galaxies is described in Steidel et al. (2003, 2004) and Reddy et al. (2008). From this sample, galaxies were identified as having an active nucleus on the basis of features in their rest-frame UV spectrum: strong Lyα emission accompanied by detectable emission in at least one other high-ionization AGN emission line, including NVλ1240, SiIV$\lambda\lambda$ 1393,1402, CIVλ1549, or HeIIλ1640. These objects were selected to be "narrow-line," or "Type II" AGNs, as the FWHM for any of the emission features was less than 2000 km s^{-1}. The average redshift of the 33 AGNs is $\langle z \rangle = 2.55 \pm 0.31$, with an average $\mathcal{R}$ magnitude of $\langle \mathcal{R} \rangle = 24.2 \pm 0.7$, and a range of $22.55 < \mathcal{R} < 25.72$. More details about the sample and its selection are provided in §3.2.

The UV, optical, and infrared photometry for this AGN sample comes from multiple imaging programs. Objects were initially selected as high-redshift galaxies from their U, G, and $\mathcal{R}$ magnitudes (Steidel et al. 2003, 2004). The UV and optical imaging for the fields containing our AGNs is detailed in full in Reddy et al. (2008). The galaxies that comprise this sample were selected from imaging characterized by a typical 3σ photometric depth of $\mathcal{R} \sim 27.0$. In order to

fully model these objects, we limited our sample to objects with near- and/or mid-infrared photometry. At the redshifts we are studying, important spectral features that indicate age are shifted to the near-IR, such as the 4000 Å break due to metal absorption lines in late type stars, and the Balmer break at 3646 Å from A-type stars. Data at these and longer wavelengths are required in order to constrain stellar population models and give accurate and robust stellar mass and age estimates (Shapley et al. 2001; Reddy et al. 2012). For 15 of our 33 objects (in the Q0100, Q0142, Q0933, Q1217, GOODS, Q1422, Q1623, Q1700, Q2343, and Q2346 fields), near-IR J and K magnitudes were obtained using the WIRC instrument on the Palomar 200" telescope, with a typical $2''$ aperture 3σ photometric depth of 22.6 (K), and 24.1 (J), in Vega magnitudes (Erb et al. 2006c).[1] The WIRC data were reduced using custom IDL scripts as described in Shapley et al. (2005b). When necessary, some of the K-band images were smoothed to match the seeing in the $\mathcal{R}$-band images. Further K-band imaging for 11 objects (in the Q0000, Q0201, Q0256, Q2233, DSF2237a, DSF2237b, Q2346 fields) was obtained using the PANIC instrument on the Magellan telescope, as described below. For 16 objects in our sample, we assembled *Spitzer* IRAC (Fazio et al. 2004) data in Channels 1 (3.6 μm), 2 (4.5 μm), 3 (5.8 μm), and 4 (8.0 μm). IRAC data for our objects come from five *Spitzer* Programs, as described in Reddy et al. (2012) in more detail. These data were reduced with custom IDL scripts that applied artifact correction and flat fielding, after which individual images were mosaiced, and drizzled. Photometry was performed by fitting point-spread functions (PSFs) to the images with positions pre-determined using optical and near-IR data. The full details of the IRAC reduction, PSF fitting, and photometry are found in Reddy et al. (2006b). We also assembled *Spitzer*/MIPS 24 μm data for 8 of our objects, as deep surveys were undertaken in the GOODS-N

[1] 24.4 (K) and 25.0 (J) in AB magnitudes

(PI: M. Dickinson) and Westphal (PI: G. Fazio) fields, and the Q1623, Q1700, and Q2343 fields were imaged under GO 1 and 3 *Spitzer* programs. The MIPS data were flat fielded with custom IDL scripts, combined, and photometry was obtained with PSF fitting, as described in Reddy et al. (2006b, 2010).

As only 15 of the narrow-line AGNs in the UV-selected sample had existing coverage at near-IR wavelengths, we imaged 11 additional objects using the PANIC instrument (Martini et al. 2004) on the 6.5m Magellan I (Baade) telescope at Las Campanas Observatory in September of 2008. These objects were observed over the course of two nights under excellent conditions (median seeing of $0\farcs5$), with one additional night lost to weather. The data were reduced with IRAF PANIC reduction scripts ("p_reduce") (Martini et al. private communication). Each science exposure was linearized, dark subtracted and flat fielded, and sky subtracted using dithered frames adjacent in time. The final images were distortion corrected and stacked. For the purposes of flux calibration, we also obtained and reduced images of Persson et al. (1998) near-IR standard stars. The typical 3σ photometric depths of the final images ranged between 19.5 and 21.5 in K (Vega magnitude), with a median of 21.0. The PANIC K-band images were smoothed to match the seeing in the $\mathcal{R}$-band images, which were typically characterized by a larger point spread function. Photometry for these data was calculated using SExtractor (Bertin & Arnouts 1996). We used SExtractor "isophotal" magnitudes, where the isophotal area adopted to calculate flux in the $\mathcal{R}$-band image was applied to the smoothed K-band image. With this procedure, we calculated $\mathcal{R}-K$ colors within a fixed isophotal area, just as the existing optical and near-IR colors had been estimated.

The optical and near-IR photometric errors for all of our objects were estimated using a Monte Carlo approach, where fake galaxies across a range of

magnitudes were added to the data and recovered using SExtractor, with the same input parameters as those used to calculate the actual photometry. This method resulted in distributions of the differences in input and recovered magnitudes in various bins of recovered magnitude. The error that we assigned to each photometric measurement was the standard deviation in the relevant bin. Photometric errors for the IRAC data were obtained with a similar method, where the photometry was calculated using a custom PSF fitting method as described in Reddy et al. (2012). The full $UG\mathcal{R}JK$+*Spitzer* photometric datasets for our objects are listed in Table 4.1.

4.3 SED Modeling

Before discussing the stellar populations of our AGN hosts, we examine their observed colors. The measured $\mathcal{R}-K$ distribution for our full sample of AGNs is shown in Figure 4.1, along with the $\mathcal{R}-K$ colors for non-active UV-selected star-forming galaxies (Reddy et al. 2012). Although these AGNs and non-active galaxies were selected using the same rest-UV photometric criteria, the redder $\mathcal{R}-K$ colors for the AGNs may be indicative of a difference in the host stellar populations of active and non-active galaxies. Specifically, these colors imply a more evolved stellar population and/or higher dust extinction for the AGN host galaxies, and we can use SPS modeling to interpret the color information for our sample of active galaxies in terms of physical properties.

In SPS modeling, the observed UV through infrared photometry of a galaxy is fit by assuming a population of stars governed by a set of parameters, including star-formation history, metallicity, initial mass function, stellar age and mass, and degree of dust extinction. Stellar population models use a stellar library of the observed spectra of stars of different spectral types, as well as a description of

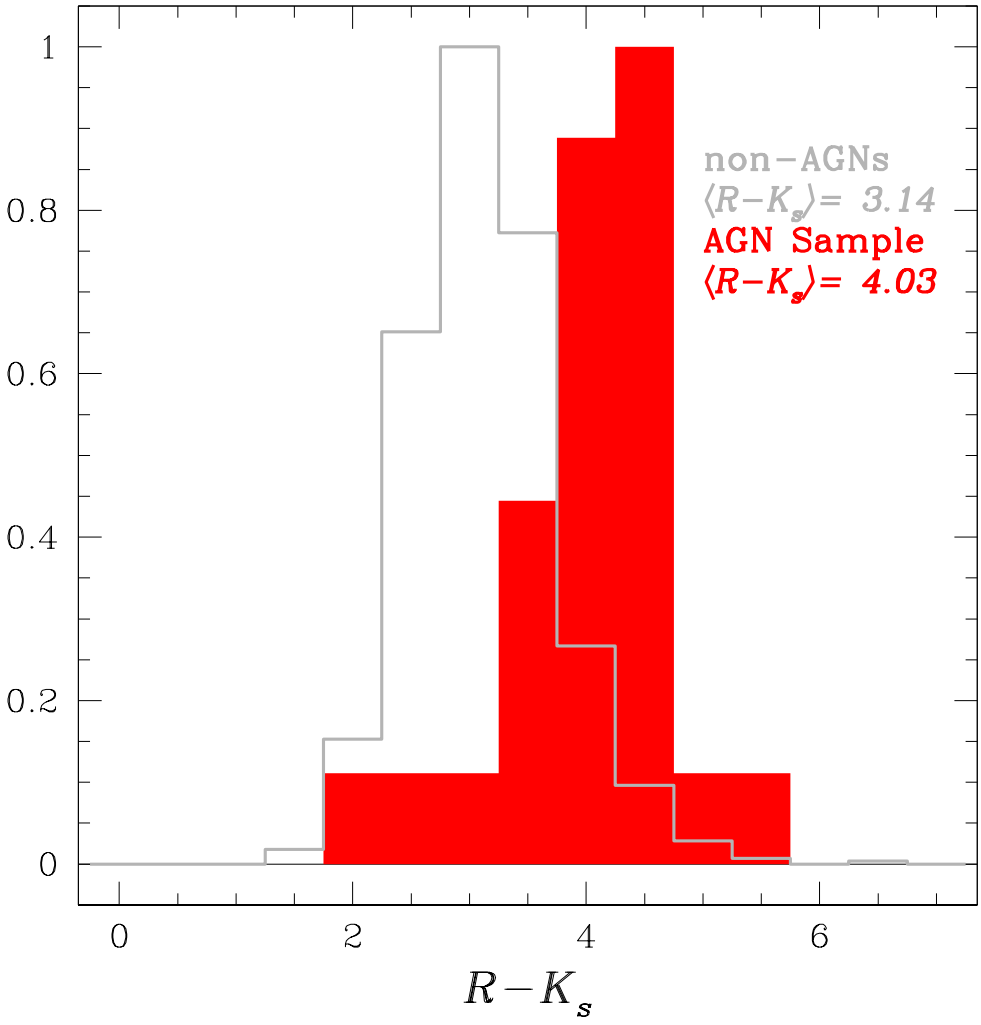

Figure 4.1 Normalized $\mathcal{R}-K$ color distribution for our sample of $z \sim 2-3$ AGNs, compared with similarly-selected non-active galaxies from Reddy et al. (2012). These two histograms have been normalized to have the same peak values for clarity, given the vastly different sample sizes. The $\mathcal{R}-K$ colors for AGNs are, on average, redder than for non-active galaxies, indicating older stellar populations and/or more dust extinction.

the evolution of stars of different masses and metallicities to produce integrated spectra for a population of co-evolving stars at various ages and for a given star-formation history. These spectra are passed through photometric filters to predict galaxy SED luminosities and colors, which are compared to observations to determine the physical properties of the host galaxies.

The SPS approach to SED fitting has been widely used to describe the stellar populations of high-redshift galaxies (Sawicki & Yee 1998; Shapley et al. 2001; Papovich et al. 2001; Shapley 2011, and references therein). For our sample of active galaxies, however, we must use caution because of the effect that non-stellar continuum and line emission may have on the fitted parameters. In order to constrain the effect of AGN emission on the stellar population synthesis modeling process, we modeled the observed SED with both a stellar population component as well as an AGN component ("SPS+AGN"). In this approach, the observed colors and magnitudes are decomposed at each wavelength into a sum of the fluxes from the underlying stellar population and emission excited by the central AGN. Our objects are narrow-lined AGNs, and thus the non-stellar emission should be limited to the rest-frame near- to mid-infrared wavelengths. At the same time, we can use our dual-component modeling for objects with photometric information at infrared wavelengths both to understand the true stellar populations of AGN host galaxies, and also to understand how the presence of an AGN affects the best-fit stellar parameters.

In this section, we describe our dual-component modeling in detail. We start by discussing our sample of AGNs with IRAC data, which we can use to describe the AGN contribution to the SED (§4.3.1). We then use our dual-component modeling procedure to calculate corrections to host galaxy parameters that account for broadband AGN emission (§4.3.2). We also correct our photometry for

the presence of strong, discrete AGN emission lines (§4.3.3), and conclude with a section detailing our systematic uncertainties (§4.3.4).

4.3.1 IRAC Data

As described in §4.2, there is $UG\mathcal{R}JK$ photometry for the majority of our sample, but only 16 AGNs have IRAC measurements. Of these 16 objects, 11 are characterized by "power-law" emission in the rest-frame near-IR, where the fluxes in the IRAC bands increase monotonically towards longer wavelengths. This emission is hypothesized to arise in an AGN from thermal or non-thermal emission near the dusty active nucleus (Rees et al. 1969; Neugebauer et al. 1979; Elvis et al. 1994). An additional two objects with IRAC coverage (Q1623-BX454 and Westphal-MM47, only including Channels 1 and 2) have flat mid-IR slopes, indicating a weak AGN as compared to the stellar population. As these objects do not have K-band data, we fit their SEDs solely with a stellar population. The final three objects (Q1217-BX46, Q1623-BX747, and Q2233-MD21) only have IRAC data in Channel 1, which was not sufficient for the purpose of discerning the presence of a power-law in the rest-frame near-IR. We fit the SEDs for these objects, including the IRAC Channel 1 data, with a stellar population only.

To place our sample of UV-selected IRAC AGNs in context, we compare it to similar power-law galaxies. In Figure 4.2, we plot the 11 objects with IRAC power-law slopes on the color-color diagrams from Lacy et al. (2004) and Stern et al. (2005), which were initially used to select galaxies with red IR colors as possible AGNs. The AGNs with detections in all four IRAC bands are plotted as red points, and, on the left figure, we use dashed lines to indicate the positions of three AGNs with only Channel 4 and Channel 2 photometry. On the left side of the figure, we show the AGN selection box from Lacy et al. (2004) with

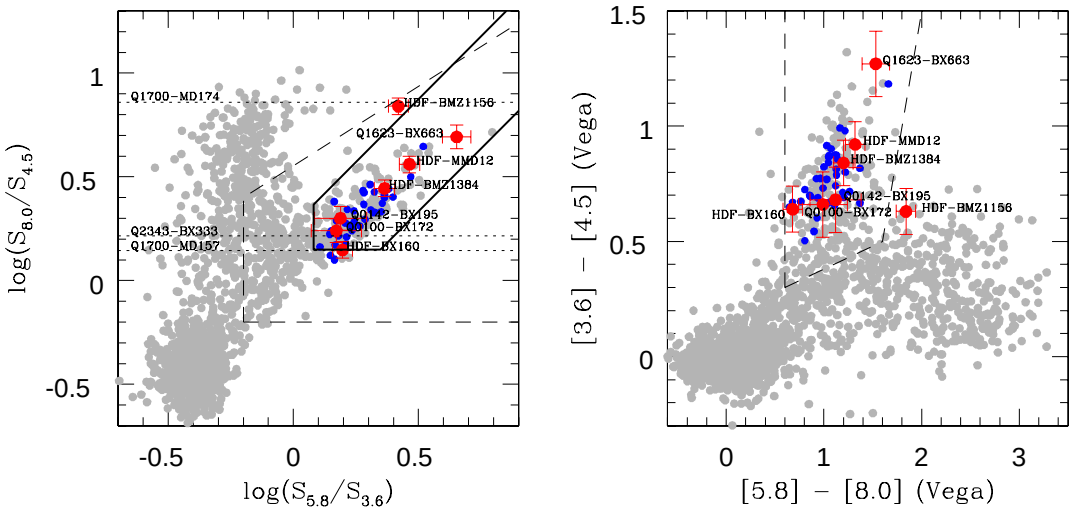

Figure 4.2 IRAC color-color plots from Lacy et al. (2004) (left) and Stern et al. (2005) (right). The $z \sim 2-3$ UV-selected AGNs with IRAC detections are shown in red. Dotted lines on the left are for objects with data only in Channels 2 and 4. The dashed lines shows the color criteria used by Lacy et al. (left) and Stern et al. (right) to select AGNs by virtue of their power-law emission. The heavy black line indicates the revised selection criteria from Donley et al. (2012). The grey points are *Spitzer* First Look Survey objects with clean detections in all four IRAC Channels (Lacy et al. 2005). This sample likely spans a wide range in redshift, though not all sources have spectroscopic coverage. Blue points are *Spitzer* power-law galaxies from Park et al. (2010) at $1.4 < z < 3.5$ for comparison. Our objects would be selected as AGNs under the Lacy et al. criteria, while all but HDF-BMZ1156 would be selected as AGNs under the Stern et al. criteria. Predictions of AGN colors as a function of redshift from Donley et al. (2012) find that strong AGNs inhabit the space occupied by HDF-BMZ1156 at $z \sim 2-3$.

long dashed lines. Each of our AGNs lies in the detection area. Donley et al. (2012) revised the selection criteria to account for contamination due to star formation, and we indicate the revised AGN selection area with a dark line. All but one of our objects fall within this revised area. On the right, we show the AGN selection criteria from Stern et al. (2005) with long dashed lines, and all but one object falls within this area. HDF-BMZ1156 falls outside of the Stern et al. and Donley et al. selection areas (although it is consistent with being included within the Donley et al. selection area when its photometric uncertainty is taken into account)[2]. The grey points on this diagram are those objects from the *Spitzer* First Look Survey with clean detections in all four IRAC Channels across all redshifts, and illustrate the full range in color-color space spanned by extragalactic sources (Fadda et al. 2004). To compare to high-redshift power-law galaxies, we have plotted a sample of $z > 1.4$ power-law sources from Park et al. (2010) on both diagrams as blue points. Our active sample spans the observed range in power-laws. The specific values for the power-law slope for our objects (α, where $f_\nu \propto \nu^\alpha$) range between -0.62 and -3.50, with an average (median) of $\alpha = -1.75\,(-1.79)$. These values show the same range as those presented in Park et al. (2010), although the objects in our sample with the most negative slope values, Q1623-BX663 and Q1700-MD174, would be among the reddest of the *Spitzer* power-law galaxies (the power law for Q1700-MD174 is fit from only the IRAC [4.5] and [8.0] point). Our galaxies are thus representative of the full range of high-redshift *Spitzer* power-law galaxies, and should illustrate AGN properties for a range of SED types. It is notable that the majority of the UV-selected AGNs in our sample with IRAC data have power-laws, supporting their identification

[2]We note that HDF-BMZ1156, formerly known as HDF-oMD49, has previously been discussed in Steidel et al. (2002) and Reddy et al. (2006a). This object was only weakly detected in the Chandra 2 Msec data, and has been identified as an example of a Compton-thick AGN by Alexander et al. (2008b), based on its combined mid-IR and X-ray properties.

as AGNs, consistent with the observation in Reddy et al. (2006a) that all but one UV-identified AGN in the GOODS-N field had significant excess flux at 8 μm.

Stellar population models, even those with large contributions from old, red stars, cannot successfully model the infrared emission seen in an IRAC power-law object. In Figure 4.3, we show a constant star formation (CSF) fit for one of our objects, HDF-MMD12, an AGN at $z = 2.648$. The best fit is very poor, with a $\chi^2 = 180$, due to the presence of the strong AGN power-law emission in the IRAC bands. Often, the SEDs of Type II AGN hosts are modeled excluding points redwards of the rest-frame optical, as the AGN emission for narrow-lined objects should be minimal at rest-frame UV and optical wavelengths (Barger et al. 2005b; Bundy et al. 2008) With our sample of IRAC AGNs, we can model the power-law AGN emission and the stellar emission together to see exactly how the presence of an AGN affects the best-fit stellar population parameters.

4.3.2 Stellar Population and AGN Modeling Procedure

In order to accurately describe the SEDs for our sample, we require a suite of stellar population models and an AGN template. For our sample of $z \sim 2-3$ AGNs we chose Bruzual & Charlot (2003, hereafter BC03) stellar population models. Recently, much attention has been focused on the degree to which thermally pulsating asymptotic giant branch (TP-AGB) stars contribute to the near-IR luminosity of a population of $0.5-2$ Gyr age stars (Maraston 2005; Maraston et al. 2006; Eminian et al. 2008). Different treatments of TP-AGB stars systematically affect derived stellar mass and ages (Maraston 2005). In order to gauge how the presence of TP-AGB stars affects our inferred stellar parameters, we also applied the stellar population models of Maraston (2005, hereafter Mar05) and Charlot & Bruzual (2012) (private communication, hereafter CB12) to our SEDs. For the

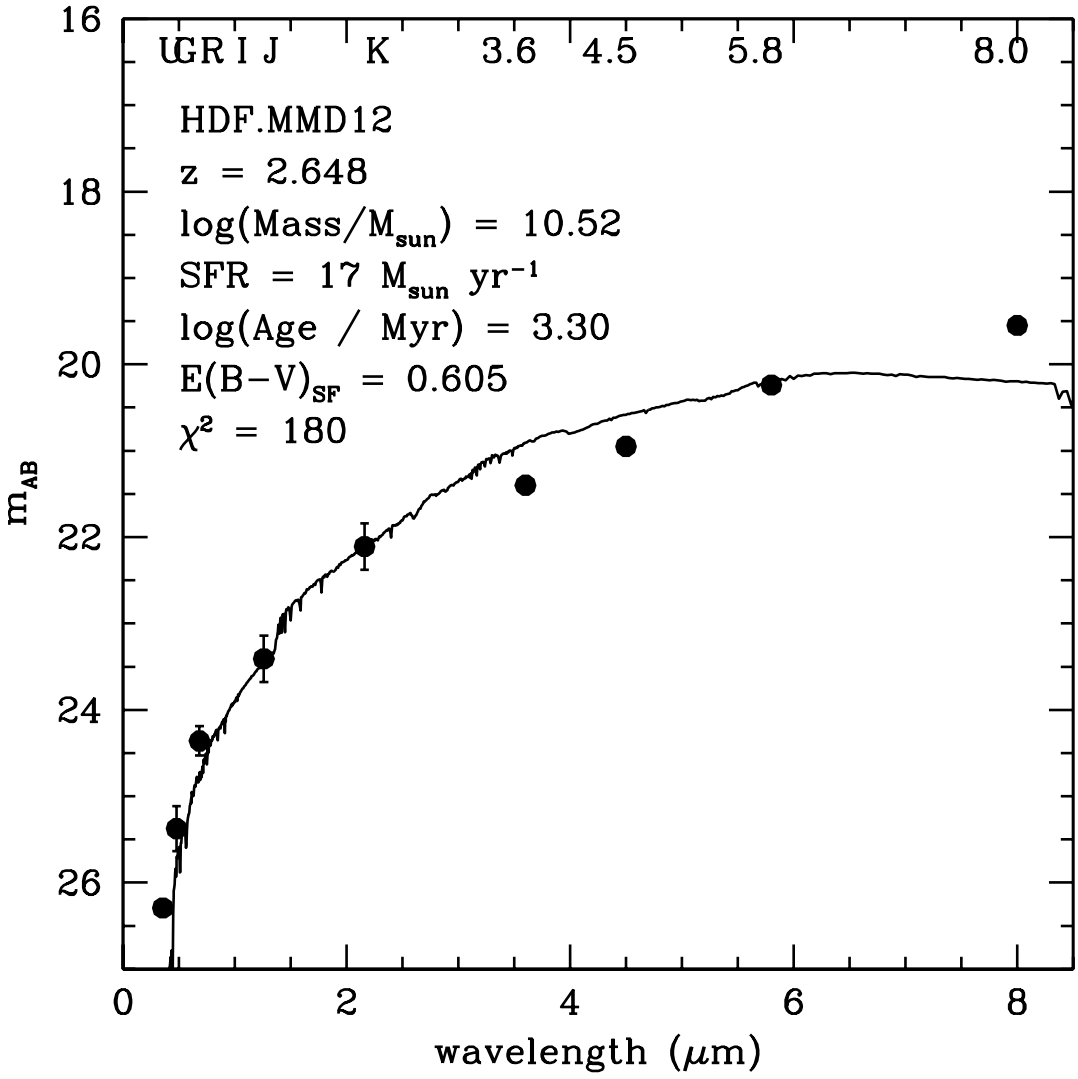

Figure 4.3 Best-fit SPS-only SED model for the AGN, HDF-MMD12. A BC03 CSF stellar model was used for the fit. The power law seen in the IRAC bands is indicative of the presence of an AGN, which results in a poor fit ($\chi^2 = 180$) for a stellar emission-only model. The errors on the IRAC points are smaller than the size of the data points. The solid curve is the fit derived taking into account all of the data.

BC03 and CB12 models, we adopted the Padova 1994 stellar evolution tracks. We selected solar metallicity models and a Chabrier (2003) initial mass function (IMF) extending from 0.1 to 100 $M_{\odot}$. We adopted solar metallicity models as non-active galaxies in a similar mass range appear to have metallicities only slightly lower than solar (Shapley et al. 2004). It should be noted that using a Salpeter IMF increases the best-fit stellar masses and star-formation rates by a factor of 1.8 with little effect on the predicted spectral shape. To account for dust extinction, we used a Calzetti et al. (2000) starburst attenuation law, which on average provides an accurate description of the reddening and attenuation of the UV stellar continuum in both nearby and distant starburst galaxies (Reddy & Steidel 2004; Reddy et al. 2006b).

For the BC03 and CB12 models, we investigated a range of star-formation histories of the form $\mathrm{SFR}(t) \propto \exp(-t/\tau)$, with e-folding times of $\tau = 0.01$, 0.02, 0.05, 0.1, 0.2, 0.3, 0.5, 1, 2, and 5 Gyr, along with CSF models. For the Mar05 models, we used τ models, but with $\tau = 0.1$, 0.25, 0.5, 1, 2, 5, and 20 Gyr, where the $\tau = 20$ Gyr is effectively a CSF model. We chose to not model with more complex star-formation histories, such as short-duration bursts superposed on top of an exponentially declining star-formation history, or exponentially increasing star formation models. Exponentially increasing star formation models have been shown to apply to galaxies at $z > 2$, and naturally arise in hydrodynamic and semi-analytic models of star formation, and are suggested by the relationship between SFR and stellar mass observed at high redshift. (Maraston et al. 2010; Papovich et al. 2011; Reddy et al. 2012). As we will discuss in §4.4.3, recent studies indicate that for $z \sim 2$ non-active LBGs, stellar masses derived from CSF models are similar to those derived using exponentially rising star-formation models (Reddy et al. 2012). At first, we report results based on both CSF and τ models for consistency with previous SED modeling studies, though, ultimately,

we will interpret the stellar population parameters derived from CSF modeling alone.

We also require a prescription for the non-stellar AGN emission in our dual-component modeling. Often, the non-stellar continuum contribution to the near-IR emission is removed by assuming that this portion of the spectrum can be represented by a power law of the form $f_\nu \propto \nu^{-\alpha}$, where f_ν is the flux density at a frequency ν (Alonso-Herrero et al. 2003; Hainline, L. et al. 2011). Since this method of modeling the AGN emission has no explicit basis in the physics of the AGN, we instead opt for the AGN model from Assef et al. (2010) to describe our AGN infrared emission. The Assef et al. AGN model was created using an iterative method, starting with the Richards et al. (2006) average quasar SED template, modified to better replicate the behavior in the UV predicted by an accretion disk model (in an attempt to minimize, in part, contamination by host galaxy emission). This template was applied to the SEDs of AGNs from the NOAO Deep Wide-Field Survey in the Boötes field, and iteratively updated to fit the full sample of data. The final AGN template is thus physically motivated, and, as the template has been both normalized to a distance of 10 pc and created to have an integrated luminosity of $10^{10} L_\odot$, its application to our data gives us an estimate of the bolometric luminosity of the AGN. The Assef et al. (2010) AGN template describes a Type I AGN, with strong emission in the rest-frame ultraviolet thought to be emitted from the accretion disk, as well as emission in the rest-frame near- to mid-IR from warm and hot dust emission. At the same time, the AGNs that we model with the Assef et al. template were selected to be Type II by virtue of narrow emission lines seen in the rest-frame UV, where accretion disk emission should be obscured by dust. To model our Type II AGNs, following the analysis of Assef et al. (2010), we apply dust extinction to the AGN template using a reddening curve derived from the Small Magellanic Cloud for

$\lambda < 3300$Å (Gordon & Clayton 1998), and following the Galactic curve at longer wavelengths (Cardelli et al. 1989). The resulting template should then consist of strong IR emission from hot dust near the active nucleus, which we use to model the IRAC power-law.

Since the objects we are modeling were selected to be Type II AGNs, we made a prior assumption of $E(B-V)_{AGN} > 1.0$. We model these objects by taking a Type I AGN template and applying extinction in order to produce a Type II AGN template to fit the SEDs. For the Type II AGNs discussed here, the rest-frame UV and optical light should be dominated by stellar emission, given the narrow emission lines in the rest-frame UV suggesting significant obscuration of the central engine (See Chapter 3). Low values of AGN extinction, on the other hand, would result in SEDs with prominent AGN continuum emission even at rest-frame UV wavelengths, as well as broad-line region emission. Although the initial modeling results for two systems, HDF-BMZ1384 and Q2343-BX333, indicated best fit values of $E(B-V)_{AGN}$ less than 1.0, we rejected such fits on the basis that these are Type II objects. Furthermore, the χ^2 values for these low $E(B-V)_{AGN}$ fits were not significantly lower than for fits with $E(B-V)_{AGN}$ at values similar to the bulk of the sample ($E(B-V)_{AGN} \sim 2-7$). The same lower limit on $E(B-V)_{AGN}$ is also adopted in Mainieri et al. (2011) for a similar SPS+AGN fitting procedure used to fit X-ray selected Type II quasars at $z > 0.8$. Throughout this chapter, we report only those fits where $E(B-V)_{AGN} > 1.0$. We also limit $E(B-V)_{AGN} < 8.0$, as larger values for the AGN extinction did not improve the fits for the objects we examined.

We used the Assef et al. AGN template, along with the stellar population models, to fit the observed SEDs of our IRAC subsample. The overall procedure we used is similar to that of Shapley et al. (2001, 2004, 2005b), but here the

predicted colors are the sum of stellar emission and non-stellar emission from our AGN model. The best-fit model therefore yields constraints on both stellar population as well as AGN parameters. The stellar parameters that we modeled included dust extinction [parameterized as $E(B-V)_{SF}$], stellar population age (t_{SF}), star-formation rate (SFR), stellar mass (M_*), and star-formation history (τ). The ages that we used ranged between 50 Myr and the age of the universe at the redshift of the modeled galaxy. This lower limit of 50 Myr was chosen to exclude models with ages younger than the dynamical timescales estimated for typical $z \sim 2-3$ LBGs (Erb et al. 2006a; Law et al. 2007). We considered stellar extinctions between $E(B-V)_{SF} = 0.0$ and 0.7. The AGN parameters included a central source extinction, $E(B-V)_{AGN}$, and a normalization constant, $N_{\rm AGN}$.

In the first step of the SED fitting procedure, we created total SPS+AGN models for each potential combination of input parameters. The stellar model flux at each wavelength (with a specific star-formation history, age, and extinction value) was summed with the AGN model flux (with a specific AGN extinction value, and multiplied by the normalization factor $N_{\rm AGN}$). In order to add the AGN template to our SPS models in a meaningful way, we used values of $N_{\rm AGN}$ that reflected how the SPS models are normalized. The Assef et al. AGN template is normalized to an AGN bolometric luminosity $L_{bol} = 10^{10} L_{\odot}$, where this luminosity is calculated by integrating the entire template longward of Lyα. In terms of the SPS models, the BC03 and CB12 CSF templates are normalized at 1 $M_{\odot}$ yr^{-1} of star formation, while the declining τ templates are normalized to have a total mass of 1 $M_{\odot}$ at $t_{SF} = \infty$. Thus, for the BC03 and CB12 CSF fits, $N_{\rm AGN} = L_{bol}/({\rm SFR} \times 10^{10})$, and for the declining τ fits, $N_{\rm AGN} = L_{bol}/(M_*(1-e^{-t/\tau}) \times 10^{10})$. The Mar05 models are all normalized to 1 $M_{\odot}$ of stars, and so $N_{\rm AGN} = L_{bol}/(M_* \times 10^{10})$ for these fits. While we report the best-fitting $N_{\rm AGN}$ values, it is useful also to compare L_{bol} between fits, which

indicates the strength of the AGN for each object.

The combined AGN and stellar model spectrum was further attenuated by IGM absorption from neutral hydrogen (Madau 1995), which only affects the predicted U and/or G magnitudes, depending on the redshift. These output SPS+AGN templates for a given set of parameters were compared to the optical through mid-IR SED for a specific object (though, not including *Spitzer* MIPS data, see §4.4.1), and a value of χ^2 for the fit was calculated. In these fits, we only modeled photometric detections. In a few cases, there were upper limits in IRAC channels that were not modeled (Ch4 for Q0142-BX256, Ch3 and Ch4 for Q1623-BX454, Ch2 for Q1623-BX74, and Ch3 for Q2233-MD21). In all cases except that of Q0142-BX256, the IRAC upper limits are entirely consistent with the best-fit SED model. We sought to scale our total models to the observed SEDs such that the calculated χ^2 was minimized, and this normalization naturally led to an estimation of the star-formation rate and stellar mass. The parameters [$E(B-V)_{SF}$, t_{SF}, SFR, M_*, τ, $E(B-V)_{AGN}$, and $N_{\rm AGN}$] resulting in the minimum χ^2 with respect to the measured photometry for an object are referred to as the "best-fit" parameters.

4.3.3 Correcting the Photometry for the Presence of Strong Emission Lines

Flux contribution from strong nebular emission lines excited by the presence of an AGN can be a significant source of contamination in broadband SEDs (Schaerer & de Barros 2011). As described in §3.4, the rest-frame UV spectra for the $z \sim 2-3$ Type II AGNs described here include emission lines such as Lyα, with an average rest-frame EW of 80 Å. This strong emission line, as well as others in the rest-frame UV, such as CIVλ1549 and HeIIλ1640, can enhance the flux

in the U or G bands (depending on redshift), and alter the observed $U-G$ or $G-\mathcal{R}$ colors. Rest-frame optical features such as Hα or [OIII]λ5007 can similarly add flux in the near-IR, and subsequently affect the measured $\mathcal{R}-K$ colors. We adopt a method of correcting for these emission lines outlined in Papovich et al. (2001), where a rest-frame EW, EW_0, for an object at a redshift, z, introduces a change in the magnitude:

$$\Delta m = -2.5 \log \left[1 + \frac{EW_0(1+z)}{\Delta\lambda} \right] \tag{4.1}$$

In this equation, $\Delta\lambda$ is the width of the filter bandpass. We calculated Δm for each measured emission line, and, where its absolute value was larger than the photometric error, we corrected for this magnitude difference to produce the final photometry.

Strong emission lines do not affect the U or G bands for 19 out of 33 AGNs in our sample at $2.17 \leq z \leq 2.48$. For the remainder, we used UV spectra (described in Chapter 3) to measure EW values for the strong emission lines such as Lyα, CIV, and HeII. Lyα was the chief contaminant to the G band for this redshift range, with the average (median) value of the magnitude difference $\Delta m = 0.36\,(0.34)$. The other UV lines were not strong enough to significantly contaminate the photometry: in objects where CIV was detected, the EW was on average (median) 48% (17%) of the EW of Lyα, and similarly, in objects where HeII was detected, the EW was on average (median) 25% (13%) of the EW of Lyα. However, for one object (HDF-BMZ1156), very strong CIV and HeII contaminated the G band (at the redshift of this object, Lyα fell bluewards of the G band), with a combined $\Delta m = 0.37$.

The K band contains Hα for 20 out of 33 AGNs, and [OIII]λ5007 for an additional 4 objects. Near-IR spectra have only been obtained for a subset of our

AGNs, as part of an ongoing project to measure the rest-frame optical spectroscopic properties for this sample (Erb et al. 2006c, Hainline et al., in prep). For this analysis, there are 9 objects with near-IR spectral coverage (8 objects with Hα measurements, and one with a measurement of [OIII]), and we have determined the Hα and [OIII] fluxes for the available lines. These spectra do not show a significant continuum, so we used the K-band magnitude in order to estimate the continuum flux density (corrected for line flux), and therefore the EW for Hα and [OIII]. The average (median) magnitude difference from the Hα emission lines is $\Delta m = 0.18\,(0.12)$. It should be cautioned that the majority of our objects do not have rest-frame optical spectra, and Hα or [OIII] could contribute to the K band photometry for these AGNs. However, we expect that the effect should not be large compared to the K-band uncertainties, based on objects with such measurements.

4.3.4 Systematic Uncertainties

While the uncertainties relating to single-component stellar population fitting are well described in Shapley et al. (2005b), the addition of an AGN component to the fits introduces new model degeneracies and systematics. For example, without an AGN component, the inferred extinction, $E(B-V)$, depends on the chosen star-formation history and age. For CSF models, a given set of galaxy $G-\mathcal{R}$ and $\mathcal{R}-K$ colors can be produced by models with older ages and less dust extinction, or younger ages and more dust extinction. Similarly, for the declining τ models, a given set of galaxy colors can be described by models with large values of t_{sf}/τ with less dust extinction or smaller values for t_{sf}/τ along with more dust extinction.

With the addition of an AGN template to the SPS modeling, we find covari-

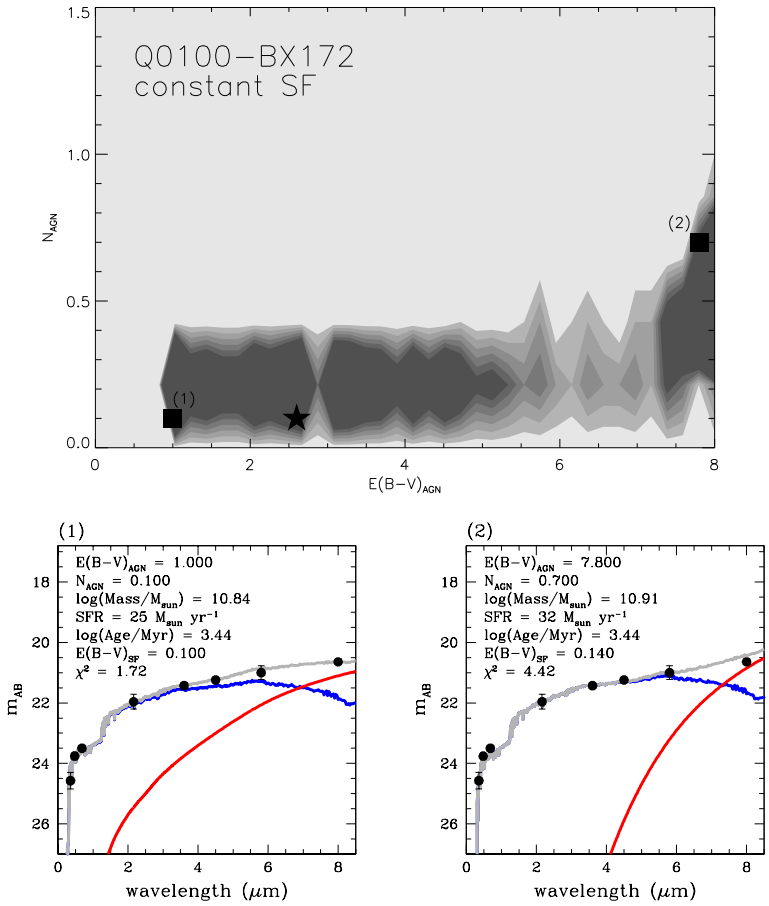

Figure 4.4 Confidence intervals for CSF SED fits to Q0100-BX172, showing the covariance between N_{AGN} and $E(B-V)_{AGN}$ in our fitting results. This plot shows the density of points from the Monte Carlo error results, where darker shading indicates a higher density of points. The black star is the best-fit value from the SED fitting as shown in Table 4.2. The majority of fits show low values for N_{AGN} across a range of $E(B-V)_{AGN}$, with both increasing together proportionally at larger values. Below the confidence interval plot, we show two sample fits for the black squares, indicating how the stellar parameters (with units of log(Age) in Myr, SFR in $M_\odot$ yr^{-1}, and log(Mass) in $M_\odot$) change with N_{AGN} and $E(B-V)_{AGN}$. The blue line is the best-fit stellar model (BC03), while the red line is the best-fit AGN model. The sum of the models in each panel is given as the grey line.

ances between AGN model extinction ($E(B-V)_{AGN}$) and normalization (N_{AGN}), as well as between the AGN parameters and the stellar parameters. Within the IRAC sample described in §4.3.1, a given set of photometric values for our individual AGNs can typically be explained by model fits with lower values of $E(B-V)_{AGN}$ along with lower values of $N_{\rm AGN}$, or higher values of $E(B-V)_{AGN}$ along with higher values of $N_{\rm AGN}$. This degeneracy has an effect on the best-fit stellar parameters. For a given object, lower $E(B-V)_{AGN}$ and $N_{\rm AGN}$ model fits result in lower values of $E(B-V)_{SF}$ and correspondingly lower SFRs. As described above, lower $E(B-V)_{SF}$ fits are also accompanied by older ages. We can explain these covariances qualitatively. For a given intrinsic AGN power-law, lower values of $E(B-V)_{AGN}$ indicate more AGN contamination at shorter wavelengths, and these fits have low values of $N_{\rm AGN}$ in order to fit the observed SED without overpredicting the $UG\mathcal{R}$ flux. The increased flux at shorter wavelengths from a low $E(B-V)_{AGN}$ AGN template is accompanied by lower $E(B-V)_{SF}$ values, as the increased AGN flux requires less dust to account for the red UV to optical continuum ($\mathcal{R}-K$ color). Our modeling procedure works by adding the AGN template (modified by some dust obscuration, and multiplied by $N_{\rm AGN}$) to a stellar population model and then normalizing the result to the observed SED to determine the SFR. As a low-$E(B-V)_{AGN}$, low-$N_{\rm AGN}$ dual-component model has more flux from the AGN at shorter wavelengths, such a model predicted that young stars contribute less flux in the rest-frame UV, which results in lower SFR values. We demonstrate this covariance using Q0100-BX172 as an example in Figure 4.4.

In order to account for covariance among the best-fit stellar and AGN parameters, errors in best-fit parameters were estimated using a Monte Carlo analysis. We created a large set ($N = 500$) of fake SEDs by varying the observed colors and magnitudes in a manner consistent with the photometric errors. Each fake SED

was modeled using the same method as for the actual data, where the best-fit stellar and AGN parameters were those that resulted in a minimization of χ^2. We estimated the 1σ errors for the best-fit model parameters by calculating the standard deviation of the distribution on each parameter from our Monte Carlo simulation results.

4.4 Stellar Population Modeling Results

4.4.1 AGN and Stellar Population Modeling Results

The dual-component SPS+AGN fits successfully reproduce the range in SEDs found in the IRAC AGN subsample. We show the SED fits for the 11 IRAC AGNs in Figures 4.5 (CSF models) and 4.6 (τ models). In each panel, the grey curve represents the best-fitting dual-component model, which is decomposed into the sum of fluxes from a stellar population (blue curve) and an Assef et al. AGN template (red curve). Also shown are the non-reduced χ^2 values output from the modeling program. The τ models fit slightly better, as indicated by χ^2 values. For the CSF models, the poorest fits, with the highest values of χ^2, are for those objects where the K-band flux was greater than predicted from the fit, as in HDF-BMZ1156, HDF-BMZ1384, and to a lesser extent Q1700-MD174 and Q2343-BX333. The underprediction of K-band flux could be a result of the choice of star-formation history (as the exponentially declining star-formation models produce better fits to the K band), or the contamination from Hα emission to the flux in the K-band. It should be noted that we have a rest-frame optical spectrum for HDF-BMZ1156, and have made a correction for the presence of Hα in this object ($\Delta m = 0.07$), and yet the CSF model still underpredicts the K band.

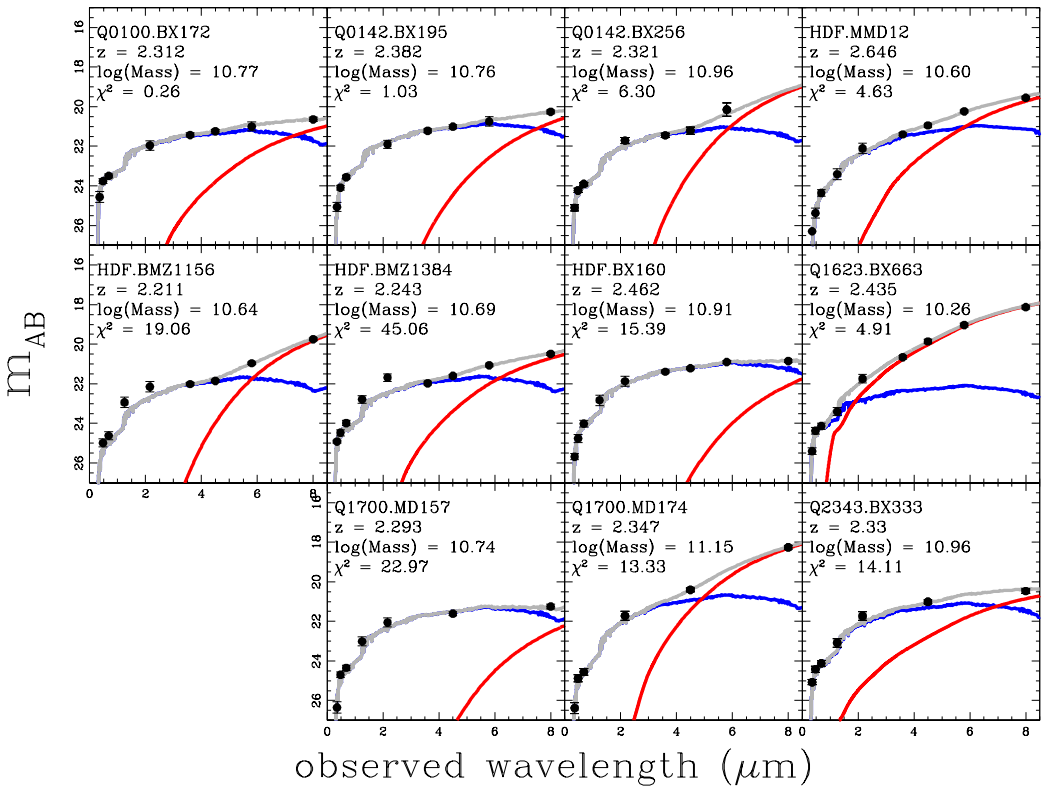

Figure 4.5 CSF SED models for the 11 objects with IRAC power-law fits. The blue line is the best-fit stellar model (BC03), while the red line is the best-fit AGN model. The sum of the models is shown as the grey line. The best-fit parameters for these models are given in Table 4.2, and the log(Mass) shown is in units of solar masses.

The best-fitting parameters for the IRAC AGNs with both CSF and declining τ models are consistent, and are reported in Table 4.2. For the CSF models, the IRAC AGNs have average (median) values and standard deviations for the best-fit parameters of $\langle \log(\mathrm{Mass})_{\mathrm{CSF}} \rangle = 10.82\,(10.76) \pm 0.22$, $\langle \mathrm{SFR}_{\mathrm{CSF}} \rangle = 56\,(37) \pm 51$ $\mathrm{M}_{\odot}$ yr^{-1}, $\langle \mathrm{E(B-V)}_{\mathrm{SF,CSF}} \rangle = 0.23\,(0.24) \pm 0.08$, and $\langle \log(\mathrm{Age})_{\mathrm{CSF}} \rangle = 3.23\,(3.21) \pm 0.25$. For the declining τ models, the IRAC AGNs have average (median) values for the best-fit parameters of $\langle \log(\mathrm{Mass})_{\tau} \rangle = 10.82\,(10.77) \pm 0.29$, $\langle \mathrm{SFR}_{\tau} \rangle =$

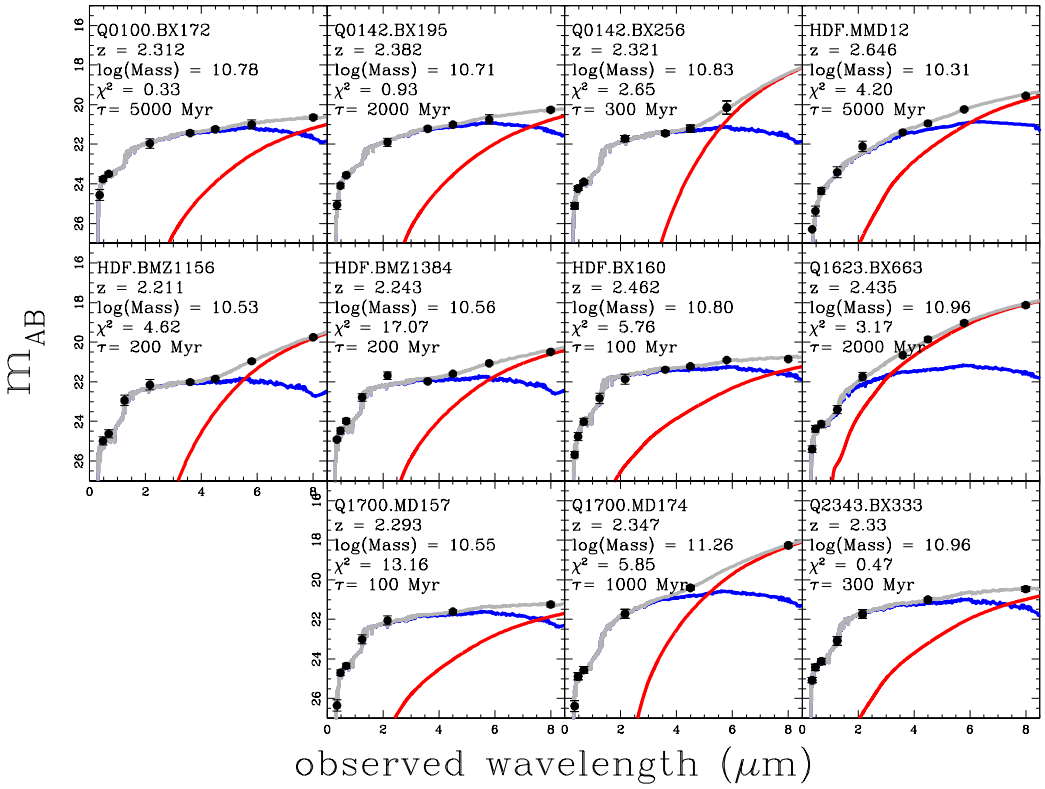

Figure 4.6 Exponentially-declining star-formation SED models for the 11 objects with IRAC power-law fits, with τ values as indicated. The colors of the lines are the same as in Figure 4.5.

$54\,(16) \pm 11$ $M_\odot$ yr^{-1}, $\langle E(B-V)_{SF,\tau}\rangle = 0.14\,(0.12) \pm 0.13$, and $\langle \log(Age)_\tau\rangle = 3.00\,(2.91) \pm 0.33$. While $E(B-V)_{SFR}$ and age are lower on average for the τ models than for the CSF models, the differences in these average values are smaller than one standard deviation of the sample distributions. We will return to the differences between the CSF and τ modeling with the full AGN sample in §4.4.3.

Based on the range in best-fitting parameters, we can split the IRAC AGN host galaxies into two populations based on the slope of the IRAC power law

(Figure 4.2). The first population contains those objects in our IRAC subsample with shallower observed power-law slopes. Most of the galaxies that comprise this population (Q2343-BX333, Q0100-BX172, Q0142-BX195, HDF-BX160, and Q1700-MD157) have dual-component fits where the AGN only becomes the dominant source of emission at $6-8\mu$m observed-frame (Fig. 4.5). These objects are best fit by models with low values of $N_{\rm AGN}$ along with a range of $E(B-V)_{AGN}$ values. The one exception is HDF-MMD12, which has a low value for $N_{\rm AGN}$ accompanied by strong AGN emission at observed-frame wavelengths shorter than 8 μm. HDF-MMD12 is best fit by a relatively young stellar population ($t_{SF} \sim 200$ Myr). This model SED has a weak Balmer break with respect to those of the other objects, and less flux from stars at longer wavelengths, in comparison to the Assef et al. AGN template.

The second population of IRAC AGNs consists of objects with much steeper (redder) power-law slopes. These objects (HDF-BMZ1384, HDF-BMZ1156, Q1700-MD174, Q0142-BX256, and Q1623-BX663) are best fit by models with larger values of $N_{\rm AGN}$, in which the AGN emission already becomes dominant at wavelengths as short as $5-6\mu$m in the observed frame. Correspondingly, the rest-frame UV AGN emission lines in the objects with steeper power-law slopes are stronger on average than those measured in the shallow power-law objects. The AGN bolometric luminosities of the steep power-law objects are also larger, on average, than those of the shallow power-law objects. Q1623-BX663 is the most extreme example. This galaxy has a steep power-law ($\alpha = -2.24$), with a large value of $N_{\rm AGN}$ accompanied by a low value for the AGN extinction. As AGN emission in this object is dominant even to the K band for CSF models, Q1623-BX663 represents a "worst-case scenario" for modeling the AGNs using $UG\mathcal{R}JK$ photometry alone and not including an AGN component. Q1623-BX663 has one of the steepest slopes observed in our IRAC subsample, and it is unlikely that

many objects in the full AGN sample will have similar AGN-dominated fits. The separation of our IRAC objects into two populations based on power-law slope indicated here applies to both the CSF and tau models. Together, these AGN populations show a wide range of AGN contamination, and should provide a representative subset for correcting the full sample for AGN emission.

As discussed in §4.3.2, we also used the CB12 and Mar05 models in our dual-component SPS+AGN fitting. Here we report the differences in derived parameters for the CSF models. For the CB12 modeling, the stellar masses and ages from the fitting are typically 70% of those derived using the BC03 models, while the CB12 SFR and $E(B-V)_{SF}$ values are statistically equivalent to the BC03 values. The Mar05 models produced similar differences. For the Mar05 modeling, the stellar masses from the fitting are typically 60% of those derived using the BC03 models, and the ages are 50% of those derived using BC03. The $E(B-V)_{SFR}$ values derived using both models were statistically the same, and the Mar05 SFR values were larger than the BC03 values by 25%. Despite these small systematic differences among stellar population models, our main conclusions regarding the AGN contamination do not depend on the specific stellar population model adopted.

We have MIPS photometry for eight of our objects with IRAC data. We do not use the MIPS data to constrain our SPS modeling, and find that for the majority of the objects with MIPS data, the best-fit AGN template overpredicts the MIPS flux in our objects by a factor of two on average. Examining the range of stellar and AGN parameters that best fit our optical through IRAC data, we find that attempting to fit for the MIPS data leads to best-fit models that systematically underpredict the IRAC fluxes, due to the shape of the Assef et al. template. Analysis of of the mid-IR SED of HDF-BMZ1156 by Alexander et al.

(2008b) sheds light on the origin of this discrepancy. Alexander et al. find that a Type II AGN template (i.e., the SED of NGC 1068) provides a good fit to the photometry of HDF-BMZ1156 at wavelengths from 16 through 70 μm. However, an additional hot ($\sim$ 1000K) dust component, often found in obscured AGNs (e.g., Alonso-Herrero et al. 2001), is required to fit the IRAC datapoints at shorter wavelengths. If the other AGNs in our sample are similar to HDF-BMZ1156, our use of a single component to describe both IRAC and longer-wavelength data will naturally overpredict the MIPS 24μm flux, since we have forced a Type II template to fit the IRAC data. At the same time, this difference is not significant for most of the sample. The range of SPS+AGN templates that fit the observed $UG\mathcal{R}JK$+IRAC data within the photometric errors is within 1σ of the MIPS uncertainty for the majority (five out of the eight) of our objects. Since we do not use the MIPS data in our SED fitting, the discrepancies between predicted and observed fluxes suggest that the L_{bol} values reported in Table 4.2 may slightly overpredict the true values.

4.4.2 Correcting for AGN Emission

To understand the true AGN host galaxy stellar populations, it is very important to correct for AGN emission in the SED of those objects without IRAC data, where we can't directly quantify the AGN contribution. Many authors fit AGN host galaxy SEDs using SPS models alone (see Bundy et al. 2008; Bluck et al. 2011, for discussions), and find that while the presence of an AGN does affect stellar mass estimates, it is not a significant difference. Here we adopt a different approach, and use our results from the SPS+AGN modeling to quantify how much the presence of an AGN affects the stellar modeling parameters. For the 11 objects in the IRAC AGN sample, we refit the SED but only through the K-

band, and using an SPS-only model. The difference in best-fit parameters based on K-band and SPS-only vs. K-band+IRAC and SPS+AGN modeling indicates how the majority of the objects in our sample without IRAC coverage must be corrected. It is valid to apply the correction factors derived from the IRAC AGN sample to our entire sample, given that the objects with IRAC coverage have similar average $\mathcal{R}$ magnitudes and $\mathcal{R}-K$ colors to those without IRAC coverage. The procedure, star-formation models, and parameters are the same as those discussed in §4.3.2, but here we do not include the AGN template in the K-band-only fits.

The resulting stellar masses and SFRs calculated with an AGN component are lower than those calculated without the AGN component. The best-fit ages and values for $E(B-V)_{SF}$ are consistent between fits with and without the AGN component. For a few objects, such as Q1623-BX663, the best-fit parameters are quite different, as this galaxy suffers from the most AGN contamination at the shorter wavelengths (Fig. 4.5). The results for HDF-BMZ1156 and HDF-BMZ1384 are also discrepant, due to the bright K magnitude for these objects, which is not well-fit in the dual-component modeling extending to IRAC wavelengths.

We analyze the AGN contamination by calculating the ratio between the parameters (M_*, SFR, $E(B-V)_{SF}$, and age) resulting from fits with the SPS+AGN modeling to the average parameters resulting from the SPS-only modeling, which we refer to as "correction factors." We calculated the ratios for the best-fit parameters, and we also analyze the AGN contamination using results from the Monte Carlo error analysis (§4.3.4). In this method, we calculated the average value for the full distribution of Monte Carlo output parameters, and then divided these averages for our SPS+AGN modeling by the averages from the

SPS-only modeling. This second method gives a better understanding of the full set of models that fit an object's SED within the error on the photometry and therefore we only report correction factors calculated in this manner. We note however that the correction factors do not depend significantly on the method used. For CSF models, the correction factors calculated for the 11 IRAC AGNs are shown in Table 4.3. While our results suggest that the $UG\mathcal{R}JK$ photometry for Type II AGNs is largely free from AGN emission, the best-fit masses and SFR values derived without including an AGN component are larger by a factor of 1.4. The values for $E(B-V)_{SF}$ are only larger by a factor of 1.1, and the ages are consistent. We use these factors to correct the best-fit parameters based on CSF SED modeling results for those objects where we do not have IRAC data under the assumption that the SPS+AGN model is more appropriate.

We apply the same analysis to calculate the correction factors for the best fitting τ models. The resulting averages are statistically similar to those calculated from the CSF modeling. The one exception is the SFR parameter, for which the τ models yield correction factors closer to unity than those indicated by the CSF models. The difference is still within one standard deviation for the distribution of CSF correction factor values. As in the case for the CSF models, we use the average Monte Carlo correction factors from the τ models to correct the τ SED modeling results for those objects where we do not have IRAC data.

We also calculated AGN correction factors using the CB12 and Mar05 modeling. The correction values calculated for both the CB12 and Mar05 modeling are similar to those calculated using the BC03 modeling. While the mass and age correction values are smaller than than those derived from the BC03 models, they differ by less than one standard deviation of the distribution of BC03 correction factors. The corrected best-fit parameters are not significantly dependent on the

choice of model (e.g., BC03, CB12, or Mar05).

4.4.3 Full Sample Modeling Results

To fit the objects in our AGN sample lacking multiple IRAC photometric measurements, we used SPS-only models (using the same procedure described in §4.3.2, but without the addition of an AGN model). For each of these objects, we corrected the best-fit mass, SFR, age, and $E(B-V)_{SF}$ for the presence of an AGN using the average correction factors reported in the previous section, and list the best fit values (both uncorrected and corrected) in Table 4.4. The errors on the corrected parameters reflect both the errors derived using the Monte Carlo bootstrapping described in §4.3.4 as well as the standard deviation of the correction factors, given in Table 4.3. SED fits for each of these objects are shown in Figures 4.7 (CSF), and 4.8 (τ). The masses indicated in these figures are the corrected best-fit masses. The χ^2 values indicate that many of the objects are well fit by the SPS models. In the case of Q0000-C7 and Q1623-BX747, the SEDs were not well fit by either the CSF or τ models. For Q0000-C7, a blue $U-G$ color leads to models that are unable simultaneously to fit both the UV and near-IR portions of the SED. For Q1623-BX747, the J, K, and Channel 1 photometric data[3] show a decline to larger wavelengths, which is not reflected in the best-fit stellar models.

We explored how the choice of star-formation history influenced the best-fit stellar parameters in Figure 4.9. As demonstrated in Shapley et al. (2005b), there are no obvious systematic differences between the masses derived for the CSF and τ models. Figure 4.9 does indicate that the best-fit $E(B-V)_{SF}$, ages, and SFRs are lower (but consistent) for the τ models than for the CSF models, although the

[3]The data set for this object has coverage in one IRAC Channel, which is not enough to determine an AGN power-law; see §4.3.1.

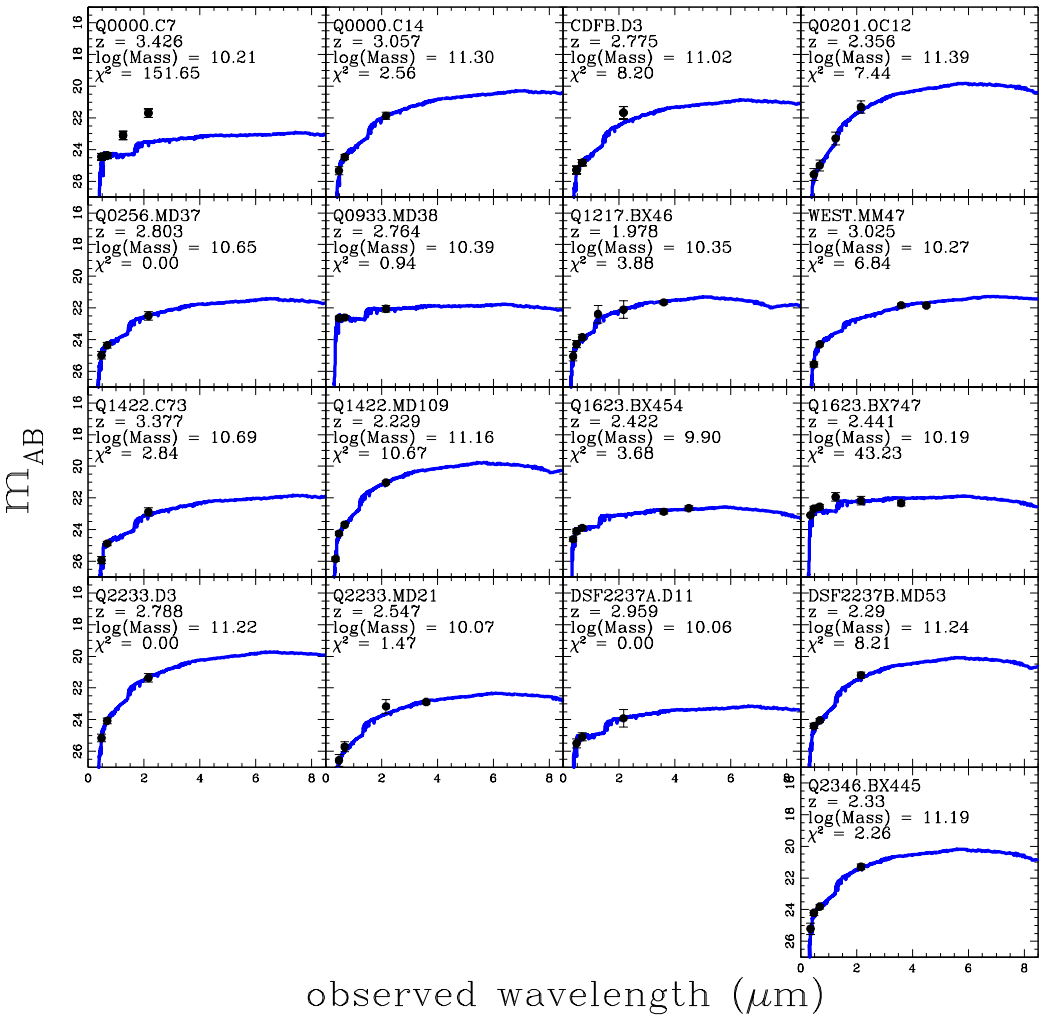

Figure 4.7 CSF SED models for the 17 objects that do not have IRAC data, or have IRAC data that is not sufficient for the purpose of discerning the presence of a power-law in the rest-frame near-IR. The models shown here are BC03 models, and do not include any contribution from an AGN. The best-fit mass for each object is given, corrected for the presence of an AGN as described in §4.4.2.

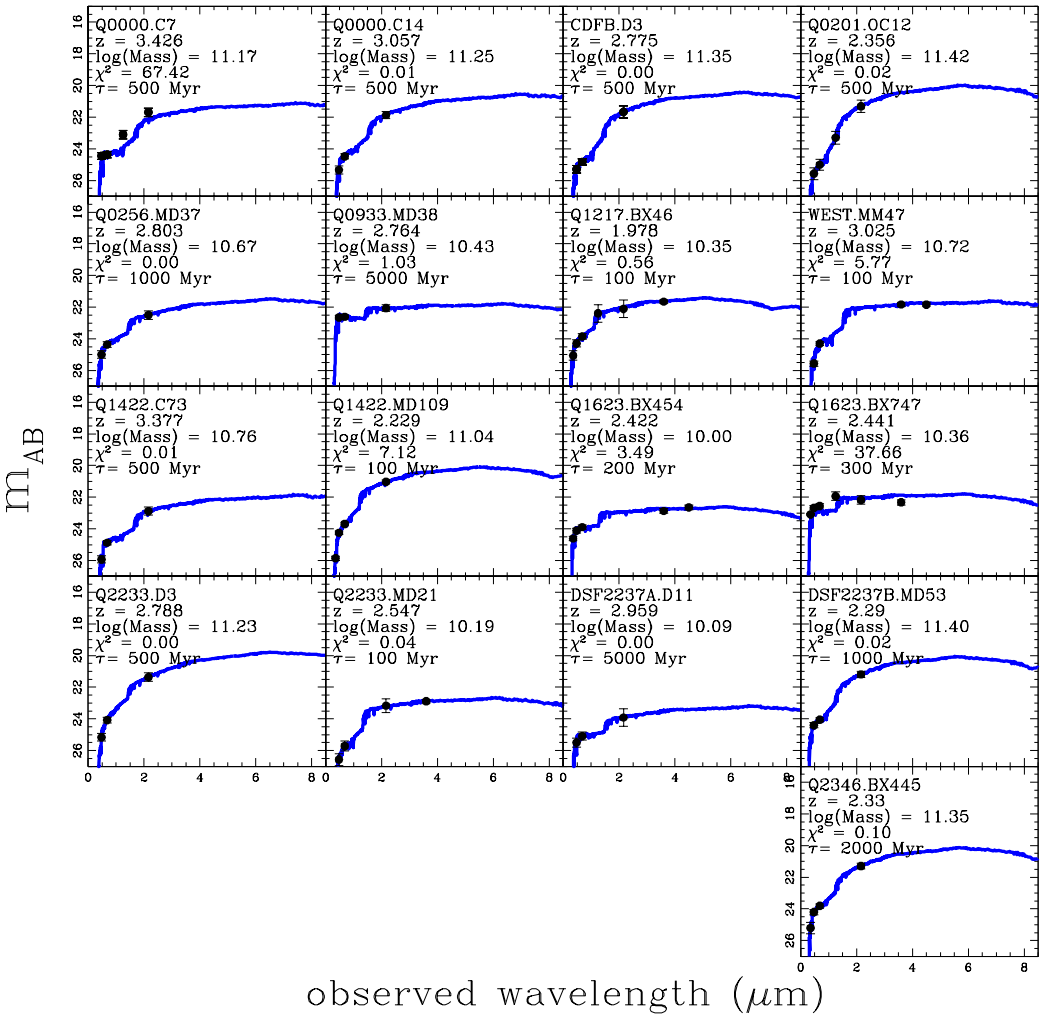

Figure 4.8 Exponentially-declining star-formation SED models for the 17 objects that do not have IRAC data, or have IRAC data that is not sufficient for the purpose of discerning the presence of a power-law in the rest-frame near-IR, with τ values as indicated. The models shown here are BC03 models, and do not include any contribution from an AGN. The best-fit mass for each object is given, corrected for the presence of an AGN as described in §4.4.2.

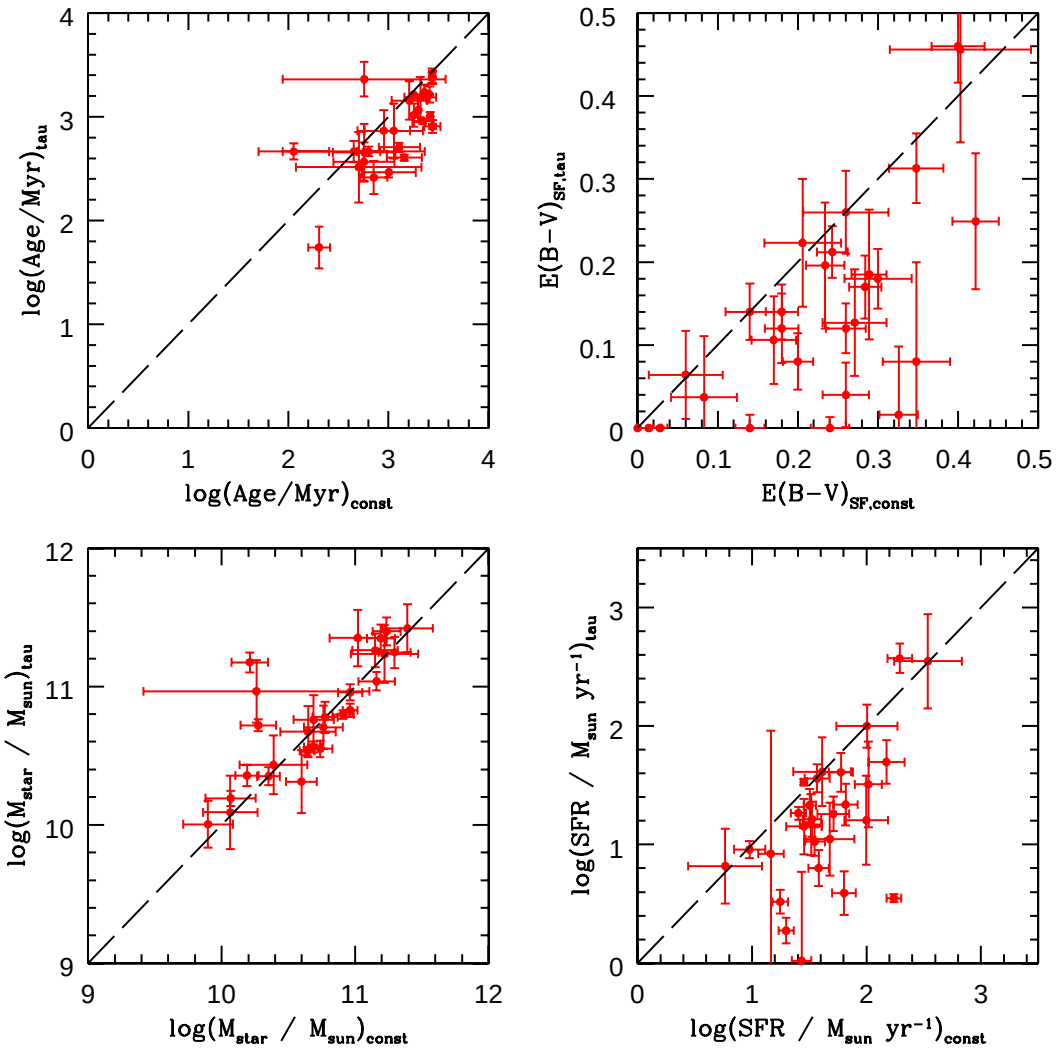

Figure 4.9 Comparison of inferred best-fit parameters for CSF models with those from the τ models (best τ), for the entire sample. The best-fit parameters for the non-IRAC objects have been corrected for the presence of an AGN. Dashed lines show the 1:1 trend between the parameters. The tight relation for stellar mass indicates that this parameter is independent of our choice of star-formation history. For the other parameters, the τ models yield lower values than those derived using CSF models.

error bars are large. As discussed in Reddy et al. (2012), a red UV continuum can be caused by an older stellar population, in particular in the case of an exponentially declining star-formation history. Such cases are accompanied by lower values of $E(B-V)_{SF}$ and therefore lower SFRs compared to the parameters from CSF modeling. In fact, a primary result from Reddy et al. is the indication that exponentially declining star-formation models result in SED-derived SFR values that are lower on average than those derived from a combination of UV and IR data[4]. At the same time, rising star-formation histories give SFRs that are similar to the SFRs derived from CSF models, along with older ages. In light of these trends, for the remainder of this chapter we will discuss only the CSF modeling results.

We summarize the full statistics for our sample of UV-selected AGNs in Figure 4.10. This figure shows histograms of the best-fit stellar parameters from SED modeling, assuming CSF histories. All 28 of the AGNs with fitted SEDs are represented in these histograms. The AGNs with IRAC coverage are plotted with their best-fit parameters from the dual-component modeling, and the AGNs without IRAC coverage are plotted with the corrected best-fit parameters, calculated as described in §4.4.3. The average values for the best-fit parameters and standard deviations are indicated on the figure with vertical lines. There is a large spread in $E(B-V)_{SF}$ values, with an average (median) of $\langle \mathrm{E(B-V)_{SF}} \rangle = 0.22\,(0.23) \pm 0.11$, and a range of $0.00 - 0.40$. The best-fit star-formation rates, with a mean of $\langle \mathrm{SFR} \rangle = 63\,(37) \pm 67$ $\mathrm{M_\odot\ yr^{-1}}$ similarly span a large range of values between 5.2 - 309 $\mathrm{M_\odot\ yr^{-1}}$. The most

[4]Reddy et al. derive the SFR_{IR+UV} by combining SFRs measured from photometry probing the rest-frame UV and IR. Observed-frame optical photometry is used to calculate the rest-frame UV (1700 Å) luminosity, and MIPS 24 μm photometry is used to calculate the rest-frame IR (8 μm) luminosity. These luminosities are converted to SFRs assuming typical galaxy ages and star-formation histories, and then combined to form SFR_{IR+UV}.

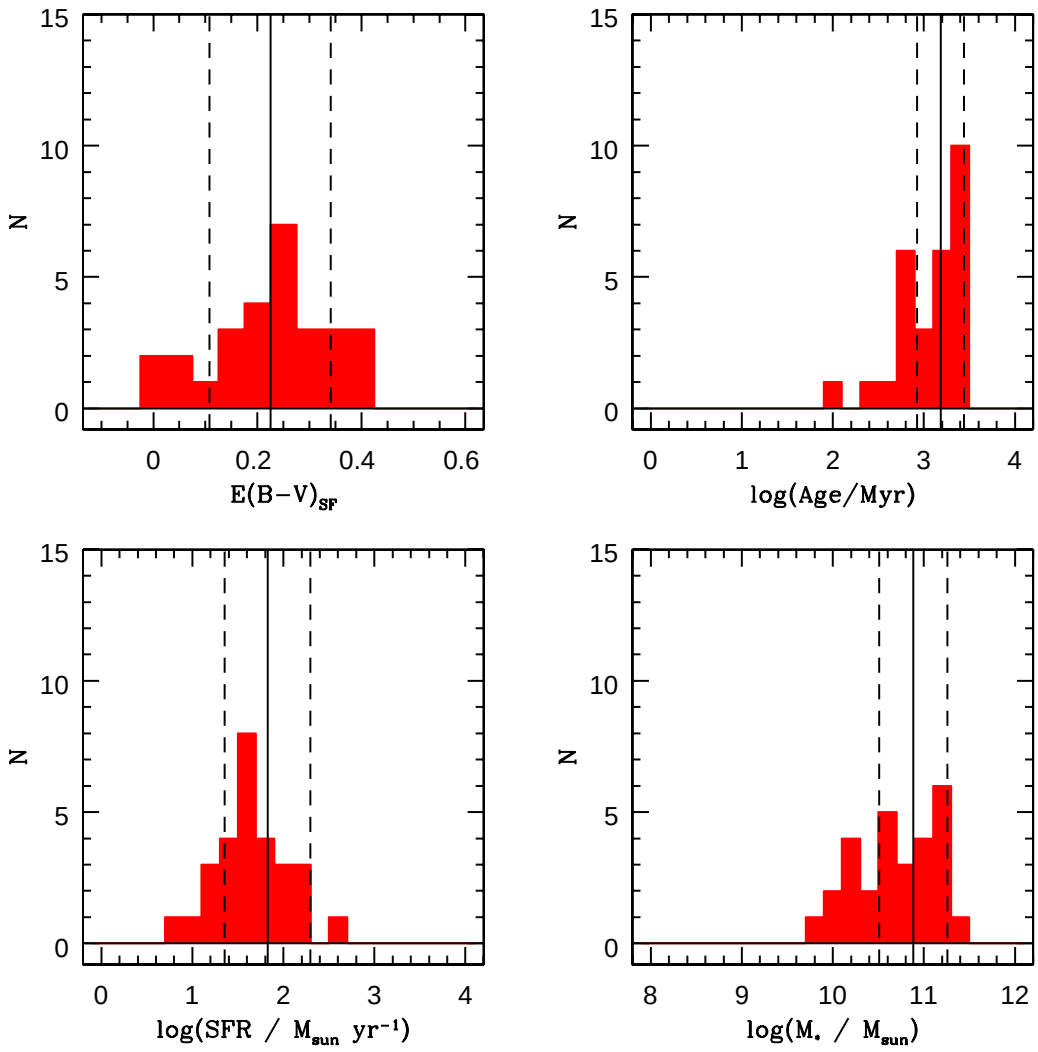

Figure 4.10 Histograms of best-fit stellar parameters for our sample of UV-Selected AGNs. These figures include both the IRAC AGNs, with parameters determined by our dual-component SF+AGN modeling as well as the non-IRAC AGNs, with parameters determined by SED modeling, and corrected for AGN emission. Vertical solid lines indicate the averages for each parameter, and the dashed lines indicate the standard deviation of the distributions. The average (median) values for the best-fit parameters are, $\langle \log(M_*/M_\odot) \rangle = 10.85\,(10.71) \pm 0.36$, $\langle \mathrm{SFR} \rangle = 63\,(37) \pm 67$ $M_\odot$ yr^{-1}, $\langle \log(\mathrm{Age/Myr}) \rangle = 3.19\,(3.18) \pm 0.26$, and $\langle E(B-V)_{SF} \rangle = 0.22\,(0.23) \pm 0.12$.

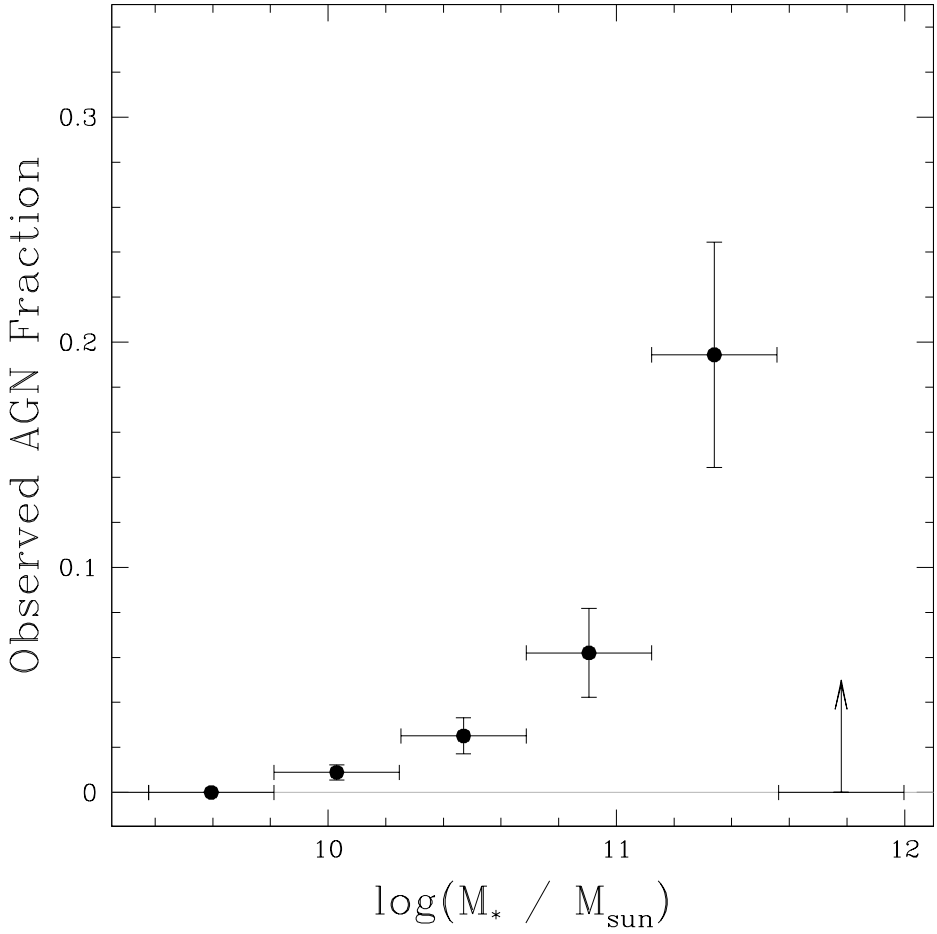

Figure 4.11 Observed AGN fraction as a function of stellar mass. The fractions were calculated by comparing the number of AGNs in a bin to the number of non-active galaxies in the full comparison sample. The AGN fraction rises steadily from $\log(M_*/M_\odot) = 10$ to $\log\ (M_*/M_\odot) = 11.5$, where it reaches a maximum of 19%. Uncertainties in observed AGN fraction were calculated by varying the masses of the AGNs by their mass errors and recalculating the AGN fractions for each bin. Horizontal error bars indicate the width of the bins. The AGN fraction in the highest-mass bin is plotted as a lower limit given the small-number statistics in this bin.

striking results, however, are the ages and masses for this sample. As suggested by the $\mathcal{R}-K$ colors shown in Figure 4.1, the best-fit masses are high: $\log(\langle \mathrm{M}_*/\mathrm{M}_\odot \rangle) = 10.85\,(10.71) \pm 0.36$. The AGNs that comprise the sample have old ages, with an average age of $\log(\langle \mathrm{age/Myr} \rangle) = 3.19\,(3.18) \pm 0.26$. These average stellar masses and ages are large compared to the typical values quoted for UV-selected non-active galaxies (Erb et al. 2006c; Shapley et al. 2001).

We can use the L_{bol} values derived from the dual-component fitting to estimate accretion rates for the IRAC AGNs. It should be noted that, as described in Section 4.4.1, the values of L_{bol} for our sample are potentially too high as a result of the overprediction of the observed MIPS flux, so the derived accretion rates and Eddington ratios should be viewed as upper limits. The accretion rate is described by the equation $\dot{M} = L_{bol}/\epsilon_{rad}c^2$, where we assume a standard accretion efficiency $\epsilon_{rad} = 0.1$. Using the values for L_{bol} from our fitting, we calculate an average (median) accretion rate for our sample of 0.3(0.1) $\mathrm{M}_\odot$ yr^{-1} with a range of $0.04 - 0.9$ $\mathrm{M}_\odot$ yr^{-1}. These rates are similar to the range of accretion rates found for optically selected Type I AGNs at $1 < z < 2.2$ from Merloni et al. (2010) (with a median accretion rate of $\dot{M} \sim 0.4 M_\odot\,\mathrm{yr}^{-1}$), and a factor of several lower than those estimated for X-ray selected Type II QSOs from Mainieri et al. (2011) (with a median accretion rate of $\dot{M} \sim 1$ $\mathrm{M}_\odot$ yr^{-1}).

The results from the SED fitting were also used to derive the properties of the central active galactic nucleus in each of our galaxies. Black hole masses are typically estimated in Type I AGNs using broad emission line widths and AGN continuum luminosities by setting $M_{BH} \propto v^2 r$, where r, the size of the AGN broad line region, is estimated from the continuum luminosity using the relationship between luminosity and BLR size based on reverberation mapping studies (e.g., Bentz et al. 2009; Barth et al. 2011). For our sample of Type II

AGNs, black hole masses were estimated using the $M_{BH} - M_{\rm bulge}$ scaling relation from Häring & Rix (2004):

$$\log(M_{BH}/M_{\odot}) = (8.20 \pm 0.10) + (1.12 \pm 0.06) \log\left(M_{bulge}/10^{11} M_{\odot}\right) \qquad (4.2)$$

For this calculation, we assumed that the stellar masses derived from our SED fitting roughly corresponded to the bulge masses for these objects. We adjusted the black hole masses for redshift evolution following the parameterization derived for Type I AGNs out to $z = 2.2$ in Merloni et al. (2010) (but see Lauer et al. 2007; Alexander et al. 2008a):

$$\Delta\log(M_{BH}/M_{*})(z) = (0.68 \pm 0.12) \log(1+z) \qquad (4.3)$$

The values for $\log(M_{BH})$ for our sample of AGNs have a range of $7.7 - 8.7$, with an average (median) of $\log(M_{BH}/M_{\odot})$= 8.36(8.29). The typical uncertainty in M_{BH} is $\sim 36\%$. For the eleven AGNs with IRAC data and L_{bol} measurements, we calculated Eddington ratios ($\lambda_{\rm Edd} = L_{bol}/L_{\rm Edd}$, where $L_{\rm Edd}/L_{\odot} = 3.2 \times 10^4\, M_{BH}/M_{\odot}$)[5]. The range is lower than that presented for X-ray selected Type II QSOs in Mainieri et al. (2011) (in which $\lambda_{\rm Edd}$ values were calculated in the same manner). The median Eddington ratio for our sample is 0.03 (with a typical uncertainty of $\sim 45\%$), while the median Eddington ratio for the Mainieri et al. sample is 0.1. Therefore the black holes hosted by the AGNs in our sample are accreting at significantly sub-Eddington rates.

[5]We calculated an Eddington ratio for Q1623-BX663 of 0.49, but this value is not meaningful due to the large calculated error on the stellar mass for this object.

4.5 AGN Host Galaxy Trends

In order to understand the impact of an AGN on its host galaxy, we must compare the UV-selected AGN host galaxy properties to those of a representative sample of non-active galaxies. As the AGNs studied here appear to be hosted by galaxies drawn from the same parent population as the non-AGN LBG sample (Steidel et al. 2002; Adelberger et al. 2005b), a comparison of the AGN and non-AGN host galaxy stellar populations in principle provides a means of testing the impact of AGN feedback. In this section, we examine a non-active sample of UV-selected galaxies, within which we isolate a sample matched in stellar mass for a controlled comparison between AGNs and non-AGNs (§4.5.1). Using these samples, we examine the relationship between SFR and stellar mass (§4.5.2), as well as rest-frame $U - V$ color and stellar mass (§4.5.3). Finally, making use of our unique spectroscopic data set, we search for connections between best-fit stellar population parameters and rest-frame UV spectroscopic features (§4.5.4).

4.5.1 Non-Active Comparison Sample

A careful examination of the demographics of the UV-selected AGNs requires the selection of a comparison sample of non-active galaxies. We assembled such a sample of UV-selected non-active galaxies, which have been spectroscopically confirmed at $z \sim 2 - 3$ (Steidel et al. 2003, 2004). This non-active comparison sample contains 1700 galaxies when limited to those in the same redshift range as our AGN sample ($1.98 < z < 3.33$). The non-AGN sample has an average redshift $\langle z \rangle = 2.55 \pm 0.36$, as compared to the average redshift for the AGN sample, $\langle z \rangle = 2.55 \pm 0.31$. We also require a comparison sample that spans a similar mass range to that of the AGN host galaxies, as recent results have demonstrated the importance of controlling for stellar mass in understanding the relationship

between AGNs and their host galaxies (Silverman et al. 2009; Xue et al. 2010; Aird et al. 2012). For each AGN in our sample, we chose six non-active sources at random, without any duplicate objects, and characterized by masses within the uncertainty of the selected AGN host mass. The size of the mass-matched sample was limited by the nature of the stellar mass distribution of the parent non-AGN sample, in which there are only six unique objects for each AGN at the massive end. Thus, the final mass-matched sample has 168 objects, as compared to the sample of 28 AGNs with stellar population fits. We will refer to the larger sample of non-AGNs as the "full non-active comparison sample," and the subsample matched in stellar mass as the "mass-matched comparison sample." The average mass for the mass-matched comparison sample is $\log(\langle \mathrm{M}_* \rangle) = 10.85 \pm 0.36$, which, by construction, is the same as for the AGNs. We modeled the photometry of non-AGNs using BC03 CSF SPS-only models as described in §4.4.3.

We used the full non-active comparison sample to calculate the observed fraction of AGNs as a function of stellar mass. In Figure 4.11, we show the results, with errors derived from the mass errors for the AGNs that went into each bin. These results indicate that the fraction of AGNs detected rises steadily as a function of stellar mass, peaking at 19% for $\log(M_*/M_\odot) = 11.25$. Above this mass, the number of non-AGNs in the full non-active sample drops to only 4 objects, and the low observed AGN fraction is most likely due to small number statistics rather than a lack of very high-mass AGN hosts. We observe AGNs predominantly in higher mass galaxies, although as described in §4.6, this trend likely reflects our increasing incompleteness towards lower stellar masses. Accordingly, these results may indicate that at least 19% of UV-selected star-forming galaxies to $\mathcal{R}$= 25.5 host actively accreting black holes. We return to this discussion in §4.6.

4.5.2 SFR - Stellar Mass Relation

Star-forming galaxies follow a tight positive correlation between SFR and stellar mass, which has been observed locally (Brinchmann et al. 2004), as well as out to intermediate (Noeske et al. 2007; Elbaz et al. 2007, $z \sim 1$) and high redshifts (Reddy et al. 2006a; Daddi et al. 2007; Reddy et al. 2012, $z \sim 2-3$). This trend is used to argue for the smooth star-formation histories of the majority of star-forming galaxies in the universe (Noeske et al. 2007; Daddi et al. 2007). This relation is characterized by roughly the same slope across a wide redshift range (although results from Noeske et al. (2007) indicate a non-linear relation for star-forming galaxies at intermediate redshifts), while the normalization has decreased by an order of magnitude from $z \sim 2$, reflecting the overall decrease in the global star-formation rate density with time (Daddi et al. 2007). We plot the SFR and stellar mass for our AGNs with red points in Figure 4.12. The errors on the points reflect the Monte Carlo errors from the SED modeling as well as the errors on the correction factors for the objects without IRAC data. We find a positive correlation for the AGN host galaxies with a best-fit slope of 0.20 ± 0.04, shallower than derived for non-AGNs.

We compared the AGN population to our non-active comparison samples in order to examine the origin of the shallow slope. In Figure 4.12 we plot log(SFR) against log(M_*) for the non-active comparison sample in grey and for the mass-matched comparison sample in blue. The non-active galaxies display a positive trend with a large scatter. The ridge of points seen at the high SFR side of the relation is an artifact of imposing a minimum age of $t_{SF} = 50$ Myr on our fits. Given the linear relation between M_* and SFR for CSF models, all points with best-fit ages of $t_{SF} = 50$ Myr will fall on a line of constant M_*/SFR. We note that the sharp cutoff for galaxies with low SFRs at a fixed stellar mass is due to the

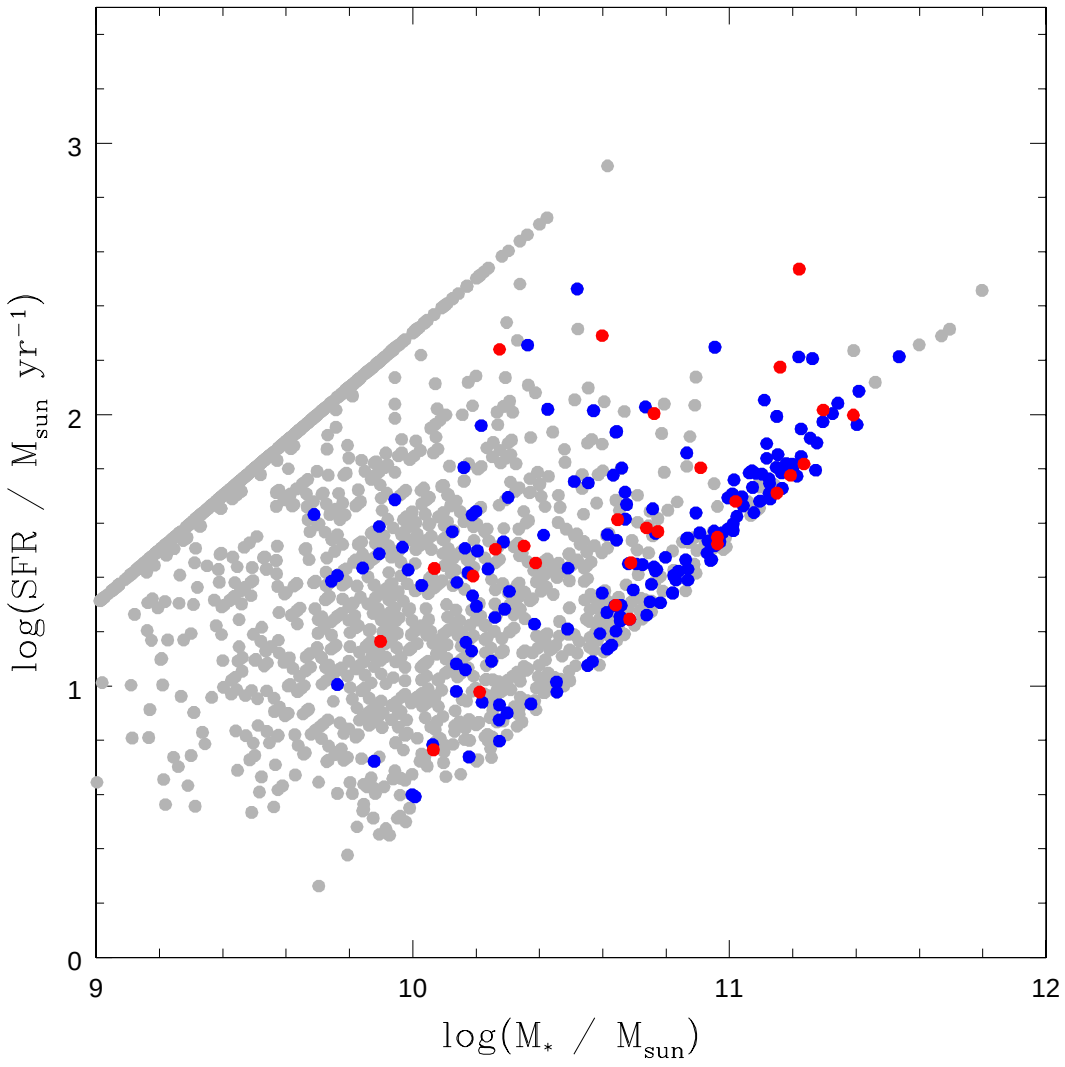

Figure 4.12 SFR vs. stellar mass for the AGNs (red points) along with the full comparison sample of non-active star-forming $UG\mathcal{R}$-selected galaxies (grey points) and the mass-matched comparison sample (blue points). AGNs are found at the high mass end of the full relation. However, both AGNs and mass-matched non-AGNs span a similar range of SFR values at a given stellar mass. The ridge of grey points at high SFRs is a result of imposing a lower age limit of $t_{SF} > 50$ Myr (see §4.5.2).

restriction on the maximum allowed age, which must be younger than the age of the universe at the redshift of each object. The lack of points at the low-mass, low-SFR end is due to a bias in the $UG\mathcal{R}$ selection technique towards selecting those galaxies with the highest SFR at a given mass, causing the slope of the relation to become shallower at the low-mass end (Reddy et al. 2012). At the high-mass end, the shallow slope reported for the AGNs is similar to what is observed among the non-active sources. Above $\log(M_*/M_\odot) = 10.5$, the $UG\mathcal{R}$ selection is biased against selecting those galaxies with the largest SFR values at a given stellar mass, as such objects will have large amounts of dust extinction and red $UG\mathcal{R}$ colors, placing them outside the $UG\mathcal{R}$ selection window. This bias tends to flatten the $\log(M_*) - \log(\mathrm{SFR})$ relation at the high-mass end. Of particular interest, the SFR values spanned by the UV-selected AGN sample ($\langle \mathrm{SFR} \rangle = 63\,(37) \pm 67$ $\mathrm{M}_\odot$ yr^{-1}) are similar to those in the mass-matched comparison sample, where the average (median) SFR is $\langle \mathrm{SFR} \rangle = 45\,(35) \pm 38$ $\mathrm{M}_\odot$ yr^{-1}.

The above trends can also be considered in terms of the specific star-formation rate ($\mathrm{sSFR} = \mathrm{SFR}/M_*$, which, for CSF models is equal to $1/t_{SF}$). We calculated an average (median) $\mathrm{sSFR} = 1.36\,(0.66)$ Gyr^{-1} for the AGN hosts, with a range of sSFR: $0.4 - 9.2$ Gyr^{-1}, indicating active star-formation. We find that the sSFR values for our mass-matched non-active sample span a similar range, with an average (median) $\mathrm{sSFR} = 1.10\,(0.47)$ Gyr^{-1}, and a range of sSFR: $0.33 - 8.78$ Gyr^{-1}. The sSFR values for our Type II UV-selected AGNs are similar to those obtained for a sample of X-ray selected Type II QSOs with active star-formation at $z \sim 2$ from Mainieri et al. (2011) ($\mathrm{sSFR} = 0.8 - 3$ Gyr^{-1} for the high-mass objects at $z \sim 2$). These authors found consistent evolution for the sSFRs of the QSO host galaxies and those of non-active BzK-selected star-forming galaxies from Pannella et al. (2009). Similarly, once we control for stellar mass, the SFR and sSFRs of AGNs are indistinguishable from those of non-AGNs.

4.5.3 Color - Stellar Mass Relation

A basic probe of the demographics of AGN activity is provided by the optical color magnitude diagram, which can also be cast in terms of galaxy color as a function of stellar mass. In the local universe, galaxies display a bimodality in their observed colors, separating into a population of lower-mass blue star-forming galaxies and a sequence of higher-mass red quiescent galaxies (e.g., Baldry et al. 2004). This same bimodality has been observed in galaxies at intermediate ($z \sim 1$, Bell et al. 2004) and higher redshifts ($z \sim 2$, Cassata et al. 2008; Kriek et al. 2008; Williams et al. 2009). The existence of these two populations out to $z \sim 2$ suggests that the mechanisms driving the evolution of galaxies from blue to red began early in the history of the universe. AGNs have been proposed as a potential driver of the evolution in the color-mass relation by providing energy to the ISM that quenches star-formation, causing a galaxy to transition from the blue population of galaxies to the red (Croton et al. 2006; Hopkins et al. 2008). In support of this scenario, X-ray and optically selected AGNs at low and intermediate redshifts are found to reside in galaxies in the transition region in optical color space between the blue and red sequences (Nandra et al. 2007; Salim et al. 2007; Coil et al. 2009; Hickox et al. 2009; Schawinski et al. 2010). However, recent AGN host galaxy studies indicate that both mass selection and dust obscuration effects may bias conclusions about the role of AGNs in galaxy evolution. Silverman et al. (2008) demonstrated that a sample of X-ray and mass selected AGNs were preferentially found in galaxies with ongoing star formation and blue optical colors. Similarly, Xue et al. (2010), using a mass-matched sample of X-ray selected AGNs, showed that the fraction of AGNs remains constant as a function of color. Aird et al. (2012) found that, when stellar-mass selection effects are taken into account, AGN hosts are preferentially found in galaxies with blue

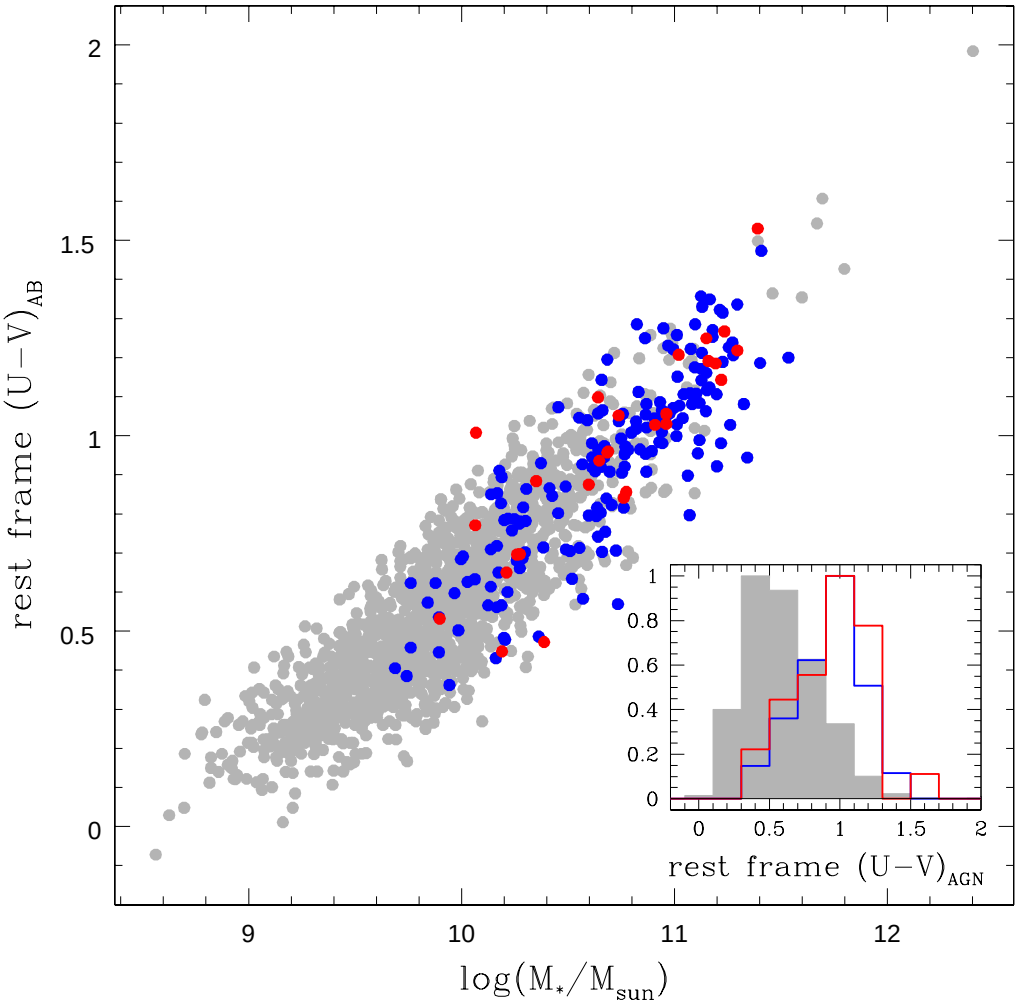

Figure 4.13 Rest-frame $U-V$ color vs. stellar mass. The rest-frame $U-V$ colors are calculated from the best-fit SEDs as described in §4.5.3. AGNs are indicated in red, the non-active comparison sample in grey, and the mass-matched sample in blue. The objects plotted were initially selected by their observed UGR colors to be strongly star forming, which leads to the tight blue sequence (Labbé et al. 2007). The UV-selected AGN hosts are located in a similar color-mass space to the mass-matched sample, but are absent below $\log(M_*/M_\odot) \sim 10$. In the inset, we plot the histograms of $U-V_{rest}$ for the three samples, using the same colors. These histograms have been normalized to have the same peak values for clarity.

and green optical colors, but can exist in galaxies of any color. Cardamone et al. (2010) corrected AGN host colors for the presence of dust, revealing that AGN hosts cleanly separate into a population of young, dusty, star-forming galaxies, and older, red, passive galaxies.

We used the results from AGN SED modeling (§4.4) to examine the positions of the UV-selected AGNs in color-mass space. We calculated rest-frame colors of AGN host galaxies using the best-fit SPS models, along with the Johnson UBV transmission curves from Maíz Apellániz (2006). The estimation of the rest-frame colors requires an assumption that the models accurately represent the stellar populations in the rest-frame UV and optical, which is supported by the good SPS+AGN dual-component modeling fits to the IRAC AGNs. In order to compare the AGN host colors to those of the non-active UV-selected star-forming galaxies, we also calculated the rest-frame colors for the non-active comparison samples described in the previous section. The $(U-V)_{rest,AB}$ vs. M_* relation is shown in Figure 4.13, where the AGNs are plotted in red and the non-active galaxies in grey. The non-AGN hosts follow a trend where the most massive galaxies are also the reddest, similar to the blue sequence observed for galaxies out to $z \sim 3$ (Labbé et al. 2007). The sample of UV-selected AGNs are preferentially hosted by high-mass galaxies and these objects are found to span the same range of $(U-V)_{rest,AB}$ colors as those of the non-AGNs in the mass-matched sample. The average (median) color for the AGN sample is $(U-V)_{rest,AB} = 0.9\,(0.9) \pm 0.2$, while for the mass-matched sample, it is $(U-V)_{rest,AB} = 1.0\,(1.0) \pm 0.3$ (inset of Figure 4.13). Xue et al. (2010), Mainieri et al. (2011), and Aird et al. (2012) found similar results for the demographics of their AGN host galaxy samples. All of these results demonstrate the importance of mass-selection in the comparison of AGN hosts to non-active galaxies. The redder colors of the AGN hosts do not indicate a lack of ongoing star-formation, but rather, more dust and perhaps older

stellar populations. The UV-selected AGNs were initially chosen based on their $UG\mathcal{R}$ colors to be star-forming, and, as discussed in the previous section, we found that all of the AGNs have sSFR > 0.4 Gyr^{-1}, indicating active star formation. Figure 4.14 demonstrates that the SFR, age, color, and dust extinction properties are similar between the AGN sample and the mass-matched comparison sample. The presence of an AGN does not seem to affect the global properties of their host galaxies in comparison to the mass-matched sample. The lack of UV-selected AGNs in host galaxies below $10^{10} M_{\odot}$ will be discussed in §4.6.

We can use the mass-matched sample to explore the $\mathcal{R}-K$ distribution shown in Figure 4.1 in more detail. The fact that AGNs occupy the red portion of this distribution can be explained by their massive host galaxies, and the relation between rest-UV/optical color and stellar mass. The average $\mathcal{R}-K$ color for the UV-selected AGN sample is 4.0 ± 0.7, while for the mass-matched sample, the average is 3.6 ± 0.6. We used the results from our dual-component modeling to estimate that the presence of an AGN caused the $\mathcal{R}-K$ color to be 0.3 mag redder than it would be in the absence of an AGN. If we subtract this difference from those AGNs where we did not use dual-component modeling, the average UV-selected AGN host galaxy $\mathcal{R}-K$ color becomes 3.6 ± 0.7. Therefore, at fixed stellar mass, the AGN host galaxies are typical in terms of their UV/optical (i.e., $\mathcal{R}-K$) colors.

4.5.4 UV Composite Spectra

In §3.5, we investigated the UV spectral properties for our sample of UV-selected AGNs. The UV portion of the galaxy spectrum contains strong emission and absorption features that we used to probe both AGN and outflow activity. At $z \sim 2-3$, the individual UV spectra have low S/N, and, to overcome this limitation,

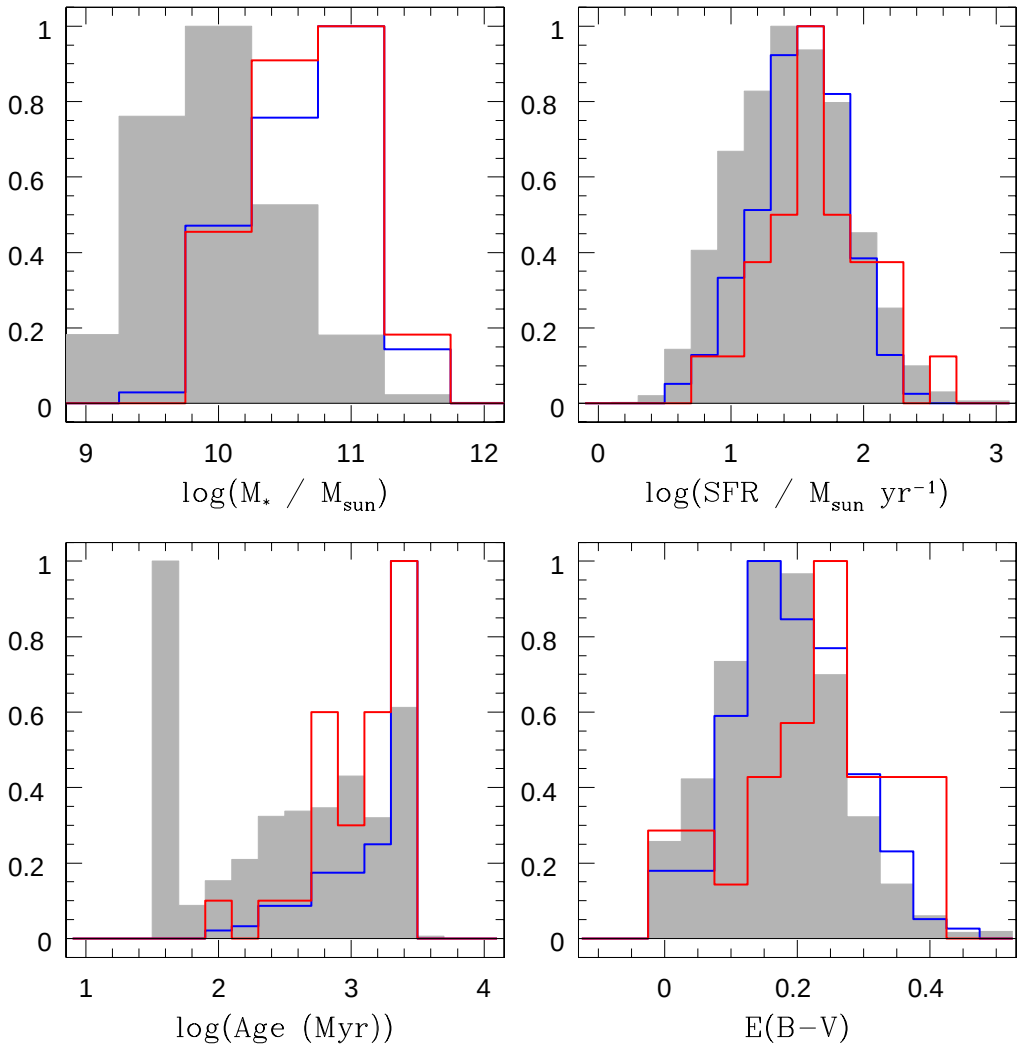

Figure 4.14 Histograms of best-fit stellar population parameters. Distributions for AGNs are shown in red, those for the full non-AGN sample in grey, and for the mass-matched sample in blue. These histograms have been normalized to have the same peak values for clarity. The AGNs have similar properties to those of the mass-matched sample on average. The AGNs have a slightly higher average extinction ($\langle E(B-V)_{SF,AGN}\rangle = 0.22 \pm 0.11$) than the mass-matched sample ($\langle E(B-V)_{SF,MM}\rangle = 0.20 \pm 0.09$).

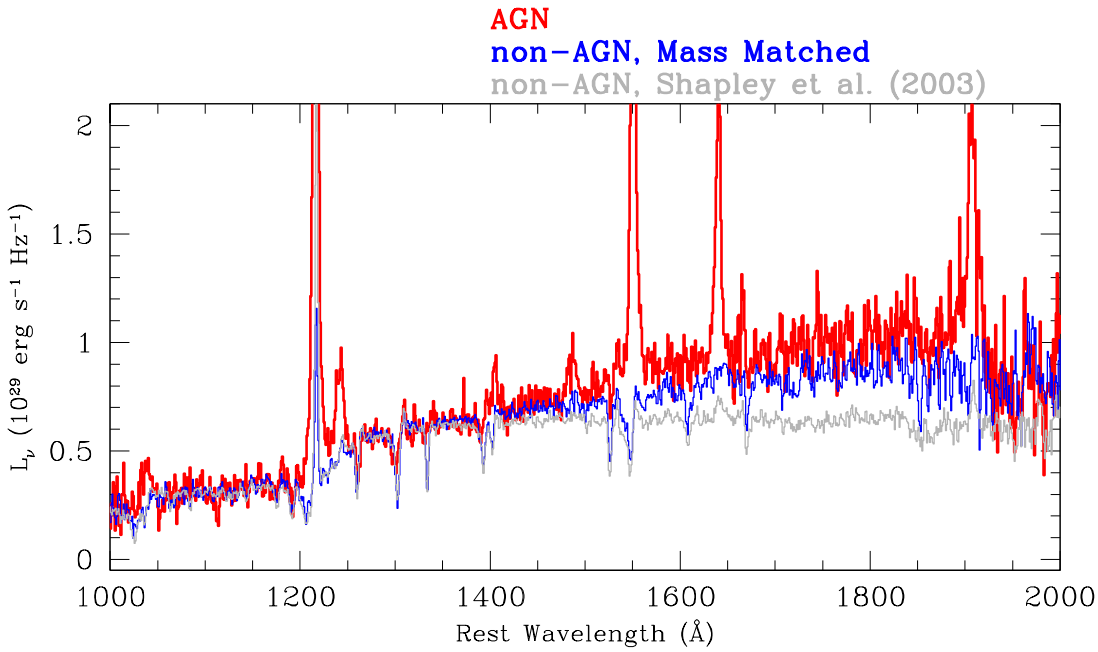

Figure 4.15 The UV composite spectra for the UV-selected active and non-active samples. We plot the AGN composite in red, the mass-matched composite in blue, and the non-AGN LBG composite from Shapley et al. (2003) in grey. The power-law slope, β, as measured directly from the AGN spectrum, is $\beta = -0.3 \pm 0.2$, while for the mass-matched composite, the slope is $\beta = -0.7 \pm 0.1$. The similar slopes may be due to the similar levels of dust extinction in these two samples. The mass-matched composite shows a much redder slope than the full non-active composite from Shapley et al. (2003), which has a measured power-law slope of $\beta = -1.49$. These spectra confirm our conclusion from the photometry that the AGN UV continuum is primarily due to stellar light, rather than AGN emission.

we averaged the individual spectra to create higher S/N composite spectra. One of the most striking results from Chapter 3 consisted of the extremely red rest-frame UV continuum of the AGN composite spectrum, relative to that of the $z \sim 3$ non-AGN composite spectrum from Shapley et al. (2003). We can now use the results from SED modeling to investigate the physical origin of this difference. Furthermore, we can analyze how the rest-frame UV spectroscopic properties of AGN vary as a function of stellar population properties.

For this analysis, we created composite spectra from sub-samples of AGNs separated by the host galaxy properties. Due to the small sample size of objects with SED fitting parameters (28 objects) and our desire to maximize the S/N of the resulting subsample composite spectra, we simply divided the sample in half for these analyses. We constructed composite spectra following the methodology of §3.3. Each individual spectrum was first shifted to the rest frame using an estimate of the systemic redshift from HeIIλ1640. We converted each spectrum from the units of flux density to those of luminosity density, scaled each one to a common median in the wavelength range of $1250 - 1380$ Å, and combined the spectra, with the four highest and lowest outliers removed at each wavelength.

In order to investigate the red UV continuum of the AGN composite spectrum, we consider the properties of the mass-matched comparison sample. Using existing rest-frame UV spectroscopy for the full non-active sample, we created a UV composite spectrum from the objects in the mass-matched comparison sample. We used the same method to create this non-AGN composite as for the AGN composite. In Figure 4.15, we compare the full AGN composite spectrum to the mass-matched non-AGN composite as well as the non-AGN LBG composite at $z \sim 3$ from Shapley et al. (2003). The UV continuum shape is commonly described by β, the slope of a power law of the form $L_\lambda \propto \lambda^\beta$, which is fit to

the continuum. For the AGN composite spectrum, $\beta = -0.3 \pm 0.2$ (See §3.4.4), which is a much redder slope compared to the LBG composite from Shapley et al. (2003), where $\beta = -1.5$. We measure a value of $\beta = -0.7 \pm 0.1$ for the mass-matched composite, redder than the full non-AGN composite[6]. The comparably red slopes of the AGN and mass-matched UV composite spectra (in contrast to the significantly bluer slope of the total LBG composite from Shapley et al. 2003) confirms that the underlying UV continuum seen for the AGN sample is predominantly due to stellar light, and not AGN emission. Furthermore, since scattered light from a buried AGN would have an intrinsically *bluer* rest-frame UV spectrum than that of a stellar population (Zakamska et al. 2006), the slight difference in UV slopes can not be attributed to AGN emission. We can naturally explain the redder slopes observed in the high-mass active and inactive samples by looking at the distributions of reddening for each subsample. In Figure 4.14, we show histograms of the best-fit properties of the AGN sample along with the full non-AGN and mass-matched comparison samples. As discussed in §4.4.3, $\langle E(B-V)_{SF,AGN} \rangle = 0.22 \pm 0.11$ for the AGNs, while for the mass-matched comparison sample, $\langle E(B-V)_{SF,MM} \rangle = 0.20 \pm 0.09$. For the sample of non-AGNs at $z \sim 3$ from Shapley et al. (2003), the estimated $\langle E(B-V)_{SF,Shapley} \rangle = 0.15 \pm 0.09$[7]. The errors on these values represent the standard deviation of the distribution of values. The average extinction values for the AGN and mass-matched samples are significantly different from the value for the non-AGNs in Shapley et al. (2003), reflecting what is observed for the UV power-law slopes.

[6]Errors on the β values were calculated following a bootstrap technique where 500 fake composite spectra were constructed from the sample of actual spectra and we measured β for each fake composite. The error represents the standard deviation of the distribution of measured β values

[7]These $E(B-V)_{SF}$ values were calculated directly from the UV photometry as described in Shapley et al. (2003).

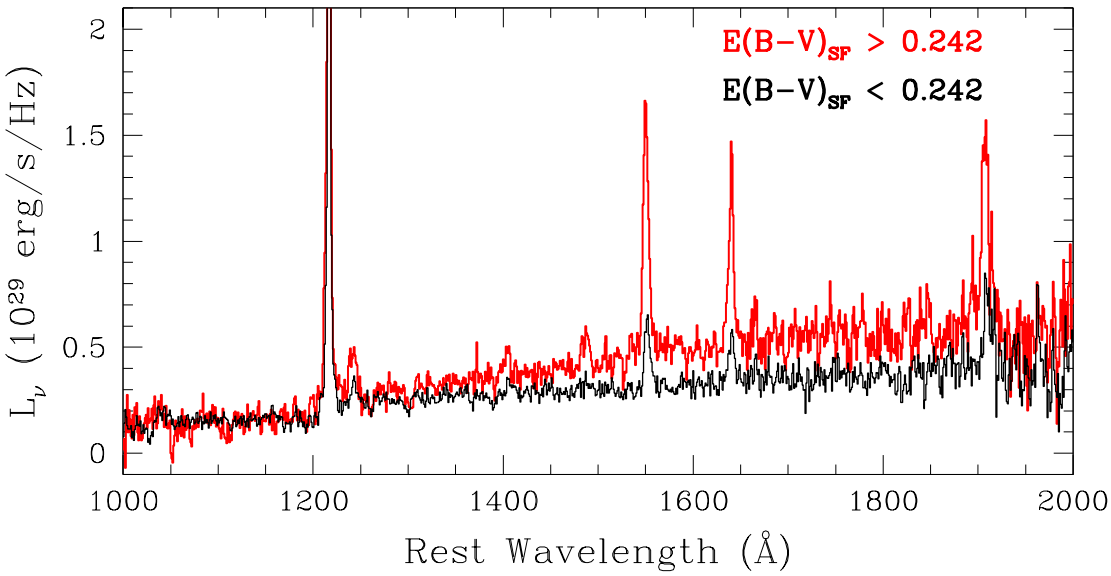

Figure 4.16 Comparison of the continuum slope between the AGN composite spectrum for objects separated by $E(B-V)_{SF}$. The composite with larger $E(B-V)_{SF}$ is significantly redder than the smaller $E(B-V)_{SF}$ composite. The UV power-law slope β, as measured directly from the $E(B-V)_{SF} > 0.242$ spectrum, is $\beta = 0.0 \pm 0.3$, while for the $E(B-V)_{SF} < 0.242$ spectrum, $\beta = -1.0 \pm 0.3$. The large average $E(B-V)_{SF}$ for our AGN sample indicated in Figure 4.10 leads to the red UV continuum seen in AGN UV composite spectrum.

We further investigated the role that extinction plays in the slope of the UV spectrum by separating our objects into two bins based on $E(B-V)_{SF}$. The AGNs were separated at the median extinction from our fits, $E(B-V)_{SF} = 0.242$, and both composites are plotted in Figure 4.16. In red, we plot the composite spectrum for those objects with $E(B-V)_{SF} > 0.242$, and in black, the composite spectrum for those objects with $E(B-V)_{SF} < 0.242$. The composite spectrum for objects with higher $E(B-V)_{SF}$ is much redder, with $\beta = 0.0 \pm 0.3$. For the AGNs with lower $E(B-V)_{SF}$, the composite spectrum has $\beta = -1.0 \pm$

0.3. This trend is also seen in the mass-matched comparison sample separated by $E(B-V)_{SF}$, where the high-extinction mass-matched composite is redder, with $\beta = -0.4 \pm 0.2$, while the low-extinction mass-matched composite has $\beta = -1.1 \pm 0.1$. The slope of the low-extinction mass-matched composite spectrum ($\langle E(B-V)_{SF,MM} \rangle = 0.12 \pm 0.05$) is similar to the slope of the low-extinction AGN composite ($\langle E(B-V)_{SF,AGN} \rangle = 0.13 \pm 0.08$), which provides more evidence that dust extinction significantly modulates the UV power-law slope in our sample of AGNs.

We also consider how rest-frame UV AGN spectroscopic properties vary with stellar mass. The continuum normalized composite spectra for the AGNs separated by stellar mass are shown in Figure 4.17[8]. We measured the luminosities and EW for the strongest UV emission lines (HI Lyα, NVλ1240, CIVλ1549, and HeIIλ1640) in both the high-mass and low-mass composites. Uncertainties on these values were calculated following a bootstrap technique where 500 fake composite spectra were constructed from the sample of spectra used in creating the real composite spectra (see Shapley et al. 2003, §3.4.1). The results are shown in Table 4.5. We find that the EW values for the CIV and HeII emission lines are stronger in the high-mass composite than the low mass composite, while the NV and Lyα lines have statistically equivalent EW values. The EW of an emission line was calculated by integrating the luminosity in the line and dividing by the average of the luminosity density of the continuum on either side of the line. As these are Type II AGNs, the observed UV continuum arises from stellar emission, which is supported by the similar UV slopes seen in the AGN UV composite and the mass-matched UV composite. We find that the emission lines used to identify the presence of an AGN (CIV and HeII) are stronger in the high-mass composite

[8]Given the correlation between stellar mass and $E(B-V)_{SF}$, a separation by stellar mass divides the sample in almost the same way as a separation by $E(B-V)_{SF}$.

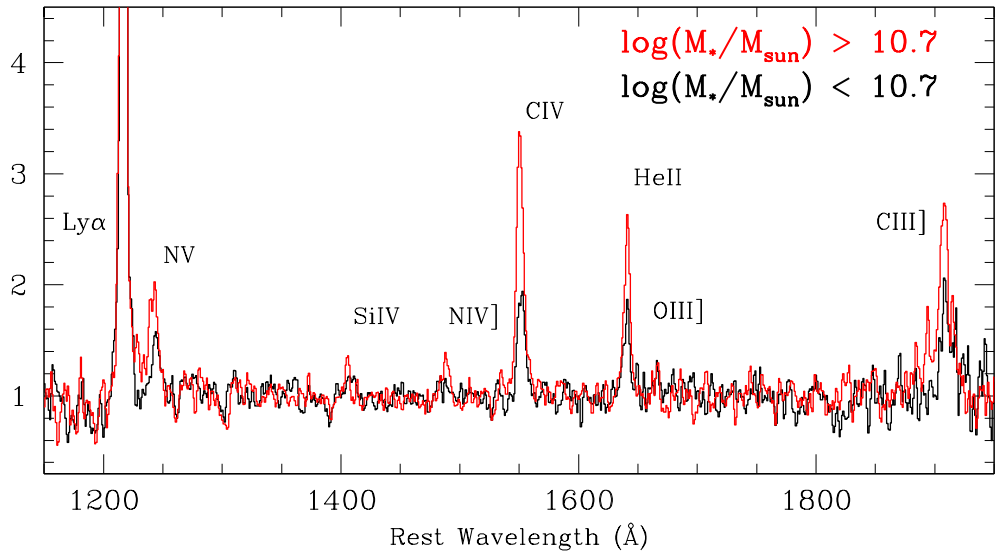

Figure 4.17 Comparison of the strong emission lines between the AGN composite spectrum for objects separated by M_*. These spectra are continuum normalized to better illustrate the line EW differences. The high-mass composite spectrum is shown in red, while the low-mass composite spectrum is shown in black. The AGN emission lines of NV, CIV, HeII are stronger in the high-mass composite, with specific EW value given in Table 4.5.

spectrum. This trend of decreasing high-ionization EW with decreasing stellar mass may explain the dearth of low-mass UV-selected AGNs in our sample. We will explore the origins and implications for this trend in the following section.

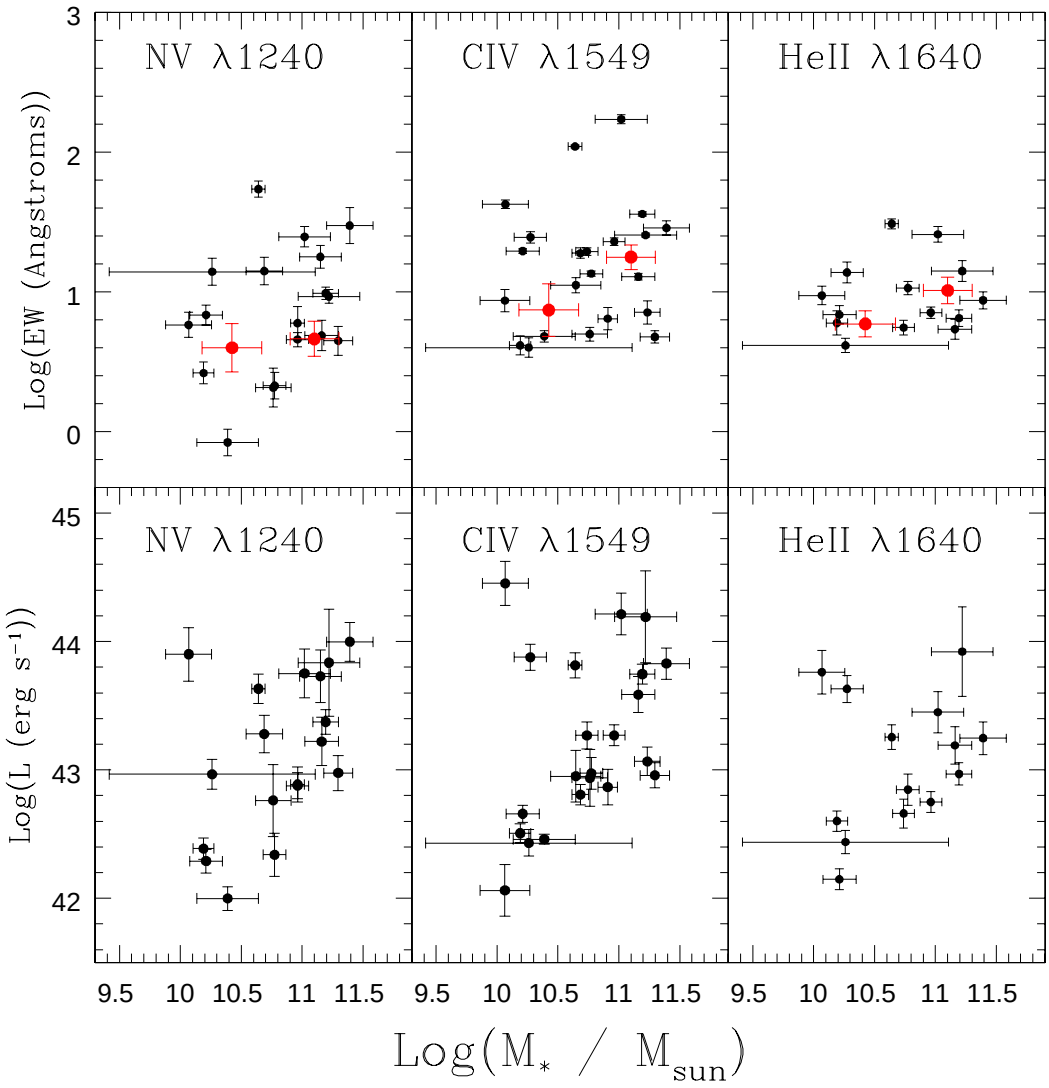

Figure 4.18 EW (top three panels) and line luminosities (bottom three panels) for the strong UV emission lines in the AGN sample plotted against stellar mass. The black points are measured from the individual AGN spectra, and the red points in the EW plots represent values measured from the composite spectra as separated into two mass bins. For CIV and HeII, the points from the composite spectra indicate that the EW values are higher in the high mass composites. The luminosity values are corrected for dust extinction using the $E(B-V)_{SF}$ values from the SED fitting, and show a positive trend with mass, such that the higher mass galaxies have intrinsically brighter emission lines.

4.6 The Demographics of UV-selected AGNs at $z \sim 2-3$

We find an apparent segregation of AGN hosts at the high-mass end of the $z \sim 2-3$ galaxy population, as shown in Figures 4.12, 4.13, and 4.14. At lower-redshift ($z \sim 0.2-1.0$), the preferential incidence of X-ray-selected AGNs in higher-mass host galaxies is explained by Aird et al. (2012) as a selection effect, arising from a constant Eddington-ratio distribution and an X-ray flux limit. For a fixed Eddington ratio, AGNs in higher-mass galaxies have higher AGN luminosities (assuming a linear correlation between M_{BH} and M_{host}), and are therefore easier to detect. We use the extinction-corrected CIV luminosity as a proxy for AGN luminosity. Without direct X-ray or UV-optical continuum measurements, we must resort to less direct measures of luminosity for our obscured sample. Here we assume that the extinction-corrected CIV luminosity from the narrow-line region traces the accretion rate onto the black hole, as shown for narrow AGN optical emission lines (e.g., [OIII]λ5007) by Yee (1980) and Shuder (1981). With this assumption, we can apply the arguments from Aird et al. (2012) to our higher-redshift AGN sample, in order to investigate the cause of the apparent segregation in host galaxy stellar mass, and the detectability of AGN activity in lower-mass host galaxies. The lack of detected AGN activity in the low-mass UV-selected sample may be explained simply as a similar selection effect. That is, if black holes are smaller on average in low-mass galaxies, then their emission may fall below our detection threshold.

In the first place, we must establish empirically how emission-line EW and luminosity vary with stellar mass. The EW of an emission feature depends on both the intrinsic luminosity of the feature as well as the continuum luminosity. In Figure 4.18, we plot emission line EW against stellar mass for objects in our AGN sample. The NV, CIV, and HeII emission lines were measured from indi-

vidual spectra. In the top panels, we also plot the EW values measured from the composite spectra separated by mass. For the luminosity values, the individual spectra were flux-normalized such that the 1500 Å continuum luminosity matched the estimated rest-frame 1500 Å luminosity calculated from G and/or $\mathcal{R}$-band photometry for these objects. We then corrected each spectrum for extinction under the assumption that the stellar extinction estimated from the SED modeling applies to the narrow-line region. The NV and CIV emission line luminosities shown in Figure 4.18 demonstrate a weak trend with mass (Spearman's rank coefficients of 0.45 and 0.43 for the NV and CIV distributions respectively, corresponding to $\sim 2\sigma$ significance) such that the higher mass galaxies have higher luminosity emission lines[9].

Of the three emission lines used to select an AGN, CIV is typically the strongest, and we focus on that line in order to test the detectability of lower-mass AGNs. As discussed above, results from Aird et al. (2012) suggest that X-ray selected AGNs out to $z \sim 1$ have a universal distribution of Eddington ratios independent of host galaxy stellar mass. If AGNs at $z \sim 2-3$ are also characterized by a universal Eddington ratio distribution, and, furthermore, if M_{BH} and M_* are correlated as in the low-redshift universe, galaxies with higher stellar masses should exhibit AGN-related emission lines with larger luminosities (i.e., a constant ratio of L_{CIV}/M_*). The assumption of a constant L_{CIV}/M_* ratio is supported by the observed correlation between CIV luminosity and stellar mass in our sample. Using this assumption along with the assumption of the correlation between M_{BH} and M_*, we can test our ability to detect UV-selected AGNs in host galaxies with a given $\log(M_*/M_\odot)$.

[9]This trend is strengthened considerably by removing Q2233-MD21, which has very luminous emission lines and a low best-fit stellar mass. The Spearman rank coefficients rise to 0.68 and 0.62, for the NV and CIV distributions respectively, corresponding to $\sim 3\sigma$ significance.

Since AGNs are easiest to find at the highest stellar masses, we use the spectra of the highest-mass AGNs in our sample to estimate the ratio of L_{CIV}/M_*. We averaged the CIV line luminosities for all AGNs in our sample with $\log(M_*/M_\odot) > 11$. Under the above assumption that emission line luminosity scales linearly with stellar mass, we used the average line luminosity at $\log(M_*/M_\odot) \sim 11$ to compute the average line luminosity for two bins of stellar mass below the minimum mass in our AGN sample: $\log(M_*/M_\odot) = 9.0-9.5$ and $\log(M_*/M_\odot) = 9.5-10.0$. Based on the results of the SED modeling for the objects in the non-AGN comparison sample in these two stellar mass bins, we applied an average level of extinction ($\langle \mathrm{E(B-V)_{SF}} \rangle = 0.10$ for the lower mass bin, and $\langle \mathrm{E(B-V)_{SF}} \rangle = 0.12$ for the higher mass bin) to predict extinction-corrected CIV luminosities. Finally, we used the objects in the lower-mass bins from the non-AGN comparison sample to estimate an average rest-frame 1500 Å continuum luminosity density from the G and $\mathcal{R}$ photometry for the objects. Based on the predicted CIV luminosities and typical UV continuum luminosity densities, we estimated the typical CIV EWs for objects in these lower-mass bins. The resulting EW values are $\mathrm{EW_{CIV}} = 3.4$ Å for the $\log(M_*/M_\odot) = 9.0-9.5$ bin, and $\mathrm{EW_{CIV}} = 6.6$ Å for the $\log(M_*/M_\odot) = 9.5-10.0$ bin.

With average CIV EWs in hand, we can now ask whether we would have identified these lines in galaxies with $\log(M_*/M_\odot) < 10$. To test whether these lines would be detectable in lower-mass galaxies, we used the individual UV spectra for 15 representative non-AGNs in each of these lower-mass bins. We calculated the uncertainty on the EW in the spectral regions around the CIV line using the rms noise in the individual spectra, and estimated that in order for the line to be detected, $\mathrm{EW_{CIV}} > 8.5$ Å for the $\log(M_*/M_\odot) = 9.0-9.5$ bin, and $\mathrm{EW_{CIV}} > 9.0$ Å for the $\log(M_*/M_\odot) = 9.5-10.0$ bin. These estimates represent a 5σ detection limit that was used for identifying CIV in the AGN spectra.

For typical spectra of objects at $\log(M_*/M_\odot) < 10.0$, the predicted CIV EW values would therefore be too low to be detected. In conclusion, if galaxies with $\log(M_*/M_\odot) < 10.0$ hosted black holes accreting at the same average Eddington ratio as in higher mass galaxies, we would be unable to detect them given the emission line sensitivity in our spectroscopic sample.

The segregation of UV-selected AGNs in high-mass ($\log M_*/M_\odot \geq 10.0$) host galaxies is naturally explained based on two key assumptions: (1) that $\langle L_{CIV}/M_{BH} \rangle$ is constant as a function of M_{BH} (i.e., a constant Edddington ratio distribution), as demonstrated for X-ray-selected AGNs at $z < 1$ (Aird et al. 2012) and supported by the observed correlation between L_{CIV} and M_* in our sample, and (2) that M_{BH} is proportional to M_*. Even if lower-mass AGN host galaxies were characterized by similar Eddington ratios to those at higher-mass, we would be unable to detect them based on their high-ionization rest-frame UV emission lines. Viewed from a different perspective, the very segregation of UV-selected AGNs in high-mass hosts suggests that M_{BH} and M_* are already correlated at $z > 2$, during the epoch when both bulges and black holes are actively growing. Alternatively, our results can be explained if there are no black holes at $z \sim 2-3$ in galaxies at $\log(M_*/M_\odot) < 10$, or if the average Eddington ratio decreases in less massive systems. This latter scenario is inconsistent with results at lower redshift from Aird et al. (2012).

The discussion thus far has focused entirely on Type II AGNs. As presented in Steidel et al. (2002), Adelberger & Steidel (2005a), and Adelberger & Steidel (2005b), within the UV-selected galaxy population, broad-line or "Type I" AGNs have a similar frequency to that of the Type II AGNs discussed here. It is important to consider if any of our conclusions regarding the demographics of AGN activity at $z \sim 2-3$ are impacted by including a description of these

Type I AGNs. Although it is not possible to make robust models of the host galaxy stellar populations of Type I objects, due to significant contamination from the active nucleus, we can investigate the typical Eddington ratios for Type I objects spanning the same range in L_{bol} as that of our Type II sample. We estimated L_{bol} for the Type I objects from their rest-frame 1350 Å luminosities (i.e., $\lambda L_{\lambda}(1350\text{Å})$, calculated using the observed G- and $\mathcal{R}$-band photometry for these objects), which we then multiplied by the bolometric correction factor of 4.3 from Vestergaard & Osmer (2009). We used the relationship between L_{bol} and M_{BH} implied by the correlations presented in Adelberger & Steidel (2005b) to estimate M_{BH} values. We find typical black hole masses of $\log(M_{BH}/M_{\odot}) \sim 8$ – comparable to the black hole masses presented section 4.3. Accordingly, the Type I objects in the a matched range of L_{bol} must have similar Eddington ratios to those of the Type II objects presented here, and appear to represent their unobscured analogs. It is worth noting that the L_{bol} distribution of Type I AGNs identified within the the UV-selected survey extends to higher luminosities than those spanned by the Type II objects, with roughly one third of Type I sample characterized by $L_{bol} > 10^{46}$ erg s^{-1}. Eddington-limited accretion in these systems corresponds to black hole masses of $\log(M_{BH}/M_{\odot}) \sim 8.4$, which represents a lower limit in black hole mass. Accordingly, it seems unlikely that these black holes are hosted by significantly lower-mass galaxies than the Type II AGNs discussed in this work. It is remarkable that both types of UV-selected AGNs at fixed bolometric luminosity are characterized by Eddington ratios < 0.1 for typical black hole masses of $\log(M_{BH}/M_{\odot}) \sim 8$. At some earlier time, these black holes must have been accreting at significantly higher Eddington ratios. An important goal will be the identification of the more active progenitors of the UV-selected AGNs at $z \sim 2 - 3$.

4.7 Conclusions

Using SPS modeling, we have examined the host galaxy populations for a sample of $z \sim 2-3$ Type-II AGNs identified by the presence of rest-frame UV emission features. The results of our AGN+SPS dual-component modeling demonstrate the importance of using long wavelength coverage to properly model the SEDs of type II AGNs. Without data longwards of $1-2\mu$m (rest frame), the masses and SFRs for our sample of AGNs would be overpredicted by an average factor of 1.4. We have used the results of our modeling to examine the host galaxy trends for our sample. Our primary results are the following:

1. The host galaxies for the UV-selected AGNs have very high average (median) masses ($\log(\langle M_*/M_\odot \rangle) = 10.85\,(10.71)\pm0.36$) and high SFRs ($\langle SFR \rangle = 63\,(37) \pm 67$ $M_\odot$ yr^{-1}).

2. We have constructed a mass-matched non-AGN sample with which to compare to the AGN hosts. The AGNs lie at the high-mass edge of the $U-V_{rest,AB}$ vs. M_* relation compared to the full non-AGN sample, but span the same range of color as the mass-matched non-AGN sample. Additionally, the AGNs have similar SFRs to the mass-matched sample, indicating that the presence of an AGN does not affect the colors or star-formation properties of these highly star-forming hosts at these redshifts.

3. A primary result from Chapter 3 is that the UV composite spectrum for the AGNs has a redder continuum than the full non-AGN composite from Shapley et al. (2003). The UV composite constructed for the objects in the mass-matched comparison sample has a red continuum that is very similar to that of the AGN composite, and we argue that this result is due to more dust extinction in the higher-mass galaxies hosting AGNs as well as

the mass-matched sample. This similarity between the UV continua of the mass-matched non-AGNs and AGNs confirms that the UV continuum of AGN hosts is dominated by starlight.

4. We separated our AGNs by stellar mass into two subsamples and created composite spectra for each of these subsamples. The CIV and HeII EWs are larger in the high-mass composite spectrum than in the low-mass composite spectrum. This trend provides evidence that the EWs of the UV emission lines used to identify the AGNs depends on stellar mass. We also observe that the dust-corrected luminosities for the NV, CIV, and HeII emission lines scale with host galaxy stellar mass. These trends would be predicted if the mass of the host galaxy scaled with the black hole mass and emission line luminosity.

5. We estimate the CIV line EW for potential AGNs hosted by galaxies of mass $\log(M_*/M_\odot) = 9.0 - 9.5$ and $\log(M_*/M_\odot) = 9.5 - 10.0$, under the assumption that line luminosity scales linearly with galaxy mass. The predicted CIV EWs (3.4 Å for the lowest mass bin, and 6.6 Å for the higher mass bin) would not be detectable at the 5σ level required for AGN identification in our sample, indicating that we cannot identify UV-selected AGNs in galaxies with stellar masses $\log(M_*/M_\odot) < 10.0$. Additionally, we can use the segregation of UV-selected AGN hosts to argue that M_{BH} and M_* are already correlated at $z > 2$.

While we have demonstrated that AGNs hosted by lower-mass galaxies would not be detected in our sample based on the presence of UV emission lines, AGNs can be identified using X-ray luminosity and IR colors. In future work, we will investigate the demographics of AGNs selected using these additional methods and obtain a more complete picture of AGN activity at $z > 2$.

Table 4.1. UV-Selected AGN Photometry

OBJECT	RA (J2000)	DEC (J2000)	$z_{Ly\alpha}$	$\mathcal{R}^{a}$	$U-G^{a}$	$G-\mathcal{R}^{a}$
Q0000-C7	00:03:28.85	-26:03:53.3	3.431	24.37 ± 0.19	-	0.07 ± 0.09
Q0000-C14	00:03:30.39	-26:01:20.7	3.057	24.47 ± 0.17	-	0.86 ± 0.18
CDFB-D3	00:53:43.02	12:22:02.5	2.777	24.82 ± 0.20	-	0.47 ± 0.14
Q0100-BX172	01:03:08.46	13:16:41.7	2.312	23.50 ± 0.09	0.81 ± 0.27	0.26 ± 0.07
Q0142-BX195	01:45:17.68	-09:44:54.2	2.382	23.56 ± 0.08	0.98 ± 0.23	0.53 ± 0.09
Q0142-BX256	01:45:15.74	-09:42:12.5	2.321	23.91 ± 0.08	0.88 ± 0.16	0.32 ± 0.07
Q0201-OC12	02:03:56.16	11:36:30.1	2.357	25.01 ± 0.34	-	0.56 ± 0.13
Q0256-MD37	02:59:02.21	00:12:03.4	2.803	24.36 ± 0.18	-	0.63 ± 0.14
Q0933-MD38	09:33:48.60	28:44:32.3	2.763	22.61 ± 0.06	-	0.04 ± 0.09
Q1217-BX46	12:19:19.94	49:40:22.7	1.980	23.85 ± 0.17	0.76 ± 0.29	0.44 ± 0.14
HDF-MMD12	12:37:19.80	62:09:56.0	2.648	24.36 ± 0.17	0.92 ± -	1.02 ± 0.20
HDF-BMZ1156	12:37:04.34	62:14:46.3	2.211	24.62 ± 0.20	-	0.37 ± 0.08
HDF-BMZ1384	12:37:23.15	62:15:38.0	2.243	23.98 ± 0.14	0.45 ± 0.06	0.49 ± 0.08
HDF-BX160	12:37:20.07	62:12:22.7	2.461	24.02 ± 0.17	0.92 ± 0.15	0.74 ± 0.12
Westphal-MM47	14:17:57.39	52:31:04.5	3.027	24.30 ± 0.13	-	1.26 ± 0.10
Q1422-C73	14:24:46.41	22:55:45.5	3.382	24.88 ± 0.14	-	1.05 ± 0.17
Q1422-MD109	14:24:42.58	22:54:46.6	2.229	23.69 ± 0.07	1.61 ± 0.14	0.56 ± 0.08
Q1623-BX454	16:25:51.42	26:43:46.3	2.422	23.89 ± 0.13	0.50 ± 0.14	0.22 ± 0.06
Q1623-BX663	16:26:04.58	26:48:00.2	2.435	24.14 ± 0.15	1.02 ± 0.17	0.24 ± 0.07
Q1623-BX747	16:26:13.46	26:45:53.2	2.441	22.55 ± 0.14	0.42 ± 0.04	0.12 ± 0.03
Q1700-MD157	17:00:52.19	64:15:29.3	2.295	24.35 ± 0.13	1.65 ± 0.28	0.35 ± 0.07
Q1700-MD174	17:00:54.54	64:16:24.8	2.347	24.56 ± 0.17	1.50 ± 0.28	0.32 ± 0.08
Q2233-D3	22:36:16.12	13:55:19.2	2.795	24.08 ± 0.18	-	1.08 ± 0.16
Q2233-MD21	22:36:35.83	13:55:42.0	2.549	25.72 ± 0.32	-	0.85 ± 0.21
DSF2237A-D11	22:40:02.99	11:52:13.9	2.959	25.09 ± 0.26	-	0.41 ± 0.13
DSF2237B-MD53	22:39:28.67	11:52:09.5	2.292	24.05 ± 0.13	-	0.35 ± 0.10
Q2343-BX333	23:46:21.51	12:47:03.2	2.397	24.12 ± 0.14	0.65 ± 0.13	0.30 ± 0.08
Q2346-BX445	23:48:13.20	00:25:15.8	2.330	23.81 ± 0.13	1.00 ± 0.36	0.39 ± 0.09

OBJECT	$\mathcal{R}-J^{b}$	$\mathcal{R}-K^{b}$	[3.6 μm]^{a}	[4.5 μm]^{a}	[5.8 μm]^{a}	[8.0 μm]^{a}
Q0000-C7	2.17 ± 0.43	4.50 ± 0.20	-	-	-	-
Q0000-C14	-	4.43 ± 0.14	-	-	-	-
CDFB-D3	-	4.97 ± 0.34	-	-	-	-
Q0100-BX172	-	3.36 ± 0.22	21.43 ± 0.10	21.24 ± 0.10	21.00 ± 0.23	20.64 ± 0.10
Q0142-BX195	-	3.48 ± 0.18	21.22 ± 0.10	21.01 ± 0.10	20.75 ± 0.24	20.26 ± 0.10
Q0142-BX256	-	4.02 ± 0.13	21.45 ± 0.10	21.21 ± 0.18	20.15 ± 0.34	-
Q0201-OC12	2.61 ± 0.40	5.51 ± 0.20	-	-	-	-
Q0256-MD37	-	3.68 ± 0.21	-	-	-	-
Q0933-MD38	-	2.37 ± 0.20	-	-	-	-
Q1217-BX46	2.36 ± 0.14	3.56 ± 0.53	21.65 ± 0.10	-	-	-
HDF-MMD12	1.85 ± 0.27	4.07 ± 0.21	21.40 ± 0.07	20.95 ± 0.07	20.24 ± 0.07	19.55 ± 0.07
HDF-BMZ1156	2.58 ± 0.20	4.29 ± 0.17	22.01 ± 0.07	21.85 ± 0.07	20.96 ± 0.07	19.75 ± 0.07
HDF-BMZ1384	2.09 ± 0.16	4.11 ± 0.14	21.97 ± 0.07	21.60 ± 0.07	21.06 ± 0.07	20.49 ± 0.07

Table 4.1—Continued

OBJECT	RA (J2000)	DEC (J2000)	$z_{Ly\alpha}$	$\mathcal{R}^{a}$	$U-G^{a}$	$G-\mathcal{R}^{a}$
HDF-BX160	2.09 ± 0.18	3.97 ± 0.20	21.39 ± 0.07	21.22 ± 0.07	20.90 ± 0.07	20.85 ± 0.07
Westphal-MM47	-	-	21.83 ± 0.10	21.84 ± 0.10	-	-
Q1422-C73	-	3.82 ± 0.21	-	-	-	-
Q1422-MD109	-	4.48 ± 0.10	-	-	-	-
Q1623-BX454	-	-	22.87 ± 0.15	22.64 ± 0.15	-	-
Q1623-BX663	1.63 ± 0.26	4.22 ± 0.14	20.66 ± 0.10	19.86 ± 0.10	19.03 ± 0.10	18.13 ± 0.10
Q1623-BX747	1.51 ± 0.11	2.19 ± 0.23	22.33 ± 0.16	-	-	-
Q1700-MD157	2.24 ± 0.10	4.12 ± 0.19	-	21.61 ± 0.10	-	21.25 ± 0.11
Q1700-MD174	-	4.66 ± 0.15	-	20.41 ± 0.10	-	18.26 ± 0.10
Q2233-D3	-	4.53 ± 0.19	-	-	-	-
Q2233-MD21	-	4.37 ± 0.31	22.89 ± 0.11	-	-	-
DSF2237A-D11	-	3.00 ± 0.50	-	-	-	-
DSF2237B-MD53	-	4.68 ± 0.14	-	-	-	-
Q2343-BX333	1.93 ± 0.14	4.21 ± 0.16	-	21.01 ± 0.10	-	20.47 ± 0.10
Q2346-BX445	-	4.34 ± 0.13	-	-	-	-

[a] U, G, $\mathcal{R}$, and IRAC magnitudes are on the AB system.

[b] $\mathcal{R}-J$ and $\mathcal{R}-K$ colors are AB−Vega.

Table 4.2. Best Fit Parameters, AGNs with IRAC Coverage

OBJECT	SF History	log[Age] Myr	log(M_*) $M_\odot$	$E(B-V)_{SF}$	SFR $M_\odot$ yr^{-1}	$E(B-V)_{AGN}$	log(N_{AGN})[a]	log($L_{bol,AGN}$) $L_\odot$
Q0100-BX172	constant	3.21 ± 0.18	10.77 ± 0.09	0.140 ± 0.030	37 ± 9	2.600 ± 2.433	-1.00 ± 0.55	10.82 ± 0.57
	5000Myr	3.16 ± 0.18	10.78 ± 0.11	0.140 ± 0.035	36 ± 10	2.800 ± 2.949	-10.80 ± 0.53	10.84 ± 0.57
Q0142-BX195	constant	2.76 ± 0.31	10.76 ± 0.15	0.260 ± 0.053	101 ± 62	4.600 ± 2.066	-1.00 ± 0.27	11.26 ± 0.35
	2000Myr	2.66 ± 0.84	10.71 ± 0.22	0.260 ± 0.079	100 ± 53	2.800 ± 3.199	-10.60 ± 0.54	11.05 ± 0.61
Q0142-BX256	constant	3.44 ± 0.08	10.96 ± 0.06	0.180 ± 0.021	33 ± 6	5.600 ± 1.010	0.18 ± 0.00	11.95 ± 0.09
	300Myr	2.91 ± 0.06	10.83 ± 0.05	0.120 ± 0.040	16 ± 5	7.600 ± 0.179	-8.60 ± 0.31	12.51 ± 0.30
HDF-MMD12	constant	2.31 ± 0.11	10.60 ± 0.12	0.400 ± 0.033	196 ± 49	2.000 ± 0.614	-1.00 ± 0.00	11.55 ± 0.08
	5000Myr	1.74 ± 0.10	10.31 ± 0.12	0.460 ± 0.084	371 ± 428	2.000 ± 0.643	-11.00 ± 0.46	11.53 ± 0.06
HDF-BMZ1156	constant	3.34 ± 0.10	10.64 ± 0.05	0.240 ± 0.024	20 ± 3	6.200 ± 0.646	0.15 ± 0.07	11.70 ± 0.08
	200Myr	2.96 ± 0.03	10.53 ± 0.03	0.000 ± 0.013	2 ± 0	5.200 ± 0.743	-9.20 ± 0.11	11.59 ± 0.11
HDF-BMZ1384	constant	3.44 ± 0.00	10.69 ± 0.07	0.140 ± 0.018	18 ± 3	2.800 ± 1.254	-0.52 ± 0.11	10.98 ± 0.15
	200Myr	2.91 ± 0.03	10.56 ± 0.10	0.000 ± 0.008	3 ± 1	2.800 ± 1.269	-9.80 ± 0.10	11.02 ± 0.10
HDF-BX160	constant	3.11 ± 0.21	10.91 ± 0.08	0.260 ± 0.029	64 ± 15	6.400 ± 1.231	-1.00 ± 0.00	11.06 ± 0.11
	100Myr	2.71 ± 0.19	10.80 ± 0.14	0.040 ± 0.228	4 ± 294	1.200 ± 0.254	-10.40 ± 0.19	10.66 ± 0.17

Table 4.2—Continued

OBJECT	SF History	log[Age] Myr	log(M_*) $M_\odot$	$E(B-V)_{SF}$	SFR $M_\odot$ yr^{-1}	$E(B-V)_{AGN}$	log(N_{AGN})[a]	log($L_{bol,AGN}$) $L_\odot$
Q1623-BX663	constant	2.76 ± 0.81	10.26 ± 0.85	0.180 ± 0.020	32 ± 4	1.000 ± 0.078	0.18 ± 0.02	11.94 ± 0.04
	2000Myr	3.36 ± 0.18	10.96 ± 0.23	0.140 ± 0.036	21 ± 8	1.400 ± 0.333	-9.40 ± 0.24	11.99 ± 0.06
Q1700-MD157	constant	3.16 ± 0.17	10.74 ± 0.09	0.260 ± 0.025	38 ± 8	7.400 ± 0.616	-1.00 ± 0.20	10.84 ± 0.18
	100Myr	2.61 ± 0.03	10.55 ± 0.06	0.120 ± 0.031	6 ± 2	1.600 ± 2.554	-10.40 ± 0.44	10.41 ± 0.11
Q1700-MD174	constant	3.44 ± 0.00	11.15 ± 0.17	0.300 ± 0.042	51 ± 16	3.600 ± 1.361	0.15 ± 0.02	12.11 ± 0.14
	1000Myr	3.38 ± 0.06	11.26 ± 0.13	0.180 ± 0.036	18 ± 6	4.000 ± 1.627	-9.40 ± 0.20	12.16 ± 0.23
Q2343-BX333	constant	3.41 ± 0.00	10.96 ± 0.09	0.200 ± 0.019	35 ± 7	1.000 ± 2.461	-1.00 ± 0.00	10.80 ± 0.10
	300Myr	3.01 ± 0.04	10.96 ± 0.06	0.080 ± 0.037	11 ± 3	1.600 ± 2.203	-10.40 ± 0.40	10.83 ± 0.14

[a]For the CSF fits, $N_{AGN} = L_{bol}/(\mathrm{SFR} \times 10^{10})$, and for the declining τ fits, $N_{AGN} = L_{bol}/(M_*(1-e^{-t/\tau}) \times 10^{10})$

Table 4.3. CSF AGN Correction Factors

OBJECT	Mass[a]	SFR[a]	Age[a]	$E(B-V)_{SF}$[a]
Q0100 − BX172	1.0 ± 0.5	1.0 ± 0.4	1.0 ± 0.6	1.0 ± 0.3
Q0142 − BX195	1.2 ± 0.6	1.1 ± 0.7	1.3 ± 1.0	1.0 ± 0.3
Q0142 − BX256	0.7 ± 0.2	0.8 ± 0.3	0.8 ± 0.2	0.9 ± 0.1
HDF − MMD12	0.9 ± 0.7	0.2 ± 1.1	2.1 ± 1.4	0.8 ± 0.2
HDF − BMZ1156	0.5 ± 0.3	0.6 ± 0.3	0.8 ± 0.2	0.9 ± 0.1
HDF − BMZ1384	0.6 ± 0.3	0.6 ± 0.4	1.0 ± 0.0	0.8 ± 0.2
HDF − BX160	0.6 ± 0.4	0.8 ± 0.4	0.8 ± 0.5	1.0 ± 0.2
Q1623 − BX663	0.3 ± 1.0	0.8 ± 0.3	0.4 ± 0.9	0.8 ± 0.1
Q1700 − MD157	0.5 ± 0.3	0.8 ± 0.3	0.6 ± 0.4	1.0 ± 0.1
Q1700 − MD174	0.9 ± 0.5	0.9 ± 0.4	1.0 ± 0.0	1.0 ± 0.2
Q2343 − BX333	1.0 ± 0.3	1.0 ± 0.3	1.0 ± 0.0	1.0 ± 0.1
average[b]	0.7 ± 0.3	0.8 ± 0.2	1.0 ± 0.4	0.92 ± 0.07

[a]Correction values represent the derived parameters from the AGN+SF modeling fit divided by the SF modeling fit through the K band data.

[b]Uncertainties for the average correction factors represent the standard deviation of the distributions.

Table 4.4. Best Fit Parameters, AGNs without IRAC Coverage

OBJECT	SF History	log[Age] Myr	log[Age]$_{corr}$ Myr	log(M$_*$) M$_\odot$	log(M$_*$)$_{corr}$ M$_\odot$
Q0000-C7	constant	3.26 ± 0.00	3.25 ± 0.19	10.35 ± 0.14	10.21 ± 0.29
	500Myr	3.26 ± 0.00	3.21 ± 0.09	11.25 ± 0.07	11.17 ± 0.15
Q0000-C14	constant	3.30 ± 0.00	3.30 ± 0.19	11.43 ± 0.12	11.30 ± 0.27
	500Myr	3.11 ± 0.11	3.06 ± 0.16	11.32 ± 0.11	11.25 ± 0.19
CDFB-D3	constant	3.36 ± 0.00	3.36 ± 0.19	11.15 ± 0.21	11.02 ± 0.36
	500Myr	3.28 ± 0.07	3.24 ± 0.12	11.42 ± 0.20	11.35 ± 0.27
Q0201-OC12	constant	3.41 ± 0.00	3.41 ± 0.19	11.53 ± 0.19	11.39 ± 0.34
	500Myr	3.26 ± 0.08	3.21 ± 0.12	11.49 ± 0.17	11.42 ± 0.24
Q0256-MD37	constant	3.06 ± 0.29	3.05 ± 0.35	10.78 ± 0.21	10.65 ± 0.36
	1000Myr	2.91 ± 0.26	2.86 ± 0.31	10.74 ± 0.18	10.67 ± 0.25
Q0933-MD38	constant	2.96 ± 0.26	2.95 ± 0.33	10.52 ± 0.25	10.39 ± 0.41
	5000Myr	2.91 ± 0.20	2.86 ± 0.24	10.51 ± 0.21	10.43 ± 0.28
Q1217-BX46	constant	2.86 ± 0.14	2.85 ± 0.24	10.49 ± 0.08	10.35 ± 0.25
	100Myr	2.46 ± 0.16	2.41 ± 0.20	10.42 ± 0.07	10.35 ± 0.15
WEST-MM47	constant	2.06 ± 0.35	2.05 ± 0.41	10.41 ± 0.13	10.27 ± 0.28
	100Myr	2.71 ± 0.08	2.66 ± 0.12	10.79 ± 0.04	10.72 ± 0.14
Q1422-C73	constant	3.26 ± 0.00	3.25 ± 0.19	10.82 ± 0.15	10.69 ± 0.30
	500Myr	3.06 ± 0.11	3.01 ± 0.15	10.83 ± 0.18	10.76 ± 0.25
Q1422-MD109	constant	3.01 ± 0.27	3.00 ± 0.34	11.29 ± 0.14	11.16 ± 0.29
	100Myr	2.51 ± 0.05	2.46 ± 0.11	11.11 ± 0.07	11.04 ± 0.15
Q1623-BX454	constant	2.76 ± 0.31	2.75 ± 0.36	10.03 ± 0.19	9.90 ± 0.33
	200Myr	2.61 ± 0.19	2.56 ± 0.23	10.08 ± 0.17	10.00 ± 0.24
Q1623-BX747	constant	2.81 ± 0.12	2.80 ± 0.23	10.32 ± 0.09	10.19 ± 0.25
	300Myr	2.71 ± 0.05	2.66 ± 0.10	10.43 ± 0.08	10.36 ± 0.16
Q2233-D3	constant	2.71 ± 0.63	2.70 ± 0.66	11.36 ± 0.25	11.22 ± 0.41
	500Myr	2.56 ± 0.34	2.51 ± 0.39	11.31 ± 0.21	11.23 ± 0.28
Q2233-MD21	constant	2.66 ± 0.71	2.65 ± 0.74	10.20 ± 0.19	10.07 ± 0.34
	100Myr	2.71 ± 0.10	2.66 ± 0.14	10.26 ± 0.06	10.19 ± 0.14
DSF2237A-D11	constant	3.32 ± 0.16	3.32 ± 0.25	10.20 ± 0.20	10.06 ± 0.35
	5000Myr	3.23 ± 0.19	3.19 ± 0.23	10.16 ± 0.27	10.09 ± 0.34
DSF2237B-MD53	constant	3.44 ± 0.00	3.44 ± 0.19	11.37 ± 0.10	11.24 ± 0.26
	1000Myr	3.41 ± 0.05	3.37 ± 0.11	11.47 ± 0.10	11.40 ± 0.18

Table 4.4—Continued

OBJECT	SF History	log[Age] Myr	log[Age]$_{corr}$ Myr	log(M$_*$) M$_\odot$	log(M$_*$)$_{corr}$ M$_\odot$
Q2346-BX445	constant	3.44 ± 0.00	3.44 ± 0.19	11.33 ± 0.10	11.19 ± 0.26
	2000Myr	3.44 ± 0.07	3.40 ± 0.12	11.42 ± 0.10	11.35 ± 0.17

OBJECT	SF History	$E(B-V)_{SF}$	$E(B-V)_{SF,corr}$	SFR M$_\odot$ yr^{-1}	SFR$_{corr}$ M$_\odot$ yr^{-1}
Q0000-C7	constant	0.015 ± 0.017	0.014 ± 1.133	12 ± 4	10 ± 5
	500Myr	0.000 ± 0.000	0.000 ± 0.000	10 ± 2	9 ± 3
Q0000-C14	constant	0.315 ± 0.024	0.289 ± 0.076	135 ± 37	104 ± 55
	500Myr	0.175 ± 0.074	0.185 ± 0.423	35 ± 29	32 ± 30
CDFB-D3	constant	0.295 ± 0.044	0.271 ± 0.149	62 ± 30	48 ± 36
	500Myr	0.120 ± 0.060	0.127 ± 0.500	12 ± 9	11 ± 9
Q0201-OC12	constant	0.460 ± 0.032	0.422 ± 0.070	129 ± 57	99 ± 68
	500Myr	0.235 ± 0.077	0.249 ± 0.328	17 ± 15	16 ± 16
Q0256-MD37	constant	0.225 ± 0.052	0.206 ± 0.231	53 ± 31	41 ± 35
	1000Myr	0.210 ± 0.073	0.223 ± 0.348	45 ± 30	41 ± 32
Q0933-MD38	constant	0.000 ± 0.000	0.000 ± 0.000	37 ± 2	28 ± 11
	5000Myr	0.000 ± 0.000	0.000 ± 0.000	37 ± 2	34 ± 9
Q1217-BX46	constant	0.255 ± 0.026	0.234 ± 0.102	43 ± 10	33 ± 16
	100Myr	0.185 ± 0.072	0.196 ± 0.389	16 ± 9	15 ± 10
WEST-MM47	constant	0.355 ± 0.026	0.326 ± 0.073	225 ± 34	174 ± 75
	100Myr	0.015 ± 0.077	0.016 ± 5.133	4 ± 0	4 ± 1
Q1422-C73	constant	0.185 ± 0.031	0.170 ± 0.168	37 ± 13	28 ± 17
	500Myr	0.100 ± 0.050	0.106 ± 0.500	15 ± 8	14 ± 9
Q1422-MD109	constant	0.380 ± 0.037	0.348 ± 0.097	194 ± 70	150 ± 91
	100Myr	0.295 ± 0.040	0.313 ± 0.136	54 ± 23	50 ± 26
Q1623-BX454	constant	0.090 ± 0.045	0.083 ± 0.500	19 ± 5	15 ± 7
	200Myr	0.035 ± 0.070	0.037 ± 2.000	9 ± 22	8 ± 22
Q1623-BX747	constant	0.030 ± 0.010	0.028 ± 0.333	33 ± 5	25 ± 11
	300Myr	0.000 ± 0.002	0.000 ± 0.000	20 ± 2	18 ± 5
Q2233-D3	constant	0.440 ± 0.096	0.403 ± 0.218	446 ± 303	344 ± 331
	500Myr	0.430 ± 0.106	0.456 ± 0.247	384 ± 351	352 ± 363
Q2233-MD21	constant	0.380 ± 0.046	0.348 ± 0.121	35 ± 7	27 ± 13

Table 4.4—Continued

OBJECT	SF History	log[Age] Myr	log[Age]$_{corr}$ Myr	log(M$_*$) M$_\odot$	log(M$_*$)$_{corr}$ M$_\odot$
	100Myr	0.075 ± 0.113	0.080 ± 1.507	1 ± 2	1 ± 2
DSF2237A-D11	constant	0.065 ± 0.050	0.060 ± 0.769	8 ± 6	6 ± 6
	5000Myr	0.060 ± 0.050	0.064 ± 0.833	7 ± 5	7 ± 5
DSF2237B-MD53	constant	0.310 ± 0.022	0.284 ± 0.071	85 ± 21	66 ± 33
	1000Myr	0.160 ± 0.036	0.170 ± 0.225	24 ± 10	22 ± 11
Q2346-BX445	constant	0.265 ± 0.021	0.243 ± 0.079	77 ± 19	60 ± 30
	2000Myr	0.200 ± 0.029	0.212 ± 0.145	44 ± 17	41 ± 20

Table 4.5. UV Emission Features for Stellar Mass Subsamples

	$\log(M_*/M_\odot) > 10.7$	$\log(M_*/M_\odot) < 10.7$
$W_{\mathrm{Ly}\alpha}$[a]	56±15	58±18
$W_{\mathrm{NV},1240}$[a]	4.6±1.4	3.7±1.6
$W_{\mathrm{CIV},1549}$[a]	17.6±3.3	7.4±3.3
$W_{\mathrm{HeII},1640}$[a]	10.2±2.4	5.0±1.1

[a]Rest-frame EW in Å, measured from the composite spectra. Uncertainties are calculated as described in §4.5.4.

CHAPTER 5

Conclusions and Future Work

5.1 Summary of Dissertation

My dissertation explores how both star formation and AGN activity drive galaxy evolution at $z \sim 2-3$, a time when both processes were at their peak levels throughout the universe. While the details of galaxies at high redshift can be difficult to observe due to the great distances involved, I have used a variety of techniques to estimate key physical properties of star-forming galaxies in the early universe. In Chapter 2, I described rest-frame optical spectroscopy for three gravitationally lensed star-forming galaxies at $z \sim 2$. The magnification afforded by gravitational lensing allowed me to measure optical line fluxes for important diagnostics of galaxy gas properties. While one of the galaxies was determined to be an AGN, the other two, the Cosmic Horseshoe and the Clone, were found to have high SFRs, sub-solar to solar metallicities, and dynamical masses typical of star-forming galaxies at the same redshift. The star forming regions in these two objects are characterized by high electron densities ($\sim 10^3$ cm^{-3}), as well as large ionization parameters, which has possible implications for the IMF in high-redshift galaxies. These results help in understanding why, on average, these and other high-redshift star-forming galaxies are offset on a key star-forming diagnostic diagram compared to local galaxies.

In Chapter 3, I presented a sample of 33 Type II AGNs at $z \sim 2-3$ that

were selected by the presence of strong rest-frame UV emission features. These galaxies were identified within a larger sample of non-active star-forming galaxies at the same redshift, which provides a key comparison for understanding AGN activity in galaxies. I created a high S/N UV composite spectrum for the AGNs, and examined the emission and absorption features. Most strikingly, I discovered a high-ionization SiIV absorption feature at a blueshift of $\Delta v = -845$ km s^{-1}. The bulk of this gas seems to be moving more rapidly than what is found for outflowing gas in non-active star forming galaxies at the same redshift (Shapley et al. 2003; Steidel et al. 2010), and could be driven by the presence of an AGN. I also separated the AGNs into bins based on Lyα EW, and discovered that the AGN emission lines (NV, CIV, and HeII) were stronger in the composite with larger Lyα EW. At the same time, the low-ionization absorption features that are used to indicate the cool gas covering fraction were weaker in the strong Lyα composite, similar to what is seen in the non-AGNs from Shapley et al. (2003). These results support the view that the covering fraction of ISM gas is playing an important role in modulating the observed Lyα emission in both AGNs and non-AGNs.

In Chapter 4, I continued the analysis of the Type II UV-selected AGN sample by carefully modeling the SEDs of these objects to gain insight into their host galaxy stellar populations. For a subsample of the AGNs with SED data out to IR wavelengths, I used a dual-component modeling technique to examine the influence of AGN emission on the best-fit SPS modeling properties. Using this method, I corrected the best-fit parameters for those AGNs where it is not possible to perform dual-component modeling. The results of this modeling showed that AGNs are hosted by high-mass galaxies ($\log(M_*/M_\odot) > 10$) with large SFRs ($\langle \mathrm{SFR/M_\odot yr^{-1}} \rangle = 63$). A comparison to a sample of non-active star-forming galaxies indicated that the best-fit properties of the AGNs are very

similar to non-active galaxies of similar mass, suggesting that AGNs are having very little effect on star-formation in these galaxies. In Ch. 3, I found that the UV composite has a significantly redder UV slope than the non-AGN composite from Shapley et al. (2003), which I attributed to increased dust extinction. This hypothesis is supported by separating the AGNs into bins based on stellar extinction, which results in strongly discrepant UV composite slopes. When I separate the AGNs by stellar mass, I find that the emission lines used to indicate the presence of an AGN are stronger in the high-mass composite. This result, as well as measurements of the line luminosity for the individual AGN UV spectra, can be explained in a scenario where AGNs hosted by galaxies with $\log(M_*/M_\odot) < 10$ would have emission lines too weak to be detected. In this scenario, AGNs at $z \sim 2-3$ are characterized by a universal Eddington ratio distribution, and, if M_{BH} and M_* are correlated as in the low-redshift universe, galaxies with lower stellar masses should exhibit AGN-related emission lines with lower luminosities. Our results can also be explained if there are no black holes at $z \sim 2-3$ in galaxies at $\log(M_*/M_\odot) < 10$, or if the average Eddington ratio decreases in less massive systems. This latter scenario is inconsistent with results at lower redshift from Aird et al. (2012).

5.2 Future Work

While I have been engaged in the research presented in this dissertation, I have also been involved in obtaining near-IR spectroscopy for the UV-selected AGNs at many different observatories, including the Keck (using the NIRSPEC instrument), Gemini (with GNIRS), and Carnegie Observatories (with FIRE). At $z \sim 2-3$, the near-IR corresponds to the rest-frame optical, which contains key emission features that can be used to understand important AGN properties

that haven't been explored in my previous work. However, due to the difficulty in obtaining optical emission line fluxes for high-redshift samples, very few AGNs at $z \sim 2-3$ have been observed spectroscopically in this wavelength range. The strong [OIII]λ5007 line is often used in AGN studies to estimate the bolometric luminosity L_{bol} of the AGN (e.g., Yee 1980; Shuder 1981; Heckman et al. 2004), and while I have one estimate of L_{bol} from the dual-component modeling for a subsample of 11 AGNs (see §4.4.3), it would benefit my work to have estimates for more objects. Dust extinction on the [OIII] line can be estimated by using the ratio of Hα to Hβ to estimate Balmer decrements. These results would allow a comparison of the black hole accretion properties between the UV-selected AGNs and AGNs both at high and low redshift. The estimated bolometric luminosities can also be used to understand the full distribution of Eddington ratios for the sample in order to confirm the results from my examination of the demographics of the AGN sample (§4.6). The rest-frame optical portion of the spectrum also contains key emission lines discussed in Chapter 2, Hβ, [OIII], [OI], Hα, [NII], and [SII], which are often used to classify AGNs in local samples. It is crucial to place the UV-selected AGNs on the BPT diagram in order to compare to local AGNs, which have been well characterized through large samples from the SDSS (Kauffmann et al. 2003). These objects were classified based on narrow UV emission lines, and it is important also to see if they would also be characterized as narrow-emission-line AGNs in the optical as well. I am currently in the process of reducing the rest-frame optical spectroscopy in order to extract science results.

AGNs can be selected using different criteria that utilize observations of emission from the central supermassive black hole at X-ray through radio wavelengths. While I concluded that the UV selection method is biased against selecting lower-mass AGNs, it might be possible to use alternative AGN selection criteria to probe lower-mass galaxies. I am beginning an analysis of the full sample of star-forming

galaxies at $z \sim 2-3$ with IRAC data in order to find objects selected as IRAC power-law AGNs using the criteria from Lacy et al. (2004), Stern et al. (2005), and Donley et al. (2012). The presence of a power-law in the near- to mid-IR is thought to only arise from the presence of dust heated by AGN emission. I will perform dual-component AGN+SPS modeling on this sample of IRAC-selected AGNs, as outlined in §4.3.2, to estimate their stellar and AGN properties and understand how they compare with the UV-selected AGN population. While such samples have been identified previously, the unique aspect of my study will be an investigation of the UV spectroscopic properties of these AGNs. I can use existing UV spectroscopy for these objects to create a high S/N UV composite, in order to compare to the Type II UV-selected AGN composite presented in Ch. 3. It is also of particular interest to see how the mass and color distributions for the sample of IR-selected AGNs compare to those of the UV-selected AGNs, as well, in order to test our conclusions regarding the demographics of the UV-selected objects.

5.3 Final Thoughts

The presence of an AGN has been regarded as an important possible mechanism for the quenching of galactic star formation. The research presented in this dissertation demonstrates that, in the sample of AGNs that I studied, although AGNs are capable of exciting rapid highly-ionized outflows, it appears that an active black hole does not have a significant effect on the large-scale galactic stellar properties of its host. At the same time, I present evidence for a link between the black hole mass and the galaxy mass at $z \sim 2-3$, establishing the M_{BH} vs. M_{Bulge} relation observed in local galaxies. The Multi-Object Spectrometer for InfraRed Exploration (MOSFIRE), recently commisioned on the Keck I telescope,

will provide excellent data for the examination of the rest-frame optical properties of AGNs at this redshift, along with near-IR instruments to be deployed on the forthcoming James Webb Space Telescope (JWST). At the same time, these new instruments will be key in detecting the weaker emission lines in the rest-frame optical spectra such as those explored using the $z \sim 2-3$ lensed galaxies in Chapter 2. The results in my dissertation will inform future explorations of these populations of galaxies at even higher redshifts as astronomers examine the earliest known galaxies.

Bibliography

Adelberger, K. L., Shapley, A. E., Steidel, C. C., Pettini, M., Erb, D. K., & Reddy, N. A. 2005a, ApJ, 629, 636

Adelberger, K. L. & Steidel, C. C. 2005a, ApJ, 630, 50

—. 2005b, ApJL, 627, L1

Adelberger, K. L., Steidel, C. C., Pettini, M., Shapley, A. E., Reddy, N. A., & Erb, D. K. 2005b, ApJ, 619, 697

Adelberger, K. L., Steidel, C. C., Shapley, A. E., Hunt, M. P., Erb, D. K., Reddy, N. A., & Pettini, M. 2004, ApJ, 607, 226

Adelberger, K. L., Steidel, C. C., Shapley, A. E., & Pettini, M. 2003, ApJ, 584, 45

Adelman-McCarthy, J. K., Agüeros, M. A., Allam, S. S., Anderson, K. S. J., Anderson, S. F., Annis, J., Bahcall, N. A., Baldry, I. K., Barentine, J. C., Berlind, A., Bernardi, M., Blanton, M. R., Boroski, W. N., Brewington, H. J., Brinchmann, J., Brinkmann, J., Brunner, R. J., Budavári, T., Carey, L. N., Carr, M. A., Castander, F. J., Connolly, A. J., Csabai, I., Czarapata, P. C., Dalcanton, J. J., Doi, M., Dong, F., Eisenstein, D. J., Evans, M. L., Fan, X., Finkbeiner, D. P., Friedman, S. D., Frieman, J. A., Fukugita, M., Gillespie, B., Glazebrook, K., Gray, J., Grebel, E. K., Gunn, J. E., Gurbani, V. K., de Haas, E., Hall, P. B., Harris, F. H., Harvanek, M., Hawley, S. L., Hayes, J., Hendry, J. S., Hennessy, G. S., Hindsley, R. B., Hirata, C. M., Hogan, C. J., Hogg, D. W., Holmgren, D. J., Holtzman, J. A., Ichikawa, S.-i., Ivezić, Ž., Jester, S., Johnston, D. E., Jorgensen, A. M., Jurić, M., Kent, S. M.,

Kleinman, S. J., Knapp, G. R., Kniazev, A. Y., Kron, R. G., Krzesinski, J., Kuropatkin, N., Lamb, D. Q., Lampeitl, H., Lee, B. C., Leger, R. F., Lin, H., Long, D. C., Loveday, J., Lupton, R. H., Margon, B., Martínez-Delgado, D., Mandelbaum, R., Matsubara, T., McGehee, P. M., McKay, T. A., Meiksin, A., Munn, J. A., Nakajima, R., Nash, T., Neilsen, Jr., E. H., Newberg, H. J., Newman, P. R., Nichol, R. C., Nicinski, T., Nieto-Santisteban, M., Nitta, A., O'Mullane, W., Okamura, S., Owen, R., Padmanabhan, N., Pauls, G., Peoples, Jr., J., Pier, J. R., Pope, A. C., Pourbaix, D., Quinn, T. R., Richards, G. T., Richmond, M. W., Rockosi, C. M., Schlegel, D. J., Schneider, D. P., Schroeder, J., Scranton, R., Seljak, U., Sheldon, E., Shimasaku, K., Smith, J. A., Smolčić, V., Snedden, S. A., Stoughton, C., Strauss, M. A., SubbaRao, M., Szalay, A. S., Szapudi, I., Szkody, P., Tegmark, M., Thakar, A. R., Tucker, D. L., Uomoto, A., Vanden Berk, D. E., Vandenberg, J., Vogeley, M. S., Voges, W., Vogt, N. P., Walkowicz, L. M., Weinberg, D. H., West, A. A., White, S. D. M., Xu, Y., Yanny, B., Yocum, D. R., York, D. G., Zehavi, I., Zibetti, S., & Zucker, D. B. 2006, ApJS, 162, 38

Aird, J., Coil, A. L., Moustakas, J., Blanton, M. R., Burles, S. M., Cool, R. J., Eisenstein, D. J., Smith, M. S. M., Wong, K. C., & Zhu, G. 2012, ApJ, 746, 90

Aird, J., Nandra, K., Laird, E. S., Georgakakis, A., Ashby, M. L. N., Barmby, P., Coil, A. L., Huang, J., Koekemoer, A. M., Steidel, C. C., & Willmer, C. N. A. 2010, MNRAS, 401, 2531

Alexander, D. M., Brandt, W. N., Smail, I., Swinbank, A. M., Bauer, F. E., Blain, A. W., Chapman, S. C., Coppin, K. E. K., Ivison, R. J., & Menéndez-Delmestre, K. 2008a, AJ, 135, 1968

Alexander, D. M., Chary, R.-R., Pope, A., Bauer, F. E., Brandt, W. N., Daddi, E., Dickinson, M., Elbaz, D., & Reddy, N. A. 2008b, ApJ, 687, 835

Alexander, D. M., Swinbank, A. M., Smail, I., McDermid, R., & Nesvadba, N. P. H. 2010, MNRAS, 402, 2211

Allam, S. S., Tucker, D. L., Lin, H., Diehl, H. T., Annis, J., Buckley-Geer, E. J., & Frieman, J. A. 2007, ApJL, 662, L51

Allen, M. G., Dopita, M. A., & Tsvetanov, Z. I. 1998, ApJ, 493, 571

Allende Prieto, C., Lambert, D. L., & Asplund, M. 2002, ApJL, 573, L137

Alloin, D., Collin-Souffrin, S., Joly, M., & Vigroux, L. 1979, AA, 78, 200

Alonso-Herrero, A., Pérez-González, P. G., Rieke, G. H., Alexander, D. M., Rigby, J. R., Papovich, C., Donley, J. L., & Rigopoulou, D. 2008, ApJ, 677, 127

Alonso-Herrero, A., Quillen, A. C., Rieke, G. H., Ivanov, V. D., & Efstathiou, A. 2003, AJ, 126, 81

Alonso-Herrero, A., Quillen, A. C., Simpson, C., Efstathiou, A., & Ward, M. J. 2001, AJ, 121, 1369

Antonucci, R. 1993, ARAA, 31, 473

Asplund, M., Grevesse, N., Sauval, A. J., Allende Prieto, C., & Kiselman, D. 2004, AA, 417, 751

Assef, R. J., Kochanek, C. S., Brodwin, M., Cool, R., Forman, W., Gonzalez, A. H., Hickox, R. C., Jones, C., Le Floc'h, E., Moustakas, J., Murray, S. S., & Stern, D. 2010, ApJ, 713, 970

Baker, A. J., Lutz, D., Genzel, R., Tacconi, L. J., & Lehnert, M. D. 2001, AA, 372, L37

Baldry, I. K., Glazebrook, K., Brinkmann, J., Ivezić, Ž., Lupton, R. H., Nichol, R. C., & Szalay, A. S. 2004, ApJ, 600, 681

Baldwin, J. A. 1977, ApJ, 214, 679

Baldwin, J. A., Phillips, M. M., & Terlevich, R. 1981, PASP, 93, 5

Barger, A. J., Cowie, L. L., Mushotzky, R. F., Yang, Y., Wang, W.-H., Steffen, A. T., & Capak, P. 2005a, AJ, 129, 578

—. 2005b, AJ, 129, 578

Barth, A. J., Pancoast, A., Thorman, S. J., Bennert, V. N., Sand, D. J., Li, W., Canalizo, G., Filippenko, A. V., Gates, E. L., Greene, J. E., Malkan, M. A., Stern, D., Treu, T., Woo, J.-H., Assef, R. J., Bae, H.-J., Brewer, B. J., Buehler, T., Cenko, S. B., Clubb, K. I., Cooper, M. C., Diamond-Stanic, A. M., Hiner, K. D., Hönig, S. F., Joner, M. D., Kandrashoff, M. T., Laney, C. D., Lazarova, M. S., Nierenberg, A. M., Park, D., Silverman, J. M., Son, D., Sonnenfeld, A., Tollerud, E. J., Walsh, J. L., Walters, R., da Silva, R. L., Fumagalli, M., Gregg, M. D., Harris, C. E., Hsiao, E. Y., Lee, J., Lopez, L., Rex, J., Suzuki, N., Trump, J. R., Tytler, D., Worseck, G., & Yesuf, H. M. 2011, ApJL, 743, L4

Baum, S. A., Gallimore, J. F., O'Dea, C. P., Buchanan, C. L., Noel-Storr, J., Axon, D. J., Robinson, A., Elitzur, M., Dorn, M., & Staudaher, S. 2010, ApJ, 710, 289

Bell, E. F., Wolf, C., Meisenheimer, K., Rix, H.-W., Borch, A., Dye, S., Kleinheinrich, M., Wisotzki, L., & McIntosh, D. H. 2004, ApJ, 608, 752

Belokurov, V., Evans, N. W., Moiseev, A., King, L. J., Hewett, P. C., Pettini, M., Wyrzykowski, L., McMahon, R. G., Smith, M. C., Gilmore, G., Sanchez, S. F., Udalski, A., Koposov, S., Zucker, D. B., & Walcher, C. J. 2007, ApJL, 671, L9

Bentz, M. C., Hall, P. B., & Osmer, P. S. 2004, AJ, 128, 561

Bentz, M. C., Walsh, J. L., Barth, A. J., Baliber, N., Bennert, V. N., Canalizo, G., Filippenko, A. V., Ganeshalingam, M., Gates, E. L., Greene, J. E., Hidas, M. G., Hiner, K. D., Lee, N., Li, W., Malkan, M. A., Minezaki, T., Sakata, Y., Serduke, F. J. D., Silverman, J. M., Steele, T. N., Stern, D., Street, R. A., Thornton, C. E., Treu, T., Wang, X., Woo, J.-H., & Yoshii, Y. 2009, ApJ, 705, 199

Bertin, E. & Arnouts, S. 1996, AAPS, 117, 393

Best, P. N., Kauffmann, G., Heckman, T. M., Brinchmann, J., Charlot, S., Ivezić, Ž., & White, S. D. M. 2005, MNRAS, 362, 25

Bianchi, S., Maiolino, R., & Risaliti, G. 2012, Advances in Astronomy, 2012

Blanton, M. R. & Moustakas, J. 2009, ARAA, 47, 159

Bluck, A. F. L., Conselice, C. J., Almaini, O., Laird, E. S., Nandra, K., & Grützbauch, R. 2011, MNRAS, 410, 1174

Bouwens, R. J., Illingworth, G. D., Franx, M., & Ford, H. 2007, ApJ, 670, 928

Brinchmann, J., Charlot, S., White, S. D. M., Tremonti, C., Kauffmann, G., Heckman, T., & Brinkmann, J. 2004, MNRAS, 351, 1151

Brinchmann, J., Pettini, M., & Charlot, S. 2008, MNRAS, 385, 769

Brusa, M., Fiore, F., Santini, P., Grazian, A., Comastri, A., Zamorani, G., Hasinger, G., Merloni, A., Civano, F., Fontana, A., & Mainieri, V. 2009, AA, 507, 1277

Bruzual, G. & Charlot, S. 2003, MNRAS, 344, 1000

Bundy, K., Georgakakis, A., Nandra, K., Ellis, R. S., Conselice, C. J., Laird, E., Coil, A., Cooper, M. C., Faber, S. M., Newman, J. A., Pierce, C. M., Primack, J. R., & Yan, R. 2008, ApJ, 681, 931

Buson, L. M. & Ulrich, M. 1990, AA, 240, 247

Calzetti, D. 2001, PASP, 113, 1449

Calzetti, D., Armus, L., Bohlin, R. C., Kinney, A. L., Koornneef, J., & Storchi-Bergmann, T. 2000, ApJ, 533, 682

Calzetti, D., Kinney, A. L., & Storchi-Bergmann, T. 1994, ApJ, 429, 582

Cardamone, C. N., Urry, C. M., Schawinski, K., Treister, E., Brammer, G., & Gawiser, E. 2010, ApJL, 721, L38

Cardelli, J. A., Clayton, G. C., & Mathis, J. S. 1989, ApJ, 345, 245

Cassata, P., Cimatti, A., Kurk, J., Rodighiero, G., Pozzetti, L., Bolzonella, M., Daddi, E., Mignoli, M., Berta, S., Dickinson, M., Franceschini, A., Halliday, C., Renzini, A., Rosati, P., & Zamorani, G. 2008, AA, 483, L39

Chabrier, G. 2003, PASP, 115, 763

Chandar, R., Leitherer, C., Tremonti, C. A., Calzetti, D., Aloisi, A., Meurer, G. R., & de Mello, D. 2005, ApJ, 628, 210

Chapman, S. C., Blain, A. W., Smail, I., & Ivison, R. J. 2005, ApJ, 622, 772

Charlot, S., Kauffmann, G., Longhetti, M., Tresse, L., White, S. D. M., Maddox, S. J., & Fall, S. M. 2002, MNRAS, 330, 876

Chomiuk, L. & Povich, M. S. 2011, AJ, 142, 197

Coil, A. L., Georgakakis, A., Newman, J. A., Cooper, M. C., Croton, D., Davis, M., Koo, D. C., Laird, E. S., Nandra, K., Weiner, B. J., Willmer, C. N. A., & Yan, R. 2009, ApJ, 701, 1484

Contini, T., Treyer, M. A., Sullivan, M., & Ellis, R. S. 2002, MNRAS, 330, 75

Crenshaw, D. M., Kraemer, S. B., & George, I. M. 2003, ARAA, 41, 117

Croton, D. J., Springel, V., White, S. D. M., De Lucia, G., Frenk, C. S., Gao, L., Jenkins, A., Kauffmann, G., Navarro, J. F., & Yoshida, N. 2006, MNRAS, 365, 11

Daddi, E., Cimatti, A., Renzini, A., Vernet, J., Conselice, C., Pozzetti, L., Mignoli, M., Tozzi, P., Broadhurst, T., di Serego Alighieri, S., Fontana, A., Nonino, M., Rosati, P., & Zamorani, G. 2004, ApJL, 600, L127

Daddi, E., Dickinson, M., Morrison, G., Chary, R., Cimatti, A., Elbaz, D., Frayer, D., Renzini, A., Pope, A., Alexander, D. M., Bauer, F. E., Giavalisco, M., Huynh, M., Kurk, J., & Mignoli, M. 2007, ApJ, 670, 156

Davidson, K., Dufour, R. J., Walborn, N. R., & Gull, T. R. 1986, ApJ, 305, 867

Di Matteo, T., Colberg, J., Springel, V., Hernquist, L., & Sijacki, D. 2008, ApJ, 676, 33

Diamond-Stanic, A. M. & Rieke, G. H. 2012, ApJ, 746, 168

Diehl, H. T., Allam, S. S., Annis, J., Buckley-Geer, E. J., Frieman, J. A., Kubik, D., Kubo, J. M., Lin, H., Tucker, D., & West, A. 2009, ApJ, 707, 686

Donley, J. L., Koekemoer, A. M., Brusa, M., Capak, P., Cardamone, C. N., Civano, F., Ilbert, O., Impey, C. D., Kartaltepe, J. S., Miyaji, T., Salvato, M., Sanders, D. B., Trump, J. R., & Zamorani, G. 2012, ArXiv e-prints

Dopita, M. A. & Evans, I. N. 1986, ApJ, 307, 431

Dye, S., Evans, N. W., Belokurov, V., Warren, S. J., & Hewett, P. 2008, MNRAS, 388, 384

Elbaz, D., Daddi, E., Le Borgne, D., Dickinson, M., Alexander, D. M., Chary, R.-R., Starck, J.-L., Brandt, W. N., Kitzbichler, M., MacDonald, E., Nonino, M., Popesso, P., Stern, D., & Vanzella, E. 2007, AA, 468, 33

Elvis, M., Wilkes, B. J., McDowell, J. C., Green, R. F., Bechtold, J., Willner, S. P., Oey, M. S., Polomski, E., & Cutri, R. 1994, ApJS, 95, 1

Eminian, C., Kauffmann, G., Charlot, S., Wild, V., Bruzual, G., Rettura, A., & Loveday, J. 2008, MNRAS, 384, 930

Erb, D. K., Shapley, A. E., Pettini, M., Steidel, C. C., Reddy, N. A., & Adelberger, K. L. 2006a, ApJ, 644, 813

Erb, D. K., Shapley, A. E., Steidel, C. C., Pettini, M., Adelberger, K. L., Hunt, M. P., Moorwood, A. F. M., & Cuby, J. 2003, ApJ, 591, 101

Erb, D. K., Steidel, C. C., Shapley, A. E., Pettini, M., Reddy, N. A., & Adelberger, K. L. 2006b, ApJ, 647, 128

—. 2006c, ApJ, 646, 107

Fadda, D., Jannuzi, B. T., Ford, A., & Storrie-Lombardi, L. J. 2004, AJ, 128, 1

Fazio, G. G., Hora, J. L., Allen, L. E., Ashby, M. L. N., Barmby, P., Deutsch, L. K., Huang, J.-S., Kleiner, S., Marengo, M., Megeath, S. T., Melnick, G. J., Pahre, M. A., Patten, B. M., Polizotti, J., Smith, H. A., Taylor, R. S., Wang, Z., Willner, S. P., Hoffmann, W. F., Pipher, J. L., Forrest, W. J., McMurty, C. W., McCreight, C. R., McKelvey, M. E., McMurray, R. E., Koch, D. G., Moseley, S. H., Arendt, R. G., Mentzell, J. E., Marx, C. T., Losch, P., Mayman, P., Eichhorn, W., Krebs, D., Jhabvala, M., Gezari, D. Y., Fixsen, D. J., Flores, J., Shakoorzadeh, K., Jungo, R., Hakun, C., Workman, L., Karpati, G., Kichak, R., Whitley, R., Mann, S., Tollestrup, E. V., Eisenhardt, P., Stern, D., Gorjian, V., Bhattacharya, B., Carey, S., Nelson, B. O., Glaccum, W. J., Lacy, M., Lowrance, P. J., Laine, S., Reach, W. T., Stauffer, J. A., Surace, J. A., Wilson, G., Wright, E. L., Hoffman, A., Domingo, G., & Cohen, M. 2004, ApJS, 154, 10

Ferrarese, L. & Merritt, D. 2000, ApJL, 539, L9

Fosbury, R. A. E., Villar-Martín, M., Humphrey, A., Lombardi, M., Rosati, P., Stern, D., Hook, R. N., Holden, B. P., Stanford, S. A., Squires, G. K., Rauch, M., & Sargent, W. L. W. 2003, ApJ, 596, 797

Franx, M., Illingworth, G. D., Kelson, D. D., van Dokkum, P. G., & Tran, K. 1997, ApJL, 486, L75

Franx, M., Labbé, I., Rudnick, G., van Dokkum, P. G., Daddi, E., Förster Schreiber, N. M., Moorwood, A., Rix, H., Röttgering, H., van de Wel, A., van der Werf, P., & van Starkenburg, L. 2003, ApJL, 587, L79

Ganguly, R. & Brotherton, M. S. 2008, ApJ, 672, 102

Gebhardt, K., Bender, R., Bower, G., Dressler, A., Faber, S. M., Filippenko,

A. V., Green, R., Grillmair, C., Ho, L. C., Kormendy, J., Lauer, T. R., Magorrian, J., Pinkney, J., Richstone, D., & Tremaine, S. 2000, ApJL, 539, L13

Glikman, E., Djorgovski, S. G., Stern, D., Bogosavljević, M., & Mahabal, A. 2007, ApJL, 663, L73

Gordon, K. D. & Clayton, G. C. 1998, ApJ, 500, 816

Grogin, N. A., Kocevski, D. D., Faber, S. M., Ferguson, H. C., Koekemoer, A. M., Riess, A. G., Acquaviva, V., Alexander, D. M., Almaini, O., Ashby, M. L. N., Barden, M., Bell, E. F., Bournaud, F., Brown, T. M., Caputi, K. I., Casertano, S., Cassata, P., Castellano, M., Challis, P., Chary, R.-R., Cheung, E., Cirasuolo, M., Conselice, C. J., Roshan Cooray, A., Croton, D. J., Daddi, E., Dahlen, T., Davé, R., de Mello, D. F., Dekel, A., Dickinson, M., Dolch, T., Donley, J. L., Dunlop, J. S., Dutton, A. A., Elbaz, D., Fazio, G. G., Filippenko, A. V., Finkelstein, S. L., Fontana, A., Gardner, J. P., Garnavich, P. M., Gawiser, E., Giavalisco, M., Grazian, A., Guo, Y., Hathi, N. P., Häussler, B., Hopkins, P. F., Huang, J.-S., Huang, K.-H., Jha, S. W., Kartaltepe, J. S., Kirshner, R. P., Koo, D. C., Lai, K., Lee, K.-S., Li, W., Lotz, J. M., Lucas, R. A., Madau, P., McCarthy, P. J., McGrath, E. J., McIntosh, D. H., McLure, R. J., Mobasher, B., Moustakas, L. A., Mozena, M., Nandra, K., Newman, J. A., Niemi, S.-M., Noeske, K. G., Papovich, C. J., Pentericci, L., Pope, A., Primack, J. R., Rajan, A., Ravindranath, S., Reddy, N. A., Renzini, A., Rix, H.-W., Robaina, A. R., Rodney, S. A., Rosario, D. J., Rosati, P., Salimbeni, S., Scarlata, C., Siana, B., Simard, L., Smidt, J., Somerville, R. S., Spinrad, H., Straughn, A. N., Strolger, L.-G., Telford, O., Teplitz, H. I., Trump, J. R., van der Wel, A., Villforth, C., Wechsler, R. H., Weiner, B. J., Wiklind, T., Wild, V., Wilson, G., Wuyts, S., Yan, H.-J., & Yun, M. S. 2011, ApJS, 197, 35

Groves, B. A., Dopita, M. A., & Sutherland, R. S. 2004, ApJS, 153, 75

Gültekin, K., Richstone, D. O., Gebhardt, K., Lauer, T. R., Tremaine, S., Aller, M. C., Bender, R., Dressler, A., Faber, S. M., Filippenko, A. V., Green, R., Ho, L. C., Kormendy, J., Magorrian, J., Pinkney, J., & Siopis, C. 2009, ApJ, 698, 198

Hainline, K. N., Shapley, A. E., Greene, J. E., & Steidel, C. C. 2011, ApJ, 733, 31

Hainline, K. N., Shapley, A. E., Kornei, K. A., Pettini, M., Buckley-Geer, E., Allam, S. S., & Tucker, D. L. 2009, ApJ, 701, 52

Hainline, L., J., Blain, A. W., Smail, I., Alexander, D. M., Armus, L., Chapman, S. C., & Ivison, R. J. 2011, ApJ, 740, 96

Hamann, F., Korista, K. T., Ferland, G. J., Warner, C., & Baldwin, J. 2002, ApJ, 564, 592

Häring, N. & Rix, H. 2004, ApJL, 604, L89

Heckman, T. M., Kauffmann, G., Brinchmann, J., Charlot, S., Tremonti, C., & White, S. D. M. 2004, ApJ, 613, 109

Hickox, R. C., Jones, C., Forman, W. R., Murray, S. S., Brodwin, M., Brown, M. J. I., Eisenhardt, P. R., Stern, D., Kochanek, C. S., Eisenstein, D., Cool, R. J., Jannuzi, B. T., Dey, A., Brand, K., Gorjian, V., & Caldwell, N. 2007, ApJ, 671, 1365

Hickox, R. C., Jones, C., Forman, W. R., Murray, S. S., Kochanek, C. S., Eisenstein, D., Jannuzi, B. T., Dey, A., Brown, M. J. I., Stern, D., Eisenhardt, P. R.,

Gorjian, V., Brodwin, M., Narayan, R., Cool, R. J., Kenter, A., Caldwell, N., & Anderson, M. E. 2009, ApJ, 696, 891

Hopkins, A. M. 2004, ApJ, 615, 209

Hopkins, A. M. & Beacom, J. F. 2006, ApJ, 651, 142

Hopkins, P. F., Hernquist, L., Cox, T. J., Di Matteo, T., Robertson, B., & Springel, V. 2006, ApJS, 163, 1

Hopkins, P. F., Hernquist, L., Cox, T. J., & Kereš, D. 2008, ApJS, 175, 356

Hopkins, P. F., Richards, G. T., & Hernquist, L. 2007, ApJ, 654, 731

Humphrey, A., Villar-Martín, M., Vernet, J., Fosbury, R., di Serego Alighieri, S., & Binette, L. 2008, MNRAS, 383, 11

Jahnke, K. & Macciò, A. V. 2011, ApJ, 734, 92

Jansen, R. A., Fabricant, D., Franx, M., & Caldwell, N. 2000, ApJS, 126, 331

Jiang, L., Fan, X., & Vestergaard, M. 2008, ApJ, 679, 962

Kauffmann, G., Heckman, T. M., Tremonti, C., Brinchmann, J., Charlot, S., White, S. D. M., Ridgway, S. E., Brinkmann, J., Fukugita, M., Hall, P. B., Ivezić, Ž., Richards, G. T., & Schneider, D. P. 2003, MNRAS, 346, 1055

Kelson, D. D. 2003, PASP, 115, 688

Kennicutt, R. C. 1998, ARAA, 36, 189

Kennicutt, R. C., Bresolin, F., & Garnett, D. R. 2003, ApJ, 591, 801

Kennicutt, Jr., R. C. & Evans, II, N. J. 2012, ArXiv e-prints

Kewley, L. J. & Dopita, M. A. 2002, ApJS, 142, 35

Kewley, L. J., Dopita, M. A., Sutherland, R. S., Heisler, C. A., & Trevena, J. 2001a, ApJ, 556, 121

Kewley, L. J. & Ellison, S. L. 2008, ApJ, 681, 1183

Kewley, L. J., Heisler, C. A., Dopita, M. A., & Lumsden, S. 2001b, ApJS, 132, 37

Khalatyan, A., Cattaneo, A., Schramm, M., Gottlöber, S., Steinmetz, M., & Wisotzki, L. 2008, MNRAS, 387, 13

Kocevski, D. D., Faber, S. M., Mozena, M., Koekemoer, A. M., Nandra, K., Rangel, C., Laird, E. S., Brusa, M., Wuyts, S., Trump, J. R., Koo, D. C., Somerville, R. S., Bell, E. F., Lotz, J. M., Alexander, D. M., Bournaud, F., Conselice, C. J., Dahlen, T., Dekel, A., Donley, J. L., Dunlop, J. S., Finoguenov, A., Georgakakis, A., Giavalisco, M., Guo, Y., Grogin, N. A., Hathi, N. P., Juneau, S., Kartaltepe, J. S., Lucas, R. A., McGrath, E. J., McIntosh, D. H., Mobasher, B., Robaina, A. R., Rosario, D., Straughn, A. N., van der Wel, A., & Villforth, C. 2012, ApJ, 744, 148

Koekemoer, A. M., Faber, S. M., Ferguson, H. C., Grogin, N. A., Kocevski, D. D., Koo, D. C., Lai, K., Lotz, J. M., Lucas, R. A., McGrath, E. J., Ogaz, S., Rajan, A., Riess, A. G., Rodney, S. A., Strolger, L., Casertano, S., Castellano, M., Dahlen, T., Dickinson, M., Dolch, T., Fontana, A., Giavalisco, M., Grazian, A., Guo, Y., Hathi, N. P., Huang, K.-H., van der Wel, A., Yan, H.-J., Acquaviva, V., Alexander, D. M., Almaini, O., Ashby, M. L. N., Barden, M., Bell, E. F., Bournaud, F., Brown, T. M., Caputi, K. I., Cassata, P., Challis, P. J., Chary, R.-R., Cheung, E., Cirasuolo, M., Conselice, C. J., Roshan Cooray, A., Croton,

D. J., Daddi, E., Davé, R., de Mello, D. F., de Ravel, L., Dekel, A., Donley, J. L., Dunlop, J. S., Dutton, A. A., Elbaz, D., Fazio, G. G., Filippenko, A. V., Finkelstein, S. L., Frazer, C., Gardner, J. P., Garnavich, P. M., Gawiser, E., Gruetzbauch, R., Hartley, W. G., Häussler, B., Herrington, J., Hopkins, P. F., Huang, J.-S., Jha, S. W., Johnson, A., Kartaltepe, J. S., Khostovan, A. A., Kirshner, R. P., Lani, C., Lee, K.-S., Li, W., Madau, P., McCarthy, P. J., McIntosh, D. H., McLure, R. J., McPartland, C., Mobasher, B., Moreira, H., Mortlock, A., Moustakas, L. A., Mozena, M., Nandra, K., Newman, J. A., Nielsen, J. L., Niemi, S., Noeske, K. G., Papovich, C. J., Pentericci, L., Pope, A., Primack, J. R., Ravindranath, S., Reddy, N. A., Renzini, A., Rix, H.-W., Robaina, A. R., Rosario, D. J., Rosati, P., Salimbeni, S., Scarlata, C., Siana, B., Simard, L., Smidt, J., Snyder, D., Somerville, R. S., Spinrad, H., Straughn, A. N., Telford, O., Teplitz, H. I., Trump, J. R., Vargas, C., Villforth, C., Wagner, C. R., Wandro, P., Wechsler, R. H., Weiner, B. J., Wiklind, T., Wild, V., Wilson, G., Wuyts, S., & Yun, M. S. 2011, ApJS, 197, 36

Korista, K. T., Bautista, M. A., Arav, N., Moe, M., Costantini, E., & Benn, C. 2008, ApJ, 688, 108

Kormendy, J. & Richstone, D. 1995, ARAA, 33, 581

Kornei, K. A., Shapley, A. E., Erb, D. K., Steidel, C. C., Reddy, N. A., Pettini, M., & Bogosavljević, M. 2010, ApJ, 711, 693

Kriek, M., van der Wel, A., van Dokkum, P. G., Franx, M., & Illingworth, G. D. 2008, ApJ, 682, 896

Kriek, M., van Dokkum, P. G., Franx, M., Illingworth, G. D., Coppi, P., Förster Schreiber, N. M., Gawiser, E., Labbé, I., Lira, P., Marchesini, D., Quadri, R.,

Rudnick, G., Taylor, E. N., Urry, C. M., & van der Werf, P. P. 2007, ApJ, 669, 776

Krug, H. B., Rupke, D. S. N., & Veilleux, S. 2010, ApJ, 708, 1145

Labbé, I., Franx, M., Rudnick, G., Schreiber, N. M. F., van Dokkum, P. G., Moorwood, A., Rix, H.-W., Röttgering, H., Trujillo, I., & van der Werf, P. 2007, ApJ, 665, 944

Lacy, M., Storrie-Lombardi, L. J., Sajina, A., Appleton, P. N., Armus, L., Chapman, S. C., Choi, P. I., Fadda, D., Fang, F., Frayer, D. T., Heinrichsen, I., Helou, G., Im, M., Marleau, F. R., Masci, F., Shupe, D. L., Soifer, B. T., Surace, J., Teplitz, H. I., Wilson, G., & Yan, L. 2004, ApJS, 154, 166

Lacy, M., Wilson, G., Masci, F., Storrie-Lombardi, L. J., Appleton, P. N., Armus, L., Chapman, S. C., Choi, P. I., Fadda, D., Fang, F., Frayer, D. T., Heinrichsen, I., Helou, G., Im, M., Laine, S., Marleau, F. R., Shupe, D. L., Soifer, B. T., Squires, G. K., Surace, J., Teplitz, H. I., & Yan, L. 2005, ApJS, 161, 41

Lauer, T. R., Faber, S. M., Richstone, D., Gebhardt, K., Tremaine, S., Postman, M., Dressler, A., Aller, M. C., Filippenko, A. V., Green, R., Ho, L. C., Kormendy, J., Magorrian, J., & Pinkney, J. 2007, ApJ, 662, 808

Law, D. R., Steidel, C. C., Erb, D. K., Pettini, M., Reddy, N. A., Shapley, A. E., Adelberger, K. L., & Simenc, D. J. 2007, ApJ, 656, 1

Lemoine-Busserolle, M., Contini, T., Pelló, R., Le Borgne, J., Kneib, J., & Lidman, C. 2003, AA, 397, 839

Lilly, S. J., Carollo, C. M., & Stockton, A. N. 2003, ApJ, 597, 730

Lin, H., Buckley-Geer, E., Allam, S. S., Tucker, D. L., Diehl, H. T., Kubik, D., Kubo, J. M., Annis, J., Frieman, J. A., Oguri, M., & Inada, N. 2009, ApJ, 699, 1242

Liu, X., Shapley, A. E., Coil, A. L., Brinchmann, J., & Ma, C. 2008, ApJ, 678, 758

Lynden-Bell, D. 1969, Nature, 223, 690

Madau, P. 1995, ApJ, 441, 18

Madau, P., Ferguson, H. C., Dickinson, M. E., Giavalisco, M., Steidel, C. C., & Fruchter, A. 1996, MNRAS, 283, 1388

Magorrian, J., Tremaine, S., Richstone, D., Bender, R., Bower, G., Dressler, A., Faber, S. M., Gebhardt, K., Green, R., Grillmair, C., Kormendy, J., & Lauer, T. 1998, AJ, 115, 2285

Mainieri, V., Bongiorno, A., Merloni, A., Aller, M., Carollo, M., Iwasawa, K., Koekemoer, A. M., Mignoli, M., Silverman, J. D., Bolzonella, M., Brusa, M., Comastri, A., Gilli, R., Halliday, C., Ilbert, O., Lusso, E., Salvato, M., Vignali, C., Zamorani, G., Contini, T., Kneib, J.-P., Le Fèvre, O., Lilly, S., Renzini, A., Scodeggio, M., Balestra, I., Bardelli, S., Caputi, K., Coppa, G., Cucciati, O., de la Torre, S., de Ravel, L., Franzetti, P., Garilli, B., Iovino, A., Kampczyk, P., Knobel, C., Kovač, K., Lamareille, F., Le Borgne, J.-F., Le Brun, V., Maier, C., Nair, P., Pello, R., Peng, Y., Perez Montero, E., Pozzetti, L., Ricciardelli, E., Tanaka, M., Tasca, L., Tresse, L., Vergani, D., Zucca, E., Aussel, H., Capak, P., Cappelluti, N., Elvis, M., Fiore, F., Hasinger, G., Impey, C., Le Floc'h, E., Scoville, N., Taniguchi, Y., & Trump, J. 2011, AA, 535, A80

Maiolino, R., Nagao, T., Grazian, A., Cocchia, F., Marconi, A., Mannucci, F., Cimatti, A., Pipino, A., Ballero, S., Calura, F., Chiappini, C., Fontana, A., Granato, G. L., Matteucci, F., Pastorini, G., Pentericci, L., Risaliti, G., Salvati, M., & Silva, L. 2008, AA, 488, 463

Maíz Apellániz, J. 2006, AJ, 131, 1184

Maraston, C. 2005, MNRAS, 362, 799

Maraston, C., Daddi, E., Renzini, A., Cimatti, A., Dickinson, M., Papovich, C., Pasquali, A., & Pirzkal, N. 2006, ApJ, 652, 85

Maraston, C., Pforr, J., Renzini, A., Daddi, E., Dickinson, M., Cimatti, A., & Tonini, C. 2010, MNRAS, 407, 830

Martin, C. L. 2005, ApJ, 621, 227

Martini, P., Persson, S. E., Murphy, D. C., Birk, C., Shectman, S. A., Gunnels, S. M., & Koch, E. 2004, in Society of Photo-Optical Instrumentation Engineers (SPIE) Conference Series, Vol. 5492, Society of Photo-Optical Instrumentation Engineers (SPIE) Conference Series, ed. A. F. M. Moorwood & M. Iye, 1653–1660

Matsuoka, K., Nagao, T., Maiolino, R., Marconi, A., & Taniguchi, Y. 2009, AA, 503, 721

McCall, M. L., Rybski, P. M., & Shields, G. A. 1985, ApJS, 57, 1

McLean, I. S., Becklin, E. E., Bendiksen, O., Brims, G., Canfield, J., Figer, D. F., Graham, J. R., Hare, J., Lacayanga, F., Larkin, J. E., Larson, S. B., Levenson, N., Magnone, N., Teplitz, H., & Wong, W. 1998, in Proc. SPIE Vol. 3354, p.

566-578, Infrared Astronomical Instrumentation, Albert M. Fowler; Ed., Vol. 3354, 566–578

Menci, N., Fontana, A., Giallongo, E., Grazian, A., & Salimbeni, S. 2006, ApJ, 647, 753

Merloni, A., Bongiorno, A., Bolzonella, M., Brusa, M., Civano, F., Comastri, A., Elvis, M., Fiore, F., Gilli, R., Hao, H., Jahnke, K., Koekemoer, A. M., Lusso, E., Mainieri, V., Mignoli, M., Miyaji, T., Renzini, A., Salvato, M., Silverman, J., Trump, J., Vignali, C., Zamorani, G., Capak, P., Lilly, S. J., Sanders, D., Taniguchi, Y., Bardelli, S., Carollo, C. M., Caputi, K., Contini, T., Coppa, G., Cucciati, O., de la Torre, S., de Ravel, L., Franzetti, P., Garilli, B., Hasinger, G., Impey, C., Iovino, A., Iwasawa, K., Kampczyk, P., Kneib, J.-P., Knobel, C., Kovač, K., Lamareille, F., Le Borgne, J.-F., Le Brun, V., Le Fèvre, O., Maier, C., Pello, R., Peng, Y., Perez Montero, E., Ricciardelli, E., Scodeggio, M., Tanaka, M., Tasca, L. A. M., Tresse, L., Vergani, D., & Zucca, E. 2010, ApJ, 708, 137

Merritt, D. & Ferrarese, L. 2001, ApJ, 547, 140

Murray, N., Quataert, E., & Thompson, T. A. 2005, ApJ, 618, 569

Nagao, T., Maiolino, R., & Marconi, A. 2006a, AA, 447, 863

Nagao, T., Marconi, A., & Maiolino, R. 2006b, AA, 447, 157

Nandra, K., Georgakakis, A., Willmer, C. N. A., Cooper, M. C., Croton, D. J., Davis, M., Faber, S. M., Koo, D. C., Laird, E. S., & Newman, J. A. 2007, ApJL, 660, L11

Nesvadba, N. P. H., Lehnert, M. D., De Breuck, C., Gilbert, A. M., & van Breugel, W. 2008, AA, 491, 407

Nesvadba, N. P. H., Lehnert, M. D., Eisenhauer, F., Gilbert, A., Tecza, M., & Abuter, R. 2006, ApJ, 650, 693

Neugebauer, G., Oke, J. B., Becklin, E. E., & Matthews, K. 1979, ApJ, 230, 79

Nilsson, K. K., Tapken, C., Møller, P., Freudling, W., Fynbo, J. P. U., Meisenheimer, K., Laursen, P., & Östlin, G. 2009, AA, 498, 13

Noeske, K. G., Weiner, B. J., Faber, S. M., Papovich, C., Koo, D. C., Somerville, R. S., Bundy, K., Conselice, C. J., Newman, J. A., Schiminovich, D., Le Floc'h, E., Coil, A. L., Rieke, G. H., Lotz, J. M., Primack, J. R., Barmby, P., Cooper, M. C., Davis, M., Ellis, R. S., Fazio, G. G., Guhathakurta, P., Huang, J., Kassin, S. A., Martin, D. C., Phillips, A. C., Rich, R. M., Small, T. A., Willmer, C. N. A., & Wilson, G. 2007, ApJL, 660, L43

Oke, J. B., Cohen, J. G., Carr, M., Cromer, J., Dingizian, A., Harris, F. H., Labrecque, S., Lucinio, R., Schaal, W., Epps, H., & Miller, J. 1995, PASP, 107, 375

Osterbrock, D. E. 1989, Astrophysics of gaseous nebulae and active galactic nuclei (University Science Books)

Pagel, B. E. J., Edmunds, M. G., Blackwell, D. E., Chun, M. S., & Smith, G. 1979, MNRAS, 189, 95

Pannella, M., Carilli, C. L., Daddi, E., McCracken, H. J., Owen, F. N., Renzini, A., Strazzullo, V., Civano, F., Koekemoer, A. M., Schinnerer, E., Scoville, N., Smolčić, V., Taniguchi, Y., Aussel, H., Kneib, J. P., Ilbert, O., Mellier, Y., Salvato, M., Thompson, D., & Willott, C. J. 2009, ApJL, 698, L116

Papovich, C., Dickinson, M., & Ferguson, H. C. 2001, ApJ, 559, 620

Papovich, C., Finkelstein, S. L., Ferguson, H. C., Lotz, J. M., & Giavalisco, M. 2011, MNRAS, 412, 1123

Park, S. Q., Barmby, P., Willner, S. P., Ashby, M. L. N., Fazio, G. G., Georgakakis, A., Ivison, R. J., Konidaris, N. P., Miyazaki, S., Nandra, K., & Rosario, D. J. 2010, ApJ, 717, 1181

Peng, C. Y. 2007, ApJ, 671, 1098

Peng, C. Y., Impey, C. D., Rix, H., Kochanek, C. S., Keeton, C. R., Falco, E. E., Lehár, J., & McLeod, B. A. 2006, ApJ, 649, 616

Pentericci, L., Grazian, A., Fontana, A., Salimbeni, S., Santini, P., de Santis, C., Gallozzi, S., & Giallongo, E. 2007, AA, 471, 433

Persson, S. E., Murphy, D. C., Krzeminski, W., Roth, M., & Rieke, M. J. 1998, AJ, 116, 2475

Pettini, M. & Pagel, B. E. J. 2004, MNRAS, 348, L59

Pettini, M., Rix, S. A., Steidel, C. C., Adelberger, K. L., Hunt, M. P., & Shapley, A. E. 2002, ApJ, 569, 742

Pettini, M., Shapley, A. E., Steidel, C. C. andC̃uby, J.-G., Dickinson, M., Moorwood, A. F. M. andÃdelberger, K. L., & Giavalisco, M. 2001, ApJ, 554, 981

Pettini, M., Steidel, C. C., Adelberger, K. L., Dickinson, M., & Giavalisco, M. 2000, ApJ, 528, 96

Quider, A. M., Pettini, M., Shapley, A. E., & Steidel, C. C. 2009, MNRAS, 398, 1263

Quider, A. M., Shapley, A. E., Pettini, M., Steidel, C. C., & Stark, D. P. 2010, MNRAS, 402, 1467

Raiter, A., Fosbury, R. A. E., & Teimoorinia, H. 2010, AA, 510, A109+

Reddy, N. A., Erb, D. K., Pettini, M., Steidel, C. C., & Shapley, A. E. 2010, ApJ, 712, 1070

Reddy, N. A., Pettini, M., Steidel, C. C., Shapley, A. E., Erb, D. K., & Law, D. R. 2012, ArXiv e-prints

Reddy, N. A. & Steidel, C. C. 2004, ApJL, 603, L13

Reddy, N. A., Steidel, C. C., Erb, D. K., Shapley, A. E., & Pettini, M. 2006a, ApJ, 653, 1004

Reddy, N. A., Steidel, C. C., Fadda, D., Yan, L., Pettini, M., Shapley, A. E., Erb, D. K., & Adelberger, K. L. 2006b, ApJ, 644, 792

Reddy, N. A., Steidel, C. C., Pettini, M., Adelberger, K. L., Shapley, A. E., Erb, D. K., & Dickinson, M. 2007, ArXiv e-prints, 706

—. 2008, ApJS, 175, 48

Rees, M. J. 1984, ARAA, 22, 471

Rees, M. J., Silk, J. I., Werner, M. W., & Wickramasinghe, N. C. 1969, Nature, 223, 788

Richards, G. T., Lacy, M., Storrie-Lombardi, L. J., Hall, P. B., Gallagher, S. C., Hines, D. C., Fan, X., Papovich, C., Vanden Berk, D. E., Trammell, G. B., Schneider, D. P., Vestergaard, M., York, D. G., Jester, S., Anderson, S. F., Budavári, T., & Szalay, A. S. 2006, ApJS, 166, 470

Rovilos, E., Fotopoulou, S., Salvato, M., Burwitz, V., Egami, E., Hasinger, G., & Szokoly, G. 2011, AA, 529, A135

Rupke, D. S., Veilleux, S., & Sanders, D. B. 2005a, ApJ, 632, 751

—. 2005b, ApJS, 160, 87

—. 2005c, ApJS, 160, 115

Salim, S., Rich, R. M., Charlot, S., Brinchmann, J., Johnson, B. D., Schiminovich, D., Seibert, M., Mallery, R., Heckman, T. M., Forster, K., Friedman, P. G., Martin, D. C., Morrissey, P., Neff, S. G., Small, T., Wyder, T. K., Bianchi, L., Donas, J., Lee, Y.-W., Madore, B. F., Milliard, B., Szalay, A. S., Welsh, B. Y., & Yi, S. K. 2007, ApJS, 173, 267

Salpeter, E. E. 1955, ApJ, 121, 161

—. 1964, ApJ, 140, 796

Santini, P., Rosario, D., Shao, L., Lutz, D., Maiolino, R., Alexander, D. M., Altieri, B., Andreani, P., Aussel, H., Bauer, F. E., Berta, S., Bongiovanni, A., Brandt, W. N., Brusa, M., Cepa, J., Cimatti, A., Daddi, E., Elbaz, D., Fontana, A., Forster Schreiber, N. M., Genzel, R., Grazian, A., Le Floc'h, E., Magnelli, B., Mainieri, V., Nordon, R., Perez Garcia, A. M., Poglitsch, A., Popesso, P., Pozzi, F., Riguccini, L., Rodighiero, G., Salvato, M., Sanchez-Portal, M., Sturm, E., Tacconi, L. J., Valtchanov, I., & Wuyts, S. 2012, ArXiv e-prints

Sawicki, M. 2001, AJ, 121, 2405

Sawicki, M. & Yee, H. K. C. 1998, AJ, 115, 1329

Schaerer, D. & de Barros, S. 2011, ArXiv e-prints

Schawinski, K., Thomas, D., Sarzi, M., Maraston, C., Kaviraj, S., Joo, S.-J., Yi, S. K., & Silk, J. 2007, MNRAS, 382, 1415

Schawinski, K., Urry, C. M., Virani, S., Coppi, P., Bamford, S. P., Treister, E., Lintott, C. J., Sarzi, M., Keel, W. C., Kaviraj, S., Cardamone, C. N., Masters, K. L., Ross, N. P., Andreescu, D., Murray, P., Nichol, R. C., Raddick, M. J., Slosar, A., Szalay, A. S., Thomas, D., & Vandenberg, J. 2010, ApJ, 711, 284

Seitz, S., Saglia, R. P., Bender, R., Hopp, U., Belloni, P., & Ziegler, B. 1998, MNRAS, 298, 945

Shakura, N. I. & Sunyaev, R. A. 1973, AA, 24, 337

Shapley, A. E. 2011, ARAA, 49, 525

Shapley, A. E., Coil, A. L., Ma, C.-P., & Bundy, K. 2005a, ApJ, 635, 1006

Shapley, A. E., Erb, D. K., Pettini, M., Steidel, C. C., & Adelberger, K. L. 2004, ApJ, 612, 108

Shapley, A. E., Steidel, C. C., Adelberger, K. L., Dickinson, M., Giavalisco, M., & Pettini, M. 2001, ApJ, 562, 95

Shapley, A. E., Steidel, C. C., Erb, D. K., Reddy, N. A., Adelberger, K. L., Pettini, M., Barmby, P., & Huang, J. 2005b, ApJ, 626, 698

Shapley, A. E., Steidel, C. C., Pettini, M., & Adelberger, K. L. 2003, ApJ, 588, 65

Shapley, A. E., Steidel, C. C., Pettini, M., Adelberger, K. L., & Erb, D. K. 2006, ApJ, 651, 688

Sheinis, A. I., Bolte, M., Epps, H. W., Kibrick, R. I., Miller, J. S., Radovan, M. V., Bigelow, B. C., & Sutin, B. M. 2002, PASP, 114, 851

Shuder, J. M. 1981, ApJ, 244, 12

Siana, B., Teplitz, H. I., Chary, R.-R., Colbert, J., & Frayer, D. T. 2008, ApJ, 689, 59

Silk, J. & Rees, M. J. 1998, AA, 331, L1

Silverman, J. D., Green, P. J., Barkhouse, W. A., Kim, D., Kim, M., Wilkes, B. J., Cameron, R. A., Hasinger, G., Jannuzi, B. T., Smith, M. G., Smith, P. S., & Tananbaum, H. 2008, ApJ, 679, 118

Silverman, J. D., Lamareille, F., Maier, C., Lilly, S. J., Mainieri, V., Brusa, M., Cappelluti, N., Hasinger, G., Zamorani, G., Scodeggio, M., Bolzonella, M., Contini, T., Carollo, C. M., Jahnke, K., Kneib, J.-P., Le Fèvre, O., Merloni, A., Bardelli, S., Bongiorno, A., Brunner, H., Caputi, K., Civano, F., Comastri, A., Coppa, G., Cucciati, O., de la Torre, S., de Ravel, L., Elvis, M., Finoguenov, A., Fiore, F., Franzetti, P., Garilli, B., Gilli, R., Iovino, A., Kampczyk, P., Knobel, C., Kovač, K., Le Borgne, J.-F., Le Brun, V., Mignoli, M., Pello, R., Peng, Y., Perez Montero, E., Ricciardelli, E., Tanaka, M., Tasca, L., Tresse, L., Vergani, D., Vignali, C., Zucca, E., Bottini, D., Cappi, A., Cassata, P., Fumana, M., Griffiths, R., Kartaltepe, J., Koekemoer, A., Marinoni, C., McCracken, H. J., Memeo, P., Meneux, B., Oesch, P., Porciani, C., & Salvato, M. 2009, ApJ, 696, 396

Simpson, C. 2005, MNRAS, 360, 565

Smail, I., Swinbank, A. M., Richard, J., Ebeling, H., Kneib, J.-P., Edge, A. C., Stark, D., Ellis, R. S., Dye, S., Smith, G. P., & Mullis, C. 2007, ApJL, 654, L33

Soltan, A. 1982, MNRAS, 200, 115

Somerville, R. S., Hopkins, P. F., Cox, T. J., Robertson, B. E., & Hernquist, L. 2008, MNRAS, 391, 481

Steidel, C. C., Adelberger, K. L., Giavalisco, M., Dickinson, M., & Pettini, M. 1999, ApJ, 519, 1

Steidel, C. C., Adelberger, K. L., Shapley, A. E., Pettini, M., Dickinson, M., & Giavalisco, M. 2003, ApJ, 592, 728

Steidel, C. C., Erb, D. K., Shapley, A. E., Pettini, M., Reddy, N., Bogosavljević, M., Rudie, G. C., & Rakic, O. 2010, ApJ, 717, 289

Steidel, C. C., Giavalisco, M., Pettini, M., Dickinson, M., & Adelberger, K. L. 1996, ApJL, 462, L17+

Steidel, C. C., Hunt, M. P., Shapley, A. E., Adelberger, K. L., Pettini, M., Dickinson, M., & Giavalisco, M. 2002, ApJ, 576, 653

Steidel, C. C., Shapley, A. E., Pettini, M., Adelberger, K. L., Erb, D. K., Reddy, N. A., & Hunt, M. P. 2004, ApJ, 604, 534

Stern, D., Eisenhardt, P., Gorjian, V., Kochanek, C. S., Caldwell, N., Eisenstein, D., Brodwin, M., Brown, M. J. I., Cool, R., Dey, A., Green, P., Jannuzi, B. T., Murray, S. S., Pahre, M. A., & Willner, S. P. 2005, ApJ, 631, 163

Teplitz, H. I., McLean, I. S., Becklin, E. E., Figer, D. F., Gilbert, A. M., Graham, J. R., Larkin, J. E., Levenson, N. A., & Wilcox, M. K. 2000, ApJL, 533, L65

Thacker, R. J., Scannapieco, E., & Couchman, H. M. P. 2006, ApJ, 653, 86

Tremonti, C. A., Heckman, T. M., Kauffmann, G., Brinchmann, J., Charlot, S., White, S. D. M., Seibert, M., Peng, E. W., Schlegel, D. J., Uomoto, A., Fukugita, M., & Brinkmann, J. 2004, ApJ, 613, 898

Tremonti, C. A., Moustakas, J., & Diamond-Stanic, A. M. 2007, ApJL, 663, L77

Ueda, Y., Akiyama, M., Ohta, K., & Miyaji, T. 2003, ApJ, 598, 886

van Dokkum, P. G., Förster Schreiber, N. M., Franx, M., Daddi, E., Illingworth, G. D., Labbé, I., Moorwood, A., Rix, H., Röttgering, H., Rudnick, G., van der Wel, A., van der Werf, P., & van Starkenburg, L. 2003, ApJL, 587, L83

van Dokkum, P. G., Franx, M., Förster Schreiber, N. M., Illingworth, G. D., Daddi, E., Knudsen, K. K., Labbé, I., Moorwood, A., Rix, H., Röttgering, H., Rudnick, G., Trujillo, I., van der Werf, P., van der Wel, A., van Starkenburg, L., & Wuyts, S. 2004, ApJ, 611, 703

van Dokkum, P. G., Kriek, M., Rodgers, B., Franx, M., & Puxley, P. 2005, ApJL, 622, L13

Vanzella, E., Giavalisco, M., Dickinson, M., Cristiani, S., Nonino, M., Kuntschner, H., Popesso, P., Rosati, P., Renzini, A., Stern, D., Cesarsky, C., Ferguson, H. C., & Fosbury, R. A. E. 2009, ApJ, 695, 1163

Verhamme, A., Schaerer, D., Atek, H., & Tapken, C. 2008, AA, 491, 89

Vernet, J., Fosbury, R. A. E., Villar-Martín, M., Cohen, M. H., Cimatti, A., di Serego Alighieri, S., & Goodrich, R. W. 2001, AA, 366, 7

Vestergaard, M. & Osmer, P. S. 2009, ApJ, 699, 800

Villar-Martín, M., Alonso-Herrero, A., di Serego Alighieri, S., & Vernet, J. 2000, AAPS, 147, 291

Villar-Martin, M., Tadhunter, C., & Clark, N. 1997, AA, 323, 21

Villar-Martín, M., Vernet, J., di Serego Alighieri, S., Fosbury, R., Humphrey, A., & Pentericci, L. 2003, MNRAS, 346, 273

Wild, V., Kauffmann, G., Heckman, T., Charlot, S., Lemson, G., Brinchmann, J., Reichard, T., & Pasquali, A. 2007, MNRAS, 381, 543

Williams, L. L. R. & Lewis, G. F. 1996, MNRAS, 281, L35

Williams, R. J., Quadri, R. F., Franx, M., van Dokkum, P., & Labbé, I. 2009, ApJ, 691, 1879

Xue, Y. Q., Brandt, W. N., Luo, B., Rafferty, D. A., Alexander, D. M., Bauer, F. E., Lehmer, B. D., Schneider, D. P., & Silverman, J. D. 2010, ApJ, 720, 368

Yee, H. K. C. 1980, ApJ, 241, 894

Yee, H. K. C., Ellingson, E., Bechtold, J., Carlberg, R. G., & Cuillandre, J.-C. 1996, AJ, 111, 1783

York, D. G., Adelman, J., Anderson, Jr., J. E., Anderson, S. F., Annis, J., Bahcall, N. A., Bakken, J. A., Barkhouser, R., Bastian, S., Berman, E., Boroski, W. N., Bracker, S., Briegel, C., Briggs, J. W., Brinkmann, J., Brunner, R., Burles, S., Carey, L., Carr, M. A., Castander, F. J., Chen, B., Colestock, P. L., Connolly, A. J., Crocker, J. H., Csabai, I., Czarapata, P. C., Davis, J. E., Doi, M., Dombeck, T., Eisenstein, D., Ellman, N., Elms, B. R., Evans, M. L., Fan, X., Federwitz, G. R., Fiscelli, L., Friedman, S., Frieman, J. A., Fukugita, M., Gillespie, B., Gunn, J. E., Gurbani, V. K., de Haas, E., Haldeman, M., Harris, F. H., Hayes, J., Heckman, T. M., Hennessy, G. S., Hindsley, R. B., Holm, S., Holmgren, D. J., Huang, C.-h., Hull, C., Husby, D., Ichikawa, S.-I., Ichikawa, T., Ivezić, Ž., Kent, S., Kim, R. S. J., Kinney, E., Klaene, M., Kleinman, A. N., Kleinman, S., Knapp, G. R., Korienek, J., Kron, R. G., Kunszt, P. Z., Lamb, D. Q., Lee, B., Leger, R. F., Limmongkol, S., Lindenmeyer, C., Long, D. C., Loomis, C., Loveday, J., Lucinio, R., Lupton, R. H., MacKinnon, B., Mannery,

E. J., Mantsch, P. M., Margon, B., McGehee, P., McKay, T. A., Meiksin, A., Merelli, A., Monet, D. G., Munn, J. A., Narayanan, V. K., Nash, T., Neilsen, E., Neswold, R., Newberg, H. J., Nichol, R. C., Nicinski, T., Nonino, M., Okada, N., Okamura, S., Ostriker, J. P., Owen, R., Pauls, A. G., Peoples, J., Peterson, R. L., Petravick, D., Pier, J. R., Pope, A., Pordes, R., Prosapio, A., Rechenmacher, R., Quinn, T. R., Richards, G. T., Richmond, M. W., Rivetta, C. H., Rockosi, C. M., Ruthmansdorfer, K., Sandford, D., Schlegel, D. J., Schneider, D. P., Sekiguchi, M., Sergey, G., Shimasaku, K., Siegmund, W. A., Smee, S., Smith, J. A., Snedden, S., Stone, R., Stoughton, C., Strauss, M. A., Stubbs, C., SubbaRao, M., Szalay, A. S., Szapudi, I., Szokoly, G. P., Thakar, A. R., Tremonti, C., Tucker, D. L., Uomoto, A., Vanden Berk, D., Vogeley, M. S., Waddell, P., Wang, S.-i., Watanabe, M., Weinberg, D. H., Yanny, B., Yasuda, N., & SDSS Collaboration. 2000, AJ, 120, 1579

Zakamska, N. L., Strauss, M. A., Krolik, J. H., Ridgway, S. E., Schmidt, G. D., Smith, P. S., Heckman, T. M., Schneider, D. P., Hao, L., & Brinkmann, J. 2006, AJ, 132, 1496